

Prof. Ulrich Schubert

Prof. Herwig Peterlik



TECHNISCHE  
UNIVERSITÄT  
WIEN

DISSERTATION

CROSS-LINKED CYANOMETALLATE  
NETWORKS OF Ni(II) AND Fe(III)  
IN SILICA

ausgeführt zum Zwecke der Erlangung des akademischen Grades  
eines Doktors der Naturwissenschaften

unter der Leitung von

O.Univ.Prof. Dipl.Ing. Dr.rer.nat. Ulrich Schubert  
E165 Institut für Materialchemie

eingereicht an der Technischen Universität Wien  
Fakultät für Technische Chemie

von

**Elisabeth Felbermair**

0505296

Quellenstraße 109/16  
1100 Wien

Wien, am 29. September 2015



*The least important things,  
sometimes, lead to the  
greatest discoveries.*

---

The First Doctor  
Doctor Who, "The Space Museum".





## Acknowledgements

I want to thank all the people that accompanied me in my life, especially during the last four years through the ups and downs of my dissertation.

First and foremost I thank Prof. Schubert for giving me the opportunity to work in his group on a very interesting and challenging topic. Furthermore I am thankful for the support and scientific freedom he gave me.

I want to thank my far-travelled student intern Anni for the fun we had during the three months working together, and for the nice visit to Dresden.

I am grateful to the people that contributed to this work, without whose help it would not have been possible: Johanna Akbarzadeh and Prof. Peterlik who performed the SAXS measurements and analysis, Andrey Sidorenko who performed the SQUID measurements and instructed me on the interpretation of the results, and Elisabeth Eitenberger who performed SEM and EDX measurements.

I thank all my current and former colleagues for the nice atmosphere, for helping hands and thoughts/ideas, and for the fun during breaks and parties: Aparna; Catarina; Christian for the occasional train rides towards Upper Austria and knowing the exact storage place of any chemical in the lab; Christine for some XRD measurements, for being an entertaining office companion and conference (room) buddy; Czaky for educating me about the geography of the Weinviertel and about climbing; Felix for the feeling of having a little brother; Harald; Johannes; Marco; Martin; Martina; Patrik; Rupert for taking exquisite care of the vacuum pumps; Sarah; Stefan C.; Stefan E.; Stephan; Sven; Van An for leaving behind a lot of scribbling-paper and a nice desk for me; Wenjing; and Yingxia for being a perfect lab companion.

Thanks to Anita for offering sweets and compliments whenever I met her on the corridor or visited her in her office, and for her friendly help in administrative tasks.

I thank André for organizing interesting and relaxing Solids4Fun summer schools and for including me in the decision on the very nice location.

I am thankful for the many amusing hours of “Werewolf” played with my Solids4Fun colleagues during the summer schools, and for the insights into physics and electrical engineering research I gained through them.

A warm thank you also to all the members of our neighbors, the Kirchner group, for “borrowing” chemicals and for the superb carnival parties with (too much) home-made Krapfen.

I want to thank my family, especially my parents, who always encouraged me to pursue my goals and to be confident and kind. I thank also my big brother Samuel, who shared his experience on studying in Vienna when I first started and moved in with him.

Finally, I thank Peter for assisting me on software issues, for spending weekends and adventurous holidays with me, and for sharing life in all its facets with me.



## Abstract

Reactions of Ni<sup>II</sup> complexes of the type [Ni(polyamine)<sub>n</sub>]<sup>2+</sup> (n = 1, 2, 3) and [Fe(CN)<sub>6</sub>]<sup>3-</sup> commonly lead to cyanometallate networks by formation of cyanide bridges Fe<sup>III</sup>–C≡N–Ni<sup>II</sup>. The resulting [Ni(polyamine)<sub>n</sub>]<sub>x</sub>[Fe(CN)<sub>6</sub>]<sub>y</sub> structures often exhibit ferromagnetism caused by magnetic coupling of unpaired electrons of the Ni<sup>II</sup> and Fe<sup>III</sup> ions through the cyanide bridges.

The polyamine ligands block coordination sites of Ni<sup>II</sup> which limits the possibilities to form cyanide bridges. This favors a low-dimensional (1D, 2D) arrangement of the cyanometallates. Diamines or tetramines are typically used for this purpose as they have high affinity to Ni<sup>II</sup>.

In this work such low-dimensional cyanometallates are embedded in SiO<sub>2</sub> by means of sol-gel processing. A chemical link is established between the cyanometallate and SiO<sub>2</sub> matrix to make the cohesion more stable. This is achieved by introducing linker groups into the organic blocking ligands. The linker consists of an alkyl chain with a trialkoxysilyl group that reacts with the SiO<sub>2</sub> precursor tetraethoxysilane (TEOS) during sol-gel processing, thus forming covalent bonds. The influence of this process on the structure of the cyanometallate network and its magnetic properties is studied by FTIR spectroscopy, SEM, EDX, SWAXS and SQUID.

Five Ni<sup>II</sup>–Fe<sup>III</sup> cyanometallates with various blocking ligands are discussed in this work and the influence of the ligands on the structure and magnetic properties assessed.

[Ni(AEAPTS)<sub>2</sub>]<sub>3</sub>[Fe(CN)<sub>6</sub>]<sub>2</sub> (AEAPTS = N-(2-aminoethyl)-3-(trimethoxysilyl)propylamine) forms a 1D double chain structure with crystalline order. The 3D order is lost during sol-gel processing, but FTIR spectroscopy confirms the survival of the cyanometallate at least in small domains or isolated double chains. Embedded in SiO<sub>2</sub> it shows magnetic ordering below 22 K indicating ferromagnetism. The T<sub>C</sub> is 10.6 K, and μ<sub>eff</sub> is 4.46 μ<sub>B</sub> at room temperature and 8.60 μ<sub>B</sub> at the maximum at ~15 K.

[Ni(silyl-2,3,2-tetramine)<sub>2</sub>]<sub>3</sub>[Fe(CN)<sub>6</sub>]<sub>2</sub>, [Ni(bissilyl-2,3,2-tetramine)<sub>2</sub>]<sub>3</sub>[Fe(CN)<sub>6</sub>]<sub>2</sub> and K[Ni(silylcyclam)][Fe(CN)<sub>6</sub>] show a similar structure as [Ni(AEAPTS)<sub>2</sub>]<sub>3</sub>[Fe(CN)<sub>6</sub>]<sub>2</sub>, and also lose the crystallinity upon sol-gel processing. These three cyanometallates embedded in SiO<sub>2</sub> show magnetic behavior similar to [Ni(AEAPTS)<sub>2</sub>]<sub>3</sub>[Fe(CN)<sub>6</sub>]<sub>2</sub> at high temperature (>50 K), but no magnetic ordering at low temperature. They are paramagnetic. [Ni(silyl-2,3,2-tetramine)<sub>2</sub>]<sub>3</sub>[Fe(CN)<sub>6</sub>]<sub>2</sub> shows a μ<sub>eff</sub> of 5.40 μ<sub>B</sub>, [Ni(bissilyl-2,3,2-tetramine)<sub>2</sub>]<sub>3</sub>[Fe(CN)<sub>6</sub>]<sub>2</sub> a μ<sub>eff</sub> of 6.81 μ<sub>B</sub> and K[Ni(silylcyclam)][Fe(CN)<sub>6</sub>] a μ<sub>eff</sub> of 3.34 μ<sub>B</sub>.

[Ni(silyl-6-aminocyclam)]<sub>3</sub>[Fe(CN)<sub>6</sub>]<sub>2</sub> does not show an as well ordered crystalline phase before sol-gel processing, but FTIR spectroscopy confirms the formation of a cyanometallate network. A 1D arrangement can be concluded from SWAXS data. The compound embedded in SiO<sub>2</sub> is also paramagnetic with a μ<sub>eff</sub> of 4.23 μ<sub>B</sub>.

A  $\text{Cu}^{\text{II}}\text{-Fe}^{\text{III}}$  cyanometallate with AEAPTS as blocking ligand is synthesized analogous to  $[\text{Ni}(\text{AEAPTS})_2]_3[\text{Fe}(\text{CN})_6]_2$  to study the influence of the metal ion on the structure and magnetic behavior.  $[\text{Cu}(\text{AEAPTS})_2]_3[\text{Fe}(\text{CN})_6]_2$  shows crystallinity before sol-gel processing, but is likely a mixture of several structures. The material obtained after sol-gel processing lost the 3D order, but small domains or isolated chains of the cyanometallate survive, as in the analogous  $\text{Ni}^{\text{II}}$  structure. Paramagnetic behavior is found for  $[\text{Cu}(\text{AEAPTS})_2]_3[\text{Fe}(\text{CN})_6]_2$  in  $\text{SiO}_2$  with a  $\mu_{eff}$  of  $3.52 \mu_{\text{B}}$ .

## Kurzfassung

Reaktionen von Ni<sup>II</sup>-Komplexen der Formel [Ni(polyamin)<sub>n</sub>]<sup>2+</sup> (n = 1, 2, 3) und [Fe(CN)<sub>6</sub>]<sup>3-</sup> führen üblicherweise zur Bildung von Cyanometallat-Netzwerken durch Aufbau von Cyanid-Brücken. Die resultierenden Strukturen [Ni(polyamin)<sub>n</sub>]<sub>x</sub>[Fe(CN)<sub>6</sub>]<sub>y</sub> zeigen oft Ferromagnetismus, der aus der magnetischen Kopplung von ungepaarten Elektronen von Ni<sup>II</sup>- und Fe<sup>III</sup>-Ionen über die Cyanid-Brücken entsteht.

Die Polyamin-Liganden blockieren Koordinationsstellen von Ni<sup>II</sup> und schränken dadurch die Möglichkeiten für den Aufbau von und die Anzahl an Cyanid-Brücken ein. Dies begünstigt die Bildung von niedrig dimensionalen (1D, 2D) Anordnungen der Cyanometallat-Netzwerke. Diamine oder Tetramine werden typischerweise für diesen Zweck eingesetzt, da sie hohe Affinität zu Ni<sup>II</sup> aufweisen.

In der vorliegenden Arbeit werden solche niedrig dimensionalen Cyanometallate in eine SiO<sub>2</sub>-Matrix eingebettet, die mittels des Sol-Gel Verfahrens hergestellt wird. Um den Zusammenhalt zwischen dem Cyanometallat und der SiO<sub>2</sub>-Matrix zu stärken werden Linker in die organischen Liganden eingeführt. Die Linker bestehen aus einer Trialkoxysilylgruppe an einer Alkylkette, die mit der SiO<sub>2</sub>-Vorstufe Tetraethoxysilan (TEOS) während des Sol-Gel-Prozesses reagiert. Dabei entstehen kovalente Bindungen zwischen Cyanometallat und SiO<sub>2</sub>-Matrix. Die Auswirkungen dieses Prozesses auf die Cyanometallat-Strukturen und deren magnetische Eigenschaften werden mittels FTIR-Spektroskopie, SEM, EDX, SWAXS und SQUID untersucht.

Fünf Ni<sup>II</sup>-Fe<sup>III</sup> Cyanometallate mit verschiedenen Polyamin-Liganden werden in dieser Arbeit besprochen und der Einfluss der Liganden auf Struktur und magnetische Eigenschaften untersucht.

[Ni(AEAPTS)<sub>2</sub>]<sub>3</sub>[Fe(CN)<sub>6</sub>]<sub>2</sub> (AEAPTS = N-(2-Aminoethyl)-3-(trimethoxysilyl)propylamin) bildet eine 1D Struktur aus Doppelketten mit einer kristallinen Anordnung. Die 3D-Ordnung geht während des Sol-Gel-Prozesses verloren, aber kleine Domänen oder isolierte Doppelketten des Cyanometallat-Netzwerkes bleiben laut FTIR-Spektroskopie erhalten. Das Material zeigt magnetische Ordnung ab 22 K, die Ferromagnetismus andeutet. Die Curie-Temperatur  $T_C$  beträgt 10.6 K. Das effektive magnetische Moment  $\mu_{eff}$  beträgt 4.46  $\mu_B$  bei Raumtemperatur und 8.60  $\mu_B$  bei dem Maximum bei ~15 K.

[Ni(silyl-2,3,2-tetramine)<sub>2</sub>]<sub>3</sub>[Fe(CN)<sub>6</sub>]<sub>2</sub>, [Ni(bissilyl-2,3,2-tetramine)<sub>2</sub>]<sub>3</sub>[Fe(CN)<sub>6</sub>]<sub>2</sub> und K[Ni(silylcyclam)][Fe(CN)<sub>6</sub>] bilden ähnliche Strukturen wie [Ni(AEAPTS)<sub>2</sub>]<sub>3</sub>[Fe(CN)<sub>6</sub>]<sub>2</sub>, und verlieren ebenso 3D Anordnung und Kristallinität während des Sol-Gel-Prozesses. Diese drei in SiO<sub>2</sub> eingebettete Cyanometallate zeigen bei hohen Temperaturen (>50 K) ähnliche magnetische Eigenschaften wie [Ni(AEAPTS)<sub>2</sub>]<sub>3</sub>[Fe(CN)<sub>6</sub>]<sub>2</sub>, aber keine magnetische Ordnung bei niedrigen Temperaturen. Sie sind paramagnetisch. Für [Ni(silyl-2,3,2-tetramine)<sub>2</sub>]<sub>3</sub>[Fe(CN)<sub>6</sub>]<sub>2</sub> beträgt  $\mu_{eff}$  5.40  $\mu_B$ , für [Ni(bissilyl-2,3,2-tetramine)<sub>2</sub>]<sub>3</sub>[Fe(CN)<sub>6</sub>]<sub>2</sub> 6.81  $\mu_B$  und für K[Ni(silylcyclam)][Fe(CN)<sub>6</sub>] 3.34  $\mu_B$ .

[Ni(silyl-6-aminocyclam)<sub>3</sub>]<sub>3</sub>[Fe(CN)<sub>6</sub>]<sub>2</sub> zeigt auch vor der Durchführung des Sol-Gel-Prozesses keine hohe Kristallinität, aber FTIR-spektroskopische Untersuchungen

bestätigen die Bildung eines Cyanometallat-Netzwerks. Eine 1D Anordnung kann aus den SWAXS-Daten geschlossen werden. Die in  $\text{SiO}_2$  eingebettete Struktur ist ebenfalls ein Paramagnet, mit einem  $\mu_{eff}$  von  $4.23 \mu_B$ .

Ein  $\text{Cu}^{\text{II}}\text{-Fe}^{\text{III}}$  Cyanometallat mit AEAPTS als Ligand wird analog zu  $[\text{Ni}(\text{AEAPTS})_2]_3\text{-}[\text{Fe}(\text{CN})_6]_2$  synthetisiert um den Einfluss des Zentralions auf die Struktur und die magnetischen Eigenschaften zu untersuchen.  $[\text{Cu}(\text{AEAPTS})_2]_3[\text{Fe}(\text{CN})_6]_2$  ist kristallin, aber vermutlich eine Mischung aus verschiedenen Strukturen. Nach dem Sol-Gel-Prozess verliert das Material die 3D Ordnung, aber kleine Domänen oder isolierte Ketten des Cyanometallat-Netzwerkes bleiben laut FTIR-Spektroskopie erhalten, wie im analogen  $\text{Ni}^{\text{II}}$ -Material. Paramagnetische Eigenschaften werden für  $[\text{Cu}(\text{AEAPTS})_2]_3[\text{Fe}(\text{CN})_6]_2$  in  $\text{SiO}_2$  beobachtet, mit einem  $\mu_{eff}$  von  $3.52 \mu_B$ .

**Part of this work has been published previously**

“Covalent Embedding of Ni<sup>II</sup>-Fe<sup>III</sup> Cyanometallate Structures in Silica by Sol-Gel Processing.” Felbermair, E; Sidorenko, A.; Paschen, S.; Akbarzadeh, J.; Peterlik, H.; Schubert, U. *Chem. Eur. J.*, **2014**, *20*, 9212–9215.





# Contents

Acknowledgements . . . . .	v
Abstract . . . . .	vii
Kurzfassung . . . . .	ix
<b>Contents</b>	<b>xiii</b>
<b>I Introduction</b>	<b>1</b>
<b>1 Sol-Gel Process</b>	<b>3</b>
1.1 Mechanisms . . . . .	4
1.2 Processing . . . . .	8
1.3 Applications . . . . .	9
1.4 Silica Gels as Matrix . . . . .	10
<b>2 Cyanometallates</b>	<b>13</b>
2.1 Cyanide . . . . .	13
2.2 Iron Cyanides . . . . .	14
2.2.1 Prussian Blues . . . . .	14
2.3 Prussian Blue Analogues . . . . .	16
2.3.1 Ni-Fe cyanometallates . . . . .	17
<b>3 Magnetism</b>	<b>21</b>
3.1 Introduction . . . . .	21
3.1.1 Curie's law . . . . .	22
3.1.2 Curie-Weiss law . . . . .	23
3.2 In Prussian Blue Analogues . . . . .	24
3.2.1 Exchange Interaction . . . . .	25
<b>4 Motivation and Aims</b>	<b>29</b>
<b>II Results and Discussion</b>	<b>31</b>
<b>5 Ni(II)–Fe(III)–Silica Gel with Silyl-ethylenediamine</b>	<b>33</b>
5.1 Synthesis . . . . .	33
5.2 FTIR . . . . .	34

5.3	SEM and EDX	35
5.4	SWAXS	36
5.5	SQUID	39
5.6	Conclusions	40
<b>6</b>	<b>Cu(II)–Fe(III)–Silica Gel with Silyl-ethylenediamine</b>	<b>43</b>
6.1	Synthesis	43
6.2	FTIR	44
6.3	SEM and EDX	45
6.4	SWAXS	46
6.5	SQUID	47
6.6	Conclusions	49
<b>7</b>	<b>Ni(II)–Fe(III)–Silica Gel with Silyl-2,3,2-Tetramine</b>	<b>51</b>
7.1	Synthesis	51
7.2	FTIR	53
7.3	SEM and EDX	55
7.4	SWAXS	55
7.5	SQUID	57
7.6	Conclusions	58
<b>8</b>	<b>Ni(II)–Fe(III)–Silica Gel with Bissilyl-2,3,2-Tetramine</b>	<b>59</b>
8.1	Synthesis	59
8.2	FTIR	61
8.3	SEM and EDX	62
8.4	SWAXS	63
8.5	SQUID	64
8.6	Conclusions	66
<b>9</b>	<b>Ni(II)–Fe(III)–Silica Gel with Silylcyclam</b>	<b>67</b>
9.1	Synthesis	68
9.1.1	Cyclam via bisaminal (butanedione)	68
9.1.2	Cyclam via bisaminal (1,2-cyclohexanedione)	71
9.1.3	Cyclam via tosyl protecting groups	73
9.1.4	Silylation	76
9.1.5	Ni-Fe gel	77
9.2	FTIR	77
9.3	SEM and EDX	79
9.4	SWAXS	80
9.5	SQUID	82
9.6	Conclusions	83
<b>10</b>	<b>Ni(II)–Fe(III)–Silica Gel with Silyl-6-aminocyclam</b>	<b>85</b>
10.1	Synthesis	86
10.1.1	Silylation	88

10.1.2 Ni-Fe gel . . . . .	89
10.2 FTIR . . . . .	89
10.3 SEM and EDX . . . . .	91
10.4 SWAXS . . . . .	91
10.5 SQUID . . . . .	93
10.6 Conclusions . . . . .	94
<b>11 Summary and Conclusion</b>	<b>97</b>
<b>III Experimental</b>	<b>101</b>
<b>12 Materials and Methods</b>	<b>103</b>
12.1 Materials . . . . .	103
12.2 Nuclear Magnetic Resonance (NMR) . . . . .	103
12.3 Fourier Transform Infrared Spectroscopy (FTIR) . . . . .	103
12.4 Superconducting Quantum Interference Device (SQUID) . . . . .	104
12.4.1 Flux quantization in superconductors . . . . .	104
12.4.2 Josephson effect . . . . .	104
12.4.3 SQUID Setups . . . . .	104
12.4.4 Measurement Instrument and Conditions . . . . .	105
12.4.5 Pascal's Method . . . . .	105
12.4.6 Effective Magnetic Moment . . . . .	106
12.5 Small- and Wide-Angle X-Ray Scattering (SWAXS) . . . . .	106
12.5.1 Measurement Instrument and Conditions . . . . .	106
12.6 pH Measurement . . . . .	107
12.7 Scanning Electron Microscopy (SEM) and Energy-Dispersive X-ray Spec- troscopy (EDX) . . . . .	107
12.8 Powder X-Ray Diffraction (pXRD) . . . . .	107
12.9 UV-Vis Spectroscopy . . . . .	107
<b>13 Ligand Syntheses</b>	<b>109</b>
13.1 Modified 2,3,2-Tetramine . . . . .	109
13.2 Modified Cyclam . . . . .	110
13.2.1 Cyclam via Bisaminal (Butanedione) . . . . .	110
13.2.2 Cyclam via Bisaminal (1,2-Cyclohexanedione) . . . . .	112
13.2.3 Cyclam via Tosyl Protecting Groups . . . . .	113
13.2.4 Silylcyclam . . . . .	116
13.2.5 Silyl-6-aminocyclam . . . . .	116
<b>14 Complex Syntheses</b>	<b>119</b>
14.1 Ni(II) Complexes . . . . .	119
14.2 Cu(II) Complexes . . . . .	120
<b>15 Cyanometallate Network Syntheses</b>	<b>121</b>

15.1 Ni(II)/Fe(III) Cyanometallates . . . . .	121
15.2 Cu(II)/Fe(III) Cyanometallates . . . . .	122
<b>16 Sol-Gel Processing</b>	<b>123</b>
16.1 Ni(II)/Fe(III) Gels . . . . .	123
16.2 Cu(II)/Fe(III) Gels . . . . .	124
<b>IV Appendix</b>	<b>125</b>
<b>Glossary</b>	<b>127</b>
<b>Bibliography</b>	<b>131</b>
<b>CV</b>	<b>145</b>

## **Part I**

# **Introduction**



# Sol-Gel Process

Already 170 years ago, in 1845, Ebelmen [1] described the first sol-gel reaction. He noticed that an alkoxy silane obtained from the reaction of  $\text{SiCl}_4$  with alcohol formed a gel upon exposure to air. Nearly 100 years later the first films from alkoxides were reported and patented by Geffcken and Berger in the 1930s [2]. In the same decade, Hurd [3] showed that the network structure of the gel is composed of a poly(silicic acid) supporting a liquid. Further, Kistler [4] synthesised an aerogel by supercritical drying in 1931 for the first time. In the late 1960s to 1970s, finally, the sol-gel process was discovered for application in materials production, e.g. to obtain multicomponent glasses from alkoxides [5, 6] or ceramic fibers from metal-organic precursors [7]. Just as often happens in other fields, also in sol-gel chemistry the applied technology preceded scientific understanding.[8, 9]

The sol-gel process is a bottom-up approach for the synthesis of (amorphous) metal oxides, especially  $\text{SiO}_2$ . Polycondensation reactions of molecular precursors in a liquid solvent build up the product. The process is defined by fast and mostly irreversible (except in very alkaline conditions) reactions and therefore kinetically controlled.

“Sol” and “gel” denote the two different stages the reaction mixture undergoes during the process, see Fig. 1.1. A *sol* is a stable colloidal suspension of solid particles or polymers that can be amorphous or crystalline. The term “colloid” describes a suspension in which the solid particles are between ~1 and 1000 nm in size. This means that the gravitational force on the particles is negligible and their interactions are dominated by weak forces, such as van der Waals interactions and surface charges. In addition, the small particles are subjected to Brownian motion which leads to frequent collisions. A *gel* is a porous, three-dimensional continuous solid network surrounding and supporting a liquid (“wet gel”).[8, 9]

The main advantages of this synthesis technique are [8, 9]:

- It is a *soft chemistry* method, i.e. it can be performed at low temperatures – compared to solid state reactions – and thus requires less energy and is cheaper. Further, environmentally friendly solvents like water or alcohols are typically used.
- Better homogeneity and higher purity of the products may be achieved by sol-gel

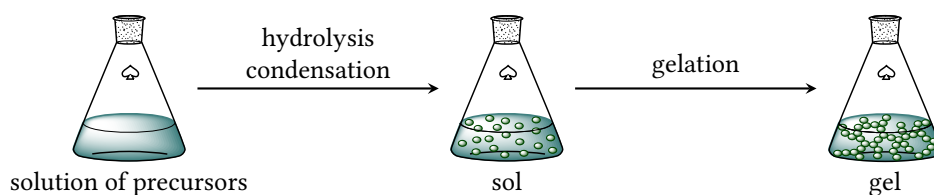


**Figure 1.1:** Schematic visualisation of the sol-gel process.

processing in comparison to solid state reactions. It is even possible to get homogeneous phases from immiscible metal oxides.

- Mixed metal oxides can be synthesised with definite stoichiometry by mixing the precursors in solution or by employing single-source precursors, i.e. molecules incorporating all desired metals in the right ratio.
- New amorphous materials may be obtained that are not accessible by other routes. New or non-equilibrium crystal phases may also form by subsequent heating.
- A variety of products can be obtained by simple post-processing: coatings, fibers, powders, (nano)particles, porous materials etc., see Sec. 1.2, p. 8.

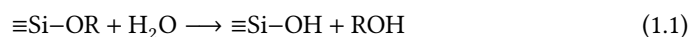
Disadvantages of sol-gel syntheses are [8, 9]:

- Only amorphous phases are initially obtained, but crystalline products may be obtained by post-synthesis heat-treatment.
- Contamination, mainly by carbon from the alkoxide precursor, often occurs in the final product.
- The precursors needed for sol-gel processing are often quite expensive or not commercially available.
- The processing times are rather long.
- The shrinkage that occurs during aging and drying (see Sec. 1.1, p. 4) may cause problems during processing.
- Residual hydroxyl groups and fine pores in the product are often undesirable but inevitable.

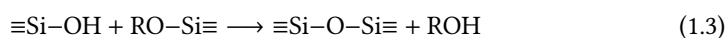
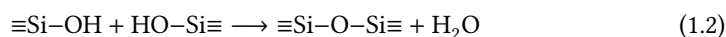
## 1.1 Mechanisms [8-10]

There are two reactions involved in the transformation of a solution of precursors to a sol and subsequently a gel, namely hydrolysis and condensation. The reaction equations for these for silica, which is in the focus of this work, are as follows:

### Hydrolysis



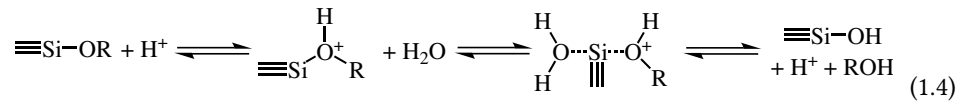
### Condensation



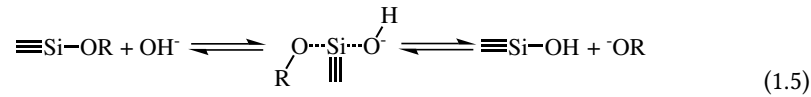
During hydrolysis an alkoxy group is cleaved and released as free alcohol while generating a hydroxyl group at the metal center. This initiation step is highly pH-dependent



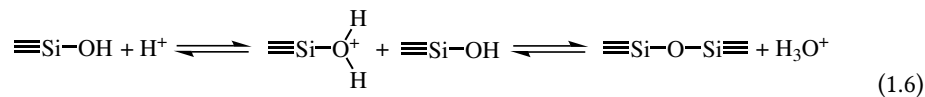
and usually achieved either by basic or acidic catalysis. In acid catalysis the pH of the reaction solution needs to be below the point of zero charge (PZC) of the metal oxide. For silica the PZC is typically around 1.5–4.5. If the pH is lowered below 1.5, charged molecules are formed by the attachment of  $H^+$  to an alkoxo group at silicon, which is the first step in hydrolysis. Subsequent cleaving of the alkoxo group as free alcohol and regeneration of  $H^+$  yields the (partially) hydrolysed siloxane as shown in Eq. 1.4.



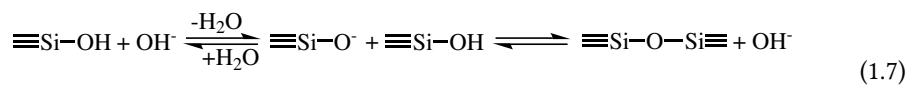
If the hydrolysis, however, is performed at a pH above PZC, it follows the base-catalyzed mechanism shown in Eq. 1.5. The hydroxide ion first attaches to the silicon atom generating a negatively charged transition state. Subsequently an alkoxide ion is cleaved which then reacts with water to produce alcohol and a hydroxide ion.



The mechanism of the condensation, too, is pH-dependent. Under acidic conditions the first step is the fast protonation of the oxygen of the hydroxide group, as shown in Eq. 1.6. The subsequent (slower) reaction with another silanol group yields the condensation product and regenerates the catalyst  $H^+$ .



As shown in Eq. 1.7, fast deprotonation of a silanol group occurs at basic pH as a first step. The condensation product is formed by slow reaction with another silanol group and the catalyst  $\text{OH}^-$  regenerated.



The pH dependencies of hydrolysis and condensation differ from each other, as shown in Fig. 1.2. Hydrolysis is faster than condensation at a pH below ~5 and above ~11. At more neutral and moderately basic pH condensation is faster than hydrolysis. This difference in relative reaction rates also influences the structure of the final product. If condensation is fast, all hydrolysed monomer is immediately consumed and particle growth dominates. This generally leads to a product with particulate, colloidal character. If, on the other hand, hydrolysis is fast, there will always be a lot of hydrolyzed species in solution that can react with each other, forming new particles and/or attaching to existing ones. In general, this leads to a polymer-like material made up of small particles.

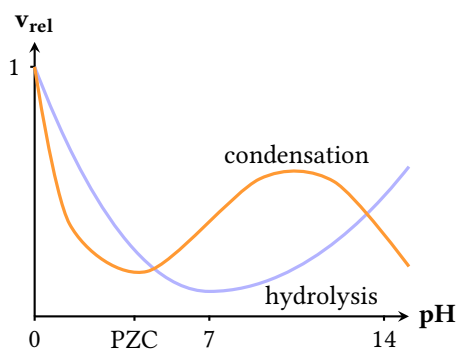


**Figure 1.2:** pH dependencies of the relative reaction rates of hydrolysis and condensation of  $\text{Si}(\text{OR})_4$ .

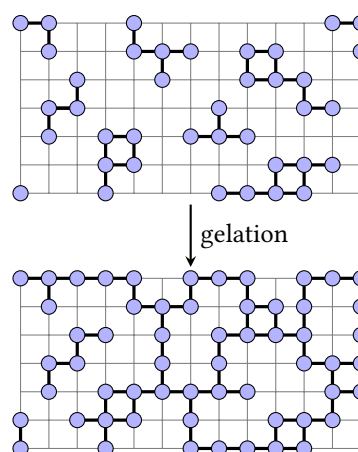


**Figure 1.3:** Scheme illustrating site percolation on a square lattice.

Apart from the pH, additional parameters influence the structure and properties of the final product:

- The employed *precursors* affect the sol-gel process via steric and inductive effects. In general, the former dominate the latter. Larger, especially branched, alkoxide groups lower the hydrolysis rate for a given pH, i.e.  $\text{Si}(\text{OMe})_4 > \text{Si}(\text{OEt})_4 > \text{Si}(\text{O}^n\text{Pr})_4 > \text{Si}(\text{O}^i\text{Pr})_4$ . Inductive effects of the substituents at Si may stabilize or destabilize a transition state during hydrolysis. The electron density at Si drops in the following sequence:  $\equiv\text{Si}-\text{R} > \equiv\text{Si}-\text{OR} > \equiv\text{Si}-\text{OH} > \equiv\text{Si}-\text{O}-\text{Si}\equiv$ . Under acidic reaction conditions, high electron density at Si stabilizes the positive charge in the transition state of hydrolysis. This means that in this case monomeric  $\text{Si}(\text{OR})_4$  hydrolyses faster than partially oligomerized species which leads to a more chain-like growth. Basic catalysis, however, leads to a negatively charged transition state which is more stable if there is less electron density at Si. Therefore, monomeric  $\text{Si}(\text{OR})_4$  reacts more slowly and a more branched structure is obtained.
- The  $-\text{OR}:\text{H}_2\text{O}$  ratio influences the product in a way that a higher proportion of  $\text{H}_2\text{O}$  leads to more residual Si-OH groups and a less condensed structure.
- The reaction kinetics are accelerated with increasing temperature. This results in faster condensation and a shorter gel time [11, 12]. Moreover, the crystallinity and grain size of the obtained gel increase with rising *temperature* [13].
- The *solvent* employed during synthesis may have an impact on the resulting structure through three different factors: its polarity, whether it is protic or non-protic, and its viscosity. Especially the polarity and proticity have strong influence through formation of H-bridges to  $\equiv\text{Si}-\text{OH}$ . The catalytic effects of acids and bases are lowered if the solvent forms H-bridges to  $\text{H}^+$  or  $\text{OH}^-$ . Additionally, protic solvents facilitate back-reactions by re-esterification [14].
- Grain sizes in the gel increase with increasing *concentration* because more solutes are present in the sol stage. Clustering and agglomeration of these solutes leads to

larger grains in the gel [15].

- Good *mixing* and *agitation* of the precursor solution is important to ensure that the reactions occur uniformly and to obtain homogeneous gels. However, agitation may disrupt domains of the formed sol or gel which usually regrow until a reaction vessel spanning gel arises.

*Gelation* occurs when the sol particles aggregate to give a three-dimensional, continuous gel network and a particular network structure is frozen. From a phenomenological viewpoint reaching the gel point is accompanied by a sharp increase in viscosity. The reaction progress can therefore be determined simply by checking if the reaction mixture still moves when the reaction vessel is tipped, or by viscoelastic measurements.

Flory [16] described the formation of a gel by considering the fraction of bonds that must be formed before an “infinitely” large molecule (spanning cluster) is formed. For this consideration all functional groups are assumed to have the same reactivity and reactions can only occur between the clusters/particles but not within. This leads to the conclusion that one third of possible siloxane bonds needs to be formed to obtain a gel.

There are two simple percolation models to explain why gelation happens rather abruptly and not continuously:

- *Site percolation*: The blue circles in the grid shown in Fig. 1.3 represent sol particles. If two sol particles sit on adjacent sites, they are considered to be aggregated, represented by a solid bond. During the sol-gel process, new sol particles are formed, they grow and aggregate. This leads to an increase in cluster size, until the gel stage is reached by formation of a cluster spanning the whole reaction vessel. This represents the gel point. Thermodynamically, the last condensation that produces the spanning cluster is not different from the condensation reactions occurring throughout the sol-gel process. It is also to be noted that unbound clusters are usually still present at the gel point.
- *Bond percolation*: A similar grid as in Fig. 1.3 may illustrate the concept of bond percolation. In this case, all sites of the grid are filled with sol particles and bonds between them are distributed randomly. During the reaction, more bonds are formed and the clusters grow. The gel point is, again, reached when a cluster spanning the reaction vessel is produced by bond formation.

Since there are still monomers and smaller clusters present in the pore liquid, further hydrolysis and condensation can occur after the gel point. The reversibility of hydrolysis and condensation may also lead to dissolution of small particles and the re-reaction of the dissolutes at thermodynamically more favorable regions. Small particles and pores disappear from the gel by this ripening/coarsening. Additionally, adjacent M-OH and M-OR groups in the gel may react with each other and cause shrinkage of the gel, which often leads to *syneresis*, the expulsion of the pore liquid. All of these processes generally increase the stiffness of the gel over time and are summarized in the term *aging*.

The final step, *drying*, proceeds in three stages if it is done by conventional evaporation techniques (heating, pressure decrease):

1. At first the gel shrinks by the volume that the evaporated solvent occupied previously. This causes further solvent to be displaced from the interior of the gel to the surface. Due to the shrinkage, unreacted M–OH and M–OR groups come close to each other and may react to form new M–O–M bonds. This leads to additional stiffening and deformation of the gel.
2. After some time the gel is too stiff for further shrinkage. Cracking of the gel is therefore probable and xerogel powders (see Sec. 1.2, p. 8 below) are usually obtained. At this point, the liquid/gas interface is located in the gel body, but a continuous liquid film is still present at the pore walls.
3. In the final stage, the liquid film is disrupted and solvent only remains in isolated pockets. It can be removed by diffusion through the gas phase of the pores in the gel.

## 1.2 Processing [8, 9]

Besides the reaction conditions during the sol-gel process, also the post-synthesis processing has a strong influence on the resulting products. As stated above, the sol-gel route is especially versatile in the shapes and structures that can be obtained. Fig. 1.4 shows a schematic overview of possible processing routes and their results.

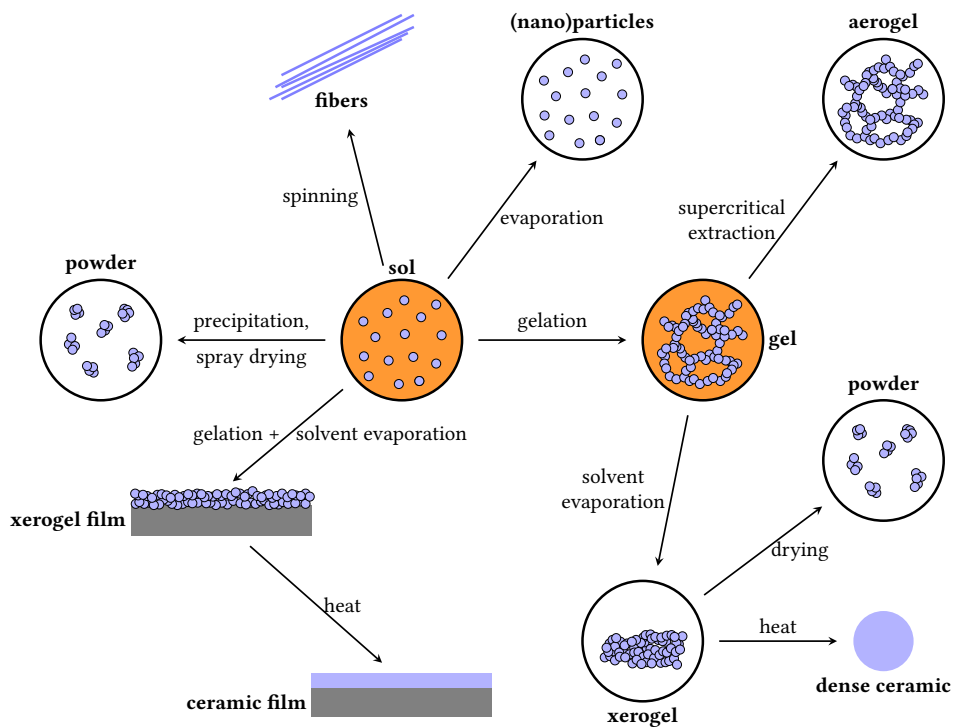


**Figure 1.4:** Possible processing of sol-gel materials.

Starting from the sol, powders can be obtained by spray drying or precipitation, and fibers by spinning. Homogeneous (ceramic) films, one of the main applications of the sol-gel process, can be produced by (spin, dip, spray) coating of a substrate with the sol and subsequent heating. Applying the *Stöber process*, (nano)particles with very narrow size distribution are synthesized. The size mainly depends on the precursor concentration, the amount of water added, the solvent and the reaction time, which need to be controlled carefully to obtain a specific particle size.

From the gel phase, mainly two routes are possible. The highly porous network structure of the gel usually collapses upon drying under normal conditions and a xerogel is obtained. This yields either a still quite porous powder, or can be pressed and sintered to a dense ceramic in the desired shape. The second possible route is to perform supercritical extraction of the solvent. The pore structure of the gel is retained by this technique and a highly porous, very light and usually translucent aerogel is obtained.

### 1.3 Applications [8, 9]

The applications of sol-gel derived materials usually try to exploit their unique properties, i.e. for sols easy film deposition, fiber drawing and growth of particles and for gels high porosity, high surface area, low refractive index, low thermal conductivity, transparency and the possibility to incorporate organic and inorganic components to form composites.

#### Coatings and thin films

Coatings may be applied to a variety of substrates to achieve various goals.

*Optical coatings* are applied to alter reflectance, transmission and/or absorption of the substrate. For example, solar cells are often furnished with anti-reflective coatings to enhance UV transmissibility and thereby the energy output. Also more mundane objects, such as eyeglasses, are often fitted with anti-reflective films. Coloured coatings are also common.

*Electrically conductive films* may be manufactured from transition metal oxide gels with conductive properties. A very interesting and widely used specimen is ITO (indium tin oxide) that finds application in, e.g., liquid crystal displays, flat panel displays, touch panels, organic light-emitting diodes (OLED), solar cells and for defrosting aircraft windshields by heating via applied voltage.[17–22]

*Protective coatings* are employed to increase corrosion and/or abrasion resistance of the substrate, to obtain better adhesion or to achieve some degree of passivation. For these purposes it is important to obtain dense, pin-hole free layers. The barrier properties are exploited to protect metal surfaces from humidity and oxidation [23]. In multilayer electronics a final protecting coating is often applied, as in optical applications, e.g., anti-scratch films on glasses.

#### Monoliths

Special shapes of sol-gel monoliths may be obtained by casting the gel into moulds. Thus optical lenses and fibers may be produced without melting and polishing, but the significant shrinkage during aging and drying has to be considered and cracking prevented.

Monoliths with controlled porosity have recently gained increasing attention for applications in chromatography columns [24]. Modifications with affinity ligands [25] broaden this area of use further.

Aerogel monoliths have first been used as Cherenkov detectors exploiting their low refractive index. The highly porous structure is also interesting as heat insulator due to its low thermal conductivity.

### **Powders and particles**

Sol-gel powders are very versatile, easily obtained and are used for many different applications. The large surface area and high porosity makes them interesting for catalysis. Porous beads of controlled particle and pore size are employed in chromatography and as molecular sieves. Further, powder abrasives, fillers and pigments may also be obtained by sol-gel processing.

### **Fibers**

Fibers drawn from sols are used as mechanical reinforcements in ceramics [26]. Another important application is found in refractory textiles which are employed, for example, in furnace belts, flame curtains and cables.

### **Composites**

A very important feature of sol-gel materials is the ease with which composites may be synthesized by mixing different precursors or by subsequent modifications. This especially provides an easy route to mixed organic-inorganic and ceramic-metal materials that exhibit synergistic properties. Examples for such materials in applications are turbine blades made from alumina reinforced by SiC, sol-gel films with incorporated epoxysilanes for scratch-resistance, and porous sol-gel matrices for catalytic metal particles.

The easy synthesis, huge variability by chemical modification and/or post-processing routes and broad application render sol-gel materials very interesting for basic as well as advanced and applied research.

## **1.4 Silica Gels as Matrix**

Silica prepared by the sol-gel process is used as matrix for many different compounds in a variety of applications and research fields. Homogeneous distribution of the active compound is easily achieved by impregnation of the porous silica obtained after drying and aging or by addition to the precursor solution or the sol and subsequent sol-gel processing.

Nanoparticles [27–29] are especially popular due to their versatile properties and possibilities for applications. A variety of nanoparticles, e.g. Si, PbS, lanthanide doped  $Y_2O_3$ , present luminescence [30–33]. CdS, PbS, Pd, Ag and similar compounds are used for optical applications [34–38]. The high surface area of sol-gel silica is often exploited to disperse catalytically active nanoparticles [39–44] – such as Ru, Pt, Pd and Au – and to increase the reactive surface which is often crucial for the reaction rate. Ge and NiS nanocrystals were shown to keep their semiconducting properties [45–47] upon embedding. Quantum dots (QD) for optical devices [48–50] were achieved from semiconducting

materials ZnS, ZnSe, CdS and CdSe. Conducting nanoparticles of e.g. RuO<sub>2</sub>, Zn, were obtained in silica [51, 52]. A variety of nanoparticles with ferromagnetic properties [53–66] were already successfully embedded in sol-gel silica. The particular magnetic behavior of the embedded nanoparticles often differs from the bulk material, but is still very interesting.

Apart from these manifold possibilities with nanoparticles, also other compounds were embedded in sol-gel silica. Organic dye molecules [67–70] are stabilized by the inert matrix. In a special case, Subbiah *et al.* [71] embedded isolated molecules of zinc phthalocyanine to improve optical switching properties. Electrolytes in silica may be employed for electrochemical redox reactions [72, 73]. Carbon nanostructures such as fullerenes [74–76] and carbon nanotubes [77] were also successfully embedded. Controlled release of drugs [78, 79], pesticides [80, 81] or even organic liquids [82] presents another important application and research field. Further, biotechnological applications that employ enzymes [83, 84] and proteins [85] embedded in sol-gel silica are known. More complex systems of embedded micelles incorporating organic molecules [86] may be developed as micro reaction vessels. Finally, also dendrimers [87], organic oligomers [88] and polymers [89] in sol-gel silica are of interest.

Despite this broad research in sol-gel silica matrices, complex cyanometallates have never before been considered for embedding, to the best of the author's knowledge.





# Cyanometallates

## 2.1 Cyanide

The cyanide ion  $\text{C}\equiv\text{N}^-$  is isoelectronic to CO and  $\text{N}_2$ . Chemically it behaves similar to halogens and therefore belongs to the group of pseudohalogens, resembling  $\text{Br}^-$  the closest. Hydrogen cyanide (HCN), is a weak acid with a  $\text{pK}_a$  of 9.21 (25 °C).[90, 91]

In coordination chemistry the cyanide ion is a very versatile ligand [92]. It forms homo- and heteroleptic (especially with CO, NO, bipyridine [93–98]) complexes with a large variety of transition metals. The 18-electron rule is not followed strictly by the cyanometallates. Complexes with 17 ( $[\text{Mn}^{\text{III}}(\text{CN})_6]^{4-}$ ,  $[\text{Fe}^{\text{III}}(\text{CN})_6]^{3-}$ ,  $[\text{Cu}^{\text{II}}(\text{CN})_4]^{2-}$ ,  $[\text{Ru}^{\text{III}}(\text{CN})_6]^{3-}$ ), 16 ( $[\text{Mn}^{\text{II}}(\text{CN})_6]^{4-}$ ,  $[\text{Ni}^{\text{II}}(\text{CN})_4]^{2-}$ ,  $[\text{W}^{\text{IV}}(\text{CN})_8]^{4-}$ ), 15 ( $[\text{Ti}^{\text{III}}(\text{CN})_7]^{4-}$ ,  $[\text{V}^{\text{II}}(\text{CN})_6]^{4-}$ ), 14 ( $[\text{Ti}^{\text{II}}(\text{CN})_6]^{4-}$ ,  $[\text{Zr}^0(\text{CN})_5]^{5-}$ ) or even only 12 ( $[\text{Ti}^0(\text{CN})_4]^{4-}$ ) electrons are known. Cyanides in complexes act as  $\sigma$ -donors and  $\pi$ -acceptors. Back-donation from the metal to the ligand often occurs to avoid excessive negative charge at the metal center.[90, 91]

Cyanide may act as monodentate, bidentate or, more rarely, tridentate ligand. As monodentate ligand it is always coordinated to the metal center through the carbon atom ( $\text{M}-\text{C}\equiv\text{N}$ ). Isocyano complexes ( $\text{M}-\text{N}\equiv\text{C}$ ) are only formed if the carbon has organic substituents, i.e. with nitriles [99, 100]. The  $\text{M}-\text{C}\equiv\text{N}$  entity is generally linear, e.g. in the complex iron cyanides  $\text{K}_4[\text{Fe}(\text{CN})_6]$  and  $\text{K}_3[\text{Fe}(\text{CN})_6]$ . The C-coordination always leads to a strong ligand field and thus to low-spin complexes. The nitrogen may also act as a donor to a metal center, thus rendering the cyanide ligand bidentate and forming cyanide bridges between two transition metals. These bridges have bond angles close to  $180^\circ$  due to the linearity of the cyanide ion. Since the cyanide is a quite small ion, very short distances between the bridged transition metals arise. The N-coordinated metal center may either be of the same element as the C-coordinated one, as in  $\text{AgCN}$  and  $\text{AuCN}$  which form polymeric chains of  $[-\text{M}-\text{C}\equiv\text{N}-\text{M}-]_n$  [101], or a different transition metal [102–106]. The N-coordination presents a weak ligand field, usually resulting in metals in high-spin states. According to the *HSAB theory* [107], the difference in the Lewis basicity of the two

ends of the cyanide bridge leads to a preference of different metals/oxidation states to the C or N side, respectively. The N side of the cyanide ion is harder and thus coordinates preferably to hard metals while the C side is softer.[90, 91, 108]

A large variety of bridged cyanometallate structures exists: linear, triangular, tetrahedral, square planar, square pyramidal, trigonal bipyramidal, octahedral, pentagonal bipyramidal, dodecahedral, square antiprismatic etc. This renders cyanometallates very attractive for building block chemistry. Depending on the coordination geometries of the employed transition metals, the connectivity and, thus, the resulting structure can be tuned.[90–92]

## 2.2 Iron Cyanides

A variety of iron cyanides is known: homoleptic  $[\text{Fe}^{\text{II}}(\text{CN})_6]^{3-}$ ,  $[\text{Fe}^{\text{III}}(\text{CN})_6]^{3-}$ ,  $[\text{Fe}^{\text{II}}(\text{CN})_5]^{4-}$  and heteroleptic  $[\text{Fe}^{\text{II}}(\text{CN})_5\text{NH}_3]^{3-}$ ,  $[\text{Fe}^{\text{II}}(\text{CN})_5\text{CO}]^{3-}$ ,  $[\text{Fe}^{\text{II}}(\text{CN})_5\text{NO}]^{3-}$ ,  $[\text{Fe}^{\text{II}}(\text{CN})_5\text{NO}_2]^{4-}$ ,  $[\text{Fe}^{\text{II}}(\text{CN})_5\text{SO}_3]^{5-}$ ,  $[\text{Fe}^{\text{II}}(\text{CN})_2(\text{CO})_2]^{2-}$ . The most important and common compounds are  $[\text{Fe}(\text{CN})_6]^{4-}$  and  $[\text{Fe}(\text{CN})_6]^{3-}$ .  $[\text{Fe}(\text{CN})_6]^{4-}$  has noble gas configuration and is thermodynamically and kinetically more stable than  $[\text{Fe}(\text{CN})_6]^{3-}$  which has only 17 valence electrons. The former is non-toxic and has many applications in industry. E.g., the potassium salt  $\text{K}_4[\text{Fe}(\text{CN})_6]$ , which forms yellow crystals, is used as wine fining agent.[90–92]

$\text{K}_3[\text{Fe}(\text{CN})_6]$  is synthesised by oxidation of  $\text{K}_4[\text{Fe}(\text{CN})_6]$  and forms red crystals. The complex has a single unpaired electron and exhibits paramagnetic susceptibility according to the Curie-Weiss law between 80 and 300 K with a Curie constant  $C$  of  $\sim 56 \text{ cm}^3 \text{ K mol}^{-1}$  and an effective magnetic moment  $\mu_{\text{eff}}$  of  $2.25 \mu_{\text{B}}$  at 300 K.[90–92]

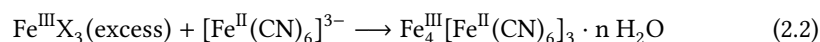
### 2.2.1 Prussian Blues

Prussian Blue is a complex iron cyanide with iron in two different oxidation states ( $\text{Fe}^{\text{II}}$  and  $\text{Fe}^{\text{III}}$ ). It was discovered by Diesbach, a German draper, in 1704 in Berlin and was the first synthetic pigment and coordination compound [90–92, 109]. The first written record of the blue dye is the description by an anonymous author in “Miscellanea berolinensia ad incrementum scientiarum: ex scriptis Societati Regiae Scientiarum exhibitis” [110]. The synthesis procedure was first described by Woodward in 1724 [111] and repeated for validation by Brown [112].

Two modifications of Prussian Blue exist, the insoluble  $\text{Fe}_4^{\text{III}}[\text{Fe}^{\text{II}}(\text{CN})_6]_3 \cdot n \text{ H}_2\text{O}$  and the soluble  $\text{KFe}^{\text{III}}[\text{Fe}^{\text{II}}(\text{CN})_6] \cdot n \text{ H}_2\text{O}$ . In both cases  $\text{Fe}^{\text{II}}$  and  $\text{Fe}^{\text{III}}$  are connected through cyanide bridges  $\text{Fe}^{\text{II}}-\text{C}\equiv\text{N}-\text{Fe}^{\text{III}}$  in which  $\text{Fe}^{\text{II}}$  is C-coordinated and  $\text{Fe}^{\text{III}}$  is N-coordinated, as would be expected from the HSAB theory [107, 113, 114]. The intense blue color of Prussian Blue arises from a metal-to-metal charge transfer process from the d-orbital of low-spin  $\text{Fe}^{\text{II}}$  to the d-orbital of high-spin  $\text{Fe}^{\text{III}}$  which is excited by yellow light [90–92, 115, 116]. Valence oscillation between  $\text{Fe}^{\text{II}}$  and  $\text{Fe}^{\text{III}}$  was disproven by Mössbauer spectroscopy by Fluck *et al.* [117] and Ito *et al.* [114].

### Insoluble Prussian Blue

Insoluble Prussian Blue is obtained by the following reactions:



At first insoluble Prussian Blue (“ferric ferrocyanide”) obtained from the reaction according to Eq. 2.1 and *Turnbull’s blue* (“ferroic ferricyanide”) obtained from the reaction shown in Eq. 2.2 were distinguished as two different species [90–92]. In the 1960s Mössbauer spectroscopy [109, 114, 117–119] proved that the two structures are actually identical and “ferric ferrocyanide” is also formed in the second reaction by rapid electron transfer between  $\text{Fe}^{\text{II}}$  and  $[\text{Fe}^{\text{III}}(\text{CN})_6]^{3-}$ .

The structure of insoluble Prussian Blue can be described by the simple illustration of a cubic crystal structure with  $\text{Fe}^{\text{II}}$  and  $\text{Fe}^{\text{III}}$  alternatingly located at the corners and  $\text{CN}^-$  forming the edges. The fcc unit cell of space group  $Pm\bar{3}m$  with  $a = 10.2 \text{ \AA}$  is shown in Fig. 2.1a [120]. It consists of one  $\text{Fe}^{\text{II}}$  ion octahedrally coordinated by six  $\text{CN}^-$  via C, one  $\text{Fe}^{\text{III}}$  ion octahedrally coordinated by six  $\text{CN}^-$  via N, three  $\text{Fe}^{\text{III}}$  ions coordinated by four  $\text{CN}^-$  via N and two  $\text{H}_2\text{O}$  (coordinated via O) and further  $\text{H}_2\text{O}$  molecules in the internal space.[90–92, 109, 121, 122]

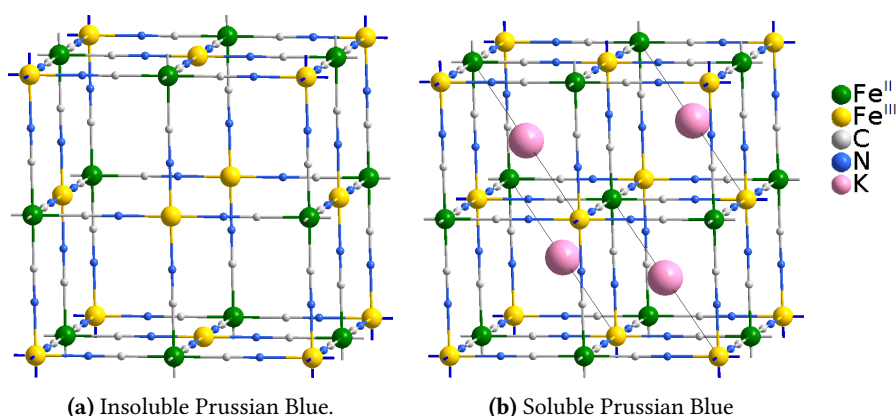
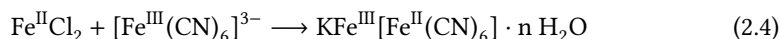
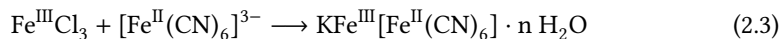


**Figure 2.1:** Crystal structures of insoluble and soluble Prussian Blue.

Insoluble Prussian Blue is ferromagnetic at low temperatures, as was shown by Borzoth *et al.* [123]. Its bulk magnetic susceptibility obeys the Curie Weiss law in the temperature range of 10 to 300 K with  $T_C = 5.5 \pm 0.5 \text{ K}$ ,  $C = 17.92 \pm 0.02 \text{ cm}^3 \text{ K mol}^{-1}$  and a Weiss constant  $\theta = 6.74 \pm 0.07 \text{ K}$ . Below  $T_C$ , ferromagnetic ordering occurs with a  $\mu_{eff}$  of  $5.98 \pm 0.02 \mu_B$  per  $\text{Fe}^{\text{III}}$ . This corresponds quite well to the spin-only value of high-spin  $\text{Fe}^{\text{III}}$ . The ferromagnetism arises from superexchange of the  $t_{2g}^3 e_g^2$  configurations of the four high-spin  $\text{Fe}^{\text{III}}$  ions in the unit cell that overlap. The rather low  $T_C$  is obtained due to the diamagnetism of half of the metal centers in the structure (low-spin  $\text{Fe}^{\text{II}}$ ). The coordinated water molecules fill the  $[\text{Fe}(\text{CN})_6]^{4-}$  vacancies in the center of the unit cell.[114, 124–126]

### Soluble Prussian Blue

Soluble Prussian Blue,  $\text{KFe}^{\text{III}}[\text{Fe}^{\text{II}}(\text{CN})_6] \cdot n \text{H}_2\text{O}$ , is obtained by the equimolar reaction of iron chloride with hexacyanoferrates:



The crystal structure is very similar to that of insoluble Prussian Blue, but denser with an additional  $\text{Fe}^{\text{II}}$  ion in the center of the unit cell and incorporated potassium. An approximate description considers two interpenetrating face-centered cubic crystal structures of  $\text{Fe}^{\text{II}}$  and  $\text{Fe}^{\text{III}}$  which are connected by  $\text{CN}^-$  ions. The fcc unit cell with  $a = 10.2 \text{ \AA}$  contains four formula units of  $\text{KFe}^{\text{III}}[\text{Fe}^{\text{II}}(\text{CN})_6]$ . As shown in Fig. 2.1b, every  $\text{Fe}^{\text{II}}$  ion is again octahedrally coordinated by six  $\text{CN}^-$  ions via C, the  $\text{Fe}^{\text{III}}$  ions are octahedrally coordinated by six  $\text{CN}^-$  ions via N and four octants are occupied by potassium ions.[90–92, 122, 127, 128]

Soluble Prussian Blue follows the Curie-Weiss law and presents a Curie constant  $C$  of 4.88, a  $T_C$  of 2 K and a  $\mu_{eff}$  for bulk magnetic susceptibility of  $6.29 \mu_B$  per  $\text{Fe}^{\text{III}}$ , [124].

### Berlin green

A related brown compound of the formula  $\text{Fe}^{\text{III}}[\text{Fe}^{\text{III}}(\text{CN})_6] \cdot n \text{H}_2\text{O}$  is obtained by oxidation of Prussian blue. By partial autoreduction of some  $\text{Fe}^{\text{III}}$  ions to  $\text{Fe}^{\text{II}}$  this compound turns green.[90–92]

## 2.3 Prussian Blue Analogues

In 1936 Keggin and Miles [122] already reported three crystal structures for Prussian Blue and its analogues. These are all fcc and only differ in the occupation/vacancies of the C-coordinated metal center and alkali counterions [128].

Prussian Blue analogues are usually obtained by mixing solutions of a cyanometallate and a metal salt or coordination complex. This renders these systems perfectly suitable for a building block approach. Each of the precursors may be chemically modified to alter the resulting structure. One building block is typically a hexa- or octacyanometallate anion, such as  $[\text{Fe}(\text{CN})_6]^{4-}$ ,  $[\text{Fe}(\text{CN})_6]^{3-}$  or  $[\text{W}(\text{CN})_8]^{3-}$ , whereas the other can be a variety of cationic transition metals or complexes. The structure and number of organic ligands on the latter influence the dimensionality of the network structure by blocking coordination sites and thus limiting the number of cyanide bridges. 0D molecular clusters [129–146], 1D chains [147–158], 2D sheet structures [105, 154, 159–192], or 3D frameworks [104, 106, 142, 193–198] have been reported. Examples are shown in Fig. 2.2. Besides this modification, changing the M:M' ratio or using different transition metals [199–203] also influences the structure and dimensionality of the cyanometallate. Changing the structure affects the magnetic properties as well, which thereby are rendered tunable [204, 205].

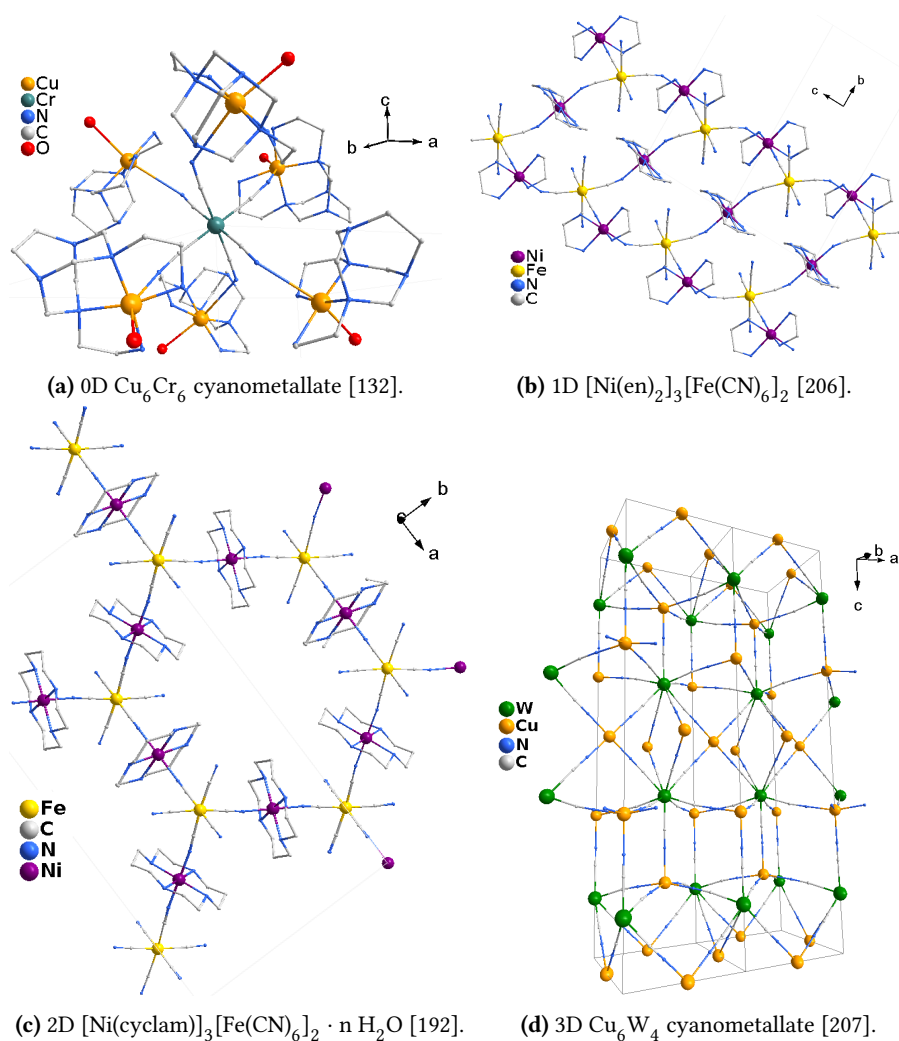


Figure 2.2: Cyanometallate structures of varying dimensionalities.

### 2.3.1 Ni-Fe cyanometallates

This work focuses mainly on  $\text{Ni}^{\text{II}}\text{-Fe}^{\text{III}}$  cyanometallates. The  $t_{2g}^6 e_g^2$  configuration of the  $d^8$  electrons of  $\text{Ni}^{\text{II}}$  may give rise to ferro- and antiferromagnetic interactions with the  $t_{2g}$  orbitals of the C-coordinated low-spin  $\text{Fe}^{\text{III}}$  ( $t_{2g}^5 e_g^0$ ) which can result in a ferro-, ferri- or antiferromagnet (see Subsection 3.2.1, p. 25). A large variety of such compounds is already known. They present structures of different dimensionalities and varying magnetic, electric and optical properties. An overview is given in Tab. 2.1.

**Table 2.1:** Fe<sup>III</sup>-Ni<sup>II</sup> and Fe<sup>II</sup>-Ni<sup>II</sup> cyanometallates.

<b>compound</b>	<b>magnet</b>	<b>ref.</b>
[Ni(ampy) <sub>2</sub> ] <sub>3</sub> [Fe(CN) <sub>6</sub> ] <sub>2</sub> · 6 H <sub>2</sub> O	ferro	[208]
0D		
[Ni(bpm) <sub>2</sub> ] <sub>3</sub> [Fe(CN) <sub>6</sub> ] <sub>2</sub> · 7 H <sub>2</sub> O	ferro	[209]
[Ni(2,2'-bipy) <sub>2</sub> ] <sub>3</sub> [Fe(CN) <sub>6</sub> ] <sub>2</sub> · 13 H <sub>2</sub> O	ferro	[210]
1D		
[Ni(en) <sub>2</sub> ] <sub>3</sub> [Fe(CN) <sub>6</sub> ] <sub>2</sub> · 2 H <sub>2</sub> O	ferro	[156]
[Ni(en) <sub>2</sub> ] <sub>3</sub> [Fe(CN) <sub>6</sub> ] <sub>2</sub> · 2 H <sub>2</sub> O	meta	[203, 206, 211-213]
[Ni(en) <sub>2</sub> ] <sub>3</sub> [Fe(CN) <sub>6</sub> ] <sub>2</sub> · 3 H <sub>2</sub> O	meta	[206]
[Ni(en) <sub>2</sub> ] <sub>3</sub> [Fe(CN) <sub>6</sub> ] <sub>2</sub>	meta	[206]
[Ni( <i>rac</i> -CTH)] <sub>3</sub> [Fe(CN) <sub>6</sub> ] <sub>2</sub>	ferro	[214]
PPh <sub>4</sub> [Ni(pn) <sub>2</sub> ][Fe(CN) <sub>6</sub> ] · H <sub>2</sub> O	ferro	[203, 211, 213, 215]
2D		
[Ni(dipn) <sub>2</sub> ] <sub>3</sub> [Fe(CN) <sub>6</sub> ] <sub>2</sub> · 10 H <sub>2</sub> O	-	[216]
[Ni(cyclam)] <sub>3</sub> [Fe(CN) <sub>6</sub> ] <sub>2</sub> · 11 H <sub>2</sub> O	ferro	[217]
[Ni(cyclam)] <sub>3</sub> [Fe(CN) <sub>6</sub> ] <sub>2</sub> · 12 H <sub>2</sub> O	meta	[218]
[Ni(cyclam)] <sub>3</sub> [Fe(CN) <sub>6</sub> ] <sub>2</sub> · 16 H <sub>2</sub> O	meta	[191]
[Ni(cyclam)] <sub>3</sub> [Fe(CN) <sub>6</sub> ] <sub>2</sub> · 22.5 H <sub>2</sub> O	meta	[192]
[Ni(N-men) <sub>2</sub> ] <sub>3</sub> [Fe(CN) <sub>6</sub> ] <sub>2</sub> · n H <sub>2</sub> O	ferro	[203, 213]
[Ni(chxn) <sub>2</sub> ] <sub>3</sub> [Fe(CN) <sub>6</sub> ] <sub>2</sub> · 2 H <sub>2</sub> O	ferro	[213, 219]
[Ni( <i>cis</i> -chxn) <sub>2</sub> ] <sub>3</sub> [Fe(CN) <sub>6</sub> ] <sub>2</sub> · 2 H <sub>2</sub> O	ferro	[220]
[Ni( <i>trans</i> -chxn) <sub>2</sub> ] <sub>3</sub> [Fe(CN) <sub>6</sub> ] <sub>2</sub> · 2 H <sub>2</sub> O	ferro	[220-224]
[Ni( <i>trans</i> -chxn) <sub>2</sub> ] <sub>2</sub> [Fe(CN) <sub>6</sub> ] · 5 H <sub>2</sub> O	antiferro	[224]
[Ni(pn) <sub>2</sub> ] <sub>2</sub> [Fe(CN) <sub>6</sub> ]ClO <sub>4</sub> · 2 H <sub>2</sub> O	meta	[203, 213, 225-227]
[Ni(pn) <sub>2</sub> ] <sub>2</sub> [Fe(CN) <sub>6</sub> ]BF <sub>4</sub> · 2 H <sub>2</sub> O	meta	[203, 213, 227]
[Ni(pn) <sub>2</sub> ] <sub>2</sub> [Fe(CN) <sub>6</sub> ]PF <sub>6</sub> · 2 H <sub>2</sub> O	meta	[203, 213, 227]
[Ni(1,1-dmen) <sub>2</sub> ] <sub>2</sub> [Fe(CN) <sub>6</sub> ]ClO <sub>4</sub> · 2 H <sub>2</sub> O	meta	[203, 213, 226, 227]
[Ni(1,1-dmen) <sub>2</sub> ] <sub>2</sub> [Fe(CN) <sub>6</sub> ]BF <sub>4</sub> · 5 H <sub>2</sub> O	ferro	[203, 213, 226, 227]
[Ni(1,1-dmen) <sub>2</sub> ] <sub>2</sub> [Fe(CN) <sub>6</sub> ]PF <sub>6</sub> · 2 H <sub>2</sub> O	meta	[203, 213, 226, 227]
[Ni(1,1-dmen) <sub>2</sub> ] <sub>2</sub> [Fe(CN) <sub>6</sub> ]NCS · H <sub>2</sub> O	meta	[203, 213, 227]
[Ni(1,1-dmen) <sub>2</sub> ] <sub>2</sub> [Fe(CN) <sub>6</sub> ]CF <sub>3</sub> SO <sub>3</sub> · 2 H <sub>2</sub> O	ferro	[203, 213, 227]
[Ni(1,1-dmen) <sub>2</sub> ] <sub>2</sub> [Fe(CN) <sub>6</sub> ]BzO · 6 H <sub>2</sub> O	ferro	[203, 213, 227]
[Ni(1,1-dmen) <sub>2</sub> ] <sub>2</sub> [Fe(CN) <sub>6</sub> ]I · 4 H <sub>2</sub> O	ferro	[203, 213, 227]
[Ni(1,1-dmen) <sub>2</sub> ] <sub>2</sub> [Fe(CN) <sub>6</sub> ]N <sub>3</sub> · 4 H <sub>2</sub> O	ferro	[203, 213, 227]
[Ni(1,1-dmen) <sub>2</sub> ] <sub>2</sub> [Fe(CN) <sub>6</sub> ]NO <sub>3</sub> · 4 H <sub>2</sub> O	ferro	[203, 213, 227]
[Ni(1,1-dmen) <sub>2</sub> ] <sub>2</sub> [Fe(CN) <sub>6</sub> ]Tf · 3.5 H <sub>2</sub> O	ferro	[228]

$[\text{Ni}(1,1\text{-dmen})_2]_2[\text{Fe}(\text{CN})_6](\text{BPDS})_{0.5} \cdot 4 \text{H}_2\text{O}$	meta	[229]
$[\text{Ni}(1,1\text{-dmen})_2]_2[\text{Fe}(\text{CN})_6](\text{BPDS})_{0.5} \cdot 2 \text{H}_2\text{O}$	meta	[229]
$[\text{Ni}(1,1\text{-dmen})_2]_2[\text{Fe}(\text{CN})_6](\text{BPDS})_{0.5}$	ferro	[229]
$[\text{Ni}(1,1\text{-dmen})_2]_2[\text{Fe}(\text{CN})_6]\text{PhBSO}_3 \cdot 5 \text{H}_2\text{O}$	ferro	[230]
$[\text{Ni}(1,1\text{-dmen})_2]_2[\text{Fe}(\text{CN})_6]\text{PhBSO}_3$	ferro	[230]
$[\text{Ni}(1,1\text{-dmen})_2]_2[\text{Fe}(\text{CN})_6]\text{TolSO}_3 \cdot 6 \text{H}_2\text{O}$	ferro	[230]
$[\text{Ni}(1,1\text{-dmen})_2]_2[\text{Fe}(\text{CN})_6]\text{TolSO}_3$	ferro	[230]
$[\text{Ni}(\text{en})_2]_2[\text{Fe}(\text{CN})_6]\text{ClO}_4$	antiferro	[203, 226]
$[\text{Ni}(\text{en})_2]_2[\text{Fe}(\text{CN})_6]\text{BF}_4$	antiferro	[203, 226]
$[\text{Ni}(\text{en})_2]_2[\text{Fe}(\text{CN})_6]\text{PF}_6$	antiferro	[203, 226]
$[\text{Ni}(\text{en})_2]_2[\text{Fe}(\text{CN})_6]\text{NO}_3 \cdot 3 \text{H}_2\text{O}$	ferro	[231]
$[\text{Ni}(\text{tn})_2]_2[\text{Fe}(\text{CN})_6]\text{NO}_3 \cdot 2 \text{H}_2\text{O}$	ferro	[231]
$[\text{Ni}(2,3,2\text{-tet})]_2[\text{Fe}(\text{CN})_6] \cdot 8 \text{H}_2\text{O}$	ferro	[232]
$[\text{Ni}(\text{Me}_2\text{azacyclam})]_3[\text{Fe}(\text{CN})_6]_2 \cdot 9 \text{H}_2\text{O}$	meta	[233]
$[\text{Ni}(\text{Et}_2\text{azacyclam})]_3[\text{Fe}(\text{CN})_6]_2 \cdot 12 \text{H}_2\text{O}$	ferro	[234]
$[\text{Ni}((\text{OH})_2\text{azacyclam})]_3[\text{Fe}(\text{CN})_6]_2 \cdot 8 \text{H}_2\text{O}$	meta	[235]

## 3D

$\text{Ni}_3[\text{Fe}(\text{CN})_6]_2$	ferro	[102]
$[\text{Ni}(\text{en})_2]_3[\text{Fe}(\text{CN})_6](\text{PF}_6)_2$	ferro	[203, 213, 236]
$[\text{Ni}(\text{tn})_2]_3[\text{Fe}(\text{CN})_6](\text{PF}_6)_2$	ferro	[203, 213, 236]
$[\text{Ni}(\text{tn})_2]_3[\text{Fe}(\text{CN})_6](\text{ClO}_4)_2$	ferro	[203, 213, 236]
$[\text{Ni}(\text{tn})_2]_5[\text{Fe}(\text{CN})_6]_3\text{ClO}_4 \cdot 2.5 \text{H}_2\text{O}$	ferro	[237]
$[\text{Ni}(\text{dipn})]_3[\text{Fe}(\text{CN})_6]_2 \cdot 7 \text{H}_2\text{O}$	ferro	[238]
$[\text{Ni}(\text{dipn})]_2[\text{Ni}(\text{dipn})(\text{H}_2\text{O})][\text{Fe}(\text{CN})_6]_2 \cdot 6 \text{H}_2\text{O}$	ferro	[213]
$[\text{Ni}(\text{dipn})]_2[\text{Ni}(\text{dipn})(\text{H}_2\text{O})][\text{Fe}(\text{CN})_6]_2 \cdot 11 \text{H}_2\text{O}$	ferro	[239, 240]
$[\text{Ni}(3,2,3\text{-tet})]_3[\text{Fe}(\text{CN})_6]_2 \cdot 12 \text{H}_2\text{O}$	meta	[241]
$[\text{Ni}(\text{tren})]_3[\text{Fe}(\text{CN})_6]_2 \cdot 6 \text{H}_2\text{O}$	ferri	[213, 242]
$\text{X}[\text{Ni}(\text{C}_3\text{H}_5\text{N}_5\text{-azacyclam})][\text{Fe}(\text{CN})_6] \cdot 4 \text{H}_2\text{O}$	meta	[243]
(X = $\text{NH}_4^+$ , $\text{Li}^+$ , $\text{Na}^+$ , $\text{K}^+$ , $\text{Rb}^+$ , $\text{Cs}^+$ )		

As is obvious from the list above, the structure is largely influenced by the ligand(s) bound to  $\text{Ni}^{\text{II}}$ . They affect the resulting cyanometallate structure by occupying and blocking coordination sites at  $\text{Ni}^{\text{II}}$ , which has usually six coordination sites in an octahedral configuration. Polyamines are predominant as they form strong coordinative bonds to  $\text{Ni}^{\text{II}}$ . 3D arrangements are obtained with small bidentate amines such as en, tn and dipn, while sterically more demanding polyamines or those with more than two coordination sites tend to be better blocking agents and result in structures with lower dimensionalities. On the other hand, sterically less demanding ligands may be arranged more easily on one side (*cis*) of  $\text{Ni}^{\text{II}}$  and thus give rise to one-dimensional rope-ladders. Unfortunately, there is no clear system behind these influences that allows for structure predictions for

new ligands.

Counterions also play an important role in tuning the dimensionality of the obtained cyanometallate. They can originate from one of the precursors in the synthesis or be added deliberately. Ion exchange is often performed to tune the distances of structural layers and control the crystallization of the product. Although only cations (e.g.  $K^+$  in soluble Prussian Blue) are incorporated in the original Prussian Blue structure, cations as well as anions may be found in the structures of Prussian Blue analogues, e.g.  $PPh_4[Ni(pn)_2][Fe(CN)_6] \cdot H_2O$  vs.  $[Ni(en)_2]_2[Fe(CN)_6]ClO_4$ . Ohba and Ōkawa [203] studied the influence of different counterions in the 2D systems  $[Ni(pn)_2]_2[Fe(CN)_6]X \cdot 2 H_2O$  ( $X = ClO_4^-, BF_4^-, PF_6^-$ ) and  $[Ni(1,1-dmen)_2]_2[Fe(CN)_6]X \cdot n H_2O$  ( $X = ClO_4^-, BF_4^-, PF_6^-, CF_3SO_3^-, BzO^-, I^-, N_3^-, NCS^-, NO_3^-$ ). They could tune the intersheet distance by introducing different anions. They found a critical intersheet distance  $d$  of 10 Å for these structures. For  $d < 10$  Å the compounds were metamagnets, while ferromagnets were obtained for  $d > 10$  Å. This transition is due to a shift in the predominant magnetic contributions. In the structures ferromagnetic coupling can be found between  $Ni^{II}$  and  $Fe^{III}$  of the same sheets, but the intersheet coupling is antiferromagnetic. If the intersheet distance is large ( $d > 10$  Å), the intrasheet ferromagnetic contributions dominate while the intersheet antiferromagnetic coupling contributes only weakly. This results in ferromagnetic behavior of the compound. If, on the other hand, the intersheet distance is small ( $d < 10$  Å), the intersheet antiferromagnetic contribution becomes strong and a metamagnet is obtained.

Not only the nature of the precursors, but also the ratio in which they are mixed during the synthesis may affect the structural arrangement, as for Prussian Blue itself (soluble vs. insoluble). This is obvious in the example of 1D  $[Ni(en)_2]_3[Fe(CN)_6]_2$  (ratio 3:2), 2D  $[Ni(en)_2]_2[Fe(CN)_6]PF_6$  (ratio 2:1) and 3D  $[Ni(en)_2]_3[Fe(CN)_6](PF_6)_2$  (ratio 3:1) [156, 203, 206, 211–213, 226, 228, 236].

Finally, even the solvent, the amount of crystal water remaining in the structure and the crystallinity may influence the resulting cyanometallate structure and its magnetism. For example,  $[Ni(1,1-dmen)_2]_2[Fe(CN)_6](BPDS)_{0.5}$  [229] has been reported to be either a metamagnet with crystal water in the structure or a ferromagnet if it is completely dried. The structure  $[Ni(en)_2]_3[Fe(CN)_6]_2 \cdot 2 H_2O$  [156, 203, 206, 211–213] was reported to be a ferromagnet if a polycrystalline sample is studied, while metamagnetic behavior was found for a single crystal of the same structure. Van Langenberg *et al.* [209] accounted a similar situation for the compound  $[Ni(bpm)_2]_3[Fe(CN)_6]_2 \cdot 7 H_2O$ , for which they found ferromagnetic behavior for most polycrystalline powders, but also found some samples that did not show magnetic order although the powder X-ray diffraction patterns were identical.

All this variability in the cyanometallate structures gives manifold possibilities for tuning and design, but unfortunately the resulting structure is hard to predict and control due to the plethora of variables.



# Magnetism

## 3.1 Introduction

Fig. 3.1 shows the five possible arrangements of magnetic moments (electron spins) in a solid, four of which only occur if there are unpaired electrons present [244–246].

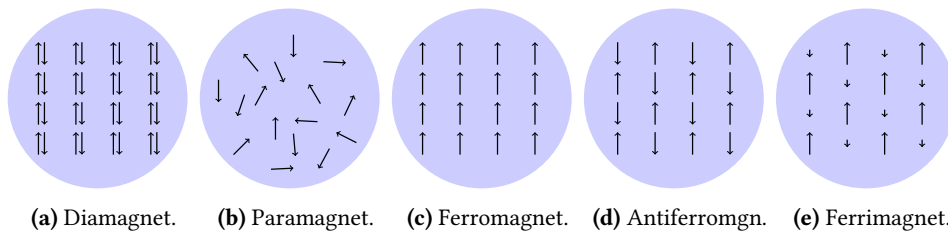


**Figure 3.1:** Possible arrangements of magnetic moments.

*Diamagnetism* describes the state of a material in which all magnetic moments are paired, as shown in Fig. 3.1a. This leads to apparent “non-magnetic” behavior. Only a weak repelling interaction of a diamagnet with an external magnetic field can be observed and a molar magnetic susceptibility  $\chi_m$  smaller than 0 arises. All materials exhibit, to a greater or lesser degree, diamagnetism (from paired closed-shell electrons), but in transition metals it is often overshadowed by other magnetic phenomena. Apart from the latter, diamagnetism is the most common magnetic order and occurs in many conventional compounds, such as most gases, most organic molecules, water and many metals such as Cu, Zn and Bi.[244–246]

*Paramagnetism* arises if there are unpaired spins present in the material, but no periodic order occurs, as sketched in Fig. 3.1b. An external magnetic field exhibits attractive forces on a paramagnet and induces order of the magnetic moments in the direction of the field. This periodic order is, however, lost as soon as the external magnetic field is switched off. Paramagnets obey Curie’s law (see Subsection 3.1.1, p. 22) and have a  $\chi_m$  smaller than zero.  $O_2$  has two unpaired electrons and presents paramagnetism. Additional examples include Mg, Al, Sn, Mo, Pt and some rare earth ions. [244–246]

Materials exhibit *ferromagnetism* if all unpaired spins in the material are ordered and point in the same direction, as shown in Fig. 3.1c. Such materials are commonly known as “magnets” as they are attracted by an external magnetic field and act as permanent magnets that retain magnetization even after the external magnetic field is switched off. A small opposing external field called *coercive field* must be applied to reverse the magnetization. This gives rise to a hysteresis as sketched in Fig. 3.2. Important examples of ferromagnetic materials are Fe, Co, Ni, NdFeB alloys (known as very strong neodymium magnets) and some rare earth metals. Ferromagnetism is exploited in various industrial applications, e.g. in hard discs, for electromagnets, generators and transformers. [244–246]

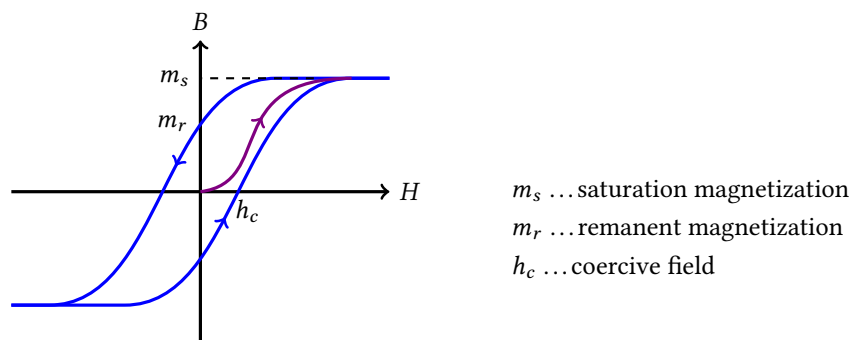


**Figure 3.2:** Visualisation of a hysteresis loop of a ferromagnetic material.

*Antiferromagnetism* occurs when unpaired electrons on neighboring sites in a material align in opposite (antiparallel) directions as sketched in Fig. 3.1d. On a perfect antiferromagnet (at very low temperatures), an external magnetic field does not have any influence as its net magnetization is zero due to the antiparallel spins. At higher temperatures, however, thermal fluctuations allow for the alignment of some spins with the magnetic field and weak ferrimagnetic-type behavior may be observed. In general, antiferromagnetism is less common than the other possible magnetic arrangements. Cr, Mn, hematite  $\text{Fe}_2\text{O}_3$ , NiO, and other transition metal oxides, however, do show this behavior. [244–246]

An arrangement of magnetic moments as shown in Fig. 3.1e results in *ferrimagnetism* of the material. All spins are paired as in antiferromagnetism, but neighboring sites have different values of magnetic moments and a sum magnetic moment arises. Ferrimagnets behave similar to ferromagnets. Hence, their best known representative, magnetite  $\text{Fe}_3\text{O}_4$ , has long been thought to belong to the latter group until Néel [247] described the former phenomenon in 1948. Compounds exhibiting this magnetic behavior besides magnetite are various ferrites and other salts incorporating Fe, and some multinuclear transition metal molecular magnets. [244–246]

### 3.1.1 Curie’s law

Magnetization in paramagnets is approximately directly proportional to the applied external field. It is approximately inversely proportional to the temperature since thermal motion of the electron spins counteracts the ordering induced by the external magnetic

field. This is expressed by Curie's law in Eq. 3.1, where  $M$  is the magnetization (in Amperes per meter),  $C$  is the material's specific *Curie constant*,  $B$  the external magnetic field (in Tesla, "magnetic induction"), and  $T$  the temperature (in Kelvin). [244–246]

$$M = C \cdot \frac{B}{T} \quad (3.1)$$

As a measure for the behavior of different paramagnetic materials, the *molar magnetic susceptibility*  $\chi_m$  is considered. It describes the proportionality of the magnetization  $M$  (in Amperes per meter) of the paramagnet to the applied external field  $H = B/\mu$  (in Amperes per meter) and is characteristic for the material [244–246]:

$$M = \frac{\rho}{M_m} \cdot \chi_m \cdot \frac{B}{\mu}, \quad (3.2)$$

where  $\rho$  is the density of the material and  $M_m$  its molecular mass.[244–246]

By adjusting  $C$  to include  $\rho$ ,  $M_m$  and the magnetic permeability  $\mu$  of the material, we get Curie's law expressed by the dependence of  $\chi_m$  on the temperature as follows [244–246]:

$$\chi_m = \frac{C}{T} \quad (3.3)$$

### 3.1.2 Curie-Weiss law

To describe the behavior of ferromagnetic, ferrimagnetic and antiferromagnetic materials, Curie's law has to be adapted to take the spontaneous interaction between adjacent spins below a certain temperature into account. This characteristic temperature at which ordering occurs is called *Curie temperature*,  $T_C$ , for ferro- and ferrimagnets and *Néel temperature*,  $T_N$ , for antiferromagnets. Above the respective ordering temperature the material behaves like a paramagnet, only below the ferro-, ferri- or antiferromagnetic properties, respectively, arise. [244–246]

The Curie-Weiss law is only valid at  $T \gg T_C \mid T_N$ , at which the following expressions for the molar magnetic susceptibility  $\chi_m$  hold:

$$\chi_m^F = \frac{C}{T - T_C}, \quad \chi_m^{AF} = \frac{C}{T - T_N}, \quad (3.4)$$

where  $C$  is the Curie constant [244–246].

Close to the ordering temperature, however, magnetic order arises that results in the need to introduce a critical exponent  $\gamma$  [244–246].

$$\chi_m^F = \frac{C}{(T - T_C)^\gamma}, \quad \chi_m^{AF} = \frac{C}{(T - T_N)^\gamma} \quad (3.5)$$

To take this critical behavior into account even at temperatures above the ordering,  $T_C \mid T_N$  is replaced by a temperature  $\theta$  which is called the *Weiss constant* [244–246].

$$\chi_m = \frac{C}{T - \theta} \quad (3.6)$$

In the interpretation of experimental data the sign of  $\theta$  is often considered to gain insight into the magnetic nature of the analyzed material. As outlined in Fig. 3.3, plotting  $1/\chi_m$  vs. temperature for  $T > T_C \mid T_N$  results in a linear function. The value of  $\theta$  can be assessed by extrapolation to  $1/\chi_m = 0$ . A negative Weiss constant indicates local antiferromagnetic interaction and a positive  $\theta$  ferromagnetism. [126, 244–246]

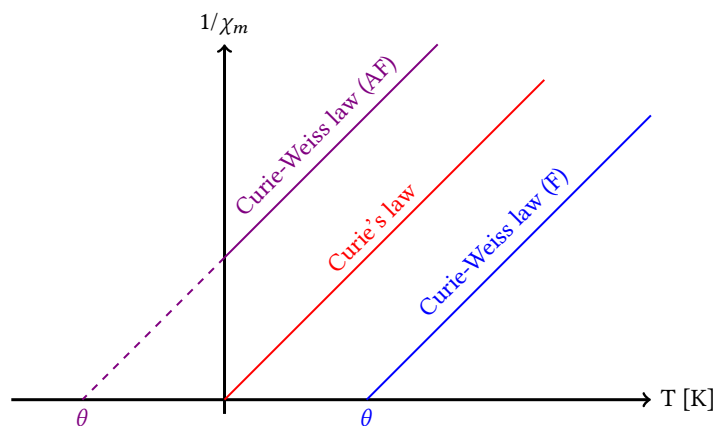


Figure 3.3: Visualisation of the interpretation of the Weiss constant  $\theta$ .

### 3.2 In Prussian Blue Analogues

As described above (see Subsection 2.2.1, p. 14), Prussian blue is ferromagnetic due to coupling between its  $\text{Fe}^{\text{III}}$  ions through  $-\text{N}\equiv\text{C}-\text{Fe}^{\text{II}}-\text{C}\equiv\text{N}-$  bridges. It has a low  $T_C$  ( $\sim 5$  K) because  $\text{Fe}^{\text{II}}$  is diamagnetic and thus the distance between the magnetic centers is quite large ( $\sim 10$  Å), which results in weak coupling. Some attempts have been made to obtain better coupling and higher  $T_C$  by substitution of  $\text{Fe}^{\text{II}}$  by paramagnetic metal centers that would ferromagnetically couple with  $\text{Fe}^{\text{III}}$  and thus cut the distance in half, to  $\sim 5$  Å. [109, 123, 248–251]

Prussian Blue analogues are interesting for magnetic studies because the cyanide ion facilitates coupling of magnetic moments between neighboring metal centers. This is due to the fact that it is a very small, compact ion and may support high spin density. Further,  $\text{M}-\text{C}\equiv\text{N}-\text{M}'$  bridges are linear (angles close to  $180^\circ$ ) which allows for strong magnetic interactions between adjacent spin centers. The superexchange mechanism of adjacent metal orbitals of  $\pi$  symmetry occurs through filled  $\pi$  and empty  $\pi^*$  cyanide orbitals. In general, singly occupied orthogonal orbitals give rise to ferromagnetic coupling while antiferromagnetic contributions stem from overlapping orbitals. The coupling between the metals increases by metal-to-ligand back-bonding from the  $\pi^*$  orbital of the cyanide to the  $t_{2g}$  orbital of the metal center, which results in a higher  $T_C$ . [109, 126, 252]

Interest in Prussian Blue analogues rose recently due to their potential to form molecule-based magnets which have possible applications in information storage devices, electric power transformers, high-fidelity speakers etc. [204]. By changing the transition metal centers and incorporating other ligands besides cyanide, the structure and magnetic properties of the resulting material may be tuned. This allows a building block approach for the design of new cyanometallate materials. Further, Prussian Blue analogues may have additional interesting properties, such as transparency or photo-switchability, and can be obtained as thin films or nanoparticles. Their chemical stability presents another desirable feature, as does the fact that the metal centers are covalently linked, which ensures good magnetic coupling. Additionally, their preparation is often possible at room temperature. [109, 126]

The magnetic ordering may, however, suffer from a few problems that are difficult to overcome [109, 253]:

- Prussian Blue analogues act as sponges. Solvent molecules or small cations are often entrapped in the large pores in the structures, which may leave the structure or be replaced by other molecules. These irregularities often disrupt the structural and magnetic ordering and lower the  $T_C$ .
- Prussian Blue analogues are usually poorly soluble and obtained by fast precipitation after mixing of two precursor solutions. This often leads to poor crystallinity, an amorphous product or a mixture of several phases. This may result in an inhomogeneous sample and, again, disruption of the structural and magnetic order.
- Linkage isomerism of the cyanide ion may occur in Prussian Blue analogues. Again, partial disorder in the structure may arise, or the magnetic coupling of neighboring metal centers may be impaired by low-spin/high-spin alterations.
- Finally, intermetallic charge transfer and redox reactions may occur between the different transition metals, which may lead to a less-than-optimal orbital coupling and a lowering of  $T_C$ .

### 3.2.1 Exchange Interaction

As elaborated above, the magnetic properties of Prussian Blue and its analogues are determined by the coupling of adjacent metal centers. The nature of this exchange interaction largely depends on the involved orbitals. Typically, the transition metals in Prussian Blue analogues are octahedrally coordinated. According to *ligand field theory* [254] this gives rise to a splitting of the d-orbitals into three  $t_{2g}$  orbitals ( $d_{xy}$ ,  $d_{xz}$ ,  $d_{yz}$ ) of lower energy and two  $e_g$  ( $d_{x^2-y^2}$ ,  $d_{z^2}$ ) orbitals of higher energy. If neighboring metal centers in the Prussian Blue structure have unpaired electrons in the same orbitals (either  $e_g$  or  $t_{2g}$ ), the orbitals overlap via cyanide  $\pi^*$  orbitals and the exchange interaction leads to a spin pairing according to the *Pauli principle*. This gives rise to antiferromagnetic coupling and a stabilization of the lowest spin multiplicity as shown in Fig. 3.4a. An unequal number of unpaired electrons on adjacent metal centers, however, leads to an arrangement in which not all spins are completely compensated, which can result in ferrimagnetic behavior.

Unpaired electrons in different, orthogonal orbitals ( $e_g$  vs.  $t_{2g}$ ) of adjacent metal centers in the Prussian Blue structure give rise to ferromagnetic coupling (Fig. 3.4b). The highest spin multiplicity is stabilized according to *Hund's rule*. [126]

Taking into account all possible arrangements of spins and orbitals on neighboring metal centers, four possibilities of coupling arise, as shown in Fig. 3.5. The interacting centers carry spins  $S_1$  and  $S_2$ , and the value of coupling is described by  $J$ , the coupling constant. The four configurations are: [109]

- Antiferromagnetic coupling (Fig. 3.5a) occurs if  $J < 0$  which leads to a total spin  $S$  of 0.
- Fig. 3.5b shows ferromagnetic coupling which results if  $J > 0$ . This configuration is rather rare in Prussian Blue analogues.

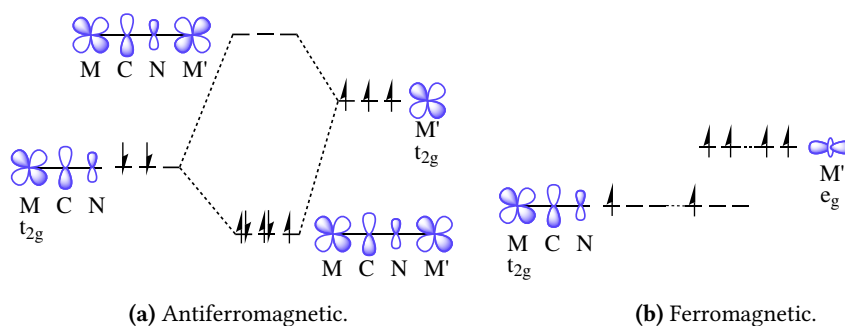


**Figure 3.4:** Superexchange interactions in Prussian Blue analogues. [196]

- Ferromagnetic coupling may also arise through a diamagnetic neighbor (Fig. 3.5c), as in Prussian Blue itself. This long range coupling, however, leads to rather low  $J$  and  $T_C$  values.
- If antiferromagnetic coupling occurs between spins of different values (Fig. 3.5d), antiferromagnetism arises.

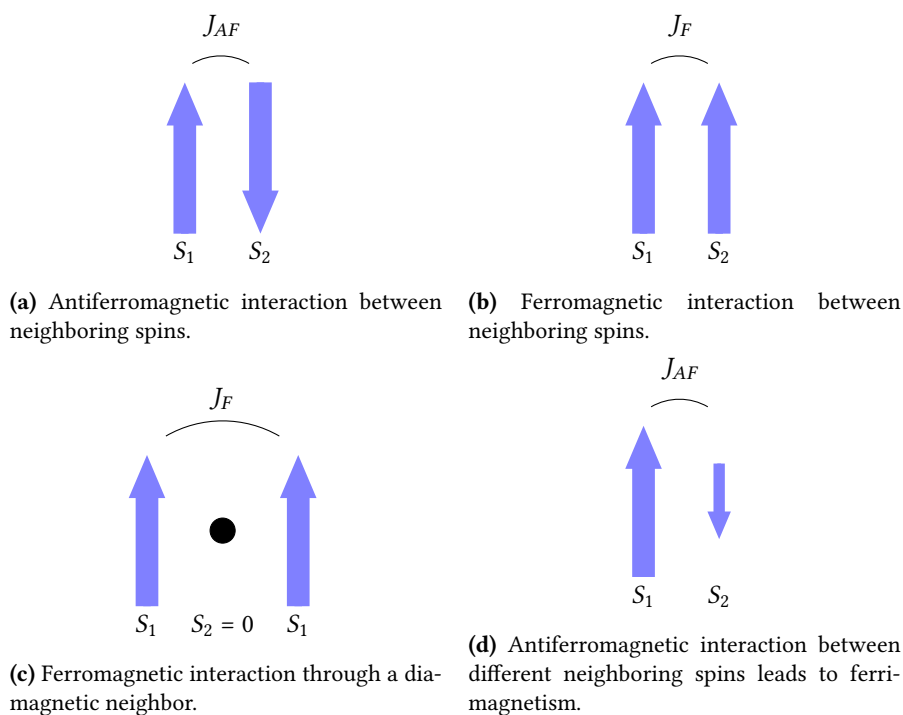


**Figure 3.5:** Possible spin arrangements in Prussian Blue analogues.[109]

From these general rules, design strategies can be drawn with respect to the transition metal centers. If the N-coordinated metal has 8 or 9 d-electrons or is low-spin  $d^7$ , the unpaired electrons will be in an  $e_g$  orbital. The low-spin C-coordinated metal, on the other hand, will have unpaired electrons, if any, only in the energetically more favorable  $t_{2g}$  orbital. The coupling of these orthogonal orbitals would, as explained above, lead to ferromagnetic interactions.

A  $d^1$ ,  $d^2$ ,  $d^3$  or low-spin  $d^4$  or  $d^5$  N-coordinated metal has only unpaired electrons in

a  $t_{2g}$  orbital. These interact with the electrons in the  $t_{2g}$  orbital of C-coordinated metal antiferromagnetically. This does not necessarily give rise to an antiferromagnet, also ferrimagnets may result, especially for  $d^2$  and  $d^3$  metals, as the amount of unpaired spins of the sites may be different.

Finally, N-coordinated metals with unpaired electrons in the  $t_{2g}$  and  $e_g$  orbitals (high-spin  $d^4$ , high-spin  $d^5$ ,  $d^6$ , high-spin  $d^7$ ) give rise to ferro- and antiferromagnetic interactions with the  $t_{2g}$  orbitals of the C-coordinated metal. In this case, usually the antiferromagnetic contributions dominate which leads to a ferrimagnet with low  $T_C$  and weak exchange coupling. [109]

For the transition metal combination that presents the focus of this work,  $Ni^{II}$ - $Fe^{III}$ , ferromagnetic interactions arise by orbital coupling in a 3D cyanide-bridged arrangement.  $Ni^{II}$  has a  $d^8$  configuration with two unpaired electrons in the  $e_g$  orbitals. In low-spin  $Fe^{III}$ , which is present in  $[Fe(CN)_6]^{3-}$ , the  $d^5$  configuration leads to one unpaired electron in the  $t_{2g}$  orbitals. As these orbitals are orthogonal, the spins are not paired and ferromagnetic interaction results.

In lower-dimensional structures, however, antiferromagnetic coupling may arise between sheets or chains. An antiferro- or metamagnet may be obtained if this contribution outweighs the ferromagnetic coupling, as described in Subsection 2.3.1, p. 17.





## Motivation and Aims

The main goal of this work is to study whether an extended low-dimensional cyanometallate network structure may be embedded in and chemically linked to a sol-gel silica ( $\text{SiO}_2$ ) matrix while preserving the structural alignment and properties of the cyanometallate. This is of interest because a combination of the complementary properties of amorphous  $\text{SiO}_2$  and magnetic cyanometallates could lead to very useful materials. As elaborated in Sec. 1.2, p. 76,  $\text{SiO}_2$  synthesized by means of the sol-gel method is very versatily processable. Sol-gel  $\text{SiO}_2$  as matrix for cyanometallates, which are usually obtained either as single crystals or as powders, may not only transfer this processability, but also link the low-dimensional structure components (2D sheets, 1D chains) covalently to each other as sketched in Fig. 4.1. This covalent linking is considered as an option to enhance the magnetic coupling between the metal centers of adjacent chains or sheets.

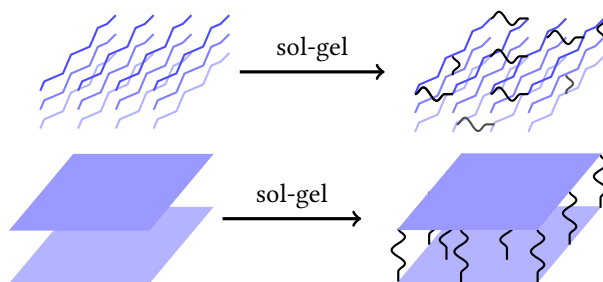


**Figure 4.1:** Cross-linking of low-dimensional cyanometallates by sol-gel  $\text{SiO}_2$ .

Cyanometallates were chosen as test species due to their fascinating properties, which – beside conventional ferro- and metamagnetism – include photo-switchability, transparency, single-chain magnetism, catalytic activity, high porosity etc. Furthermore, cyanometallates are very versatile and exist in various dimensionalities (0D, 1D, 2D, 3D), which can be tuned by changing the metal centers or blocking ligands.

The focus of the present work lies on cyanometallate networks of  $\text{Ni}^{\text{II}}$  and  $\text{Fe}^{\text{III}}$ . This combination was chosen for several reasons. The most important one was the variety

of such cyanometallates studied in literature, as elaborated in Subsection 2.3.1, p. 17. Furthermore,  $[\text{Fe}(\text{CN})_6]^{3-}$  is commercially available and comparatively non-toxic, which makes its handling quite convenient. Its advantage over  $[\text{Fe}(\text{CN})_6]^{4-}$  is the unpaired d-electron that can magnetically couple to the unpaired d-electrons of  $\text{Ni}^{\text{II}}$ , which leads to more interesting magnetic properties.  $\text{Ni}^{\text{II}}$  was not only selected due to its  $d^8$  electron configuration which is ideal for magnetic coupling of orbitals, but also because it binds to a variety of polyamine blocking ligands. These blocking ligands render the cyanometallate network tunable regarding the structural dimensionality and, additionally, offer the possibility to introduce sol-gel processable groups in the network backbone by chemical modification.

Polyamine blocking ligands with trialkoxysilyl groups ( $-\text{SiOR}_3$ ,  $R = \text{Me, Et}$ ) should be synthesized to achieve the main goal. Subsequent complexation with  $\text{Ni}^{\text{II}}$  and network formation with  $\text{K}_3[\text{Fe}(\text{CN})_6]$  should be performed to obtain the cyanometallate structure. Sol-gel processing should then be carried out by addition of TEOS and a base catalyst to build up the matrix around and cross-links within the pre-organized cyanometallate network. The characterization of the resulting sol-gel material should be focused on its magnetic properties and structural elucidation to determine whether the cyanometallate network is disrupted by sol-gel processing.

The blocking ligand usually has a quite strong impact on the cyanometallate structure, as discussed in Subsection 2.3.1, p. 17. Diamines and tetramines should be examined to evaluate the effect the blocking ligand has on the embedded cyanometallate. Additionally, rigid cyclam (1,4,8,11-tetraazacyclotetradecane,  $\text{C}_{10}\text{H}_{24}\text{N}_4$ ), which can coordinate through its four amine groups only in a plane, should be compared to more flexible open-chain tetramines.

Further, the influence of the number of anchor groups should be studied as part of this work. This should be done by comparing the structures and magnetic properties of two cyanometallate networks incorporating the same polyamine, but with one or two  $-\text{SiOR}_3$  groups, respectively.

Finally, a cyanometallate network of  $\text{Cu}^{\text{II}}$  and  $\text{Fe}^{\text{III}}$  should be synthesized and embedded in sol-gel  $\text{SiO}_2$  to allow for an assessment of the impact of the metal center on the magnetic behavior.  $\text{Cu}^{\text{II}}$  is a  $d^9$  transition metal ion. Instead of two unpaired d-electrons as in  $\text{Ni}^{\text{II}}$  it only has one and therefore is expected to present weaker magnetic coupling to  $\text{Fe}^{\text{III}}$ .

## **Part II**

# **Results and Discussion**



## Ni<sup>II</sup>-Fe<sup>III</sup>-SiO<sub>2</sub> Gel with Silyl-ethylenediamine

N-(2-aminoethyl)-3-aminopropyltrimethoxysilane (“silyl-ethylenediamine”, AEAPTS) is similar to N-methylethylenediamine (N-men). The substituent at the secondary nitrogen atom, however, is significantly larger. N-men was employed as a ligand by Ohba and Ōkawa [203, 213] in the cyanometallate  $[\text{Ni}(\text{N-men})_2]_3[\text{Fe}(\text{CN})_6]_2 \cdot n \text{H}_2\text{O}$  which has a 2D structure and is ferromagnetic.



Figure 5.1: Structures of AEAPTS and N-men.

### 5.1 Synthesis

Details of the experimental procedures and reaction conditions of the synthesis of  $[\text{Ni}(\text{AEAPTS})_2]_3[\text{Fe}(\text{CN})_6]_2$  gel are described in Part III, p. 103. This formula, however, is not a completely correct representation of the structure. The trimethoxysilyl groups of the blocking ligands react during the sol-gel process, which means it is not actually AEAPTS any more, but instead its hydrolyzed and condensed form.

The synthesis of  $[\text{Ni}(\text{AEAPTS})_2]_3[\text{Fe}(\text{CN})_6]_2$  embedded in SiO<sub>2</sub> gel starting from commercial AEAPTS requires three steps, as shown in Fig. 5.2. First, complexation yields the dark violet  $[\text{Ni}(\text{AEAPTS})_3]\text{Cl}_2$  by addition of three molar equivalents of AEAPTS to a methanol solution of anhydrous NiCl<sub>2</sub> [255]. The second step, cyanometallate network formation, is performed by the addition of K<sub>3</sub>[Fe(CN)<sub>6</sub>] in methanol to a methanol solution of the Ni<sup>II</sup> complex. The cyanometallate  $[\text{Ni}(\text{AEAPTS})_2]_3[\text{Fe}(\text{CN})_6]_2$  precipitates immediately as a brown powder. The coordination sites of Ni<sup>II</sup> are saturated, however, by the three diamine ligands. This means cyano bridges can only form if (at least) one AEAPTS

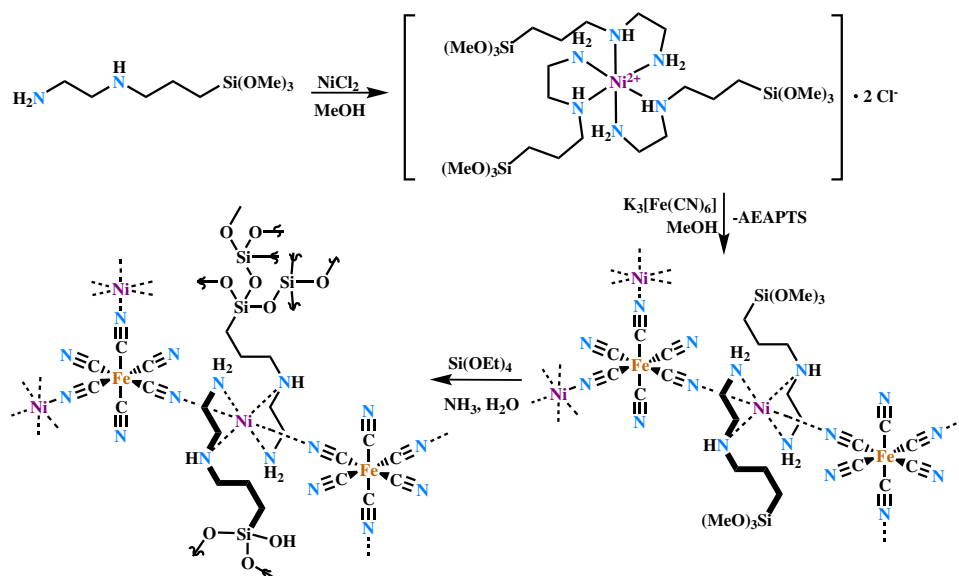


Figure 5.2: Synthesis of  $[\text{Ni}(\text{AEAPTS})_2]_3[\text{Fe}(\text{CN})_6]_2$  gel.

ligand is cleaved to unblock coordination sites of  $\text{Ni}^{\text{II}}$ . This need to unblock coordination sites before cyanide ligands can attack  $\text{Ni}^{\text{II}}$  retards the reaction and thus provides better structural control and crystallinity [203].

Sol-gel processing is subsequently performed at  $70\text{ }^\circ\text{C}$  [29].  $[\text{Ni}(\text{AEAPTS})_2]_3[\text{Fe}(\text{CN})_6]_2$  is dissolved/suspended in  $0.2\text{ M}$  aqueous  $\text{NH}_3$  and tetraethoxysilane (TEOS) is added as matrix former and cross-linker. The reaction mixture is poured on a glass plate after stirring for two days and the solvent allowed to evaporate under ambient conditions. The formed solid, in which  $[\text{Ni}(\text{AEAPTS})_2]_3[\text{Fe}(\text{CN})_6]_2$  is tethered to the silica network by co-condensation of the  $-\text{Si}(\text{OMe})_3$  groups of AEAPTS, is scraped off, washed with water and dried to yield a fine powder.

## 5.2 FTIR

Each intermediate and the final product were analyzed by FTIR spectroscopy, shown in Fig. 5.3.

The FTIR spectrum of AEAPTS shows the expected absorption bands. The amine functions – one primary and one secondary – give rise to absorption maxima at  $3195$ ,  $3303$  and  $3371\text{ cm}^{-1}$  due to  $\text{NH}/\text{NH}_2$  stretching, at  $1592\text{ cm}^{-1}$  due to  $\text{NH}_2$  bending and at  $808$  and  $777\text{ cm}^{-1}$  due to  $\text{NH}/\text{NH}_2$  wagging. The trimethoxysilyl group causes absorption maxima at  $1076$ ,  $1190$  and  $2839\text{ cm}^{-1}$  due to  $\text{Si}-\text{OCH}_3$  vibrations. The bands arising from  $\text{Si}-\text{CH}_2$  and  $\text{C}-\text{NH}/\text{C}-\text{NH}_2$  are hidden behind the lower two bands.

Few changes occur in the FTIR spectrum upon complexation by  $\text{Ni}^{\text{II}}$ . All characteristic bands discussed above stay essentially the same, but the characteristic amine groups are slightly shifted upon coordination. The band due to  $\text{NH}_2$  bending shows a maximum at  $1598\text{ cm}^{-1}$  and the band arising from  $\text{NH}/\text{NH}_2$  wagging at  $812$  and  $786\text{ cm}^{-1}$ . Additional

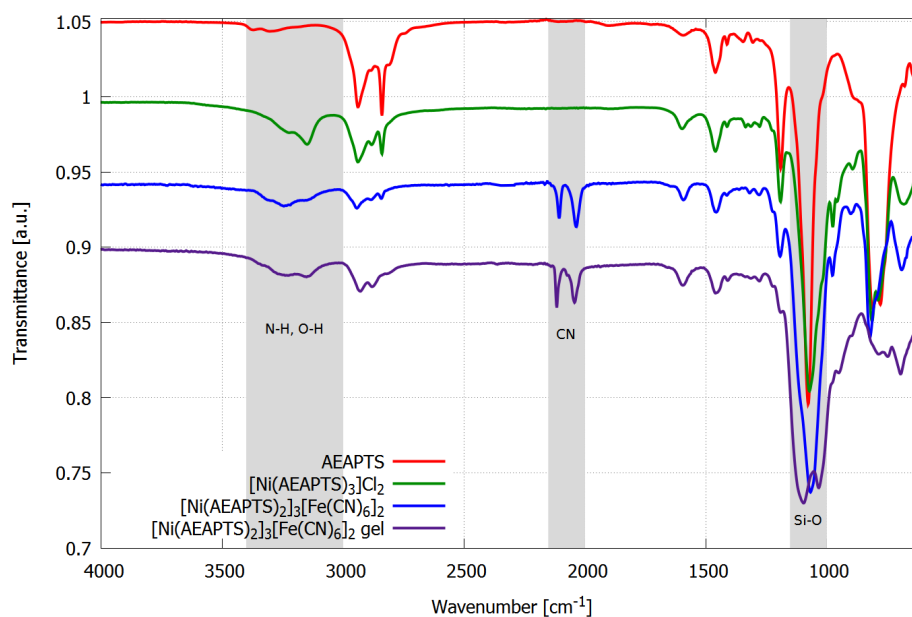


**Figure 5.3:** FTIR spectra of AEAPTS,  $[\text{Ni}(\text{AEAPTS})_3]\text{Cl}_2$ ,  $[\text{Ni}(\text{AEAPTS})_2]_3[\text{Fe}(\text{CN})_6]_2$  and  $[\text{Ni}(\text{AEAPTS})_2]_3[\text{Fe}(\text{CN})_6]_2$  gel.

stronger bands at  $3149$  and  $3231\text{ cm}^{-1}$  may be due to vibrations of  $-\text{OH}$  groups from coordinated and crystal MeOH.

Two new bands appear in the cyanometallate network  $[\text{Ni}(\text{AEAPTS})_2]_3[\text{Fe}(\text{CN})_6]_2$  with absorption maxima at  $2035$  and  $2106\text{ cm}^{-1}$ . These are characteristic for cyano groups. The corresponding band in  $\text{K}_3[\text{Fe}(\text{CN})_6]$  is at  $2116\text{ cm}^{-1}$ . The band at  $2106\text{ cm}^{-1}$  can therefore be assigned to non-bridging  $\text{C}\equiv\text{N}$  ligands. The additional band at  $2035\text{ cm}^{-1}$ , on the other hand, arises due to bridging cyano groups. This is a clear evidence, besides the precipitation and colour change of the product, for the successful network formation.

The bands characteristic for  $\text{Si}-\text{OCH}_3$  at  $1076$ ,  $1190$  and  $2839\text{ cm}^{-1}$  disappear in the FTIR spectrum of  $[\text{Ni}(\text{AEAPTS})_2]_3[\text{Fe}(\text{CN})_6]_2$  gel, the material after sol-gel processing. However, two new absorption maxima at  $1033$  and  $1095\text{ cm}^{-1}$  appear in the region characteristic for  $\text{Si}-\text{O}$ . They arise from the  $\text{Si}-\text{O}-\text{Si}$  entities of the amorphous  $\text{SiO}_2$  network. The fact that the FTIR spectrum otherwise remains nearly unchanged, i.e. that the characteristic bands for the cyano and amine groups are still present, indicates that the cyanometallate network is retained upon sol-gel processing.

### 5.3 SEM and EDX

The SEM shown in Fig. 5.4 was recorded at a voltage of  $10\text{ kV}$ . It proves the homogeneity of  $[\text{Ni}(\text{AEAPTS})_2]_3[\text{Fe}(\text{CN})_6]_2$  gel. No crystallites of the cyanometallate are discernible. This indicates that no (visible) phase separation occurs.

EDX measurement (Fig. 5.5) confirmed a homogeneous distribution of the metals and, thus, the cyanometallate network in  $[\text{Ni}(\text{AEAPTS})_2]_3[\text{Fe}(\text{CN})_6]_2$  gel. A Ni:Fe ratio of  $\sim 3.3:2$  was found from the atomic percentages (Tab. 5.1) obtained by quantitative analysis. This

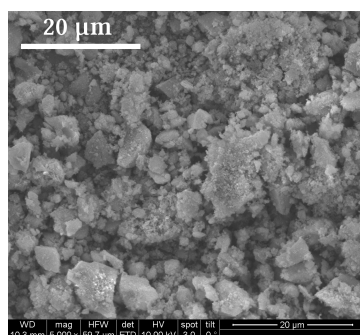


**Figure 5.4:** SEM of  $[\text{Ni}(\text{AEAPTS})_2]_3[\text{Fe}(\text{CN})_6]_2$  gel.

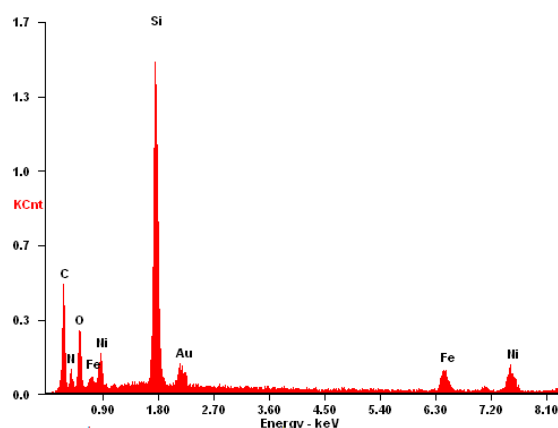


**Figure 5.5:** EDX plot (energy [keV] vs. intensity) of  $[\text{Ni}(\text{AEAPTS})_2]_3[\text{Fe}(\text{CN})_6]_2$  gel.

corresponds quite well to the metal ratio used for the preparation of  $[\text{Ni}(\text{AEAPTS})_2]_3[\text{Fe}(\text{CN})_6]_2$  and is expected for a cyanometallate of  $\text{Ni}^{\text{II}}$  and  $\text{Fe}^{\text{III}}$  due to charge balance. The small excess of nickel may arise from the fact that the  $\text{Ni}^{\text{II}}$  compound is covalently linked to the silica matrix through the diamine ligand while excess  $[\text{Fe}(\text{CN})_6]^{3-}$  is not bound in the network and thus may be removed by washing with water.

**Table 5.1:** EDX analysis of  $[\text{Ni}(\text{AEAPTS})_2]_3[\text{Fe}(\text{CN})_6]_2$  gel.

element	at. %
C (K)	57.55
N (K)	14.01
O (K)	13.83
Si (K)	10.52
Fe (K)	1.55
Ni (K)	2.54
Total	100

**Table 5.2:** Experimental vs. fitted reflections for hexagonal crystal structure for  $[\text{Ni}(\text{AEAPTS})_2]_3[\text{Fe}(\text{CN})_6]_2$ .

peak	fit	$q_{\text{max}}$ [ $\text{nm}^{-1}$ ]
$d_{100}$	4.772	4.8
$d_{110}$	8.265	8.4
$d_{200}$	9.543	9.5
$d_{002}$	11.599	11.6
$d_{102}$	12.542	12.5
$d_{210}$	12.625	–
$d_{300}$	14.315	14.3
$d_{202}$	15.02	15.0

## 5.4 SWAXS

SWAXS measurements of  $[\text{Ni}(\text{AEAPTS})_2]_3[\text{Fe}(\text{CN})_6]_2$  and  $[\text{Ni}(\text{AEAPTS})_2]_3[\text{Fe}(\text{CN})_6]_2$  gel were performed (Fig. 5.6). Structural changes of the cyanometallate network upon embedding in  $\text{SiO}_2$  can be determined by comparison of the two curves.

$[\text{Ni}(\text{AEAPTS})_2]_3[\text{Fe}(\text{CN})_6]_2$  (black curve in Fig. 5.6) exhibits distinct Bragg reflections. Tab. 5.2 shows that indexing of the reflections, labelled accordingly in the insert of Fig. 5.6, for a hexagonal unit cell with lattice parameters  $a = b = 15.2 \text{ \AA}$  and  $c = 10.8 \text{ \AA}$ , is in good agreement with the experimental  $q_{\text{max}}$  values. A structure model consistent with the SWAXS data is sketched in Fig. 5.7. The metal centers  $\text{Ni}^{\text{II}}$  and  $\text{Fe}^{\text{III}}$  are represented by



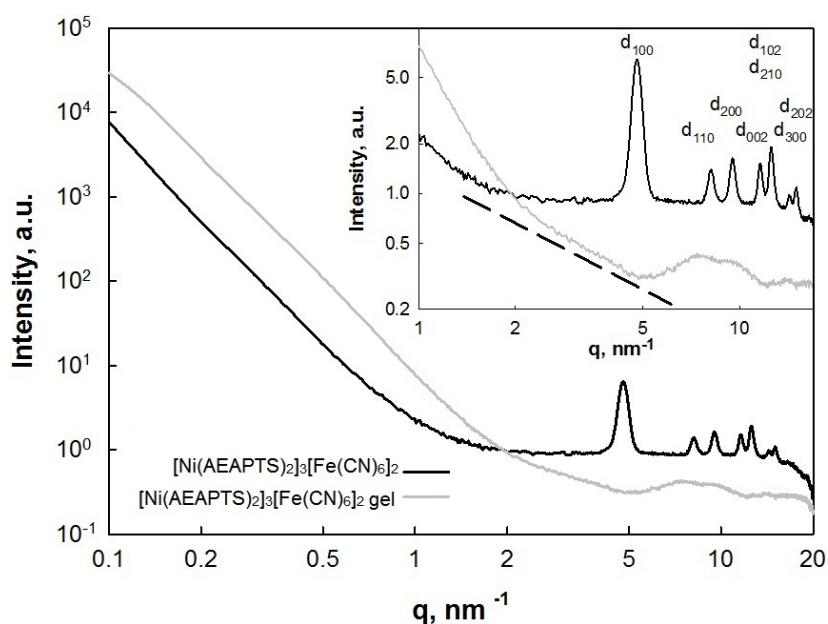


**Figure 5.6:** SWAXS measurements of  $[\text{Ni}(\text{AEAPTS})_2]_3[\text{Fe}(\text{CN})_6]_2$  and  $[\text{Ni}(\text{AEAPTS})_2]_3[\text{Fe}(\text{CN})_6]_2$  gel.

a violet cross and a yellow bar, respectively. Solid black lines represent cyanide bridges. The  $ac$  plane is depicted in Fig. 5.7a, in which double chains align parallel. The double chains consist of two  $-\text{Fe}^{\text{III}}-\text{C}\equiv\text{N}-\text{Ni}^{\text{II}}-$  chains which are shifted relative to each other by  $5.04 \text{ \AA}$  in  $c$  direction. This distance corresponds quite well to the typical size of a  $\text{Fe}^{\text{III}}-\text{C}\equiv\text{N}-\text{Ni}^{\text{II}}$  repeat unit [122]. A *cis* arrangement of the cyano ligands at  $\text{Ni}^{\text{II}}$  is therefore to be expected. This results in a rope-ladder network structure with the amine blocking ligands pointing into the interstice between the double chains. Fig. 5.7b shows a view of the  $ab$  plane. The double chains are aligned in a hexagonal arrangement along the  $c$  axis. A  $\text{Ni}^{\text{II}}:\text{Fe}^{\text{III}}$  ratio of 1:1 would be expected for such chains, but this is impossible due to charge imbalances. This can be avoided by introducing  $\text{Fe}^{\text{III}}$  vacancies randomly in the cyanometallate network.

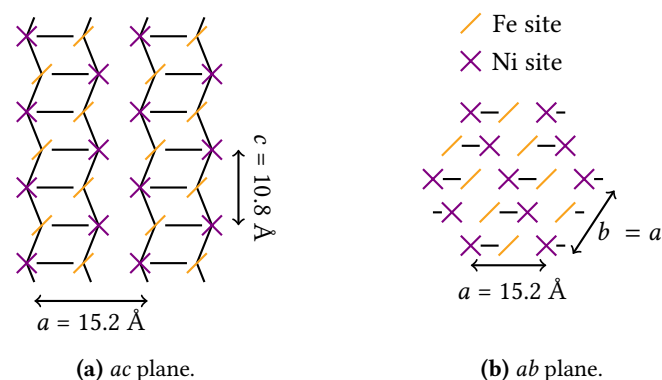


**Figure 5.7:** Structure model for double chains arranged in hexagonal lattice.

An alternative structure model, that takes the 3:2 Ni:Fe ratio into account, is similar to the structure of  $[\text{Ni}(\text{en})_2]_3[\text{Fe}(\text{CN})_6]_2 \cdot n \text{H}_2\text{O}$  as discussed by Ohba *et al.* and Herchel *et al.* [156, 206]. The structure is built by more complex double chains where in one direction

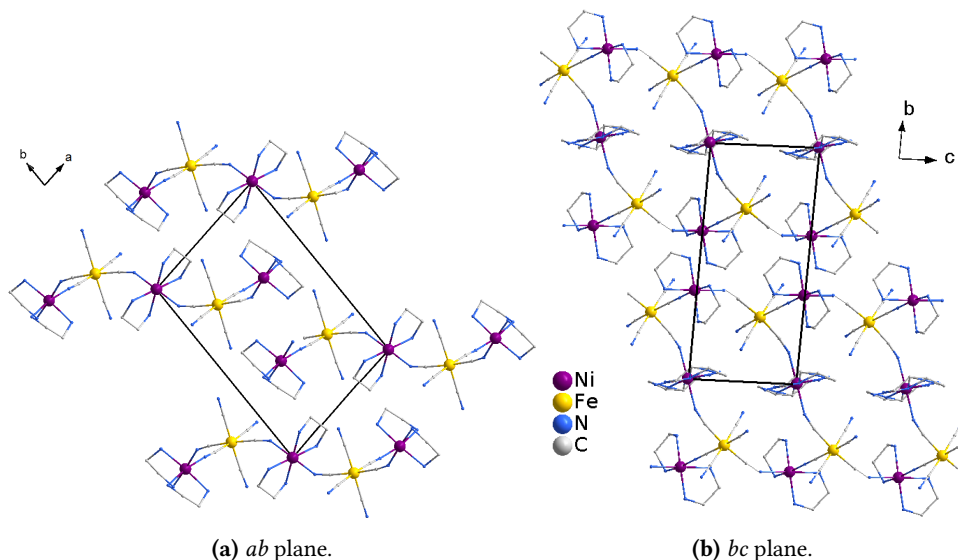


**Figure 5.8:** Crystal structure of  $[\text{Ni}(\text{en})_2]_3[\text{Fe}(\text{CN})_6]_2 \cdot 2 \text{H}_2\text{O}$ . [156]

$\text{Fe}^{\text{III}}$  and  $\text{Ni}^{\text{II}}$  alternate and two strands of such  $-\text{Fe}^{\text{III}}-\text{C}\equiv\text{N}-\text{Ni}^{\text{II}}-$  chains are connected by  $\text{C}\equiv\text{N}-\text{Ni}^{\text{II}}-\text{N}\equiv\text{C}$  bridges, as shown in Fig. 5.8b. Each 1D chain is thus made up of repeat units of three  $\text{Ni}^{\text{II}}$  and two  $\text{Fe}^{\text{III}}$  alternatingly connected by cyano bridges, as shown in Fig. 5.8a. This results in a  $\text{Ni}_3\text{Fe}_2$  stoichiometry with two cyanide bridges and two diamine blocking ligands at every  $\text{Ni}^{\text{II}}$  and three cyanide bridges and three non-bridging cyano groups in *mer* arrangement at every  $\text{Fe}^{\text{III}}$ . The arrangement of the double chains leads to a triclinic crystal structure for  $[\text{Ni}(\text{en})_2]_3[\text{Fe}(\text{CN})_6]_2 \cdot n \text{H}_2\text{O}$ . A similar arrangement of double chains with slightly tighter packing can be rationalized for  $[\text{Ni}(\text{AEAPTS})_2]_3[\text{Fe}(\text{CN})_6]_2$  by fitting an orthorhombic lattice with  $a = 7.85 \text{ \AA}$ ,  $b = 13.11 \text{ \AA}$  and  $c = 5.35 \text{ \AA}$  (axes as depicted in Fig. 5.8) This gives excellent agreement between fit and experiment, as shown in Tab. 5.3. The reflections of the SWAXS curve are indexed accordingly in Fig. 5.9.

**Table 5.3:** Experimental vs. fitted reflections for orthorhombic crystal structure for  $[\text{Ni}(\text{AEAPTS})_2]_3[\text{Fe}(\text{CN})_6]_2$ .

peak	fit	$q_{\text{max}}$ [ $\text{nm}^{-1}$ ]
$d_{010}$	4.761	4.8
$d_{100}$	8.191	8.4
$d_{110}$	9.523	9.5
$d_{020}$	11.636	11.6
$d_{001}$	12.572	12.5
$d_{011}$	14.230	14.3
$d_{101}$	15.006	15.0

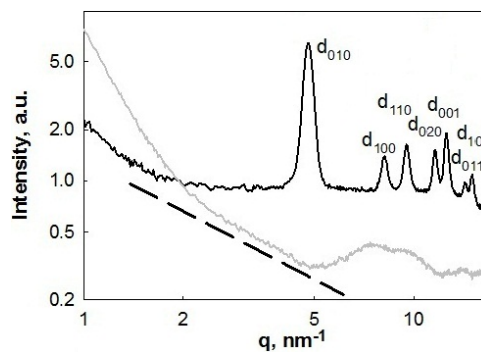


**Figure 5.9:** Reflections indexed for orthorhombic crystal structure for  $[\text{Ni}(\text{AEAPTS})_2]_3[\text{Fe}(\text{CN})_6]_2$ .

AEAPTS and ethylenediamine (en) are closely related diamines, which renders the similarity of the structures plausible. This orthorhombic model is, thus, preferable to the previously described hexagonal model and describes all requirements satisfactorily, i.e. Ni:Fe ratio 3:2, two cyanide bridges at Ni<sup>II</sup> leaving four coordination sites at Ni<sup>II</sup> for the diamine blocking ligand and three bridging cyano groups at every Fe<sup>III</sup>.

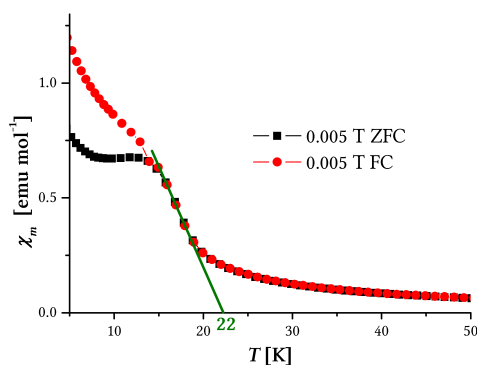
The SWAXS curve of [Ni(AEAPTS)<sub>2</sub>]<sub>3</sub>[Fe(CN)<sub>6</sub>]<sub>2</sub> gel (gray curve in Fig. 5.6) shows no distinct reflections. This means that the 3D crystalline order of the cyanometallate is destroyed after sol-gel processing. The slope of q<sup>-1</sup> between 2 and 5 nm<sup>-1</sup>, indicated by the dashed line in the insert of Fig. 5.6, suggests elongated objects which are randomly dispersed in the silica matrix. These 1D objects are probably the Fe<sup>III</sup>-C≡N-Ni<sup>II</sup> double chains which are ripped apart during sol-gel processing, but stay mostly intact. This explanation is supported by FTIR spectroscopy where the absorption band for bridging cyano groups is present in [Ni(AEAPTS)<sub>2</sub>]<sub>3</sub>[Fe(CN)<sub>6</sub>]<sub>2</sub> gel (Fig. 5.3), and by the magnetic behavior of the material discussed below (Sec. 5.5, p. 39).

## 5.5 SQUID

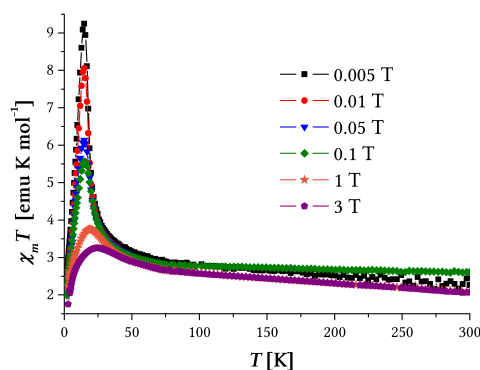
Field cooled (FC) and zero-field cooled (ZFC) measurements of [Ni(AEAPTS)<sub>2</sub>]<sub>3</sub>[Fe(CN)<sub>6</sub>]<sub>2</sub> gel were performed at different temperatures and external fields. The experimental results were corrected for diamagnetic contributions with the theoretical value calculated according to Pascal's method described in Subsection 12.4.5, p. 105.

Fig. 5.10 shows the molar susceptibility  $\chi_m$  vs. temperature  $T$  curve of [Ni(AEAPTS)<sub>2</sub>]<sub>3</sub>-[Fe(CN)<sub>6</sub>]<sub>2</sub> gel measured in FC and ZFC setup at an external field of 0.005 T. The onset of magnetic order can be determined at 22 K from the deviation of the curves from the characteristic 1/T drop of paramagnets, especially pronounced in the ZFC experiment. The increase of  $\chi_m$  upon heating the zero-field cooled sample in a small field arises due to the onset of parallel alignment of the magnetic moments with the external field close to the blocking temperature. At even higher temperatures, however, thermal fluctuations break up the alignment and the curve drops with 1/T in the superparamagnetic region. The magnetic ordering also causes a deviation from 1/T behavior in the FC measurement.  $\chi_m$  increases upon cooling at the blocking temperature due to the alignment of the magnetic moments with the external field, while above we also see superparamagnetic behavior.

The plot of  $\chi_m T$  vs.  $T$  in Fig. 5.11 presents a strong deviation from linearity at low temperature. Not only linear but constant behavior would be expected across the whole temperature range for a paramagnet, however, as  $\chi_m T = C$  ( $C \dots$  Curie constant, see Subsection 3.1.2, p. 23). The deviation from constant  $\chi_m T$  is therefore a further indication of magnetic order at low temperature. The effective magnetic moment  $\mu_{eff}$ , a measure for comparison of magnetic behavior, can be assessed from this plot through the relation  $\mu_{eff} = 2.82787 \sqrt{\chi_m T}$ . This gives a  $\mu_{eff}$  of 4.46  $\mu_B$  ( $\chi_m T = 2.50$  emu K mol<sup>-1</sup>) at room temperature while a  $\mu_{eff}$  of 8.60  $\mu_B$  (9.25 emu K cm<sup>-1</sup>) is found at the maximum at ~15 K and 0.005 T external field. This maximum corresponds quite well to the spin-only value of 8.94  $\mu_B$  expected for two low-spin Fe<sup>III</sup> ( $S = 1/2$ ,  $g = 2$ ) and three high-spin Ni<sup>II</sup> ( $S = 1$ ,



**Figure 5.10:**  $\chi_m$  vs.  $T$  FC and ZFC of  $[\text{Ni}(\text{AEAPTS})_2]_3[\text{Fe}(\text{CN})_6]_2$  gel.



**Figure 5.11:**  $\chi_m T$  vs.  $T$  of  $[\text{Ni}(\text{AEAPTS})_2]_3[\text{Fe}(\text{CN})_6]_2$  gel at various external fields.

$g = 2$ ) which are ferromagnetically coupled, which fits the structure model satisfactorily. For comparison,  $[\text{Ni}(\text{N-men})_2]_3[\text{Fe}(\text{CN})_6]_2 \cdot 12 \text{H}_2\text{O}$  has a significantly higher maximum of  $25.4 \mu_B$  at  $7.0 \text{ K}$  [203, 213]. The reason for the increased value is additional orbital coupling between  $\text{Ni}^{\text{II}}$  and  $\text{Fe}^{\text{III}}$ . The drop of the curves below  $10 \text{ K}$  may be due to antiferromagnetic interactions between the chains/sheets that align at these very low temperatures. This behavior is well known for similar cyanometallate networks from the literature [192, 208, 211, 212, 225–227, 231, 234, 235, 243]

According to the Curie-Weiss law  $1/\chi_m$  equals  $T/C - T_C/C$ , which is a linear equation ( $y = k \cdot x + d$ ) with a slope  $k = 1/C$  and a y-intercept  $d = T_C/C$ . The Curie temperature  $T_C$ , therefore, can be assessed from a linear Curie-Weiss fit of the  $1/\chi_m$  vs.  $T$  curve shown in Fig. 5.12. The fit parameters are listed in Tab. 5.4. A  $T_C$  for  $[\text{Ni}(\text{AEAPTS})_2]_3[\text{Fe}(\text{CN})_6]_2$  gel of  $10.7 \text{ K}$  is found by inverting the sign of  $d$  and multiplying by  $C$ . The positive  $T_C$  further indicates a ferromagnetic ordering of the  $\text{Ni}^{\text{II}}$  and  $\text{Fe}^{\text{III}}$  centres. The value is also quite close to the  $T_C$  reported for bulk ferromagnetic ordering of  $[\text{Ni}(\text{N-men})_2]_3[\text{Fe}(\text{CN})_6]_2 \cdot 12 \text{H}_2\text{O}$ , which was found to be  $10.8 \text{ K}$  [203, 213]. This may indicate structural similarities between the two cyanometallate networks.

Magnetization  $M$  vs. external field  $\mu_0 H$  curves at different temperatures are plotted in Fig. 5.13. A difference in magnetic behavior below and above  $T_C$  is obvious. The curve measured at  $50.8 \text{ K}$  shows simple linear behavior, which indicates paramagnetism. The measurements performed below  $10 \text{ K}$ , however, show a narrow hysteresis. For better visibility of the hysteresis loop a magnification of the origin is shown in Fig. 5.13b. A remanent magnetisation of  $300$  and  $90 \text{ emu mol}^{-1}$  and a coercivity of  $0.03$  and  $0.02 \text{ T}$  are observed at  $2.15$  and  $5.7 \text{ K}$ , respectively.

## 5.6 Conclusions

$[\text{Ni}(\text{AEAPTS})_2]_3[\text{Fe}(\text{CN})_6]_2$  was synthesized and covalently embedded in silica. AEAPTS acts as both a blocking ligand at  $\text{Ni}^{\text{II}}$  and a linker to tether the cyanometallate structure to the silica matrix during sol-gel processing through reaction of the trimethoxysilyl groups.

The FTIR spectrum of  $[\text{Ni}(\text{AEAPTS})_2]_3[\text{Fe}(\text{CN})_6]_2$  gel clearly showed bands for  $\text{Fe}^{\text{III}}$ –

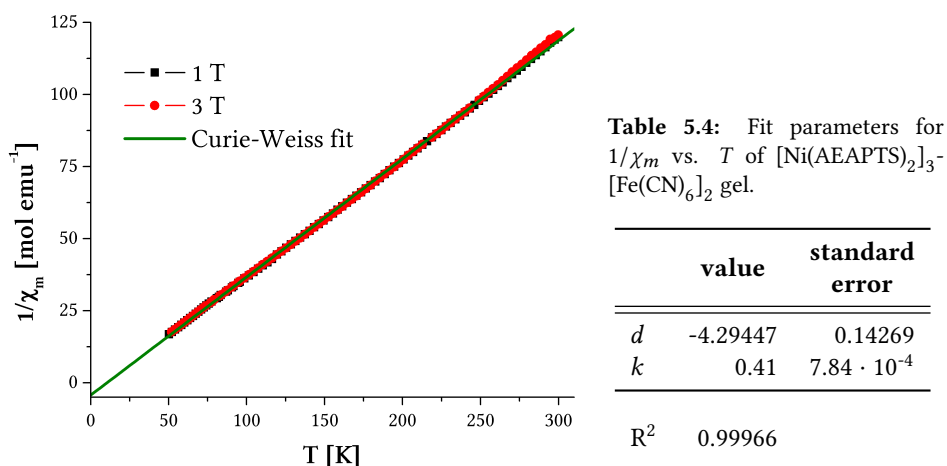


Figure 5.12:  $1/\chi_m$  vs.  $T$  of  $[\text{Ni}(\text{AEAPTS})_2]_3$ - $[\text{Fe}(\text{CN})_6]_2$  gel with Curie-Weiss fit.

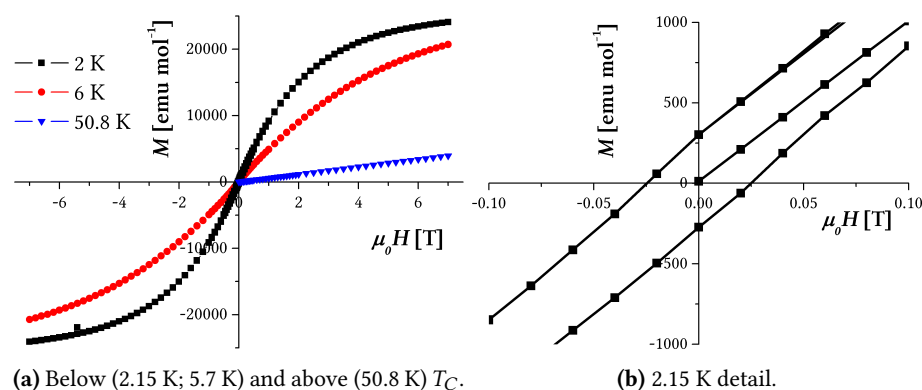


Figure 5.13:  $M$  vs.  $\mu_0 H$  of  $[\text{Ni}(\text{AEAPTS})_2]_3[\text{Fe}(\text{CN})_6]_2$  gel.

$\text{C}\equiv\text{N}-\text{Ni}^{\text{II}}$  cyanide bridges and the condensation of the trialkoxysilyl groups of the blocking ligands and TEOS during the sol-gel process. A Ni:Fe ratio of  $\sim 3:2$  was found by EDX which was expected due to charge balance. Structural investigation by SWAXS showed a hexagonal or orthorhombic crystal structure for the cyanometallate while after sol-gel processing an amorphous material with embedded 1D elongated structures was obtained. This led to the conclusion that cyanometallate structures are retained in double chains in the gel, but structural alignment in three dimensions is disrupted.

SQUID measurements showed that  $[\text{Ni}(\text{AEAPTS})_2]_3[\text{Fe}(\text{CN})_6]_2$  gel exhibits magnetic ordering below 22 K with an effective magnetic moment  $\mu_{eff}$  of  $4.46 \mu_B$  at room temperature and a maximum of  $8.60 \mu_B$  at  $\sim 15$  K. The  $T_C$  of 10.7 K and hysteretic behavior at low temperatures are indications for ferromagnetism of the material.



## Cu<sup>II</sup>-Fe<sup>III</sup>-SiO<sub>2</sub> Gel with Silyl-ethylenediamine

A material containing a Cu<sup>II</sup>/Fe<sup>III</sup> cyanometallate was synthesized with silyl-ethylenediamine (AEAPTS) as blocking ligand to study the influence of the metal center on the structure and the magnetic properties. Cu<sup>II</sup> complexes with amino ligands are quite common in cyanometallates, too, and very similar to the Ni<sup>II</sup> complexes studied in this work.

A structure with a similar blocking ligand to AEAPTS, N-propylethylenediamine (N-pren), was studied by Bertini *et al.* [256]. [Cu(N-pren)<sub>2</sub>]<sub>3</sub>[Fe(CN)<sub>6</sub>]<sub>2</sub> forms a 2D structure and exhibits paramagnetic properties.

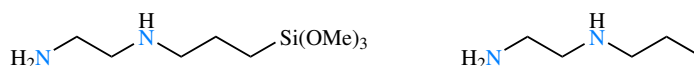


Figure 6.1: Structures of AEAPTS and N-pren.

### 6.1 Synthesis

Details of the experimental procedures and reaction conditions of the synthesis of [Cu(AEAPTS)<sub>2</sub>]<sub>3</sub>[Fe(CN)<sub>6</sub>]<sub>2</sub> gel are described in Part III, p. 103. This formula, however, is not a completely correct representation of the structure. The trimethoxysilyl groups of the blocking ligands react during the sol-gel process, which means it is not actually AEAPTS any more, but instead its hydrolyzed and condensed form.

The synthesis of [Cu(AEAPTS)<sub>2</sub>]<sub>3</sub>[Fe(CN)<sub>6</sub>]<sub>2</sub> embedded in SiO<sub>2</sub> gel starting from commercial AEAPTS (Fig. 6.2) is carried out in three stages, as for the analogous Ni<sup>II</sup> containing material, see Sec. 5.1, p. 33. The dark blue complex [Cu(AEAPTS)<sub>3</sub>]Cl<sub>2</sub> is obtained by mixing three molar equivalents of AEAPTS with anhydrous CuCl<sub>2</sub> in MeOH. Analogous to the Ni<sup>II</sup> complex, a three-fold excess of the ligand results in a complex with a ratio Cu:ligand of 1:3, as shown by Bennett *et al.* [257]. The cyanometallate

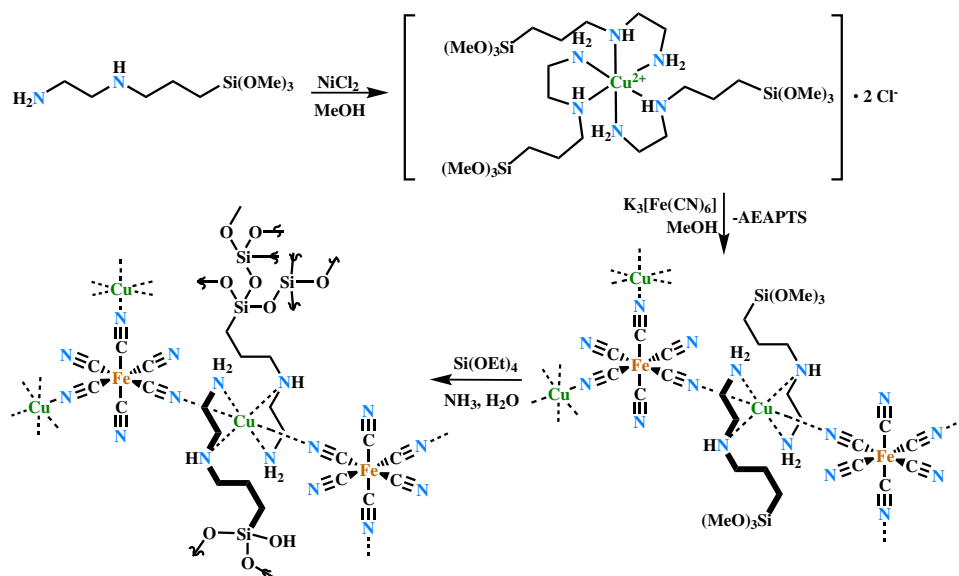


Figure 6.2: Synthesis of  $[\text{Cu}(\text{AEAPTS})_2]_3[\text{Fe}(\text{CN})_6]_2$  gel.

network  $[\text{Cu}(\text{AEAPTS})_2]_3[\text{Fe}(\text{CN})_6]_2$  precipitates from the reaction of  $\text{K}_3[\text{Fe}(\text{CN})_6]$  and  $[\text{Cu}(\text{AEAPTS})_3]\text{Cl}_2$  in a 2:3 ratio in methanol by cleaving of one AEAPTS ligand to unblock coordination sites of  $\text{Cu}^{\text{II}}$ . As is known from literature [203] and described above (Chapter 5, p. 33), one AEAPTS ligand has to be cleaved to unblock coordination sites and allow cyanide bridges to be formed. This retards the reaction and should thus provide better structural control and crystallinity. Subsequently TEOS is added to a suspension of  $[\text{Cu}(\text{AEAPTS})_2]_3[\text{Fe}(\text{CN})_6]_2$  in 0.2 M aqueous  $\text{NH}_3$  at 70 °C [29]. After drying on a glass plate and washing with water a fine purple powder of  $[\text{Cu}(\text{AEAPTS})_2]_3[\text{Fe}(\text{CN})_6]_2$  tethered to  $\text{SiO}_2$  is obtained.

## 6.2 FTIR

FTIR spectra of each intermediate and the final product are shown in Fig. 6.3.

The FTIR spectrum of AEAPTS shows the expected absorption bands. The amine functions – one primary and one secondary – give rise to absorption maxima at 3195, 3303 and 3371  $\text{cm}^{-1}$  due to  $\text{NH}/\text{NH}_2$  stretching, at 1592  $\text{cm}^{-1}$  due to  $\text{NH}_2$  bending and at 808 and 777  $\text{cm}^{-1}$  due to  $\text{NH}/\text{NH}_2$  wagging. The trimethoxysilyl group causes absorption maxima at 1074, 1190 and 2840  $\text{cm}^{-1}$  due to  $\text{Si}-\text{OCH}_3$  vibrations. The bands arising from  $\text{Si}-\text{CH}_2$  and  $\text{C}-\text{NH}/\text{C}-\text{NH}_2$  are hidden behind the lower two bands.

Few changes occur in the FTIR spectrum upon complexation by  $\text{Cu}^{\text{II}}$ . All characteristic bands discussed above stay essentially the same, but the characteristic amine bands are slightly shifted upon coordination. The  $\text{NH}_2$  bending band shows a maximum at 1590  $\text{cm}^{-1}$  and the band arising from  $\text{NH}/\text{NH}_2$  wagging at 808 and 784  $\text{cm}^{-1}$ . Additional stronger bands at 3126 and 3233  $\text{cm}^{-1}$  may be due to vibrations of  $-\text{OH}$  groups from coordinated and crystal MeOH.

A band appears in the cyanometallate network  $[\text{Cu}(\text{AEAPTS})_2]_3[\text{Fe}(\text{CN})_6]_2$  with an



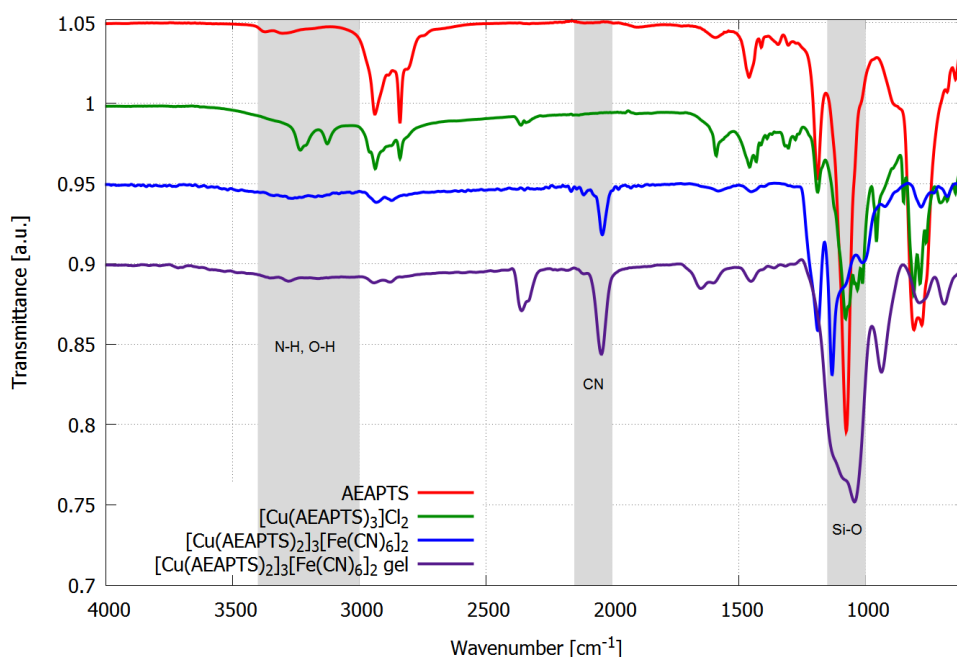


**Figure 6.3:** FTIR spectra of AEAPTS,  $[\text{Cu}(\text{AEAPTS})_3]\text{Cl}_2$ ,  $[\text{Cu}(\text{AEAPTS})_2]_3[\text{Fe}(\text{CN})_6]_2$  and  $[\text{Cu}(\text{AEAPTS})_2]_3[\text{Fe}(\text{CN})_6]_2$  gel.

absorption maximum at 2040 and a small shoulder at 2113  $\text{cm}^{-1}$ . This is the region characteristic for cyano groups. The corresponding band in  $\text{K}_3[\text{Fe}(\text{CN})_6]$  is at 2116  $\text{cm}^{-1}$ . The band at 2113  $\text{cm}^{-1}$  can therefore be assigned to non-bridging cyano ligands. The additional band at 2040  $\text{cm}^{-1}$ , on the other hand, arises due to bridging cyano groups. This is clear evidence, besides the precipitation and colour change of the product, for the successful network formation. The amine bands, especially those arising from  $\text{NH}/\text{NH}_2$  stretching, are weak, but still present. The strong bands in the Si–O region are further evidence for the presence of the blocking ligand in the cyanometallate network.

The bands characteristic for Si–OCH<sub>3</sub> at 1079, 1189 and 2839  $\text{cm}^{-1}$  disappear in the FTIR spectrum of  $[\text{Cu}(\text{AEAPTS})_2]_3[\text{Fe}(\text{CN})_6]_2$  gel, the material after sol-gel processing. However, a new absorption maximum at 1043 with a shoulder at 1091  $\text{cm}^{-1}$  appears in the region characteristic for Si–O. This stems from the Si–O–Si entities of the amorphous  $\text{SiO}_2$  network. The fact that the FTIR spectrum otherwise remains nearly unchanged, i.e. the characteristic bands for the cyano and amine groups are still present – although weak in some cases –, indicates that the cyanometallate network is retained upon sol-gel processing.

### 6.3 SEM and EDX

The SEM shown in Fig. 6.4 was recorded at a voltage of 10 kV. It proves the homogeneity of  $[\text{Cu}(\text{AEAPTS})_2]_3[\text{Fe}(\text{CN})_6]_2$  gel. No crystallites of the cyanometallate are discernible. This indicates that no (visible) phase separation occurs.

EDX measurement (Fig. 5.5) confirmed a homogeneous distribution of the metals

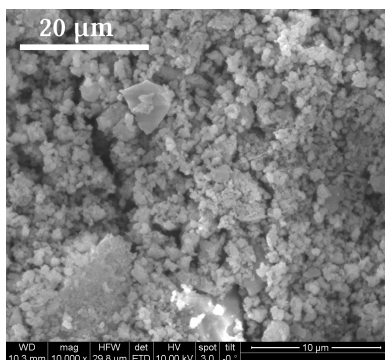


Figure 6.4: SEM of  $[\text{Cu}(\text{AEAPTS})_2]_3[\text{Fe}(\text{CN})_6]_2$  gel.

Table 6.1: EDX analysis of  $[\text{Cu}(\text{AEAPTS})_2]_3[\text{Fe}(\text{CN})_6]_2$  gel.

element	at. %
C (K)	55.23
N (K)	11.31
O (K)	13.62
Si (K)	12.72
Cl (K)	0.17
Fe (K)	2.61
Cu (K)	4.35
Total	100

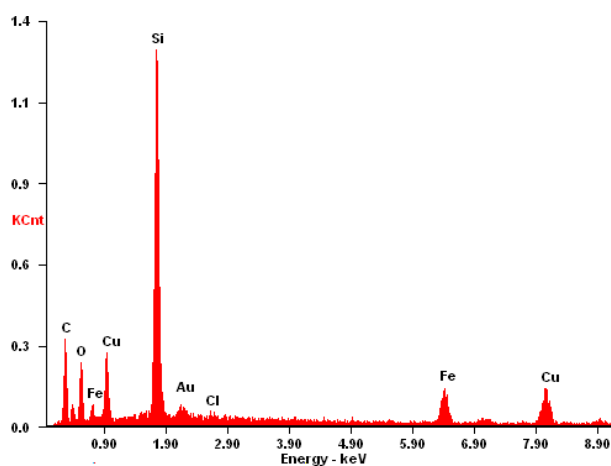


Figure 6.5: EDX plot (energy [keV] vs. intensity) of  $[\text{Cu}(\text{AEAPTS})_2]_3[\text{Fe}(\text{CN})_6]_2$  gel.

and, thus, the cyanometallate network in  $[\text{Cu}(\text{AEAPTS})_2]_3[\text{Fe}(\text{CN})_6]_2$  gel. A Cu:Fe ratio of  $\sim 3.3:2$  was found from the atomic percentages (Tab. 6.1) obtained by quantitative analysis. This corresponds quite well to the metal ratio used for the preparation of  $[\text{Cu}(\text{AEAPTS})_2]_3[\text{Fe}(\text{CN})_6]_2$  and is expected for a cyanometallate of  $\text{Cu}^{\text{II}}$  and  $\text{Fe}^{\text{III}}$  due to charge balance. The small excess of copper may arise from the fact that the  $\text{Cu}^{\text{II}}$  compound is covalently linked to the silica matrix through the diamine ligand while unreacted  $\text{K}_3[\text{Fe}(\text{CN})_6]$  is not bound in the network and thus may be removed by washing with water.

#### 6.4 SWAXS

SWAXS measurements of  $[\text{Cu}(\text{AEAPTS})_2]_3[\text{Fe}(\text{CN})_6]_2$  and  $[\text{Cu}(\text{AEAPTS})_2]_3[\text{Fe}(\text{CN})_6]_2$  gel were performed (Fig. 6.6). Structural changes of the cyanometallate network upon embedding in  $\text{SiO}_2$  can be determined by comparison of the two curves.

$[\text{Cu}(\text{AEAPTS})_2]_3[\text{Fe}(\text{CN})_6]_2$  (black curve in Fig. 6.6) exhibits distinct Bragg reflections, which shows that the  $\text{Cu}^{\text{II}}/\text{Fe}^{\text{III}}$  cyanometallate exhibits some crystallinity. A satisfactory crystal structure fit, as discussed for the analogous  $\text{Ni}^{\text{II}}$  material in Sec. 5.4, p. 36, could

not be performed. There may be various coexisting phases in the material that give rise to the many overlapping reflections. Whether these reflections arise from a cyanometallate network with  $\text{Fe}^{\text{III}}-\text{C}\equiv\text{N}-\text{Cu}^{\text{II}}$  bridges cannot be proven. However, starting materials – such as  $\text{K}_3[\text{Fe}(\text{CN})_6]$  – and side products – such as  $\text{KCl}$  – can be excluded.

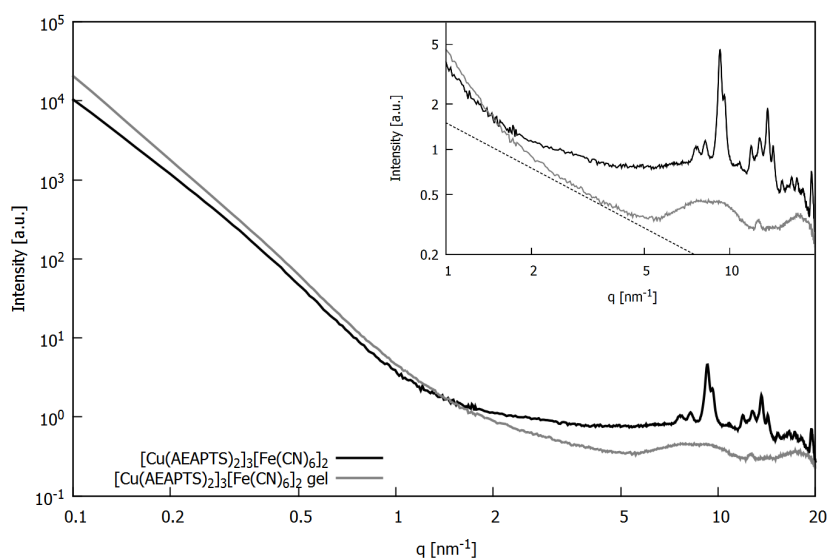


**Figure 6.6:** SWAXS measurements of  $[\text{Cu}(\text{AEAPTS})_2]_3[\text{Fe}(\text{CN})_6]_2$  and  $[\text{Cu}(\text{AEAPTS})_2]_3[\text{Fe}(\text{CN})_6]_2$  gel.

The SWAXS curve of  $[\text{Cu}(\text{AEAPTS})_2]_3[\text{Fe}(\text{CN})_6]_2$  gel (gray curve in Fig. 6.6) shows no distinct reflections. This means that the 3D crystalline order of the cyanometallate is destroyed after sol-gel processing. The slope of  $q^{-1}$  between 2 and 5  $\text{nm}^{-1}$ , indicated by the dashed line in the insert of Fig. 6.6, suggests elongated objects which are randomly dispersed in the silica matrix. These 1D objects are probably  $\text{Fe}^{\text{III}}-\text{C}\equiv\text{N}-\text{Cu}^{\text{II}}$  (double) chains which give rise to the absorption bands for bridging cyano group in the FTIR spectrum (Fig. 6.3), similar to the ones of  $[\text{Ni}(\text{AEAPTS})_2]_3[\text{Fe}(\text{CN})_6]_2$  gel described in Sec. 5.4, p. 36.

## 6.5 SQUID

Field cooled (FC) and zero-field cooled (ZFC) measurements of  $[\text{Cu}(\text{AEAPTS})_2]_3[\text{Fe}(\text{CN})_6]_2$  gel were performed at different temperatures and external fields. The experimental results were corrected for diamagnetic contributions with the theoretical value calculated according to Pascal's method described in Subsection 12.4.5, p. 105.

Measurement of  $\chi_m$  at different temperatures and external fields (Fig. 6.7) clearly indicate paramagnetic behavior of the material.  $\chi_m$  is positive but small and no effects besides an increase with decreasing temperature occur as expected from Curie's law (Subsection 3.1.1, p. 22).

From the  $\chi_m T$  vs.  $T$  plot in Fig. 6.8 the Curie constant  $C$  can be calculated according to Curie's law ( $C = \chi_m \cdot T$ , Subsection 3.1.1, p. 22) by fitting a straight line with slope = 0. The average value obtained for the measurements at external fields of 1 T and 3 T is 1.61. This gives a  $\mu_{\text{eff}}$  of 3.58  $\mu_{\text{B}}$  ( $\mu_{\text{eff}} = 2.82787 \sqrt{C}$ ).

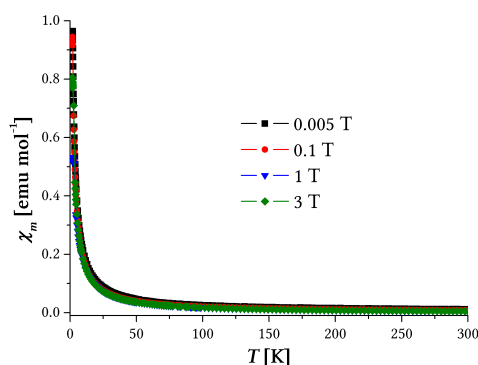


**Figure 6.7:**  $\chi_m$  vs.  $T$  of  $[\text{Cu}(\text{AEAPTS})_2]_3\text{-}[\text{Fe}(\text{CN})_6]_2$  gel at various external fields.

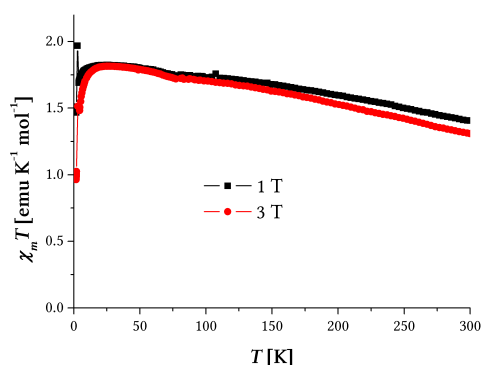


**Figure 6.8:**  $\chi_m T$  vs.  $T$  of  $[\text{Cu}(\text{AEAPTS})_2]_3\text{-}[\text{Fe}(\text{CN})_6]_2$  gel at various external fields.

An alternative route to calculate  $C$  is from the slope of  $1/\chi_m$  vs.  $T$  (Fig. 6.9), which is equal to  $1/C$  ( $1/\chi_m = T/C$ ). An average for  $C$  of 1.50 is obtained by this method from the measurements at external fields of 1 T and 3 T. The  $\mu_{eff}$ , therefore, is  $3.46 \mu_B$ .

The average  $\mu_{eff}$  is  $3.52 \mu_B$ . This is well below the spin-only value for three  $\text{Cu}^{\text{II}}$  ( $S = 1/2$ ,  $g = 2$ ) and two low-spin  $\text{Fe}^{\text{III}}$  ( $S = 1/2$ ,  $g = 2$ ) of  $8.65 \mu_B$ . Partial antiferromagnetic arrangement of neighboring chains/sheets of the cyanometallate structure may be the reason for the lower  $\mu_{eff}$ . Another explanation would be that not all of the metal centers couple because the structural arrangement is not favorable for exchange interactions.

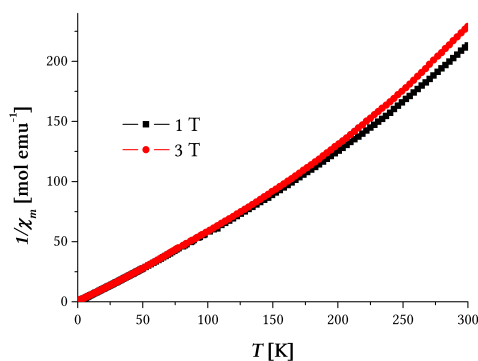


**Figure 6.9:**  $1/\chi_m$  vs.  $T$  of  $[\text{Cu}(\text{AEAPTS})_2]_3\text{-}[\text{Fe}(\text{CN})_6]_2$  gel at various external fields.

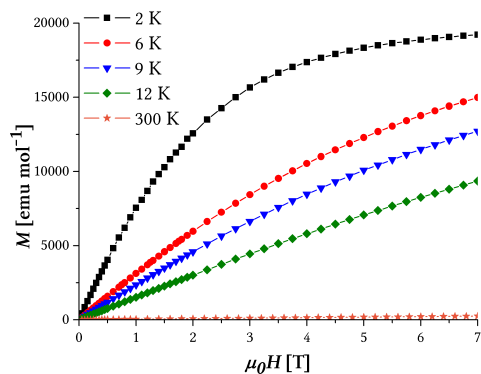


**Figure 6.10:**  $M$  vs.  $\mu_0 H$  of  $[\text{Cu}(\text{AEAPTS})_2]_3\text{-}[\text{Fe}(\text{CN})_6]_2$  gel at various temperatures.

The magnetization  $M$  versus external field  $\mu_0 H$  was measured at various temperatures (Fig. 6.10). The curves are characteristic of a paramagnet with a linear increase of  $M$  with the external field, following Curie's law. Deviation from linear behavior occurs only at low temperatures and high fields. This is due to saturation effects which arise because all magnetic dipoles are already aligned with the external field and an increase cannot lead to further magnetization of the sample. At 2 K the saturation magnetization of  $[\text{Cu}(\text{AEAPTS})_2]_3\text{-}[\text{Fe}(\text{CN})_6]_2$  gel is nearly reached at 7 T and lies at  $\sim 19,230 \text{ emu mol}^{-1}$ .

## 6.6 Conclusions

$[\text{Cu}(\text{AEAPTS})_2]_3[\text{Fe}(\text{CN})_6]_2$  was synthesized and covalently embedded in silica. AEAPTS acts as both a blocking ligand at  $\text{Cu}^{\text{II}}$  and a linker to tether the cyanometallate structure to the silica matrix during sol-gel processing through reaction of the trimethoxysilyl groups.

The FTIR spectrum of  $[\text{Cu}(\text{AEAPTS})_2]_3[\text{Fe}(\text{CN})_6]_2$  gel clearly showed bands for  $\text{Fe}^{\text{III}}-\text{C}\equiv\text{N}-\text{Cu}^{\text{II}}$  cyanide bridges and the condensation of the trialkoxysilyl groups of the blocking ligands and TEOS during sol-gel processing. A Cu:Fe ratio of ~3:2 was found by EDX which was expected due to charge balance. Structural investigation by SWAXS showed crystallinity for the cyanometallate while after sol-gel processing an amorphous material with embedded 1D elongated structures was obtained. This led to the conclusion that, in accordance with the results for the equivalent  $[\text{Ni}(\text{AEAPTS})_2]_3[\text{Fe}(\text{CN})_6]_2$  gel, cyanometallate structures are retained in (double) chains in the gel, but structural alignment in three dimensions is disrupted.

SQUID measurements showed that  $[\text{Cu}(\text{AEAPTS})_2]_3[\text{Fe}(\text{CN})_6]_2$  gel is a paramagnet. The susceptibility follows the Curie law. An effective magnetic moment  $\mu_{eff}$  of  $3.52 \mu_{\text{B}}$  was found which is lower than the spin-only value. This may be due to spin-orbit coupling of  $\text{Cu}^{\text{II}}$  and  $\text{Fe}^{\text{III}}$  in the cyanometallate network.

In conclusion,  $[\text{Cu}(\text{AEAPTS})_2]_3[\text{Fe}(\text{CN})_6]_2$  gel showed no magnetic ordering — at temperatures above 2 K — in contrast to the corresponding  $\text{Ni}^{\text{II}}$  material. This difference in behavior may be due to  $d^9$ - $\text{Cu}^{\text{II}}$  having one more d-electron than  $d^8$ - $\text{Ni}^{\text{II}}$  and thus only one unpaired d-electron that can couple with the lone electron of  $\text{Fe}^{\text{III}}$ . This, of course, makes the exchange interaction weaker, as explained in Subsection 3.2.1, p. 25, and may be too weak to give rise to magnetic order. Another explanation for the different behavior may be worse structural alignment of the  $\text{Cu}^{\text{II}}$  cyanometallate. This is evidenced by the SWAXS curves of the cyanometallates before sol-gel processing. The  $\text{Ni}^{\text{II}}$  sample showed a orthogonal crystal structure (Sec. 5.3, p. 35) while for the  $\text{Cu}^{\text{II}}$  equivalent no clear crystal phase could be attributed to the reflections. This could indicate a mixture of crystal phases in the material arising from looser structural arrangement.



# Ni<sup>II</sup>-Fe<sup>III</sup>-SiO<sub>2</sub> Gel with Silyl-2,3,2-tetramine

Silyl-2,3,2-tetramine is a tetradentate ligand with one pendant propyltrimethoxysilane group (Fig. 7.1). This means that one ligand is able to block four coordination sites of Ni<sup>II</sup>. The ligand has been employed by Koo *et al.* to obtain the 2D [Ni(2,3,2-tetramine)]<sub>3</sub>-[Fe(CN)<sub>6</sub>]<sub>2</sub> · 8 H<sub>2</sub>O cyanometallate network with ferromagnetic properties [232]. 3,2,3-tetramine, a similar ligand, led to a 3D metamagnetic cyanometallate network [241]. Another tetramine, tren, can coordinate only at one side of Ni<sup>II</sup> due to its geometry, leading to a *cis*-coordination of the cyano groups. A network with this blocking ligand, 3D ferromagnetic [Ni(tren)]<sub>3</sub>[Fe(CN)<sub>6</sub>]<sub>2</sub> · 6 H<sub>2</sub>O, was studied by Fallah *et al.* [242].

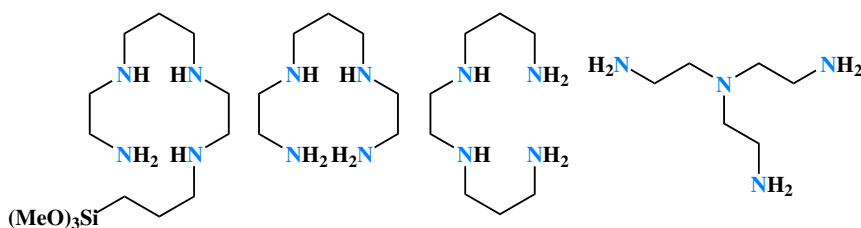


Figure 7.1: Structures of silyl-2,3,2-tetramine, 2,3,2-tetramine, 3,2,3-tetramine and tren.

## 7.1 Synthesis

The procedure to synthesize silyl-2,3,2-tetramine is sketched in Fig. 7.2. Experimental details are described in Part III, p. 103.

2,3,2-Tetramine is obtained by reaction of 1,3-dibromopropane and ethylenediamine in basic medium [258]. The pure product is isolated in 47% yield after filtration and distillation. The <sup>1</sup>H NMR spectrum of the distillate is shown in Fig. 7.3. The singlet at 1.15 ppm arises from NH and NH<sub>2</sub> hydrogens, the quintet at ~1.5 ppm from the CH<sub>2</sub> in β position of the NH group, and the multiplet at ~2.5–2.7 from all the hydrogens of the α-CH<sub>2</sub>.

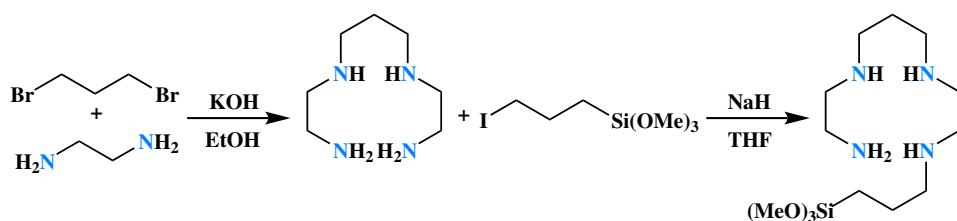


Figure 7.2: Synthesis of silyl-2,3,2-tetramine.

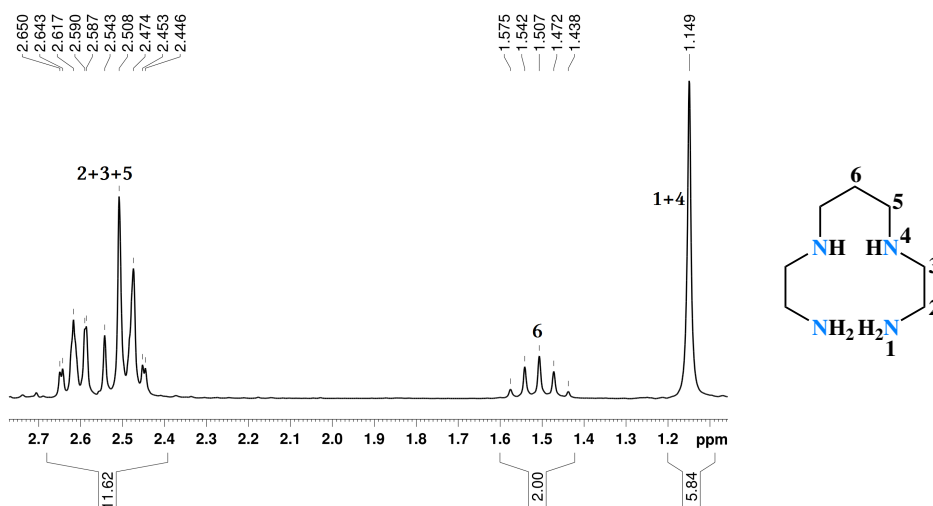


Figure 7.3:  $^1\text{H}$  NMR spectrum of 2,3,2-tetramine.

Monosilylation of one primary amine is achieved by the reaction of 2,3,2-tetramine with sodium hydride and 3-iodopropyltrimethoxysilane [259, 260]. The  $^1\text{H}$  NMR spectrum of the product after filtration is shown in Fig. 7.4. The signal at 0.6 ppm stems from the  $\text{CH}_2$  group in  $\alpha$  position to the  $\text{Si}(\text{OMe})_3$  group, the multiplet around 1.6 ppm from the superimposed  $\text{CH}_2$  groups  $\beta$  to the  $\text{Si}(\text{OMe})_3$  and to the  $\text{NH}$  groups. The remaining  $\text{CH}_2$  groups which are all in  $\alpha$  position to nitrogen give rise to signals between 2.4 and 2.7 ppm. The singlet at 3.52 ppm arises from the methoxy groups. Its integral is too low because the spectrum was recorded in  $d_4$ -MeOD and continuous exchange occurs.  $\text{NH}$  and  $\text{NH}_2$  are not visible in the spectrum, also due to rapid exchange in the polar solvent.

The  $\text{Ni}^{\text{II}}$  complex is obtained as a violet precipitate by the addition of one equivalent of silyl-2,3,2-tetramine to a solution of  $\text{NiCl}_2$  in methanol (Fig. 7.5). The cyanometallate network embedded in  $\text{SiO}_2$  is subsequently obtained in a manner analogous to the synthesis of  $[\text{Ni}(\text{AEAPTS})_2]_3[\text{Fe}(\text{CN})_6]_2$  (Sec. 5.1, p. 33). Addition of  $\text{K}_3[\text{Fe}(\text{CN})_6]$  to  $[\text{Ni}(\text{silyl-2,3,2-tetramine})\text{Cl}_2]$  yields a brown powder which is reacted with TEOS in basic medium ( $\text{NH}_3$ ) to give  $[\text{Ni}(\text{silyl-2,3,2-tetramine})_3[\text{Fe}(\text{CN})_6]_2$  gel as brown powder. The formula  $[\text{Ni}(\text{silyl-2,3,2-tetramine})_3[\text{Fe}(\text{CN})_6]_2$  gel is not a completely correct representation of the structure. The trimethoxysilyl groups of the blocking ligand react during the sol-gel process, which means it is chemically changed.



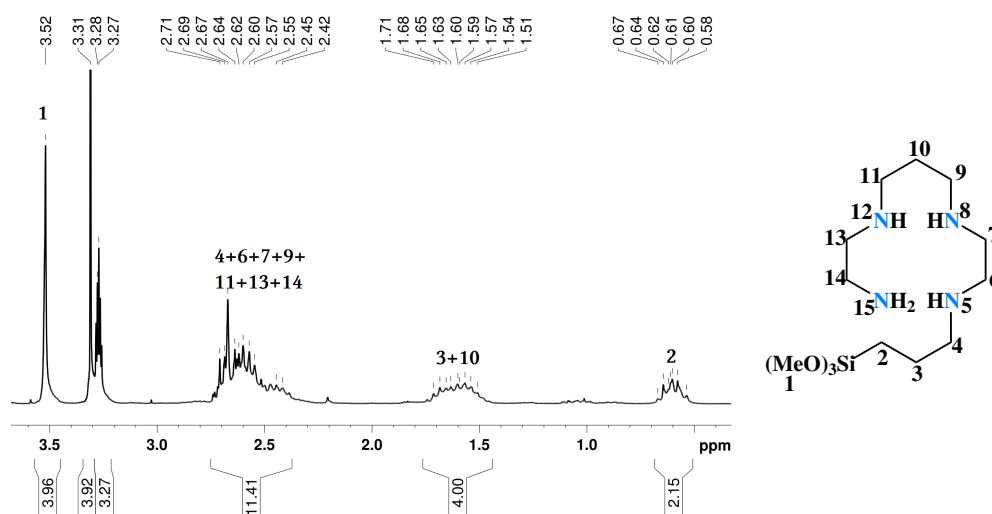


Figure 7.4:  $^1\text{H}$  NMR spectrum of silyl-2,3,2-tetramine.

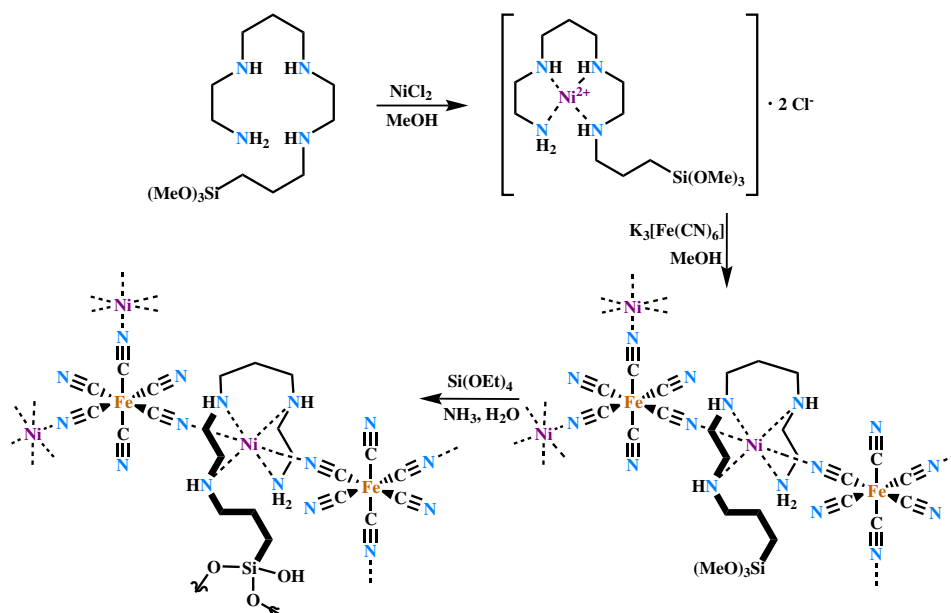
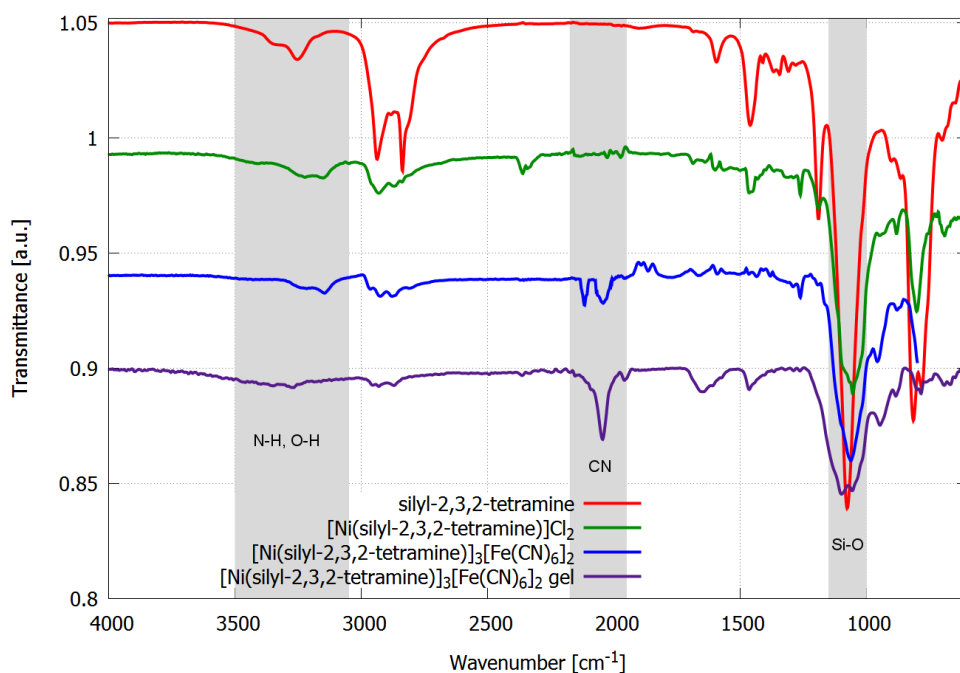


Figure 7.5: Synthesis of  $[\text{Ni}(\text{silyl-2,3,2-tetramine})]_3[\text{Fe}(\text{CN})_6]_2$  gel.

## 7.2 FTIR

The FTIR spectra of the free ligand, the  $\text{Ni}^{\text{II}}$  complex, the cyanometallate network and the sol-gel material are shown in Fig. 7.6.

The spectrum of the silyl-2,3,2-tetramine ligand shows characteristic bands for amine groups and Si–O vibrations. The amine functions — one primary and three secondary — give rise to a broad band with absorption maxima at  $3348$  and  $3254\text{ cm}^{-1}$  due to NH/NH<sub>2</sub> stretching, at  $1594\text{ cm}^{-1}$  due to NH<sub>2</sub> bending and at  $814$  and  $781\text{ cm}^{-1}$  due to NH/NH<sub>2</sub> wagging. The trimethoxysilyl group causes absorption maxima at  $1076$ ,  $1190$  and  $2838\text{ cm}^{-1}$  due to Si–OCH<sub>3</sub> vibrations. The bands arising from Si–CH<sub>2</sub> and C–NH/C–NH<sub>2</sub> are also



**Figure 7.6:** FTIR spectra of silyl-2,3,2-tetramine,  $[\text{Ni}(\text{silyl-2,3,2-tetramine})]\text{Cl}_2$ ,  $[\text{Ni}(\text{silyl-2,3,2-tetramine})]_3[\text{Fe}(\text{CN})_6]_2$  and  $[\text{Ni}(\text{silyl-2,3,2-tetramine})]_3[\text{Fe}(\text{CN})_6]_2$  gel.

in the region of  $1070\text{--}1200\text{ cm}^{-1}$  but hidden behind the stronger signals from  $\text{Si-OCH}_3$ .

The characteristic bands of the ligand decrease in intensity upon complexation by  $\text{Ni}^{\text{II}}$ , but are still present. The amine bands shift a few wavenumbers to 3395, 3223, 1599 and  $800\text{ cm}^{-1}$ . The broadened band at  $\sim 1070\text{ cm}^{-1}$  may indicate beginning condensation of  $\text{Si-OCH}_3$  groups as the measurement was performed at ambient conditions. The band at  $1190\text{ cm}^{-1}$ , however, proves the presence of substantial amounts of unreacted  $\text{Si-OCH}_3$  groups.

Absorption maxima characteristic of the cyano group arise at 2115 and  $2042\text{ cm}^{-1}$  in the spectrum of the cyanometallate network  $[\text{Ni}(\text{silyl-2,3,2-tetramine})]_3[\text{Fe}(\text{CN})_6]_2$ . The corresponding band in  $\text{K}_3[\text{Fe}(\text{CN})_6]$  is at  $2116\text{ cm}^{-1}$ . The band at  $2115\text{ cm}^{-1}$  can therefore be assigned to non-bridging  $\text{C}\equiv\text{N}$  ligands. The additional band at  $2042\text{ cm}^{-1}$ , on the other hand, is due to bridging cyano groups. This is a clear evidence, besides the precipitation and colour change of the product, for the successful network formation.

The bands characteristic for  $\text{Si-OCH}_3$  with maxima at 1076, 1190 and  $2838\text{ cm}^{-1}$  disappear after sol-gel processing. However, two new maxima on a broad band arise at 1056 and  $1098\text{ cm}^{-1}$  in the region characteristic of  $\text{Si-O}$  vibrations. They stem from the  $\text{Si-O-Si}$  entities of the amorphous  $\text{SiO}_2$  network. One broad band with a maximum at  $2045\text{ cm}^{-1}$  is present in the region characteristic of  $\text{C}\equiv\text{N}$  vibrations. The apparent disappearance of the non-bridging mode might suggest that further cyanide bridges are formed during the sol-gel process. This would require loss of blocking ligands to make coordination sites at  $\text{Ni}^{\text{II}}$  accessible. The presence of the characteristic amine bands, however, shows that the ligand is contained in the material, negating substitution by cyanide bridges. This supports the interpretation that the broadened  $\text{C}\equiv\text{N}$  band includes superimposed vibrations

of bridging and non-bridging cyano groups.

### 7.3 SEM and EDX

The SEM shown in Fig. 7.7 was recorded at a voltage of 10 kV. It proves the homogeneity of  $[\text{Ni}(\text{silyl-2,3,2-tetramine})]_3[\text{Fe}(\text{CN})_6]_2$  gel. No crystallites of the cyanometallate are discernible. This indicates that no (visible) phase separation occurs.

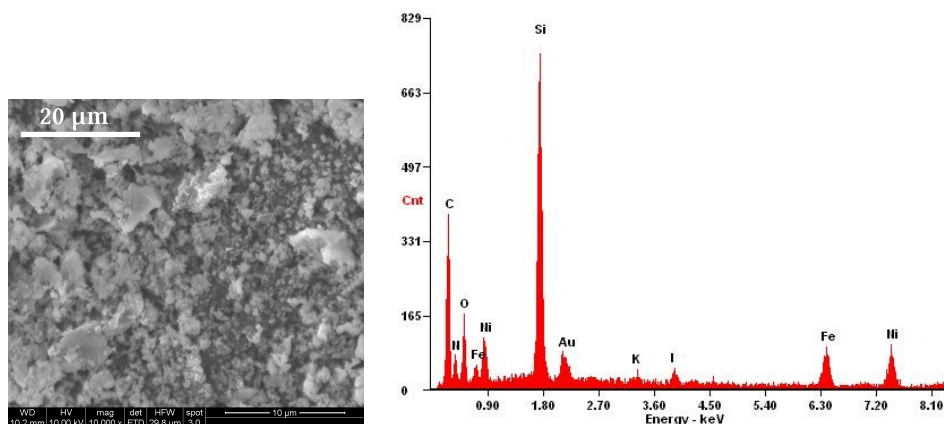


**Figure 7.7:** SEM of  $[\text{Ni}(\text{silyl-2,3,2-tetramine})]_3[\text{Fe}(\text{CN})_6]_2$  gel.

**Figure 7.8:** EDX plot (energy [keV] vs. intensity) of  $[\text{Ni}(\text{silyl-2,3,2-tetramine})]_3[\text{Fe}(\text{CN})_6]_2$  gel.

EDX measurement (Fig. 7.8) confirmed a homogeneous distribution of the metals and, thus, the cyanometallate network in  $[\text{Ni}(\text{silyl-2,3,2-tetramine})]_3[\text{Fe}(\text{CN})_6]_2$  gel. A Ni:Fe ratio of  $\sim 2.6:2$  was found from the atomic percentages (Tab. 7.1) obtained by quantitative analysis. This corresponds quite well to the metal ratio used for the preparation of  $[\text{Ni}(\text{silyl-2,3,2-tetramine})]_3[\text{Fe}(\text{CN})_6]_2$  and is expected for a cyanometallate of  $\text{Ni}^{\text{II}}$  and  $\text{Fe}^{\text{III}}$  due to charge balance. The excess of Fe may indicate that a part of  $[\text{Fe}(\text{CN})_6]^{3-}$  forms less than three cyanide bridges to  $\text{Ni}^{\text{II}}$  which causes deviation from the ideal stoichiometry. Charge balance is kept by incorporation of traces of  $\text{K}^+$  ions into the material.

### 7.4 SWAXS

SWAXS measurements of  $[\text{Ni}(\text{silyl-2,3,2-tetramine})]_3[\text{Fe}(\text{CN})_6]_2$  and  $[\text{Ni}(\text{silyl-2,3,2-tetramine})]_3[\text{Fe}(\text{CN})_6]_2$  gel were performed (Fig. 7.9). Structural changes of the cyanometallate network upon embedding in  $\text{SiO}_2$  can be determined by comparison of the two curves.

$[\text{Ni}(\text{silyl-2,3,2-tetramine})]_3[\text{Fe}(\text{CN})_6]_2$  (black curve in Fig. 7.9) exhibits distinct Bragg reflections. Tab. 7.2 shows that indexing of the reflections, labelled accordingly in the insert of Fig. 7.9, for an orthorhombic unit cell with lattice parameters  $a = 7.9 \text{ \AA}$ ,  $b = 13.2 \text{ \AA}$  and  $c = 5.8 \text{ \AA}$  is in excellent agreement with the experimental  $q_{\text{max}}$  values. The lattice constants are very similar to the values obtained for the orthorhombic structure of  $[\text{Ni}(\text{AEPTS})_2]_3[\text{Fe}(\text{CN})_6]_2$ . This leads to the assumption that the structures are analogous and similar to the one described for  $[\text{Ni}(\text{en})_2]_3[\text{Fe}(\text{CN})_6]_2 \cdot n \text{ H}_2\text{O}$  by Ohba *et al.* and

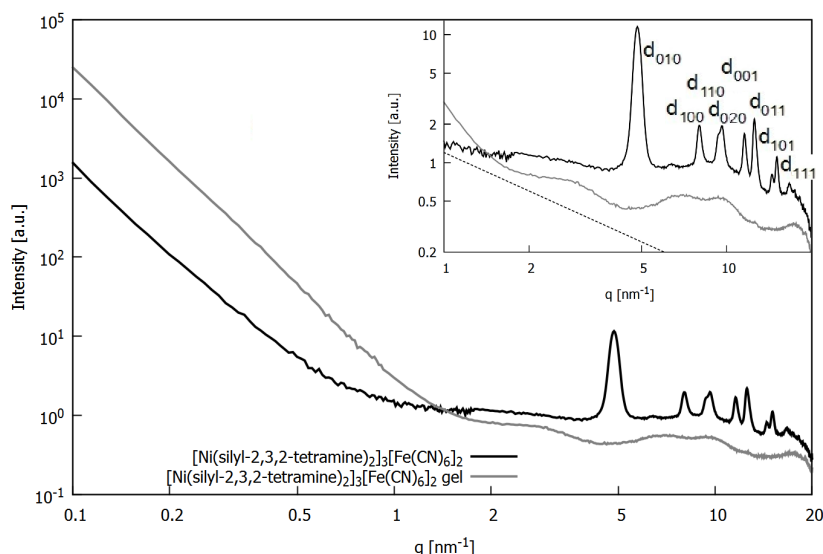
**Table 7.1:** EDX analysis of  $[\text{Ni}(\text{silyl-2,3,2-tetramine})_3\text{-Fe}(\text{CN})_6]_2$  gel.

element	at. %
C (K)	60.74
N (K)	13.66
O (K)	12.18
Si (K)	8.32
K (K)	0.17
I (L)	0.34
Fe (K)	2.01
Ni (K)	2.58
Total	100

**Table 7.2:** Experimental vs. fitted reflections for orthorhombic lattice for  $[\text{Ni}(\text{silyl-2,3,2-tetramine})_3\text{-Fe}(\text{CN})_6]_2$  gel.

peak	fit	$q_{\text{max}}$ [ $\text{nm}^{-1}$ ]
$d_{010}$	4.792	4.8
$d_{100}$	8.007	8.4
$d_{110}$	9.332	9.1
$d_{020}$	9.584	9.6
$d_{001}$	11.752	11.6
$d_{011}$	12.691	12.5
$d_{101}$	14.221	14.5
$d_{111}$	15.006	15.1

Herchel *et al.* [156, 206], as discussed in Sec. 5.4, p. 36. The structure is assumed to be built of 1D double chains of three  $\text{Ni}^{\text{II}}$  with two cyano bridges and one tetramine ligand and two  $\text{Fe}^{\text{III}}$  with three cyano bridges and three non-bridging cyano ligands. These 1D structures are extending along the  $c$ -axis and assembled in an orthorhombic lattice with  $\text{Ni}^{\text{II}}$  at the edges, similar to the arrangement shown in Fig. 5.8, p. 38.

**Figure 7.9:** SWAXS measurements of  $[\text{Ni}(\text{silyl-2,3,2-tetramine})_3\text{Fe}(\text{CN})_6]_2$  and  $[\text{Ni}(\text{silyl-2,3,2-tetramine})_3\text{Fe}(\text{CN})_6]_2$  gel.

The SWAXS curve of  $[\text{Ni}(\text{silyl-2,3,2-tetramine})_3\text{Fe}(\text{CN})_6]_2$  gel (gray curve in Fig. 7.9) shows no distinctive reflections. This means that the 3D crystalline order of the cyanometallate is destroyed after sol-gel processing. The slope of  $q^{-1}$  between 2 and 5  $\text{nm}^{-1}$  indicated by the dashed line in the insert of Fig. 7.9 suggests elongated objects which are randomly dispersed in the silica matrix. These 1D objects are probably  $\text{Fe}^{\text{III}}\text{-C}\equiv\text{N-Ni}^{\text{II}}$  (double) chains which give rise to the absorption band for bridging cyano groups (Fig. 7.6).

## 7.5 SQUID

Field cooled (FC) and zero-field cooled (ZFC) measurements of  $[\text{Ni}(\text{silyl-2,3,2-tetramine})]_3[\text{Fe}(\text{CN})_6]_2$  gel were performed at different temperatures and external fields. The experimental results were corrected for diamagnetic contributions with the theoretical value calculated according to Pascal's method described in Subsection 12.4.5, p. 105.

Measurement of  $\chi_m$  at different temperatures and external fields (Fig. 7.10) yields curves that are a clear indication of paramagnetic behavior of the material.  $\chi_m$  is positive but small, and no effects besides an increase with decreasing temperature occur as expected from Curie's law (Subsection 3.1.1, p. 22).

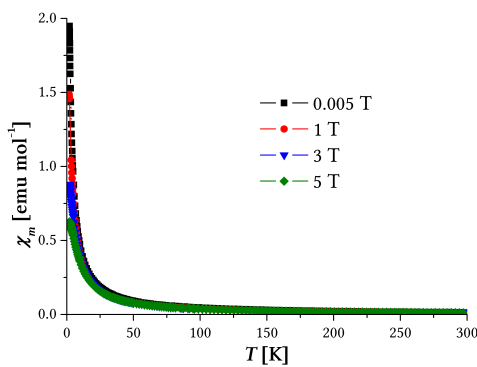


**Figure 7.10:**  $\chi_m$  vs.  $T$  of  $[\text{Ni}(\text{silyl-2,3,2-tetramine})]_3[\text{Fe}(\text{CN})_6]_2$  gel at various external fields.

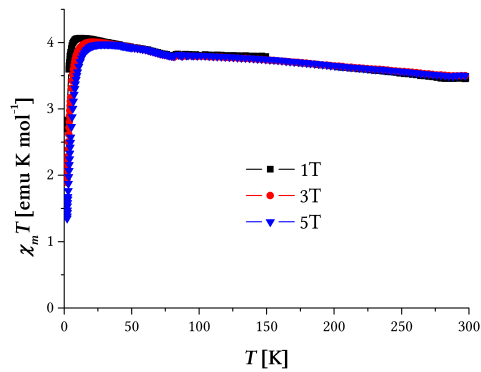


**Figure 7.11:**  $\chi_m T$  vs.  $T$  of  $[\text{Ni}(\text{silyl-2,3,2-tetramine})]_3[\text{Fe}(\text{CN})_6]_2$  gel at various external fields.

The Curie constant  $C$  can be calculated according to Curie's law ( $C = \chi_m \cdot T$ , Subsection 3.1.1, p. 22) from the  $\chi_m T$  vs.  $T$  plot in Fig. 7.11 by fitting a straight line with slope = 0. The average value obtained for the measurements at external fields of 1 T, 3 T and 5 T is 3.67. This gives a  $\mu_{eff}$  of  $5.42 \mu_B$  ( $\mu_{eff} = 2.82787 \sqrt{C}$ ).

An alternative route to calculate  $C$  is from the slope of  $1/\chi_m$  vs.  $T$  (Fig. 7.12), which is equal to  $1/C$  ( $1/\chi_m = T/C$ ). An average for  $C$  of 3.61 is obtained by this method from the measurements at external fields of 1 T, 3 T and 5 T. The  $\mu_{eff}$ , therefore, is  $5.37 \mu_B$ .

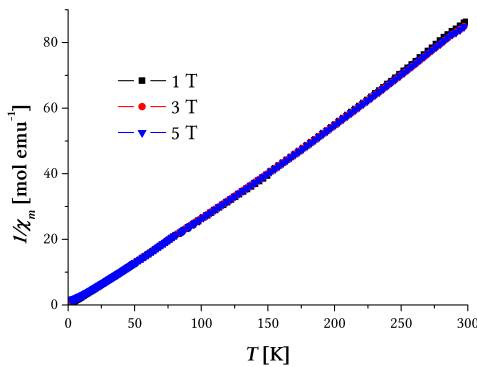


**Figure 7.12:**  $1/\chi_m$  vs.  $T$  of  $[\text{Ni}(\text{silyl-2,3,2-tetramine})]_3[\text{Fe}(\text{CN})_6]_2$  gel at various external fields.

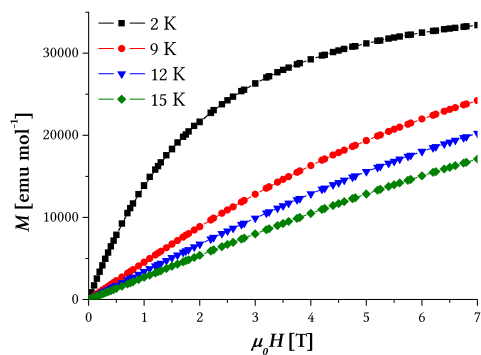


**Figure 7.13:**  $M$  vs.  $\mu_0 H$  of  $[\text{Ni}(\text{silyl-2,3,2-tetramine})]_3[\text{Fe}(\text{CN})_6]_2$  gel at various temperatures.

The average  $\mu_{eff}$  is 5.40  $\mu_B$ . This is well below the spin-only value for three Ni<sup>II</sup> ( $S = 1$ ,  $g = 2$ ) and two low-spin Fe<sup>III</sup> ( $S = 1/2$ ,  $g = 2$ ) of 8.94  $\mu_B$ . Partial antiferromagnetic arrangement of neighboring chains/sheets of the cyanometallate structure may be the reason for the lower  $\mu_{eff}$ . Another explanation would be that not all of the metal centers couple because the structural arrangement is not favorable for exchange interactions.

The magnetization  $M$  versus external field  $\mu_0 H$  was measured at various temperatures (Fig. 7.13). The curves are characteristic of a paramagnet with a linear increase of  $M$  with increasing external field, following Curie's law. Deviation from linear behavior occurs only at low temperatures and high fields. This is due to saturation effects which arise because all magnetic dipoles are already aligned with the external field and an increase cannot lead to further magnetization of the sample. At 2 K the saturation magnetization of [Ni(silyl-2,3,2-tetramine)]<sub>3</sub>[Fe(CN)<sub>6</sub>]<sub>2</sub> gel is nearly reached at 7 T and lies at  $\sim 33,450$  emu mol<sup>-1</sup>.

## 7.6 Conclusions

[Ni(silyl-2,3,2-tetramine)]<sub>3</sub>[Fe(CN)<sub>6</sub>]<sub>2</sub> was synthesized and covalently embedded in silica. The ligand was obtained by reaction of 2,3,2-tetramine with 3-iodopropyltrimethoxysilane and employed as both a blocking ligand at Ni<sup>II</sup> and a linker to tether the cyanometallate structure to the silica matrix during sol-gel processing through reaction of the trimethoxysilyl groups.

The FTIR spectrum of [Ni(silyl-2,3,2-tetramine)]<sub>3</sub>[Fe(CN)<sub>6</sub>]<sub>2</sub> gel showed bands for Fe<sup>III</sup>–C≡N–Ni<sup>II</sup> cyanide bridges and the condensation of the trialkoxysilyl groups during the sol-gel process. A Ni:Fe ratio of  $\sim 2.6:2$  was found by EDX which is close to 3:2, expected due to charge balance. The excess of Fe may be due to part of the [Fe(CN)<sub>6</sub>]<sup>3-</sup> forms less than three cyanide bridges. Structural investigation by SWAXS showed presence of a crystalline phase for the cyanometallate while after sol-gel processing an amorphous material with embedded 1D elongated structures was obtained. This led to the conclusion that cyanometallate structures are retained as double chains in the gel, but structural alignment in three dimensions is disrupted.

SQUID measurements showed that [Ni(silyl-2,3,2-tetramine)]<sub>3</sub>[Fe(CN)<sub>6</sub>]<sub>2</sub> gel is a paramagnet. The susceptibility follows the Curie law. An effective magnetic moment  $\mu_{eff}$  of 5.40  $\mu_B$  was found which is lower than the spin-only value. This may be due to spin-orbit coupling of Ni<sup>II</sup> and Fe<sup>III</sup> in the cyanometallate network. The different behavior compared to ferromagnetic [Ni(AEAPTS)<sub>2</sub>]<sub>3</sub>[Fe(CN)<sub>6</sub>]<sub>2</sub> gel may be due to higher flexibility of the diamine ligands AEAPTS compared to the tetramine. This may enable re-adjustment of the AEAPTS containing cyanometallate network in the SiO<sub>2</sub> matrix to still allow for ferromagnetic coupling of Fe<sup>III</sup> and Ni<sup>II</sup>. E.g. *cis* arrangement of the cyano bridges at Ni<sup>II</sup>, which is usually structurally not favored, may occur to ease stress in the structure.

# Ni<sup>II</sup>-Fe<sup>III</sup>-SiO<sub>2</sub> Gel with Bissilyl-2,3,2-tetramine

Bissilyl-2,3,2-tetramine is a tetradentate ligand that can block four coordination sites of Ni<sup>II</sup> similar to silyl-2,3,2-tetramine (Chapter 7, p. 51), but has two pendant propyltrimethoxysilyl groups (Fig. 7.1). As stated above (Chapter 7, p. 51), the ligand without pendant side chains has been employed by Koo *et al.* to obtain the 2D [Ni(2,3,2-tetramine)]<sub>3</sub>[Fe(CN)<sub>6</sub>]<sub>2</sub> · 8 H<sub>2</sub>O cyanometallate network which exhibits ferromagnetic properties [232].

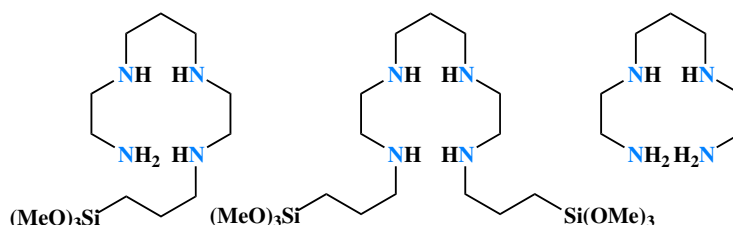


Figure 8.1: Structures of silyl-2,3,2-tetramine, bissilyl-2,3,2-tetramine and 2,3,2-tetramine.

## 8.1 Synthesis

The bissilylated ligand was synthesized from 1,3-dibromopropane and AEAPTS in basic medium (Fig. 8.2) similar to the synthesis of 2,3,2-tetramine (Sec. 7.1, p. 51, [258]). Experimental details are described in Part III, p. 103.

1,3-Dibromopropane in dry methanol is added dropwise to AEAPTS. The reaction mixture is heated to reflux and dry triethylamine added. The product is isolated as viscous yellow liquid after filtration and distilling off solvents and reactants.

The <sup>1</sup>H NMR spectrum of the product is shown in Fig. 8.3. The multiplet at 0.65 ppm stems from the CH<sub>2</sub> groups in  $\alpha$  position to the trimethoxysilyl groups. At 1.65 and

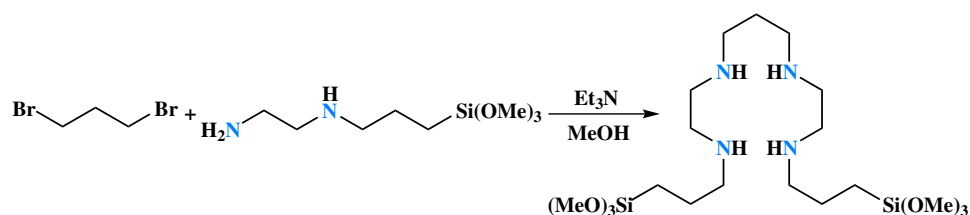


Figure 8.2: Synthesis of bis(2,3,2-tetramine)silyl.

1.87 ppm the signals arising from the central  $\text{CH}_2$  groups of the propyltrimethoxysilyl and the bisaminopropyl chains, respectively, are found. All the  $\text{CH}_2$  groups in  $\alpha$  position of a secondary amine are superimposed in the region 2.45–2.96 ppm while the methoxy groups give rise to a singlet at 3.56 ppm.

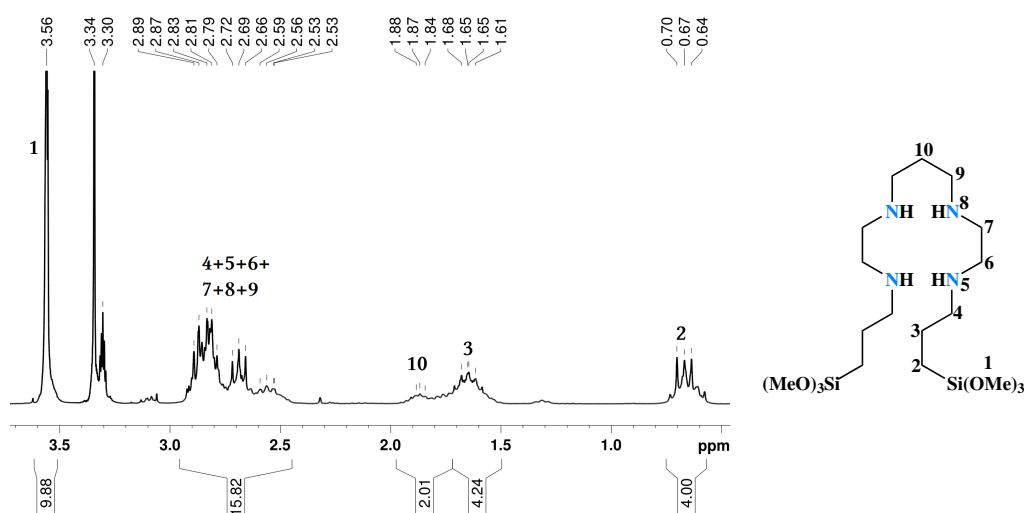


Figure 8.3:  $^1\text{H}$  NMR spectrum of bis(2,3,2-tetramine)silyl.

The  $\text{Ni}^{\text{II}}$  complex is synthesized by the addition of one equivalent of bis(2,3,2-tetramine)silyl to a solution of  $\text{NiCl}_2$  in methanol and obtained as a violet precipitate (Fig. 8.4). The cyanometallate network embedded in  $\text{SiO}_2$  is subsequently obtained analogous to the synthesis of  $[\text{Ni}(\text{AEAPTS})_2]_3[\text{Fe}(\text{CN})_6]_2$  (Sec. 5.1, p. 33). Addition of  $\text{K}_3[\text{Fe}(\text{CN})_6]$  to  $[\text{Ni}(\text{bis(2,3,2-tetramine)silyl})]\text{Cl}_2$  yields a brown powder which is reacted with TEOS in basic medium ( $\text{NH}_3$ ) to give  $[\text{Ni}(\text{bis(2,3,2-tetramine)silyl})]_3[\text{Fe}(\text{CN})_6]_2$  gel as brown powder. The formula  $[\text{Ni}(\text{bis(2,3,2-tetramine)silyl})]_3[\text{Fe}(\text{CN})_6]_2$  gel is not a completely correct representation of the structure. The trimethoxysilyl groups of the blocking ligand react during the sol-gel process, which means it is chemically changed.



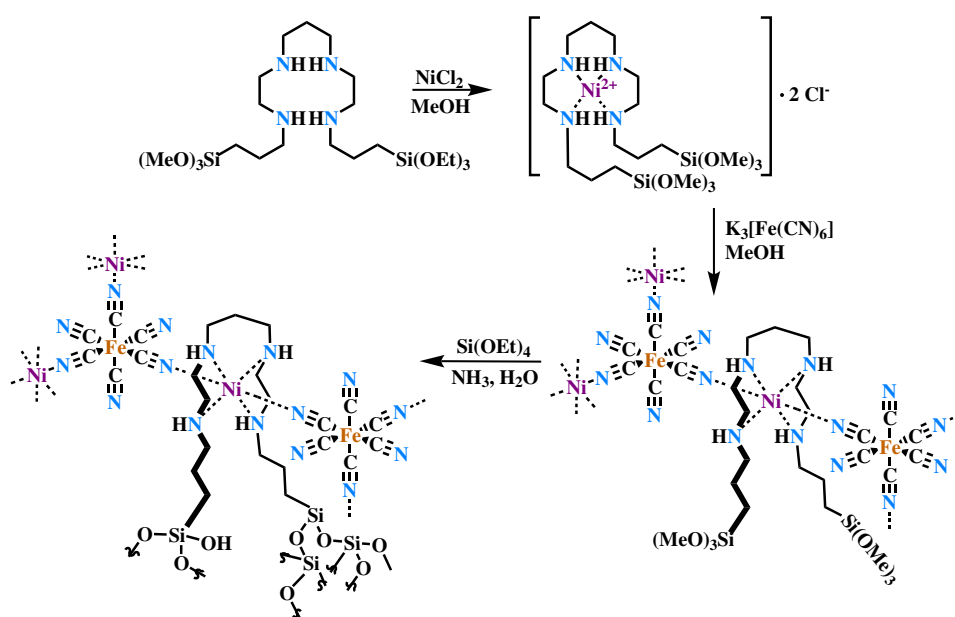


Figure 8.4: Synthesis of  $[\text{Ni}(\text{bissilyl-2,3,2-tetramine})]_3[\text{Fe}(\text{CN})_6]_2$  gel.

## 8.2 FTIR

The FTIR spectra of the free ligand, the  $\text{Ni}^{\text{II}}$  complex, the cyanometallate network and the sol-gel material are shown in Fig. 8.5.

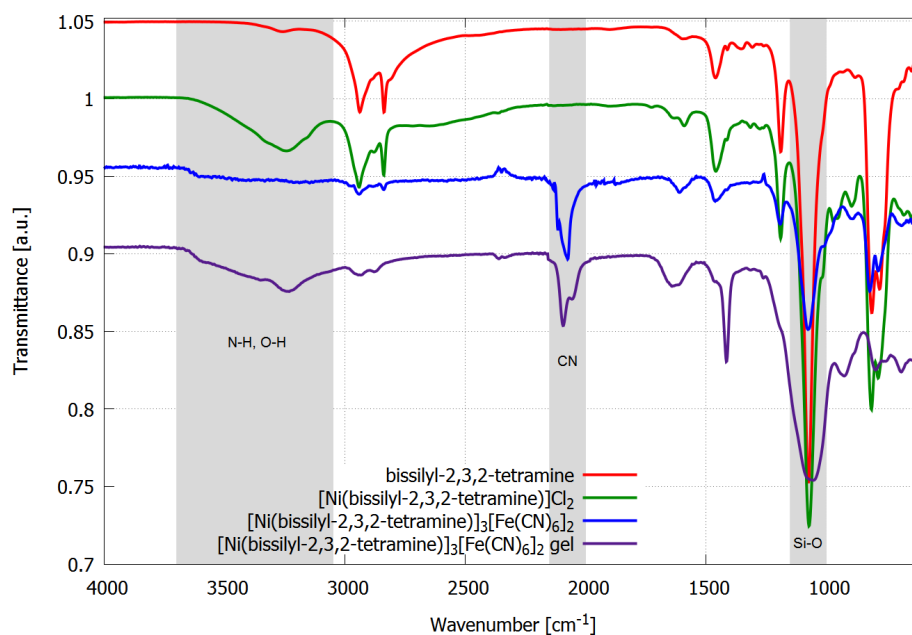


Figure 8.5: FTIR spectra of bissilyl-2,3,2-tetramine,  $[\text{Ni}(\text{bissilyl-2,3,2-tetramine})]\text{Cl}_2$ ,  $[\text{Ni}(\text{bissilyl-2,3,2-tetramine})]_3[\text{Fe}(\text{CN})_6]_2$  and  $[\text{Ni}(\text{bissilyl-2,3,2-tetramine})]_3[\text{Fe}(\text{CN})_6]_2$  gel.

The spectrum of the bissilyl-2,3,2-tetramine ligand shows characteristic bands for amine groups and Si–O vibrations. The secondary amine functions give rise to a broad band with absorption maxima at  $3258\text{ cm}^{-1}$  due to NH stretching and at  $811$  and  $788\text{ cm}^{-1}$  due to NH wagging. The trimethoxysilyl groups cause absorption maxima at  $1075$ ,  $1189$  and  $2838\text{ cm}^{-1}$  due to Si–OCH<sub>3</sub> vibrations. The bands arising from Si–CH<sub>2</sub> and C–NH are also in the region of  $1070$ – $1200\text{ cm}^{-1}$  but hidden behind the stronger signals from Si–OCH<sub>3</sub>.

Few changes occur in the FTIR spectrum upon complexation by Ni<sup>II</sup>. The amine bands are shifted by a few wavenumbers to  $3244$ ,  $813$  and  $785\text{ cm}^{-1}$  which indicates complexation by Ni<sup>II</sup>. The characteristic bands of the trimethoxysilyl groups stay unchanged, as do the signals arising from the carbon backbone.

Absorption maxima characteristic of the cyano group arise at  $2115$  and  $2057\text{ cm}^{-1}$  in the spectrum of the cyanometallate network  $[\text{Ni}(\text{bissilyl-2,3,2-tetramine})]_3[\text{Fe}(\text{CN})_6]_2$ . The corresponding band in  $\text{K}_3[\text{Fe}(\text{CN})_6]$  is at  $2116\text{ cm}^{-1}$ . The band at  $2115\text{ cm}^{-1}$  can therefore be assigned to non-bridging C≡N ligands. The additional band at  $2057\text{ cm}^{-1}$ , on the other hand, is due to bridging cyano groups. This is clear evidence, besides the precipitation and colour change of the product, for successful network formation. The bands from the ligand show lower intensity, but are all present and again more pronounced in the sol-gel material. This precludes that the ligand is cleaved in the network formation.

The bands characteristic for Si–OCH<sub>3</sub> with maxima at  $1075$ ,  $1189$  and  $2838\text{ cm}^{-1}$  disappear after sol-gel processing. However, a new maximum on a broad band arises at  $1070\text{ cm}^{-1}$  in the region characteristic of Si–O vibrations. They stem from the Si–O–Si entities of the amorphous SiO<sub>2</sub> network. The two bands of bridging and non-bridging cyano groups are present, as are the signals of the amine groups and carbon backbone, indicating that (part of) the cyanometallate structure is retained.

### 8.3 SEM and EDX

The SEM shown in Fig. 8.6 was recorded at a voltage of 10 kV. It proves the homogeneity of  $[\text{Ni}(\text{bissilyl-2,3,2-tetramine})]_3[\text{Fe}(\text{CN})_6]_2$  gel. No crystallites of the cyanometallate network are discernible. This indicates that no (visible) phase separation occurs.

EDX measurement (Fig. 8.7) confirmed a homogeneous distribution of the metals and thus the cyanometallate network in  $[\text{Ni}(\text{bissilyl-2,3,2-tetramine})]_3[\text{Fe}(\text{CN})_6]_2$  gel. A Ni:Fe ratio of  $\sim 2.8:2$  was found from the atomic percentages (Tab. 8.1) obtained by quantitative analysis. This corresponds quite well to the metal ratio used for the preparation of  $[\text{Ni}(\text{bissilyl-2,3,2-tetramine})]_3[\text{Fe}(\text{CN})_6]_2$  and is expected for a cyanometallate of Ni<sup>II</sup> and Fe<sup>III</sup> due to charge balance. The excess of Fe may indicate that a part of  $[\text{Fe}(\text{CN})_6]^{3-}$  forms less than three cyanide bridges to Ni<sup>II</sup> which causes deviation from the ideal stoichiometry, as discussed for the similar structure  $[\text{Ni}(\text{silyl-2,3,2-tetramine})]_3[\text{Fe}(\text{CN})_6]_2$  gel in Sec. 7.3, p. 55. Charge balance is kept by incorporation of traces of K<sup>+</sup> ions into the material.

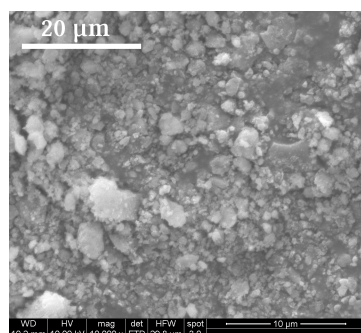


**Figure 8.6:** SEM of  $[\text{Ni}(\text{bissilyl-2,3,2-tetramine})]_3[\text{Fe}(\text{CN})_6]_2$  gel.

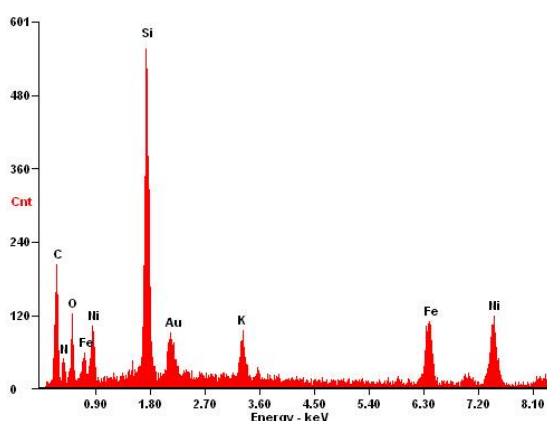


**Figure 8.7:** EDX plot (energy [keV] vs. intensity) of  $[\text{Ni}(\text{bissilyl-2,3,2-tetramine})]_3[\text{Fe}(\text{CN})_6]_2$  gel.

**Table 8.1:** EDX analysis of  $[\text{Ni}(\text{silyl-2,3,2-tetramine})]_3[\text{Fe}(\text{CN})_6]_2$  gel.

element	at. %
C (K)	56.86
N (K)	12.29
O (K)	10.79
Si (K)	9.5
K (K)	1.33
Fe (K)	3.81
Ni (K)	5.42
Total	100

**Table 8.2:** Experimental vs. fitted reflections for  $[\text{Ni}(\text{silyl-2,3,2-tetramine})]_3[\text{Fe}(\text{CN})_6]_2$ .

peak	fit	$q_{\text{max}}$ [ $\text{nm}^{-1}$ ]
$d_{010}$	4.792	4.8
$d_{100}$	8.007	8.4
$d_{110}$	9.332	9.1
$d_{020}$	9.584	9.6
$d_{001}$	11.752	11.6
$d_{011}$	12.691	12.5
$d_{101}$	14.221	14.5
$d_{111}$	15.006	15.1

## 8.4 SWAXS

SWAXS measurements of  $[\text{Ni}(\text{bissilyl-2,3,2-tetramine})]_3[\text{Fe}(\text{CN})_6]_2$  and  $[\text{Ni}(\text{bissilyl-2,3,2-tetramine})]_3[\text{Fe}(\text{CN})_6]_2$  gel were performed (Fig. 8.8). Structural changes of the cyanometallate network upon embedding in  $\text{SiO}_2$  can be determined by comparison of the two curves.

$[\text{Ni}(\text{bissilyl-2,3,2-tetramine})]_3[\text{Fe}(\text{CN})_6]_2$  (black curve in Fig. 8.8) exhibits distinct Bragg reflections. A structure practically identical to the one proposed for  $[\text{Ni}(\text{silyl-2,3,2-tetramine})]_3[\text{Fe}(\text{CN})_6]_2$  (Sec. 7.4, p. 55) can be fitted with excellent agreement, as Tab. 8.2 shows. The reflections are labelled accordingly for an orthorhombic unit cell with lattice parameters  $a = 7.9 \text{ \AA}$ ,  $b = 13.2 \text{ \AA}$  and  $c = 5.8 \text{ \AA}$  in the insert of Fig. 8.8. The same lattice constants were found for  $[\text{Ni}(\text{silyl-2,3,2-tetramine})]_3[\text{Fe}(\text{CN})_6]_2$ , but some uncertainty in the exact positions of the maxima arises from the quite broad reflections which stem from small crystalline domains. The additional side chain of the blocking ligand seems to have little influence on the crystal structure which, again, leads to the assumption that the structure is similar to the one described for  $[\text{Ni}(\text{en})_2]_3[\text{Fe}(\text{CN})_6]_2 \cdot n \text{ H}_2\text{O}$  by Ohba *et al.* and Herchel *et al.* [156, 206], as discussed in Sec. 5.4, p. 36. It is probably built of 1D double chains of three  $\text{Ni}^{\text{II}}$  with two cyano bridges and one tetramine ligand and two

$\text{Fe}^{\text{III}}$  with three cyano bridges and three non-bridging cyano ligands. These 1D structures are extending along the  $c$ -axis and assembled in an orthorhombic lattice with  $\text{Ni}^{\text{II}}$  at the edges, similar to the arrangement shown in Fig. 5.8, p. 38.

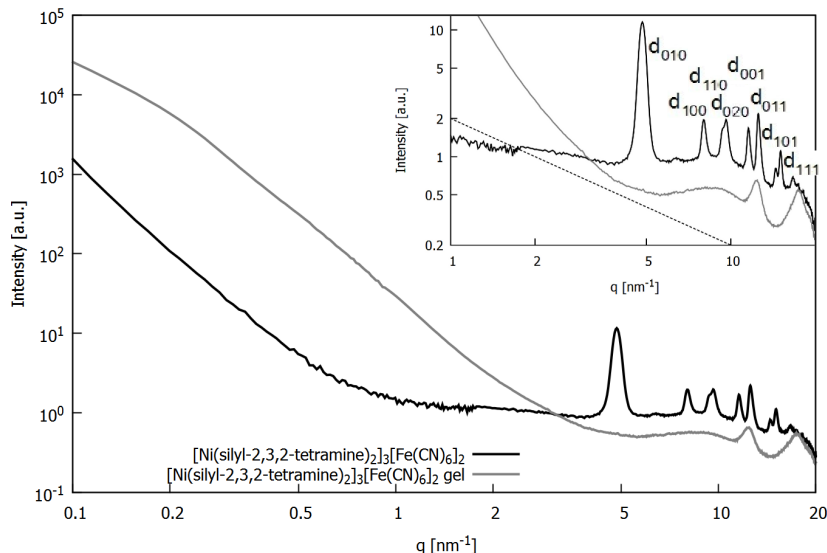


**Figure 8.8:** SWAXS measurements of  $[\text{Ni}(\text{bissilyl-2,3,2-tetramine})_2]_3[\text{Fe}(\text{CN})_6]_2$  and  $[\text{Ni}(\text{bissilyl-2,3,2-tetramine})_2]_3[\text{Fe}(\text{CN})_6]_2$  gel.

The SWAXS curve of  $[\text{Ni}(\text{bissilyl-2,3,2-tetramine})_2]_3[\text{Fe}(\text{CN})_6]_2$  gel (gray curve in Fig. 8.8) shows no distinctive reflections. This means that the 3D crystalline order of the cyanometallate is destroyed after sol-gel processing. The slope of  $q^{-1}$  between 3.5 and 5  $\text{nm}^{-1}$  indicated by the dashed line in the insert of Fig. 8.8 suggests elongated objects which are randomly dispersed in the silica matrix. These 1D objects are probably  $\text{Fe}^{\text{III}}\text{--C}\equiv\text{N--Ni}^{\text{II}}$  (double) chains which give rise to the absorption band for bridging cyano groups (Fig. 8.5).

## 8.5 SQUID

Field cooled (FC) and zero-field cooled (ZFC) measurements of  $[\text{Ni}(\text{bissilyl-2,3,2-tetramine})_2]_3[\text{Fe}(\text{CN})_6]_2$  gel were performed at different temperatures and external fields. The experimental results were corrected for diamagnetic contributions with the theoretical value calculated according to Pascal's method described in Subsection 12.4.5, p. 105.

Measurement of  $\chi_m$  at different temperatures and external fields (Fig. 8.9) yields curves that are a clear indication of paramagnetic behavior of the material.  $\chi_m$  is positive but small and no effects besides an increase with decreasing temperature occur as expected from Curie's law (Subsection 3.1.1, p. 22).

From the  $\chi_m T$  vs.  $T$  plot in Fig. 8.10 the Curie constant  $C$  can be calculated according to Curie's law ( $C = \chi_m \cdot T$ , Subsection 3.1.1, p. 22) by fitting a straight line with slope = 0. The average value obtained for the measurements at external fields of 1 T, 3 T and 5 T is 5.83. This gives a  $\mu_{\text{eff}}$  of 6.83  $\mu_{\text{B}}$  ( $\mu_{\text{eff}} = 2.82787\sqrt{C}$ ).

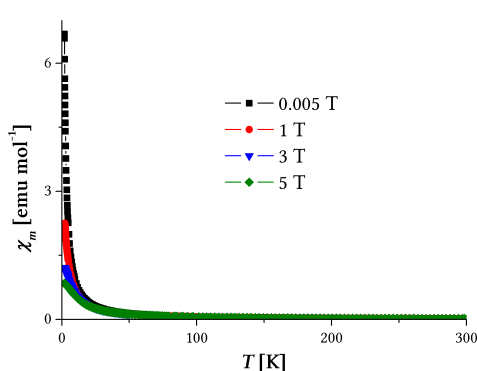


**Figure 8.9:**  $\chi_m$  vs.  $T$  of  $[\text{Ni}(\text{bissilyl-2,3,2-tetramine})]_3[\text{Fe}(\text{CN})_6]_2$  gel at various external fields.

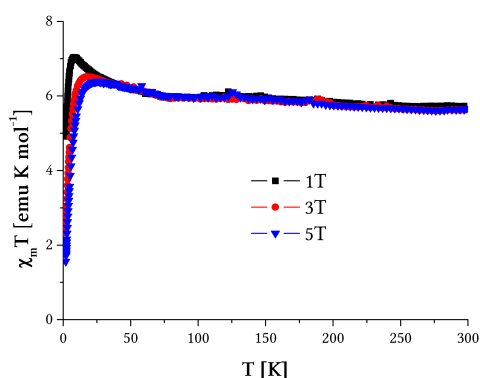


**Figure 8.10:**  $\chi_m T$  vs.  $T$  of  $[\text{Ni}(\text{bissilyl-2,3,2-tetramine})]_3[\text{Fe}(\text{CN})_6]_2$  gel at various external fields.

An alternative route to calculate  $C$  is from the slope of  $1/\chi_m$  vs.  $T$  (Fig. 8.11), which is equal to  $1/C$  ( $1/\chi_m = T/C$ ). An average for  $C$  of 5.77 is obtained by this method from the measurements at external fields of 1 T, 3 T and 5 T. The  $\mu_{eff}$ , therefore, is  $6.79 \mu_B$ .

The average  $\mu_{eff}$  is  $6.81 \mu_B$ . This is well below the spin-only value for three  $\text{Ni}^{\text{II}}$  ( $S = 1$ ,  $g = 2$ ) and two low-spin  $\text{Fe}^{\text{III}}$  ( $S = 1/2$ ,  $g = 2$ ) of  $8.94 \mu_B$ . Partial antiferromagnetic arrangement of neighboring chains/sheets of the cyanometallate structure may be the reason for the lower  $\mu_{eff}$ . Another explanation would be that not all of the metal centers couple because the structural arrangement is not favorable for exchange interactions.

The magnetization  $M$  versus external field  $\mu_0 H$  was measured at various temperatures (Fig. 8.12). The curves are characteristic of a paramagnet with a linear increase of  $M$  with the external field, following Curie's law. Deviation from linear behavior occurs only at low temperatures and high fields. This is due to saturation effects which arise because all magnetic dipoles are already aligned with the external field and an increase cannot lead to further magnetization of the sample. At 2 K the saturation magnetization of  $[\text{Ni}(\text{bissilyl-2,3,2-tetramine})]_3[\text{Fe}(\text{CN})_6]_2$  gel is nearly reached at 7 T and lies at  $\sim 47,448 \text{ emu mol}^{-1}$ .

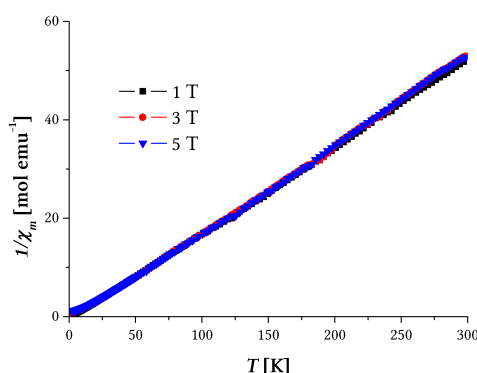


**Figure 8.11:**  $1/\chi_m$  vs.  $T$  of  $[\text{Ni}(\text{bissilyl-2,3,2-tetramine})]_3[\text{Fe}(\text{CN})_6]_2$  gel at various external fields.

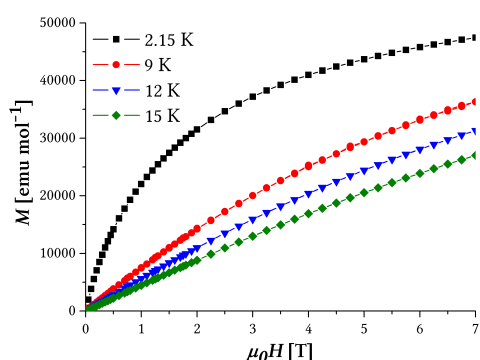


**Figure 8.12:**  $M$  vs.  $\mu_0 H$  of  $[\text{Ni}(\text{bissilyl-2,3,2-tetramine})]_3[\text{Fe}(\text{CN})_6]_2$  gel at various temperatures.

## 8.6 Conclusions

$[\text{Ni}(\text{bissilyl-2,3,2-tetramine})]_3[\text{Fe}(\text{CN})_6]_2$  was synthesized and covalently embedded in silica. The ligand was obtained by reaction of 1,3-dibromopropane and AEAPTS and employed as both a blocking ligand at  $\text{Ni}^{\text{II}}$  and a linker to tether the cyanometallate structure to the silica matrix during sol-gel processing through reaction of the trimethoxysilyl groups.

The FTIR spectrum of  $[\text{Ni}(\text{bissilyl-2,3,2-tetramine})]_3[\text{Fe}(\text{CN})_6]_2$  gel showed bands for  $\text{Fe}^{\text{III}}-\text{C}\equiv\text{N}-\text{Ni}^{\text{II}}$  cyanide bridges and the condensation of the trimethoxysilyl groups during the sol-gel process. A Ni:Fe ratio of  $\sim 2.8:2$  was found by EDX which is close to 3:2, expected due to charge balance. The excess of Fe may be due to part of the  $[\text{Fe}(\text{CN})_6]^{3-}$  forms less than three cyanide bridges. Structural investigation by SWAXS showed presence of a crystalline phase for the cyanometallate while after sol-gel processing an amorphous material with embedded 1D elongated structures was obtained. This leads to the conclusion that cyanometallate structures are retained as (double) chains in the gel, but structural alignment in three dimensions is disrupted.

SQUID measurements showed that  $[\text{Ni}(\text{bissilyl-2,3,2-tetramine})]_3[\text{Fe}(\text{CN})_6]_2$  gel is a paramagnet. The susceptibility follows the Curie law. An effective magnetic moment  $\mu_{eff}$  of  $6.81 \mu_{\text{B}}$  was found which is lower than the spin-only value. This may be due to spin-orbit coupling of  $\text{Ni}^{\text{II}}$  and  $\text{Fe}^{\text{III}}$  in the cyanometallate network. The different behavior compared to ferromagnetic  $[\text{Ni}(\text{AEAPTS})_2]_3[\text{Fe}(\text{CN})_6]_2$  gel may be due to higher flexibility of the diamine ligands AEAPTS compared to the tetramine. This may enable re-adjustment of the AEAPTS containing cyanometallate network in the  $\text{SiO}_2$  matrix to still allow for ferromagnetic coupling of  $\text{Fe}^{\text{III}}$  and  $\text{Ni}^{\text{II}}$ . E.g. *cis* arrangement of the cyano bridges at  $\text{Ni}^{\text{II}}$ , which is usually structurally not favored, may occur to ease stress in the structure.

No big effect of the second side chain with trimethoxysilyl group in the 2,3,2-tetramine blocking ligand can be found by comparison of  $[\text{Ni}(\text{silyl-2,3,2-tetramine})]_3[\text{Fe}(\text{CN})_6]_2$  (gel) and  $[\text{Ni}(\text{bissilyl-2,3,2-tetramine})]_3[\text{Fe}(\text{CN})_6]_2$  (gel). The structures before sol-gel processing were nearly identical, as determined by SWAXS measurement. The magnetic properties are also quite similar. Both structures were found to be paramagnets, but the  $\mu_{eff}$  differs slightly. This may be due to different domain sizes of the cyanometallate structures retained in the gel or small variations in the cyanometallate loads of the gels.

# Ni<sup>II</sup>-Fe<sup>III</sup>-SiO<sub>2</sub> Gel with Silylcyclam

Cyclic tetramines are analogues of crown ethers. They are more rigid than open tetramines and coordinate strongly to Ni<sup>II</sup>.

1,4,8,11-Tetraazacyclotetradecane (cyclam), shown in Fig. 9.1, has the right cavity size to fit Ni<sup>II</sup> and enclose it, thus ensuring *trans*-coordination of the CN<sup>-</sup> bridges. [Ni(cyclam)]<sup>2+</sup> by reaction with [Fe(CN)<sub>6</sub>]<sup>3-</sup> forms a 2D honeycomb structure of the formula [Ni(cyclam)]<sub>3</sub>[Fe(CN)<sub>6</sub>]<sub>2</sub> · n H<sub>2</sub>O [191, 192, 217, 218]. The cyanometallate network exhibits ferro- or metamagnetic behavior depending on the water content. This is due to the fact that ferromagnetic intralayer coupling and antiferromagnetic interlayer coupling of Ni<sup>II</sup> and Fe<sup>III</sup> are present in this structure. Depending on the distance of the 2D sheets, which is influenced by guest/solvent molecules, ferro- or metamagnetic behavior arises.

The cavity of the similar cyclic tetramine 1,4,7,10-tetraazacyclododecane (cyclen), however, is too small for Ni<sup>II</sup> and thus caps the metal from one side giving rise to *cis*-coordination of the CN<sup>-</sup> bridges, as shown by Bartlett *et al.* [261]. They synthesized a 0D cluster of the formula [Ni(cyclen)]<sub>3</sub>[TpFe(CN)<sub>3</sub>]<sub>2</sub>(BF<sub>4</sub>)<sub>4</sub> (Tp<sup>-</sup> = hydrotris(1-pyrazolyl)borate), which is a single-molecule magnet.

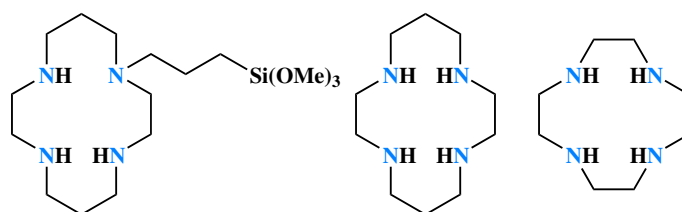


**Figure 9.1:** Structures of silylcyclam, cyclam and cyclen.

In this work, the cyclic tetramine cyclam was modified with a nitrogen-bonded propyl-trimethoxysilyl group bound to a nitrogen atom with the aim of achieving a similar 2D cyanometallate structure as [Ni(cyclam)]<sub>3</sub>[Fe(CN)<sub>6</sub>]<sub>2</sub> covalently embedded in SiO<sub>2</sub>.

## 9.1 Synthesis

The synthesis of cyclam requires multiple steps and high yields are usually not achieved. In this work four different routes were carried out. All of them gave only moderately satisfactory results due to low yields and/or intricate procedures using high volumes of dry solvents. The different routes and their results are discussed shortly in the following while experimental details and reaction conditions are described in Part III, p. 103.

### 9.1.1 Cyclam via bisaminal (butanedione)

Cyclam can be obtained from 2,3,2-tetramine by a four-step synthesis process described by Hervé *et al.* [262], shown in Fig. 9.2.

2,3,2-tetramine is obtained as described in Sec. 7.1, p. 51 and subsequently reacted with one molar equivalent of 2,3-butanedione in dry acetonitrile to yield 2,3,2-tetramine butyl bisaminal. The yellow powder is then reacted with 1,3-dibromopropane in weak basic medium ( $K_2CO_3$ ) which may only attack the secondary, not the tertiary amines. The bisaminal protecting group thus not only directs the attack of 1,3-dibromopropane on the desired nitrogens of 2,3,2-tetramine, but also assists in the formation of an intramolecular alkyl bridge between the secondary amines by fixing their arrangement in a favorable conformation and bringing them close to each other. Cyclam butyl bisaminal is isolated after filtration and column chromatography and the bisaminal protecting group removed by addition of HCl to a EtOH solution. Cyclam hydrochloride is collected by removing the solvent and recrystallization from EtOH and converted to the free amine form by elution over an Amberlyst A26 ion exchange resin. The overall yield of cyclam is ~29%.

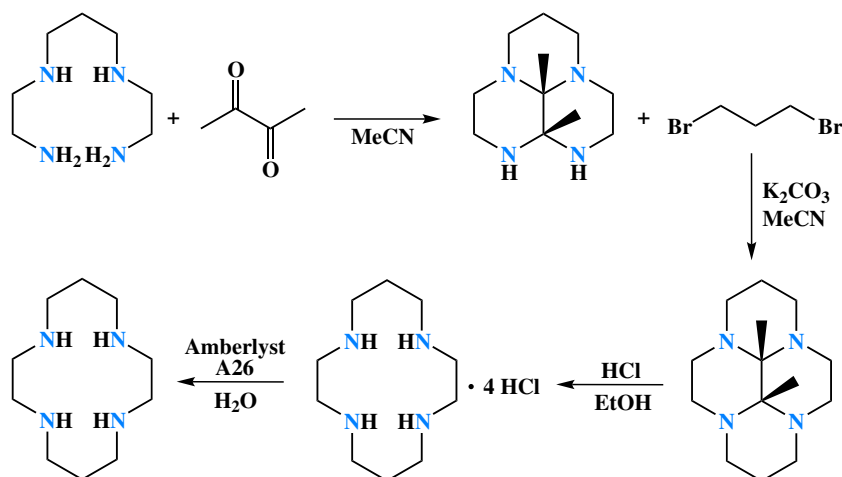


Figure 9.2: Synthesis of cyclam via butyl bisaminal.

The success of the synthesis steps was confirmed by spectroscopy techniques, especially  $^1H$  NMR spectroscopy.

The spectrum obtained from a sample of 2,3,2-tetramine butyl bisaminal is shown in Fig. 9.3. The methyl groups in  $\alpha$  position to the secondary and tertiary amines give rise to singlets at 1.12 and 1.25 ppm, respectively. The  $CH_2$  group in  $\beta$  position to the tertiary



amines causes a broad multiplet at ~2.1 ppm while its neighboring CH<sub>2</sub> groups produce a multiplet around 2.40 ppm. The CH<sub>2</sub> groups between the secondary and tertiary amino groups result in multiplets between 2.58 and 3.36 ppm. The complicated patterns occur due to differences in interaction with the methyl groups between hydrogens that are on the same side of the tetramine ring as the methyl groups and the ones on the opposite side leading to small differences in chemical shift and J-coupling.

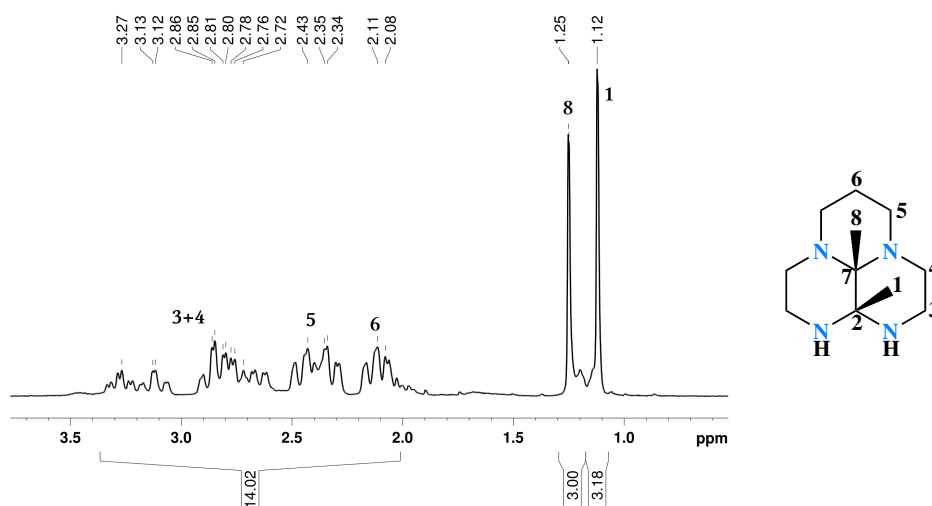


Figure 9.3: <sup>1</sup>H NMR spectrum of 2,3,2-tetramine butyl bisaminal.

The spectrum of cyclam butyl bisaminal is shown in Fig. 9.4. The methyl groups in this molecule are symmetrically equivalent and give rise to one singlet at 1.17 ppm. The CH<sub>2</sub> groups in  $\beta$  position to the tertiary amines again cause a broad multiplet at ~2.1 ppm. The CH<sub>2</sub> groups in  $\alpha$  position to the nitrogens give rise to superimposed multiplets in the region 2.2–3.6 ppm. The complicated patterns, again, arise from the presence of the methyl groups in the bisaminal protecting group located on one side of the tetramine ring. The success of the reaction may, however, be assessed from the disappearance of one singlet stemming from the methyl groups and the correct integral ratio of the methyl groups (6 H) to the CH<sub>2</sub> groups of the cyclam ring (20 H).

The highly symmetric cyclam hydrochloride gives rise to a very simple <sup>1</sup>H NMR spectrum after removal of the bisaminal protecting group, as shown in Fig. 9.5. The CH<sub>2</sub> groups in  $\beta$  position to the amino groups give rise to a quintet at 1.96 ppm while its neighboring CH<sub>2</sub> groups show a triplet at 3.17 ppm. The ethylene groups between the amino groups result in a singlet at 3.27 ppm.

The <sup>1</sup>H NMR spectrum of the free amine form of cyclam shows mainly a shift of the signals to higher fields (Fig. 9.6). The CH<sub>2</sub> groups in  $\alpha$  position to one amino group and in  $\beta$  to another one are especially affected, as would be expected. The quintet of the CH<sub>2</sub> groups in  $\beta$  position to the amino groups is shifted by 0.24 to 1.72 ppm. The triplet of the CH<sub>2</sub> groups of the propylene bridges in  $\alpha$  position to amino groups shifts by 0.25 to 2.92 ppm. The singlet of the CH<sub>2</sub> groups of the ethylene bridge is shifted by 0.43 to 2.84 ppm. The change in solubility is further evidence of the successful removal of HCl besides the <sup>1</sup>H NMR signal shifts. The hydrochloride is soluble only in strongly polar

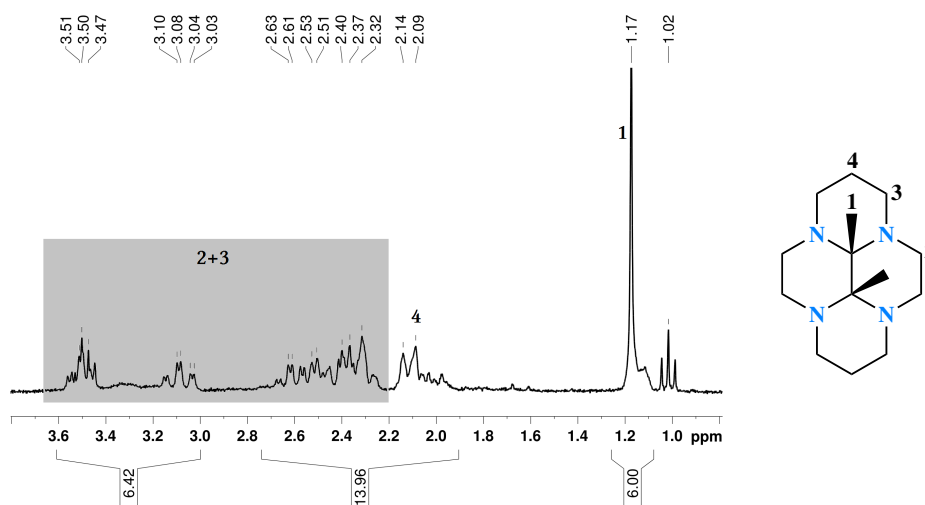


Figure 9.4: <sup>1</sup>H NMR spectrum of cyclam butyl bisaminal.

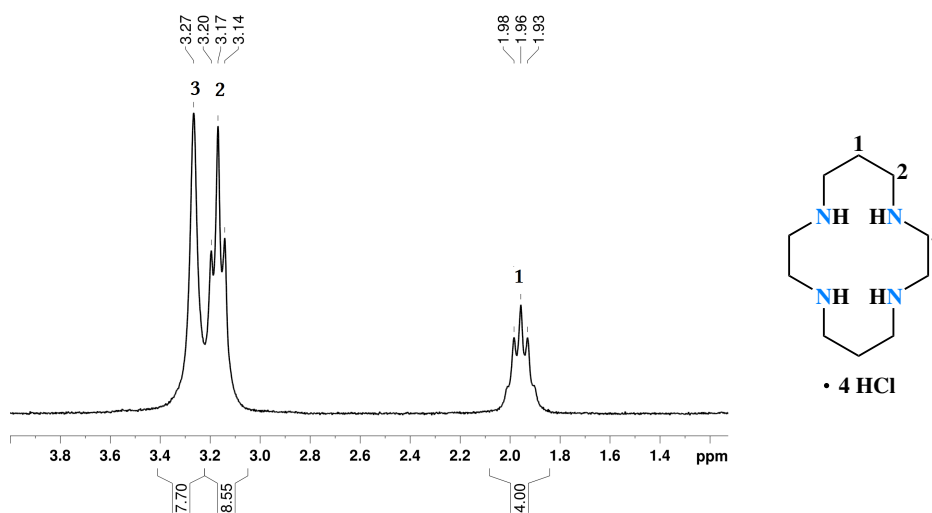


Figure 9.5: <sup>1</sup>H NMR spectrum of cyclam hydrochloride.

solvents, especially H<sub>2</sub>O, while the free amine form is soluble also in various organic solvents such as chloroform. Measurement of the pH of an aqueous solution of the sample also helps to determine the success of the reaction. A solution of cyclam hydrochloride is strongly acidic while free amine cyclam is basic.

Additional techniques were used to assess the success of the performed reactions, especially <sup>13</sup>C NMR and FTIR spectroscopy which will not be discussed here. Lists of <sup>13</sup>C NMR shifts and FTIR bands can be found in the experimental section in Chapter 13, p. 109.

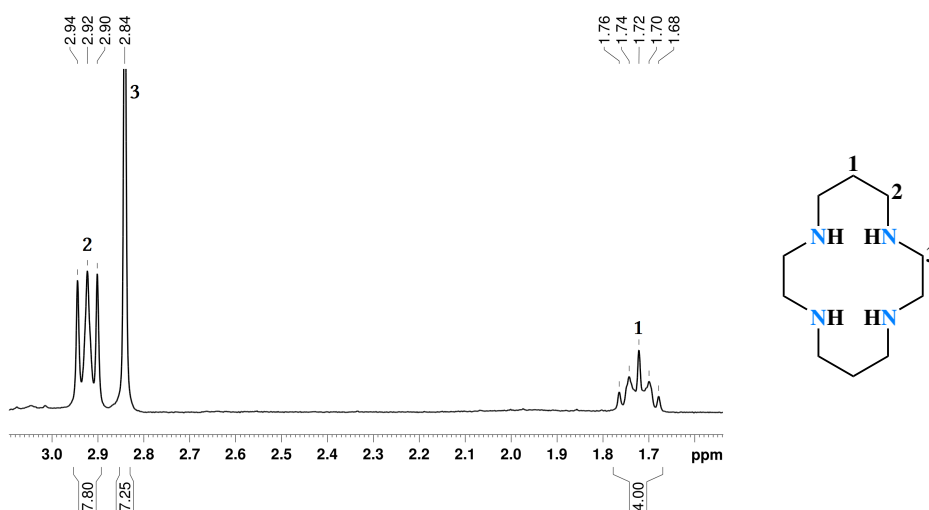


Figure 9.6:  $^1\text{H}$  NMR spectrum of cyclam.

### 9.1.2 Cyclam via bisaminal (1,2-cyclohexanedione)

Prokhorov *et al.* [263] described a similar synthesis as the one described in the previous subsection employing a different protecting group, 1,2-cyclohexanedione. The stages of the four-step route are shown in Fig. 9.7. 2,3,2-tetramine is again synthesized as described in Sec. 7.1, p. 51. Addition of one molar equivalent of 1,2-cyclohexanedione in EtOH gives 2,3,2-tetramine cyclohexyl bisaminal which is isolated by precipitation and recrystallization. Reaction of the white needles with  $\text{Cs}_2\text{CO}_3$  and 1,3-dibromopropane in dry acetonitrile yields cyclam cyclohexyl bisaminal as light yellow powder after recrystallization. The bisaminal protecting group again directs the electrophilic attack to the secondary amines of one molecule, thus forming a propylene bridge, as in the synthesis employing 2,3-butanedione. The protecting group is removed by addition of 1M HCl and the free amine form of cyclam obtained after stirring with  $\text{K}_2\text{CO}_3$  and recrystallization. The overall yield of cyclam is  $\sim 35\%$ .

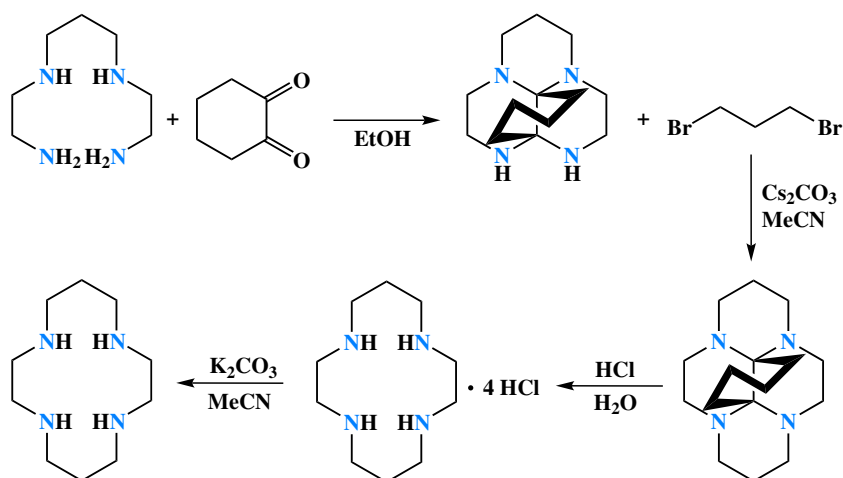
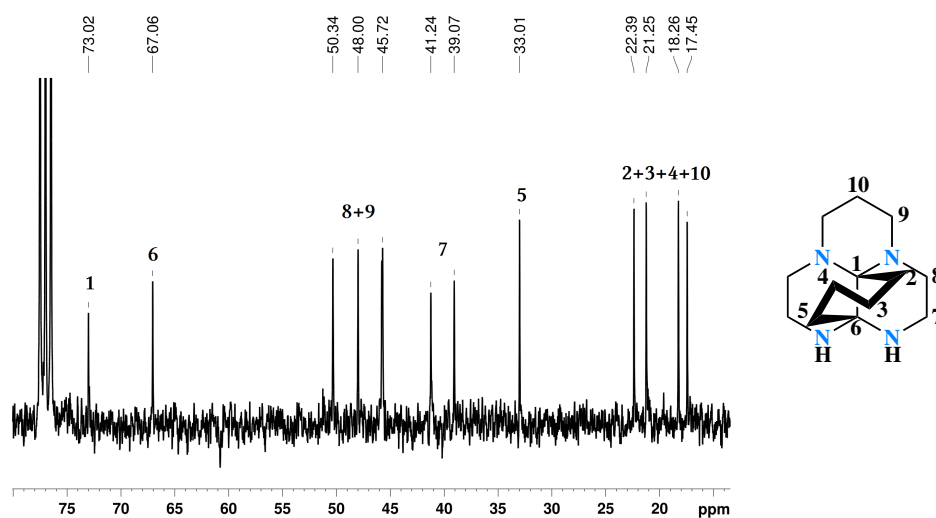


Figure 9.7: Synthesis of cyclam via cyclohexyl bisaminal.

The  $^1\text{H}$  NMR spectrum of 2,3,2-tetramine cyclohexyl bisaminal is quite complicated and crowded. The  $^{13}\text{C}$  NMR spectrum is clearer, as shown in Fig. 9.8, and therefore discussed here. The four  $\text{CH}_2$  groups of the cyclohexyl protecting group give rise to peaks at 17.45, 18.26, 22.39 (or 21.25) and 33.01 ppm. Exact assignment would only be possible by 2D NMR techniques, but was not considered necessary for this work. The peak shifted to lower field, however, may be assigned to the  $\text{CH}_2$  group closest to the secondary amines. The peak at 21.25 ppm (or 22.39 ppm) arises from the  $\text{CH}_2$  group of the propylene bridge in  $\beta$  position to the amino groups. The  $\text{CH}_2$  groups in  $\alpha$  position to the secondary amines present two peaks at 39.07 and 41.24 ppm due to different interactions with the unsymmetrically bent bisaminal bridge. The  $\text{CH}_2$  groups of the ethylene and propylene bridges in  $\alpha$  position to the tertiary amino groups gives rise to peaks at 45.72, 45.80, 48.00 and 50.34 ppm. The quaternary carbons binding to the secondary and tertiary amino groups result in peaks at 67.06 and 73.02 ppm, respectively.



**Figure 9.8:**  $^{13}\text{C}$  NMR spectrum of 2,3,2-tetramine cyclohexyl bisaminal.

A similar complexity as for 2,3,2-tetramine cyclohexyl bisaminal is found in the  $^1\text{H}$  NMR spectrum of cyclam cyclohexyl bisaminal. Therefore the  $^{13}\text{C}$  NMR spectrum will be discussed also in this case, which is shown in Fig. 9.9. The  $\text{CH}_2$  groups of the cyclohexyl bridge give rise to two peaks at 17.04 and 17.63 ppm. The peak at 21.52 ppm arises from the  $\text{CH}_2$  group of the propylene bridge in  $\beta$  position to the amino groups. The  $\text{CH}_2$  groups in  $\alpha$  position to the amino groups result in four peaks at 44.98, 45.59, 48.18 and 49.51 ppm, again suggesting that the molecule is not completely symmetrical. The quaternary carbons show a very weak signal at 72.82 ppm which is similar to the peak for the quaternary carbon next to the tertiary amino groups in 2,3,2-tetramine cyclohexyl bisaminal. This is an indication of successful reaction, besides the apparent higher symmetry of the molecule.

Removal of the cyclohexyl bisaminal protecting group with HCl results in an equivalent  $^1\text{H}$  NMR spectrum as the one measured after deprotection of cyclam butyl bisaminal shown in Fig. 9.5. Correspondingly, the  $^1\text{H}$  NMR spectrum of the free amine obtained

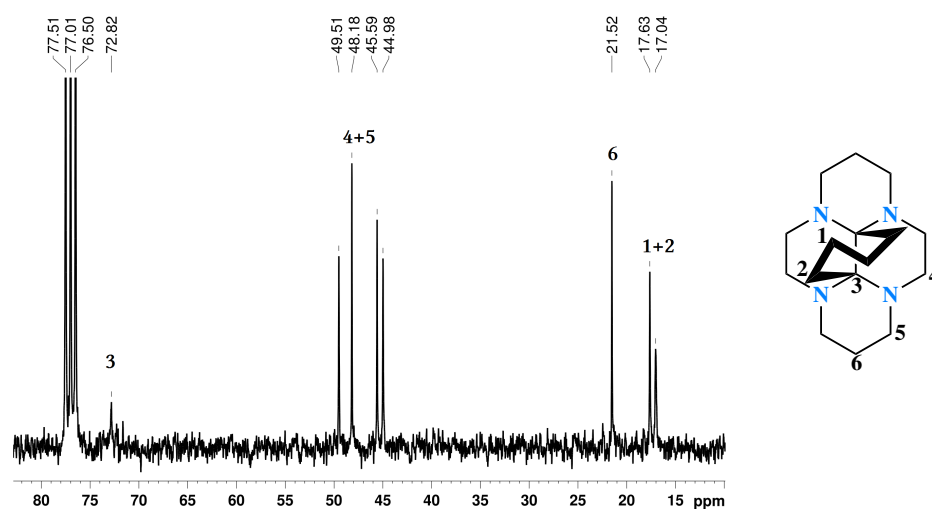


Figure 9.9: <sup>13</sup>C NMR spectrum of cyclam cyclohexyl bisaminal.

by treatment with  $K_2CO_3$  is equal to the one shown in 9.6 obtained after elution over Amberlyst A26 ion exchange resin.

### 9.1.3 Cyclam via tosyl protecting groups

Cyclam may be synthesized by application of tosyl protecting groups which direct the attack of a biselectrophile to the terminal nitrogens. Two syntheses with different tetramines and biselectrophiles have been performed.

Fig. 9.10 shows the three-step synthesis of cyclam starting from 2,3,2-tetramine, which was obtained as described in Sec. 7.1, p. 51. Addition of four molar equivalents of tosyl chloride to a basic solution of 2,3,2-teramine results in tetratosyl 2,3,2-tetramine as a white precipitate [264] that can be purified by extraction. Tetratosyl cyclam is obtained by slow addition of 1,3-dibromopropane in basic medium in high dilution (50 mL of dry MeCN/mmol) [265]. Low concentration of the tetramine is important to avoid reaction of one biselectrophile with two tetramine molecules possibly leading to polymer formation. Equivalently, low concentration of the biselectrophile is necessary to avoid reaction of one tetramine with two biselectrophile molecules. Removal of the protecting groups was the step with the most material losses. Heating to reflux in concentrated  $H_2SO_4$ , subsequent treatment with NaOH and extraction of the basic solution [264] was the only successful route, but gave only about 18% yield. This gives rise to an overall yield of cyclam of only 12%.

The synthesis route starting from 3,2,3-tetramine, which is commercially available, is shown in Fig. 9.11. Tetratosyl 3,2,3-tetramine is synthesized as described above for 2,3,2-tetramine. Ring formation to cyclam is achieved by slow addition of bistosyl ethylene glycol in basic medium in high dilution (50 mL of dry MeCN/mmol) [266]. Removal of the tosyl protecting groups is again performed by boiling in  $H_2SO_4$  and subsequent treatment with NaOH, also in this case leading to a low overall yield of cyclam of 13%.

The <sup>1</sup>H NMR spectrum of tetratosyl 2,3,2-tetramine shown in Fig. 9.12 shows the ex-

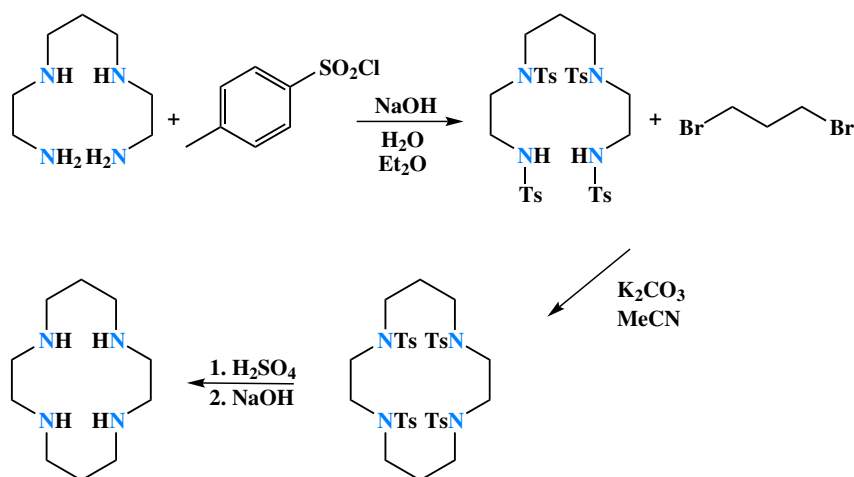


**Figure 9.10:** Synthesis of cyclam via tetratosyl 2,3,2-tetramine.

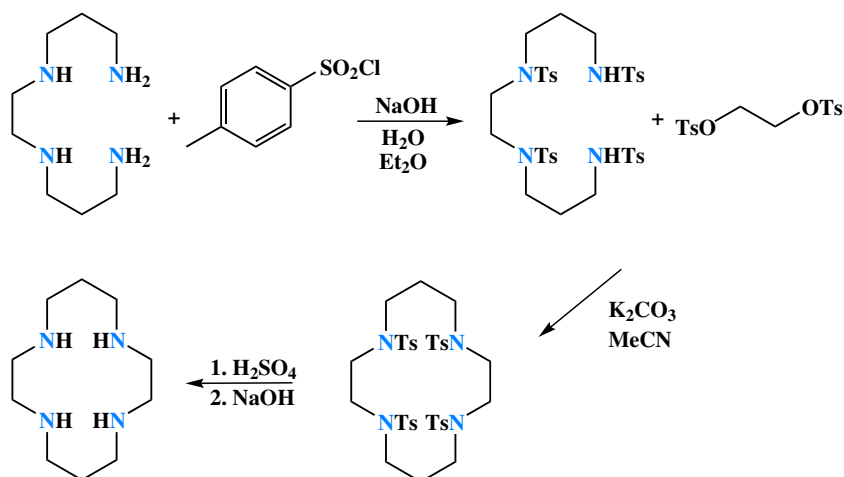


**Figure 9.11:** Synthesis of cyclam via tetratosyl 3,2,3-tetramine.

pected peaks. The quintet at 1.75 ppm stems from the CH<sub>2</sub> group of the propylene bridge in  $\beta$  position to the amino groups. The methyl groups of the tosyl entities give rise to a large singlet at 2.42 ppm. The signals of the CH<sub>2</sub> groups in  $\alpha$  position of the amino groups overlap in the region between 3.0 and 3.3 ppm. The CH groups of the benzene ring of the tosyl groups give rise to signals above 7 ppm, characteristic of hydrogen bound to sp<sup>2</sup> carbon. The broad doublet at higher field stems from the CH groups further away from the SO<sub>2</sub> groups. The other CH groups result in two sets of doublets due to the fact that the primary and secondary amines present different chemical environment which influences the nearer hydrogen atoms stronger.

Tetratosyl 3,2,3-tetramine presents a similar, but clearly different <sup>1</sup>H NMR spectrum shown in Fig. 9.13. The CH<sub>2</sub> groups of the propylene bridges in  $\beta$  position to the amino groups give rise to a quintet at 1.65 ppm with an integral of 4 H. Two singlets at 2.28 and 2.31 ppm arise from the methyl groups of the tosyl entities. The CH<sub>2</sub> groups neighboring the secondary amines give rise to a triplet at ~2.8 ppm that is partially superimposed by the

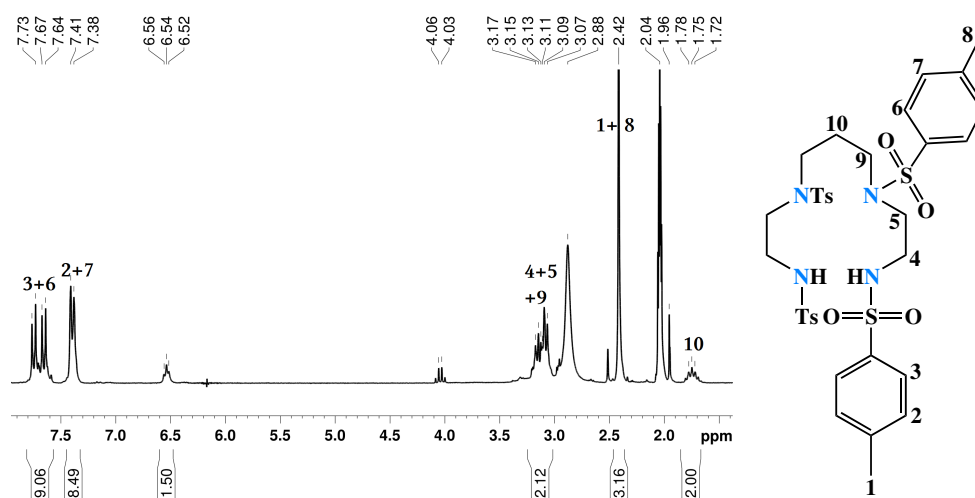


Figure 9.12:  $^1\text{H}$  NMR spectrum of tetratosyl 2,3,2-tetramine.

broad singlet stemming from  $\text{H}_2\text{O}$  present in the  $d_6$ -acetone solvent. The triplet arising from the  $\text{CH}_2$  groups of the propylene bridges in  $\alpha$  position to the tertiary amino groups overlaps with the singlet stemming from the  $\text{CH}_2$  groups of the ethylene bridge in the region between 3.0 and 3.1 ppm. The apparent triplet at 7.27 ppm can be determined to be two overlapping doublets arising from the CH groups of the benzene ring further away from the  $\text{SO}_2$  group. The other CH groups result in a broad doublet at 7.60 ppm.

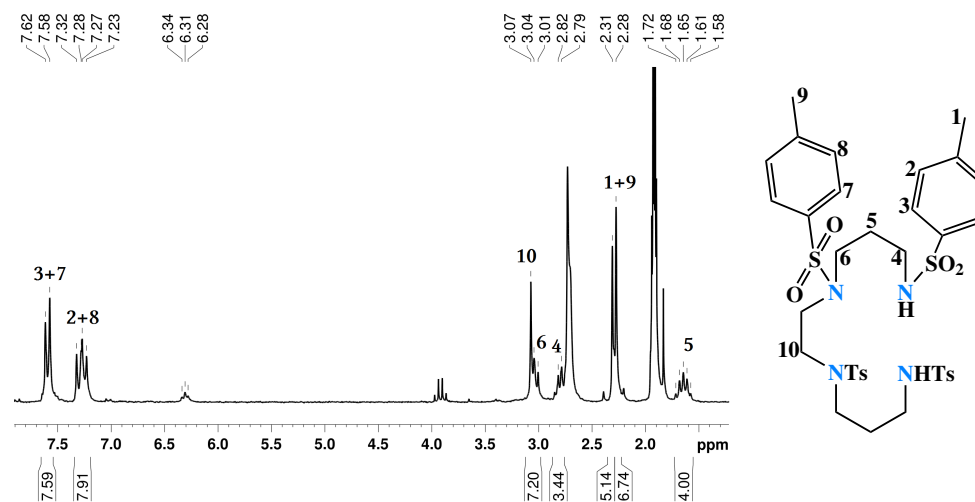


Figure 9.13:  $^1\text{H}$  NMR spectrum of tetratosyl 3,2,3-tetramine.

Both routes give tetratosyl cyclam after ring formation, which has a simple  $^1\text{H}$  NMR spectrum (Fig. 9.14) due to high symmetry of the molecule. A quintet arises at 1.87 ppm from the  $\text{CH}_2$  groups of the propylene bridges in  $\beta$  position to the amino groups. The methyl groups of the tosyl entities give rise to a singlet at 2.44 ppm. The triplet at 3.14 ppm stems from the  $\text{CH}_2$  groups of the propylene bridges in  $\alpha$  position to the amino groups and the singlet at 3.22 from the  $\text{CH}_2$  groups of the ethylene bridges. The CH groups of the benzene ring give rise to two doublets at 7.34 and 7.70 ppm.

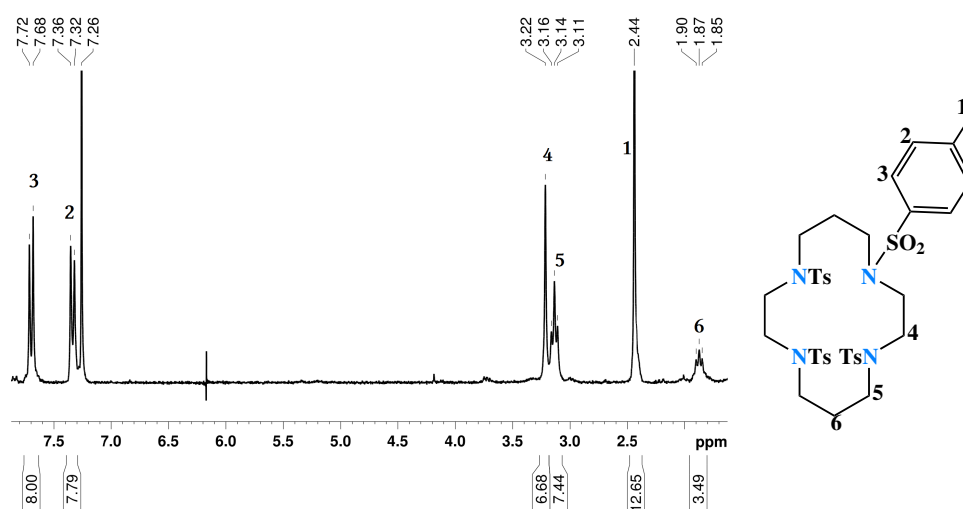


Figure 9.14:  $^1\text{H}$  NMR spectrum of tetratosyl cyclam.

Cyclam, obtained by removing the tosyl protecting groups and conversion to the free amine form in basic medium, has a  $^1\text{H}$  NMR spectrum equivalent to the one shown in Fig. 9.6.

#### 9.1.4 Silylation

Cyclam is modified with a trimethoxysilylpropyl group to act as a connector between the cyanometallate network and sol-gel  $\text{SiO}_2$ . This is achieved by the slow addition of sodium hydride and subsequently 3-iodopropyltrimethoxysilane to a suspension of cyclam in dry MeCN. Purification is done by filtration, dissolution in  $\text{CH}_2\text{Cl}_2$  and another filtration. The viscous liquid obtained after evaporation of the solvent is mostly mono silylated cyclam, but additional signals in the  $^1\text{H}$  NMR spectrum shown in Fig. 9.16 indicate most likely a mixture of mono, bis, tris and tetrakis silylation.

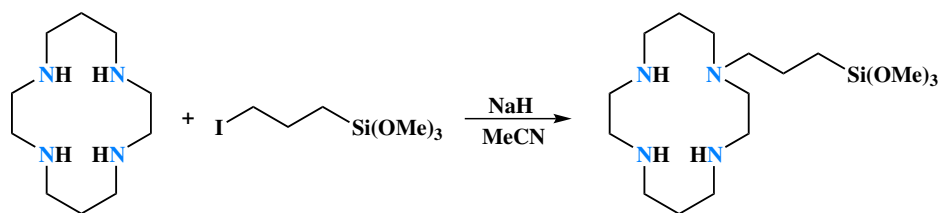


Figure 9.15: Silylation of cyclam.

The  $^1\text{H}$  NMR signals arising from the mono silylated cyclam are the most prominent ones. The  $\text{CH}_2$  group in  $\alpha$  position to the trimethoxysilyl group gives rise to a triplet at 0.48 ppm. The signal between 1.35 and 1.71 ppm stems from the  $\text{CH}_2$  groups in  $\beta$  position to the trimethoxysilyl group and the ones of the propyl bridges in  $\beta$  position to the amino groups. All signals arising from  $\text{CH}_2$  groups in  $\alpha$  position to amino groups are overlapping in the region between 2.22 and 2.70 ppm. Various signals of methoxy groups are present at about 3.4 ppm which are the main indicators for a product mixture and



multiple substitution. The mixture was used for the cyanometallate synthesis without further purification.

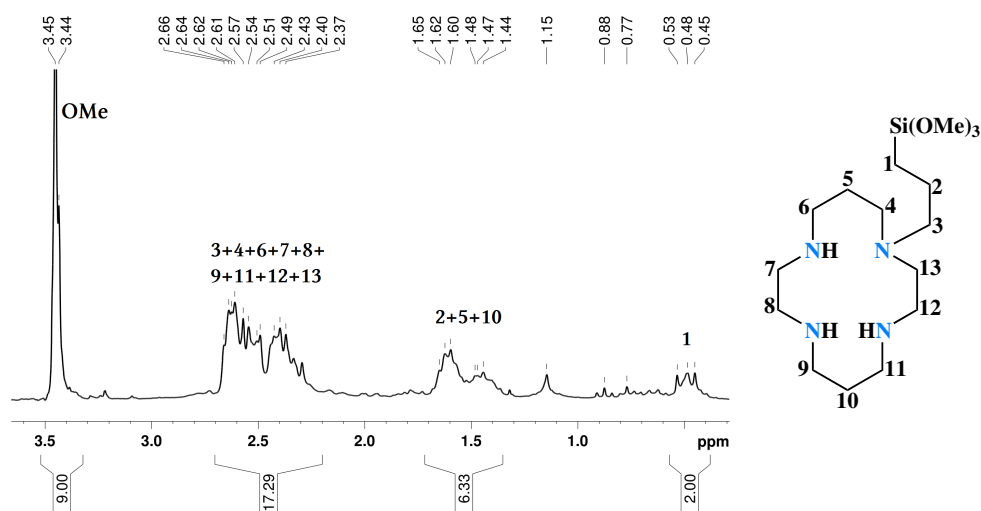


Figure 9.16:  $^1\text{H}$  NMR spectrum of silylcyclam.

### 9.1.5 $\text{Ni}^{\text{II}}\text{-Fe}^{\text{III}}$ gel

The synthesis steps to the final product,  $\text{K}[\text{Ni}(\text{silylcyclam})][\text{Fe}(\text{CN})_6]$  gel, are shown in Fig. 9.17. The formula  $\text{K}[\text{Ni}(\text{silylcyclam})][\text{Fe}(\text{CN})_6]$  gel is not a completely correct representation of the structure. The trimethoxysilyl groups of the blocking ligand react during the sol-gel process, which means it is chemically changed. Silylcyclam reacts with  $\text{NiCl}_2$  in dry MeOH to the complex  $[\text{Ni}(\text{silylcyclam})]\text{Cl}_2$  which is isolated as brown powder. Addition of  $\text{K}_3[\text{Fe}(\text{CN})_6]$  to a dry MeOH solution of  $[\text{Ni}(\text{silylcyclam})]\text{Cl}_2$  leads to rapid precipitation of the cyanometallate network as a brown powder. The cyanometallate structure embedded in  $\text{SiO}_2$  is finally obtained by sol-gel processing in basic medium ( $\text{NH}_3$ ) with TEOS as cross-linker and matrix former. Again, a bright brown powder is obtained.

## 9.2 FTIR

Each intermediate and the final product were analyzed by FTIR spectroscopy, shown in Fig. 9.18.

The FTIR spectrum of silylcyclam shows the expected absorption bands. The secondary amine functions give rise to absorption maxima at  $3201$  and  $3305\text{ cm}^{-1}$  due to NH stretching and a broad band with a maximum at  $814\text{ cm}^{-1}$  due to NH wagging. For secondary amines only one band in this region would be expected, but since the mono silylated cyclam is not fully symmetrical, more bands arise. Further, a mixture of mono, bis, tris and tetrakis substitution is assumed to be obtained by silylation with 3-iodopropyltrimethoxysilane, as explained above (Subsection 9.1.4, p. 76). This leads to multiple signals of the amino groups of the different species overlapping, which results in multiple maxima and broadened bands. The trimethoxysilyl group causes absorption maxima at  $1072$ ,

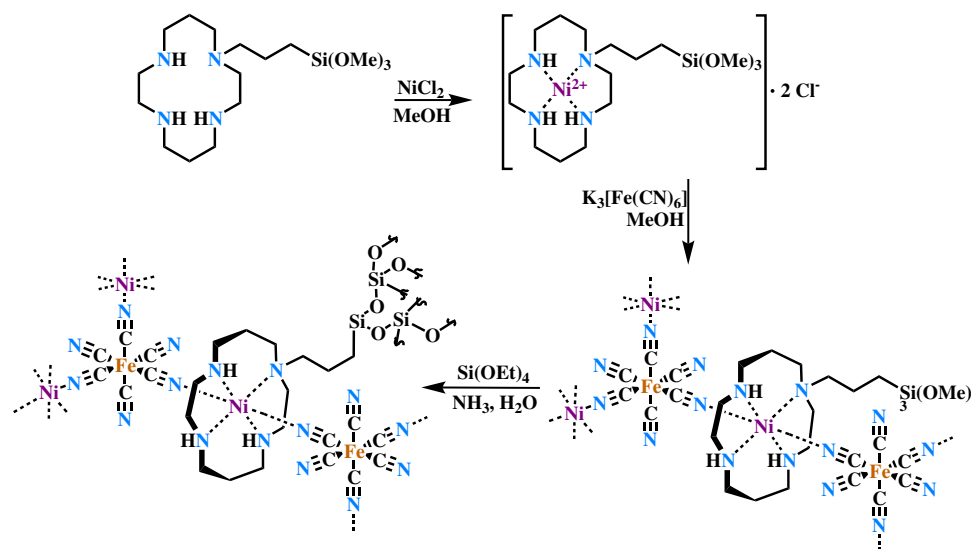


Figure 9.17: Synthesis of K[Ni(silylcyclam)][Fe(CN)<sub>6</sub>] gel.

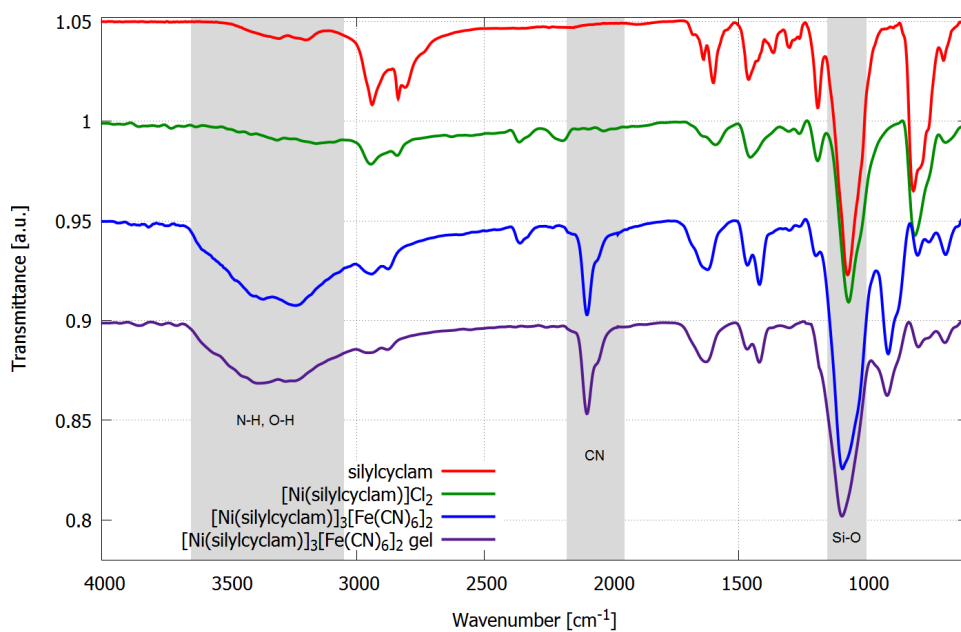


Figure 9.18: FTIR spectra of silylcyclam, [Ni(silylcyclam)]Cl<sub>2</sub>, K[Ni(silylcyclam)][Fe(CN)<sub>6</sub>] and K[Ni(silylcyclam)][Fe(CN)<sub>6</sub>] gel.

1189 and 2837 cm<sup>-1</sup> due to Si–OCH<sub>3</sub> vibrations. The characteristic vibrations of Si–CH<sub>2</sub> and C–NH are either found in the smaller bands above 1200 cm<sup>-1</sup> or hidden behind the lower Si–OCH<sub>3</sub> bands, but could not be assigned with high confidence.

Few changes occur in the FTIR spectrum upon complexation by Ni<sup>II</sup>. NH stretching seems to be greatly suppressed, but very weak signals with maxima at 3314 and 3190 cm<sup>-1</sup> can be observed. The band arising from NH wagging is also slightly shifted to 811 cm<sup>-1</sup>.

Two new overlapping bands appear in the cyanometallate network K[Ni(silylcyclam)]–[Fe(CN)<sub>6</sub>] with absorption maxima at 2054 and 2095 cm<sup>-1</sup>. These are characteristic of

the cyano group. The corresponding band in  $K_3[Fe(CN)_6]$  is at  $2116\text{ cm}^{-1}$ . The band at  $2095\text{ cm}^{-1}$  can therefore be assigned to non-bridging  $C\equiv N$  ligands that may, however, form H-bridges to MeOH present in the cyanometallate network. The additional band at  $2054\text{ cm}^{-1}$ , on the other hand, is due to bridging cyano groups. This is clear evidence, besides the precipitation and colour change of the product, for the successful network formation. Broadening of the band at  $1072\text{ cm}^{-1}$  suggests onset of condensation of the trimethoxysilyl groups.

The bands characteristic for  $Si-OCH_3$  at  $1072$ ,  $1189$  and  $2837\text{ cm}^{-1}$  have disappeared in the FTIR spectrum of  $K[Ni(\text{silylclam})][Fe(CN)_6]$  gel, the material after sol-gel processing. However, a new broad band with an absorption maximum at  $1095\text{ cm}^{-1}$  appears in the region characteristic for  $Si-O$ . It arises from the  $Si-O-Si$  entities of the amorphous  $SiO_2$  network. The fact that the FTIR spectrum otherwise remains nearly unchanged, i.e. the characteristic bands for the cyano and amino groups are still present, indicates that the cyanometallate network is retained upon sol-gel processing.

### 9.3 SEM and EDX

The SEM shown in Fig. 9.19 was recorded at a voltage of 10 kV. It proves the homogeneity of  $K[Ni(\text{silylclam})][Fe(CN)_6]$  gel. No crystallites of the cyanometallate network are discernible. This indicates that no (visible) phase separation occurs.

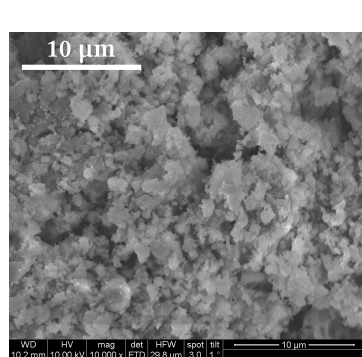


**Figure 9.19:** SEM of  $K[Ni(\text{silylclam})][Fe(CN)_6]$  gel.

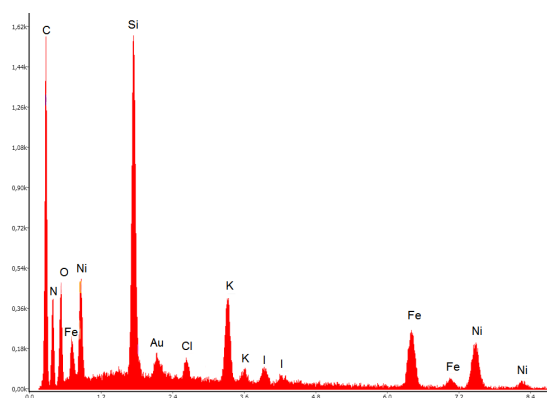


**Figure 9.20:** EDX plot (intensity vs. energy [keV]) of  $K[Ni(\text{silylclam})][Fe(CN)_6]$  gel.

EDX measurement (Fig. 9.20) confirmed a homogeneous distribution of the metals and, thus, the cyanometallate network in  $K[Ni(\text{silylclam})][Fe(CN)_6]$  gel. A Ni:Fe ratio of  $\sim 3:2.8$  was found from the atomic percentages (Tab. 9.1) obtained by quantitative analysis. This is close to a 1:1 ratio. The charge balance is kept by residual  $K^+$  ions incorporated in the cyanometallate structure. Similar metal ratios have been reported for  $PPh_4[Ni(\text{pn})_2][Fe(CN)_6] \cdot H_2O$  [203, 211, 213, 215] and  $X[Ni(C_3H_5N_5\text{-azacyclam})][Fe(CN)_6] \cdot 4 H_2O$  ( $X = NH_4^+$ ,  $Li^+$ ,  $Na^+$ ,  $K^+$ ,  $Rb^+$ ,  $Cs^+$ ) [243]. These two structures are very different, however.  $PPh_4[Ni(\text{pn})_2][Fe(CN)_6] \cdot H_2O$  is a 1D cyanometallate made up of  $Fe^{III}-C\equiv N-Ni^{II}$  zig-zag chains exhibiting ferromagnetic behavior while

**Table 9.1:** EDX analysis of  $\text{K}[\text{Ni}(\text{silylcyclam})][\text{Fe}(\text{CN})_6]$  gel.

element	at. %
C (K)	38.41
N (K)	34.67
O (K)	18.37
Si (K)	3.6
Cl (K)	0.25
K (K)	1.12
I (K)	0.2
Fe (K)	1.62
Ni (K)	1.76
Total	100

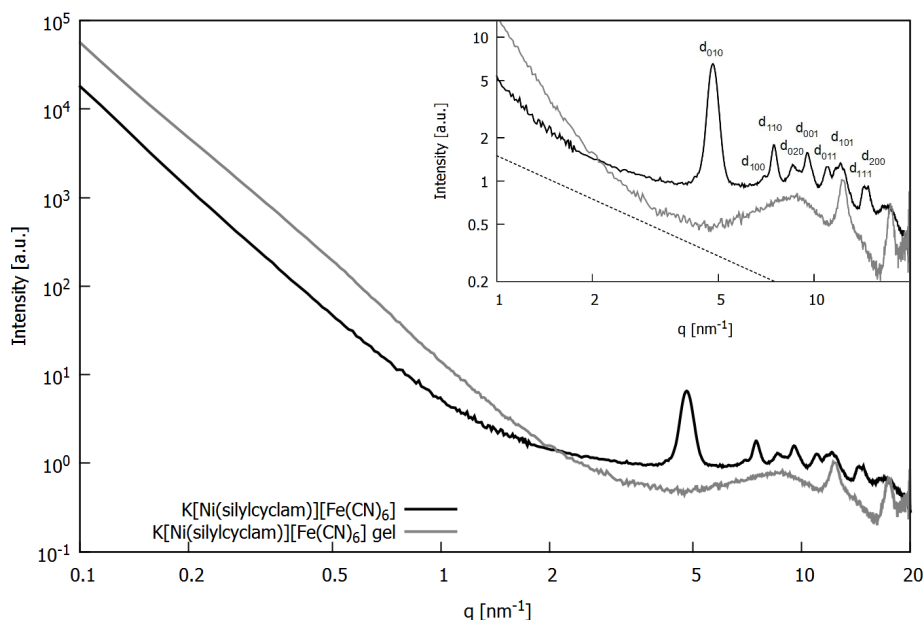
**Table 9.2:** Experimental vs. fitted reflections for orthorhombic crystal structure for  $\text{K}[\text{Ni}(\text{silylcyclam})][\text{Fe}(\text{CN})_6]$ .

peak	fit	$q_{\text{max}}$ [ $\text{nm}^{-1}$ ]
$d_{010}$	4.744	4.8
$d_{100}$	7.310	6.8
$d_{110}$	8.714	8.6
$d_{020}$	9.488	9.5
–	–	11.0
$d_{001}$	11.516	11.6
$d_{011}$	12.455	12.1
$d_{101}$	13.640	12.4
$d_{111}$	14.442	14.4
$d_{200}$	14.619	14.8

$\text{X}[\text{Ni}(\text{C}_3\text{H}_5\text{N}_5\text{-azacyclam})][\text{Fe}(\text{CN})_6] \cdot 4 \text{H}_2\text{O}$  is a 3D metamagnetic structure. Conclusions on the structure can therefore not be drawn from the metal ratios.

#### 9.4 SWAXS

SWAXS measurements of  $\text{K}[\text{Ni}(\text{silylcyclam})][\text{Fe}(\text{CN})_6]$  and  $\text{K}[\text{Ni}(\text{silylcyclam})][\text{Fe}(\text{CN})_6]$  gel were performed (Fig. 9.21). Structural changes of the cyanometallate network upon embedding in  $\text{SiO}_2$  can be determined by comparison of the two curves.

**Figure 9.21:** SWAXS measurements of  $\text{K}[\text{Ni}(\text{silylcyclam})][\text{Fe}(\text{CN})_6]$  and  $\text{K}[\text{Ni}(\text{silylcyclam})][\text{Fe}(\text{CN})_6]$  gel.

$\text{K}[\text{Ni}(\text{silylcyclam})][\text{Fe}(\text{CN})_6]$  (black curve in Fig. 9.21) exhibits distinct Bragg reflections. Tab. 9.2 shows that indexing of the reflections, labelled accordingly in the insert

of Fig. 9.21, for an orthorhombic unit cell with lattice parameters  $a = 8.6 \text{ \AA}$ ,  $b = 13.2 \text{ \AA}$  and  $c = 5.5 \text{ \AA}$  is in quite good agreement with the experimental  $q_{\text{max}}$  values. The lattice constants are similar to the values obtained for the orthorhombic structures of the  $\text{Ni}^{\text{II}}-\text{Fe}^{\text{III}}$  cyanometallates discussed above. This leads to the assumption that the structures are analogous and similar to the one described for  $[\text{Ni}(\text{en})_2]_3[\text{Fe}(\text{CN})_6]_2 \cdot n \text{ H}_2\text{O}$  by Ohba *et al.* and Herchel *et al.* [156, 206], as discussed in Sec. 5.4, p. 36. The structure is assumed to be built of 1D double chains of three  $\text{Ni}^{\text{II}}$  with two cyano bridges and one tetramine ligand and two  $\text{Fe}^{\text{III}}$  with three cyano bridges and three non-bridging cyano ligands. These 1D structures are extending along the  $c$ -axis and assembled in an orthorhombic lattice with  $\text{Ni}^{\text{II}}$  at the edges, similar to the arrangement shown in Fig. 5.8, p. 38.

Three experimental  $q_{\text{max}}$  values cannot be fitted satisfactorily with the orthorhombic model, however. A monoclinic lattice with  $a = 8.5 \text{ \AA}$ ,  $b = 5.7 \text{ \AA}$ ,  $c = 15.1 \text{ \AA}$  and  $\beta = 119.96^\circ$  gives better agreement between fit and experimental data, as shown in Tab. 9.3 and Fig. 9.22. Only the small, possibly erroneous reflection at  $6.8 \text{ nm}^{-1}$  is not represented satisfactorily by this crystal structure. The structure can still be rationalized by alignment of 1D double chains of  $\text{Fe}^{\text{III}}-\text{C}\equiv\text{N}-\text{Ni}^{\text{II}}$  bridges similar to  $[\text{Ni}(\text{en})_2]_3[\text{Fe}(\text{CN})_6]_2 \cdot n \text{ H}_2\text{O}$  and the structures discussed above. Compared to the structure reported for  $[\text{Ni}(\text{en})_2]_3[\text{Fe}(\text{CN})_6]_2 \cdot n \text{ H}_2\text{O}$ , depicted in Fig. 5.8, p. 38, the axes  $b$  and  $c$  are interchanged. The unit cell dimensions lie in a similar range, but are slightly shorter while  $\beta$  is slightly larger than the equivalent angle between the axes  $a$  and  $b$  shown in Fig. 5.8a, p. 38.

**Table 9.3:** Experimental vs. fitted reflections for monoclinic crystal structure for  $\text{K}[\text{Ni}(\text{silylcyclam})][\text{Fe}(\text{CN})_6]$ .

peak	fit	$q_{\text{max}}$ [ $\text{nm}^{-1}$ ]
$d_{001}$	4.787	4.8
$d_{101}$	7.406	6.8
$d_{100}$	8.526	8.6
$d_{102}$	9.101	–
$d_{002}$	9.574	9.5
$d_{010}$	11.111	11.0
$d_{10-1}$	11.574	11.6
$d_{011}$	12.098	12.1
$d_{103}$	12.516	12.4
$d_{003}$	14.361	14.4
$d_{012}$	14.667	14.8

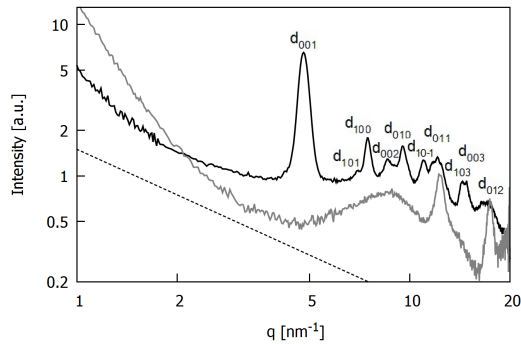


**Figure 9.22:** Reflections indexed for monoclinic crystal structure for  $\text{K}[\text{Ni}(\text{silylcyclam})][\text{Fe}(\text{CN})_6]$ .

The SWAXS curve of  $\text{K}[\text{Ni}(\text{silylcyclam})][\text{Fe}(\text{CN})_6]$  gel (gray curve in Fig. 9.21) shows three broad reflections that may arise from nano crystals of the  $\text{SiO}_2$  gel. A crystal lattice could not be fitted due to strong background signals at higher  $q$ . It is obvious, however, that the structure has changed after sol-gel processing due to shift and disappearance of the reflections. The slope of  $q^{-1}$  between 3 and  $5 \text{ nm}^{-1}$  indicated by the dashed line in the insert of Fig. 9.21 suggests elongated objects which are randomly dispersed in the silica matrix. These 1D objects are probably  $\text{Fe}^{\text{III}}-\text{C}\equiv\text{N}-\text{Ni}^{\text{II}}$  (double) chains which give rise to

the absorption band for bridging cyano group (Fig. 9.18).

## 9.5 SQUID

Field cooled (FC) and zero-field cooled (ZFC) measurements of  $\text{K}[\text{Ni}(\text{silylcyclam})][\text{Fe}(\text{CN})_6]$  gel were performed at different temperatures and external fields. The experimental results were corrected for diamagnetic contributions with the theoretical value calculated according to Pascal's method described in Subsection 12.4.5, p. 105.

Measurement of  $\chi_m$  at different temperatures and external fields (Fig. 9.23) yields curves that are a clear indication of paramagnetic behavior of the material.  $\chi_m$  is positive but small and no effects besides an increase with decreasing temperature occur as expected from Curie's law (Subsection 3.1.1, p. 22).

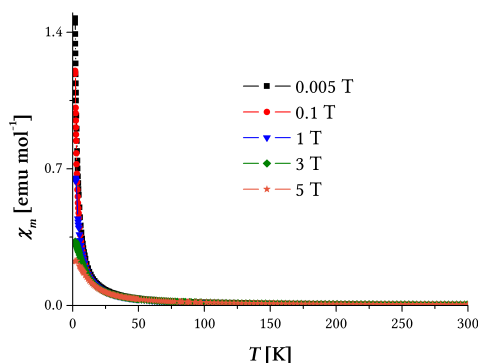


**Figure 9.23:**  $\chi_m$  vs.  $T$  of  $\text{K}[\text{Ni}(\text{silylcyclam})][\text{Fe}(\text{CN})_6]$  at various external fields.

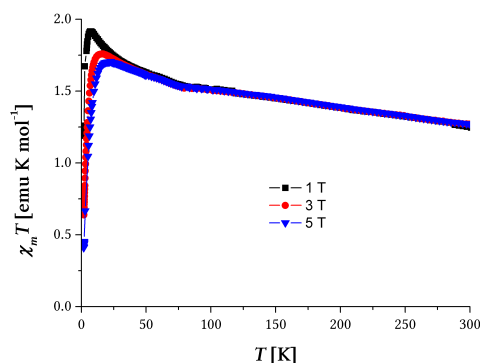


**Figure 9.24:**  $\chi_m T$  vs.  $T$  of  $\text{K}[\text{Ni}(\text{silylcyclam})][\text{Fe}(\text{CN})_6]$  at various external fields.

The Curie constant  $C$  can be calculated according to Curie's law ( $C = \chi_m \cdot T$ , Subsection 3.1.1, p. 22) from the  $\chi_m T$  vs.  $T$  plot in Fig. 9.24 by fitting a straight line with slope = 0. The average value obtained for the measurements at external fields of 1 T, 3 T and 5 T is 1.41. This gives a  $\mu_{eff}$  of  $3.36 \mu_B$ .

An alternative route to calculate  $C$  is from the slope of  $1/\chi_m$  vs.  $T$  (Fig. 9.25), which is equal to  $1/C$  ( $1/\chi_m = T/C$ ). An average for  $C$  of 1.36 is obtained by this method from the measurements at external fields of 1 T, 3 T and 5 T. The  $\mu_{eff}$ , therefore, is  $3.32 \mu_B$  ( $\mu_{eff} = 2.82787\sqrt{C}$ ).

The average  $\mu_{eff}$  is  $3.34 \mu_B$ . This is well below the spin-only value for one  $\text{Ni}^{\text{II}}$  ( $S = 1$ ,  $g = 2$ ) and one low-spin  $\text{Fe}^{\text{III}}$  ( $S = 1/2$ ,  $g = 2$ ) of  $4.56 \mu_B$ . Partial antiferromagnetic arrangement of neighboring chains/sheets of the cyanometallate structure may be the reason for the lower  $\mu_{eff}$ . Another explanation would be that not all of the metal centers couple because the structural arrangement is not favorable for exchange interactions.

The magnetization  $M$  versus external field  $\mu_0 H$  was measured at various temperatures (Fig. 9.26). The curves are characteristic of a paramagnet with a linear increase of  $M$  with the external field, following Curie's law. Deviation from linear behavior occurs only at low temperatures and high fields. This is due to saturation effects which arise because all magnetic dipoles are already aligned with the external field and an increase

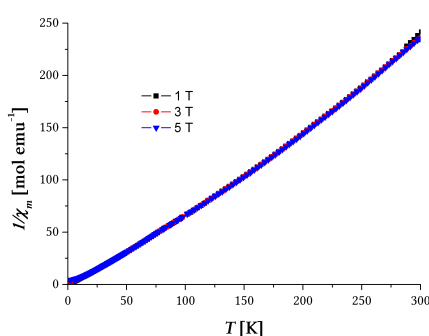


**Figure 9.25:**  $1/\chi_m$  vs.  $T$  of  $\text{K}[\text{Ni}(\text{silyl-cyclam})][\text{Fe}(\text{CN})_6]$  at various external fields.

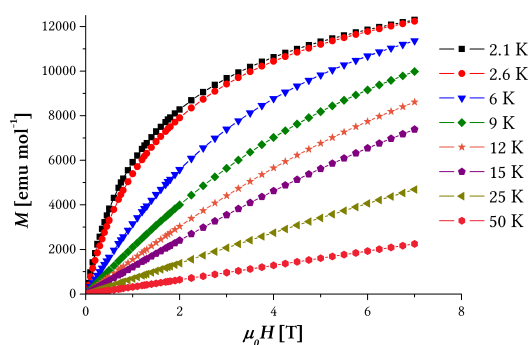


**Figure 9.26:**  $M$  vs.  $\mu_0 H$  of  $\text{K}[\text{Ni}(\text{silyl-cyclam})][\text{Fe}(\text{CN})_6]$  at various temperatures.

cannot lead to further magnetization of the sample. At 2 K the saturation magnetization of  $\text{K}[\text{Ni}(\text{silyl-cyclam})][\text{Fe}(\text{CN})_6]$  gel is nearly reached at 7 T and lies at  $\sim 12300 \text{ emu mol}^{-1}$ .

## 9.6 Conclusions

The cyclic tetramine ligand cyclam was synthesized via three routes. All of them were successful as was confirmed by NMR spectroscopy and other characterization methods, but produced rather low yields. Cyclam was subsequently modified with a propyltrimethoxysilyl pendant side chain by reaction with 3-iodopropyltrimethoxysilane. This yielded mostly mono substitution, but also some products with substitutions at several amine functions. The mixture was used as obtained for the synthesis of the  $\text{Ni}^{\text{II}}\text{-Fe}^{\text{III}}$  cyanometallate  $\text{K}[\text{Ni}(\text{silyl-cyclam})][\text{Fe}(\text{CN})_6]$  embedded in  $\text{SiO}_2$ .

The FTIR spectrum of  $\text{K}[\text{Ni}(\text{silyl-cyclam})][\text{Fe}(\text{CN})_6]$  gel showed bands for  $\text{Fe}^{\text{III}}\text{-C}\equiv\text{N-Ni}^{\text{II}}$  cyanide bridges and the condensation of the trialkoxysilyl groups during the sol-gel process. A  $\text{Ni}:\text{Fe}:\text{K}$  ratio of  $\sim 1.1:1:0.7$  was found by EDX which is close to 1:1:1, as expected due to charge balance. Structural investigation of  $\text{K}[\text{Ni}(\text{silyl-cyclam})][\text{Fe}(\text{CN})_6]$  by SWAXS showed the presence of a crystalline phase for the cyanometallate while after sol-gel processing an amorphous material with embedded 1D elongated structures was obtained. This led to the conclusion that cyanometallate structures are retained as (double) chains in the gel, but structural alignment in three dimensions is disrupted.

SQUID measurements showed that  $\text{K}[\text{Ni}(\text{silyl-cyclam})][\text{Fe}(\text{CN})_6]$  gel is a paramagnet. The susceptibility follows the Curie law. An effective magnetic moment  $\mu_{\text{eff}}$  of  $3.34 \mu_{\text{B}}$  was found which is lower than the spin-only value. This may be due to spin-orbit coupling of  $\text{Ni}^{\text{II}}$  and  $\text{Fe}^{\text{III}}$  in the cyanometallate network. The different behavior compared to ferromagnetic  $[\text{Ni}(\text{AEAPTS})_2]_3[\text{Fe}(\text{CN})_6]_2$  gel may be due to higher flexibility of the diamine ligands AEAPTS compared to the tetramine. This may enable re-adjustment of the AEAPTS containing cyanometallate network in the  $\text{SiO}_2$  matrix to still allow for ferromagnetic coupling of  $\text{Fe}^{\text{III}}$  and  $\text{Ni}^{\text{II}}$ . E.g. *cis* arrangement of the cyano bridges at  $\text{Ni}^{\text{II}}$ , which is usually structurally not favored, may occur to ease stress in the structure.

Comparison with the open tetramines discussed in Chapters 7 and 8 (p. 51 and 59) shows differences especially in the cyanometallate networks before sol-gel processing.

The 3D arrangement is related, but distinctively different, showing a monoclinic crystal lattice for the compound with silyl cyclam while for the modified 2,3,2-tetramines an orthorhombic structure was found. The ratio of Ni:Fe is also different, which supports the difference in crystal structures. The magnetic properties after sol-gel processing, however, are quite similar. The structures were found to be paramagnets, but the  $\mu_{eff}$  differs. The lower value for  $K[Ni(\text{silyl cyclam})][Fe(CN)_6]$  arises due to fewer metal centers contributing per formula unit.



## $\text{Ni}^{\text{II}}-\text{Fe}^{\text{III}}-\text{SiO}_2$ Gel with Silyl-6-aminocyclam

The N-modification of the cyclam ring in silylcyclam (Chapter 9) may have an influence on the coordination. To study this a different approach for the incorporation of the trialkoxysilyl group into the amine ligand is tried.

Cyclam can be synthesized with side chains on the carbon backbone. As shown in Fig. 10.1, a functional group may be bound directly to the C2 of a propylene bridge [267, 268]. Another strategy is the introduction of further amine groups, yielding an “azacyclam” [233–235, 243].

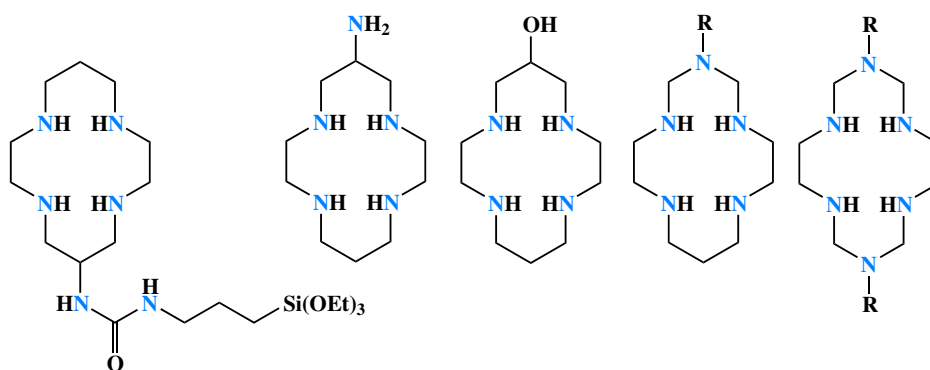


**Figure 10.1:** Structures of silyl-6-aminocyclam, 6-aminocyclam, 6-hydroxycyclam, alkylazacyclam and bisalkylazacyclam.

If the side chain carries an appropriate functional group, such as a primary or secondary amine or a hydroxyl group, modification with a trialkoxysilyl group is possible. In this chapter the results of the synthesis of silyl-6-aminocyclam, also shown in Fig. 10.1, and its use as a ligand in a  $\text{Ni}^{\text{II}}-\text{Fe}^{\text{III}}$  cyanometallate gel will be discussed.

## 10.1 Synthesis

Silyl-6-aminocyclam is synthesized as sketched in Fig. 10.2. The synthesis, as described by Kimura *et al.* [267], starts from 2,3,2-tetramine – which is obtained as described in Sec. 7.1, p. 51 – and diethyl aminomalonate hydrochloride mixed in 1:1 ratio in methanol. 6-Aminodioxocyclam is isolated as hydrochloride salt by recrystallization and transformed to the free amine by elution over an Amberlyst A26 ion exchange resin. The reduction of the keto groups [269, 270] is performed using  $\text{BH}_3 \cdot \text{THF}$  generated in-situ from  $\text{NaBH}_4$  and  $\text{I}_2$  in dry THF. The fully reduced 6-aminocyclam is isolated as hydrochloride salt after quenching excess  $\text{NaBH}_4$  and  $\text{BH}_3 \cdot \text{THF}$  with  $\text{H}_2\text{O}$  and  $\text{HCl}$  and converted to the free amine on an Amberlyst A26 ion exchange resin. For further purification the pentamine was precipitated as hydrobromide salt from ethanol and subsequently again transformed to the free amine by means of an Amberlyst A26 column. 6-Aminocyclam is thus obtained with an overall yield of 86% from 2,3,2-tetramine.

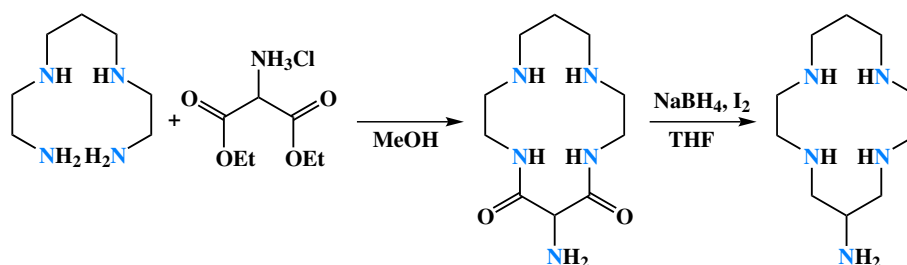


Figure 10.2: Synthesis of 6-aminocyclam.

The success of the synthesis steps was confirmed by spectroscopic techniques, especially  $^1\text{H}$  NMR spectroscopy.

The  $^1\text{H}$  NMR spectrum of 6-aminodioxocyclam is shown in Fig. 10.3. The quintet at 1.68 ppm arises from the  $\text{CH}_2$  group of the propylene bridge in  $\beta$  position to the secondary amino groups. The multiplet in the region between 2.5 and 3.0 ppm stems from the  $\text{CH}_2$  groups in  $\alpha$  position to the secondary amino groups. The  $\text{CH}_2$  groups in  $\alpha$  position to the secondary amide groups give rise to the complicated multiplets at about ~3.3 and ~3.6 ppm. The signal is split into two multiplets. The multiplet at 3.6 ppm arises from the hydrogen atoms pointing on the same side of the cyclam ring as the primary amino group while the one at 3.3 ppm stems from the ones on the opposite side. The singlet at 4.12 ppm stems from the CH group between the keto groups. The integral is only 0.60 instead of 1 because of the keto-enol resonance that results in the structures shown in Fig. 10.4. The remaining 0.4 H are bound in a hydroxyl group which is not visible in the  $^1\text{H}$  NMR spectrum due to the fast exchange of polar hydrogens in  $\text{D}_2\text{O}$ .

After reduction, the  $^1\text{H}$  NMR spectrum shows only two sets of signals, as seen in Fig. 10.5. The quintet at 1.88 ppm again arises from the  $\text{CH}_2$  group of the propylene bridge in  $\beta$  position to the secondary amino groups. All the other signals are overlapping in the region between 2.5 and 3.5 ppm. Especially the shift of the CH group indicates successful reduction to 6-aminocyclam which is confirmed by comparison with spectra from literature.

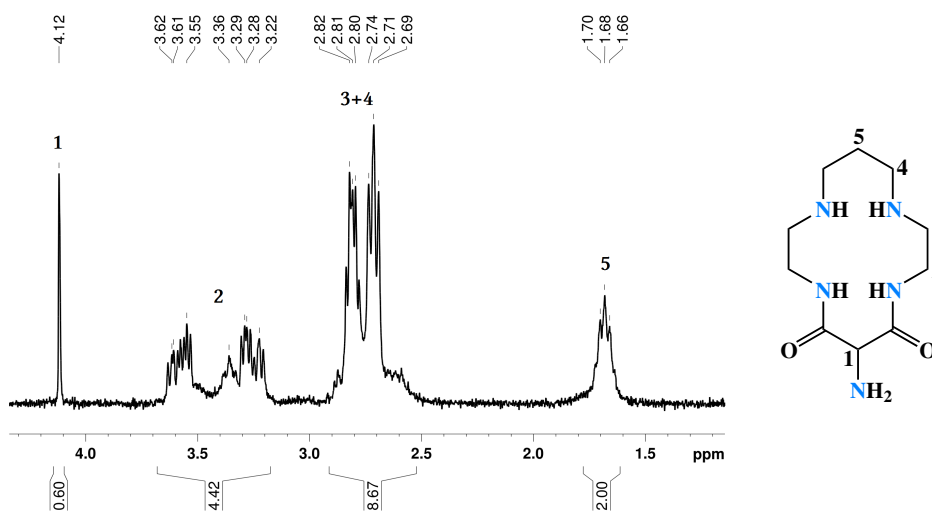
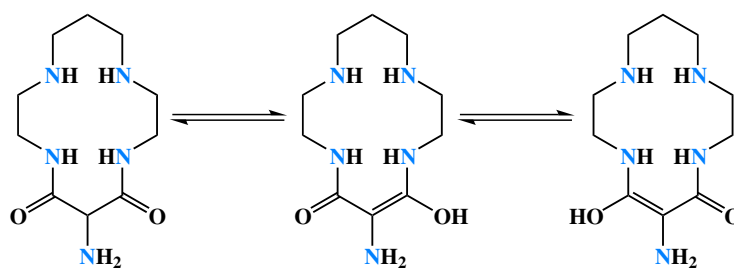
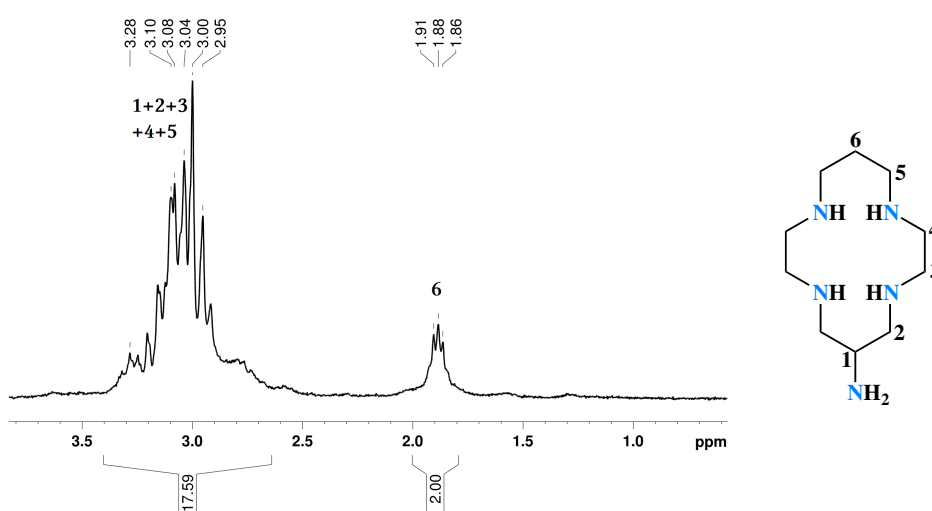
Figure 10.3:  $^1\text{H}$  NMR spectrum of 6-aminodioxocyclam.

Figure 10.4: Resonance structures of 6-aminodioxocyclam.

Figure 10.5:  $^1\text{H}$  NMR spectrum of 6-aminocyclam.

### 10.1.1 Silylation

6-Aminocyclam was modified with a trialkoxysilyl group by reaction with 3-isocyanopropyltrimethoxysilane [259, 260] in dry MeCN and pyridine as base, as shown in Fig. 10.6. The starting material 6-aminocyclam was removed by filtration and the product was isolated from the filtrate by removal of the solvent. As shown in the  $^1\text{H}$  NMR spectrum (Fig. 10.7) and discussed below, mostly mono silylated product is obtained, but some multiple silylation occurs by reaction of 3-isocyanopropyltrimethoxysilane with secondary amines of the ring backbone.

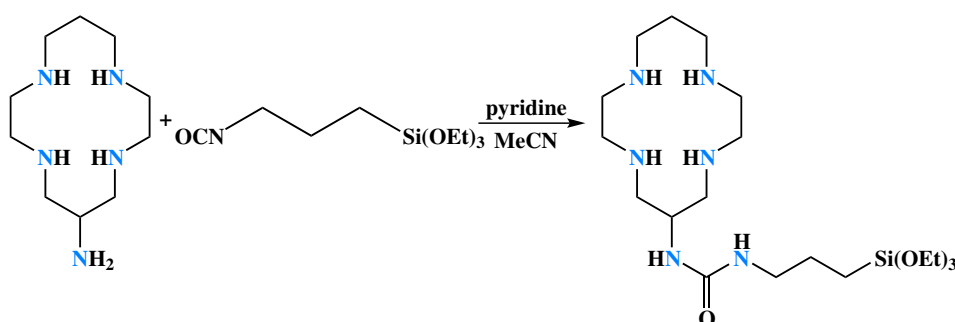


Figure 10.6: Synthesis of silyl-6-aminocyclam.

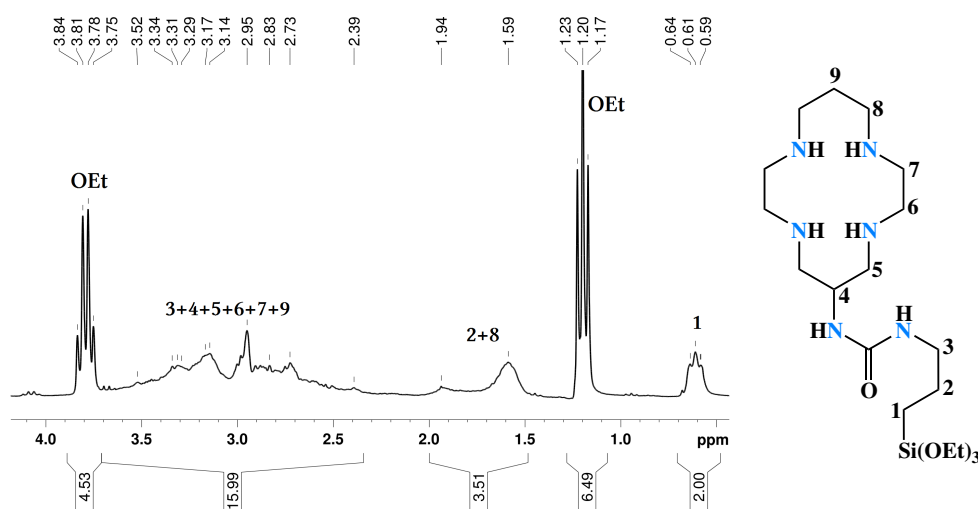


Figure 10.7:  $^1\text{H}$  NMR spectrum of silyl-6-aminocyclam.

The triplet at 0.61 ppm stems from the  $\text{CH}_2$  group in  $\alpha$  position of Si. The ethoxy groups give rise to a sharp triplet at 1.20 ppm and a quartet at 3.79 ppm. In the region between 1.48 and 2.03 ppm the multiplets of the  $\text{CH}_2$  group in  $\beta$  position of Si and the  $\text{CH}_2$  group of the propylene bridge in  $\beta$  position of the cyclam backbone amines overlap. All remaining signals of  $\text{CH}_2$  and the CH group are found in the region between 2.34 and 3.58 ppm. The presence of the signals of both the propyltriethoxysilyl chain and the cyclam backbone prove successful silylation. However, the integrals of the signals stemming from the propyltriethoxysilyl chain are a little too high. This leads to the conclusion

that partial multiple silylation occurs in which case amino groups of the cyclam backbone also react. Additional evidence is the broadened signals indicating a mixture of very similar compounds. The mixture was used for the cyanometallate synthesis without further purification.

### 10.1.2 Ni<sup>II</sup>-Fe<sup>III</sup> gel

Silyl-6-aminocyclam is employed as a ligand in a Ni<sup>II</sup>-Fe<sup>III</sup> cyanometallate network (Fig. 10.8) by first forming the complex [Ni(silyl-6-aminocyclam)]Cl<sub>2</sub> by reaction with anhydrous NiCl<sub>2</sub> in MeOH. Addition of K<sub>3</sub>[Fe(CN)<sub>6</sub>] to a dry MeOH solution of [Ni(silyl-6-aminocyclam)]Cl<sub>2</sub> leads to rapid precipitation of the cyanometallate network as a brown powder. [Ni(silyl-6-aminocyclam)]<sub>3</sub>[Fe(CN)<sub>6</sub>]<sub>2</sub> embedded in SiO<sub>2</sub> is obtained by sol-gel processing in basic medium (NH<sub>3</sub>) with TEOS as cross-linker and matrix former. The formula [Ni(silyl-6-aminocyclam)]<sub>3</sub>[Fe(CN)<sub>6</sub>]<sub>2</sub> gel is not a completely correct representation of the structure. The triethoxysilyl groups of the blocking ligand react during the sol-gel process, which means it is chemically changed.

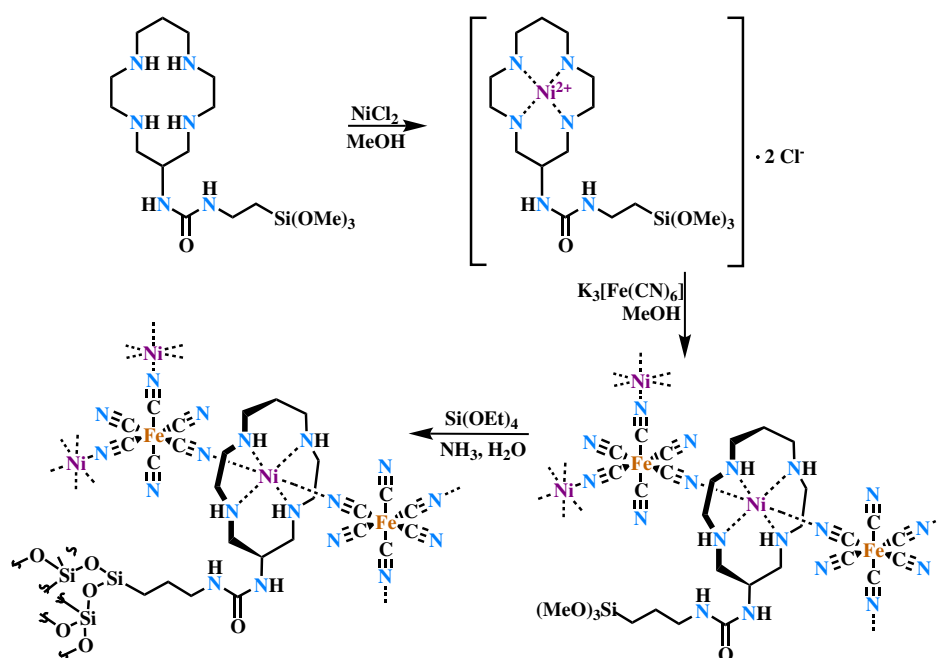
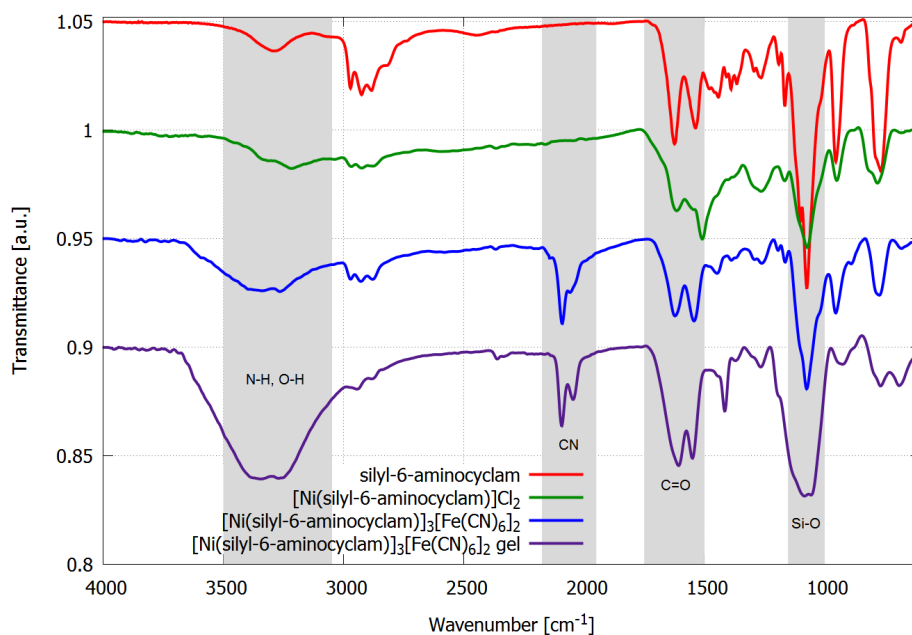


Figure 10.8: Synthesis of [Ni(silyl-6-aminocyclam)]<sub>3</sub>[Fe(CN)<sub>6</sub>]<sub>2</sub> gel.

## 10.2 FTIR

Each intermediate and the final product were analyzed by FTIR spectroscopy, shown in Fig. 10.9.

The FTIR spectrum of silyl-6-aminocyclam shows the expected absorption bands. The secondary amine functions give rise to an absorption maximum at 3294 cm<sup>-1</sup> due to NH stretching and a broad band with a maximum at 765 cm<sup>-1</sup> due to NH wagging. The band



**Figure 10.9:** FTIR spectra of silyl-6-aminocyclam,  $[\text{Ni}(\text{silyl-6-aminocyclam})]\text{Cl}_2$ ,  $[\text{Ni}(\text{silyl-6-aminocyclam})]_3[\text{Fe}(\text{CN})_6]_2$  and  $[\text{Ni}(\text{silyl-6-aminocyclam})]_3[\text{Fe}(\text{CN})_6]_2$  gel.

arising from the amide groups is overlapped by the broad band from the amino groups. The strong band with a maximum at  $1624\text{ cm}^{-1}$  is characteristic for the carbonyl group of an amide. The triethoxysilyl group causes absorption maxima at  $953$ ,  $1073$ ,  $1101$ ,  $1165$  and  $1190\text{ cm}^{-1}$ . The characteristic vibrations of  $\text{Si-CH}_2$  and  $\text{C-NH}$  are either found in the smaller bands above  $1200\text{ cm}^{-1}$  or hidden behind the  $\text{Si-OCH}_2\text{CH}_3$  bands at lower wavenumbers, but could not be assigned with satisfying confidence.

A few changes occur in the FTIR spectrum upon complexation by  $\text{Ni}^{\text{II}}$ . The maximum corresponding to NH stretching is shifted to  $3216\text{ cm}^{-1}$  and an additional band from coordinated MeOH arises in this region. The band arising from NH wagging is also slightly shifted to  $780\text{ cm}^{-1}$ . The carbonyl band is also still present. In the Si–O region the doublet is blurred into a broad band with a minimum at  $1072\text{ cm}^{-1}$ , but the small bands at  $951$  and  $1165\text{ cm}^{-1}$  prove that the compound has not gelled.

Two new overlapping bands with absorption maxima at  $2059$  and  $2091\text{ cm}^{-1}$  appear in the cyanometallate network  $[\text{Ni}(\text{silyl-6-aminocyclam})]_3[\text{Fe}(\text{CN})_6]_2$ . These are characteristic of the cyano group. The corresponding band in  $\text{K}_3[\text{Fe}(\text{CN})_6]$  is at  $2116\text{ cm}^{-1}$ . The band at  $2091\text{ cm}^{-1}$  can therefore be assigned to non-bridging  $\text{C}\equiv\text{N}$  ligands that may, however, form H-bridges to MeOH present in the cyanometallate network. The additional band at  $2059\text{ cm}^{-1}$ , on the other hand, is due to bridging cyano groups. This is clear evidence, besides the precipitation and colour change of the product, for the successful network formation. The bands arising from the amino, amido and triethoxysilyl groups are partially shifted, but still present.

The bands characteristic for  $\text{Si-OCH}_2\text{CH}_3$  at  $953$ ,  $1073$ ,  $1101$ ,  $1165$  and  $1190\text{ cm}^{-1}$  have disappeared in the FTIR spectrum of  $[\text{Ni}(\text{silyl-6-aminocyclam})]_3[\text{Fe}(\text{CN})_6]_2$  gel, the mate-

rial after sol-gel processing. However, a broad band with two absorption maxima at 1056 and 1083  $\text{cm}^{-1}$  appears in the region characteristic for Si–O. It arises from the Si–O–Si entities of the amorphous  $\text{SiO}_2$  network. The fact that the FTIR spectrum otherwise remains nearly unchanged, i.e. the characteristic bands for the cyano, amino and amido groups are still present, indicates that the cyanometallate network is retained upon sol-gel processing.

### 10.3 SEM and EDX

The SEM shown in Fig. 10.10 was recorded at a voltage of 10 kV. It proves the homogeneity of  $[\text{Ni}(\text{silyl-6-aminocyclam})]_3[\text{Fe}(\text{CN})_6]_2$  gel. No crystallites of the cyanometallate network are discernible. This indicates that no (visible) phase separation occurs.

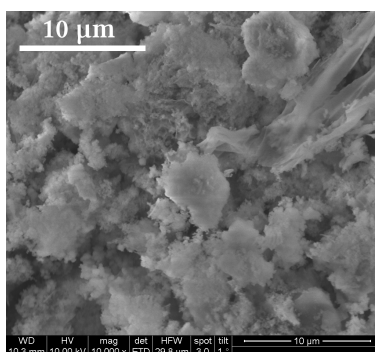


**Figure 10.10:** SEM of  $[\text{Ni}(\text{silyl-6-aminocyclam})]_3[\text{Fe}(\text{CN})_6]_2$  gel.

EDX measurement (Fig. 10.11) confirmed a homogeneous distribution of the metals and, thus, the cyanometallate network in  $[\text{Ni}(\text{silyl-6-aminocyclam})]_3[\text{Fe}(\text{CN})_6]_2$  gel. A Ni:Fe ratio of  $\sim 3:2.1$  was found from the atomic percentages (Tab. 10.1) obtained by quantitative analysis. This corresponds quite well to the metal ratio used for the preparation of  $[\text{Ni}(\text{silyl-6-aminocyclam})]_3[\text{Fe}(\text{CN})_6]_2$  and is expected for a cyanometallate of  $\text{Ni}^{\text{II}}$  and  $\text{Fe}^{\text{III}}$  due to charge balance. The small excess of iron is compensated by  $\text{K}^+$  ions. Unreacted  $\text{K}_3[\text{Fe}(\text{CN})_6]$  may be excluded as the source since in the FTIR spectrum (Fig. 10.9) shows no residual band at 2116  $\text{cm}^{-1}$ . Presence of  $[\text{Fe}(\text{CN})_6]^{3-}$  with less than three bridging cyano groups is assumed instead.

### 10.4 SWAXS

SWAXS measurements of  $[\text{Ni}(\text{silyl-6-aminocyclam})]_3[\text{Fe}(\text{CN})_6]_2$  and  $[\text{Ni}(\text{silyl-6-aminocyclam})]_3[\text{Fe}(\text{CN})_6]_2$  gel were performed (Fig. 10.12). Structural changes of the cyanometallate network upon embedding in  $\text{SiO}_2$  can be determined by comparison of the two curves.

$[\text{Ni}(\text{silyl-6-aminocyclam})]_3[\text{Fe}(\text{CN})_6]_2$  (black curve in Fig. 10.12) exhibits Bragg reflections arising from the crystalline  $\text{Ni}^{\text{II}}/\text{Fe}^{\text{III}}$  cyanometallate. A satisfactory crystal structure fit could not be performed as the crystallinity seems to be less pronounced than for the previously discussed structures (Chap. 5–9, 67). The worse crystalline order may be due

**Table 10.1:** EDX analysis of  $[\text{Ni}(\text{silyl-6-aminocyclam})]_3[\text{Fe}(\text{CN})_6]_2$  gel.

element	at. %
C (K)	38.77
N (K)	31.99
O (K)	19.77
Si (K)	5.31
K (K)	0.61
Fe (K)	1.47
Ni (K)	2.08
Total	100

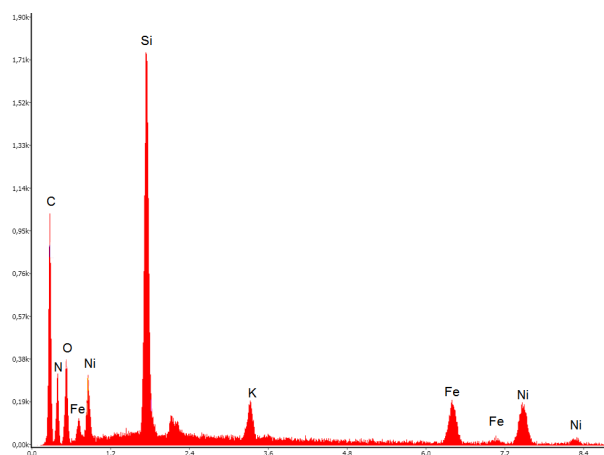


**Figure 10.11:** EDX plot (intensity vs. energy [keV]) of  $[\text{Ni}(\text{silyl-6-aminocyclam})]_3[\text{Fe}(\text{CN})_6]_2$  gel.

to the significantly longer side chain and/or the additional amine functions of the blocking ligand that may additionally coordinate to  $\text{Ni}^{\text{II}}$  or solvent molecules. Between 5 and  $15 \text{ nm}^{-1}$  a drop of the curve with  $q^{-1}$ , indicated by the dashed line in the insert of Fig. 10.12, is superimposed by the Bragg reflections. This suggests the presence of elongated objects in the material.

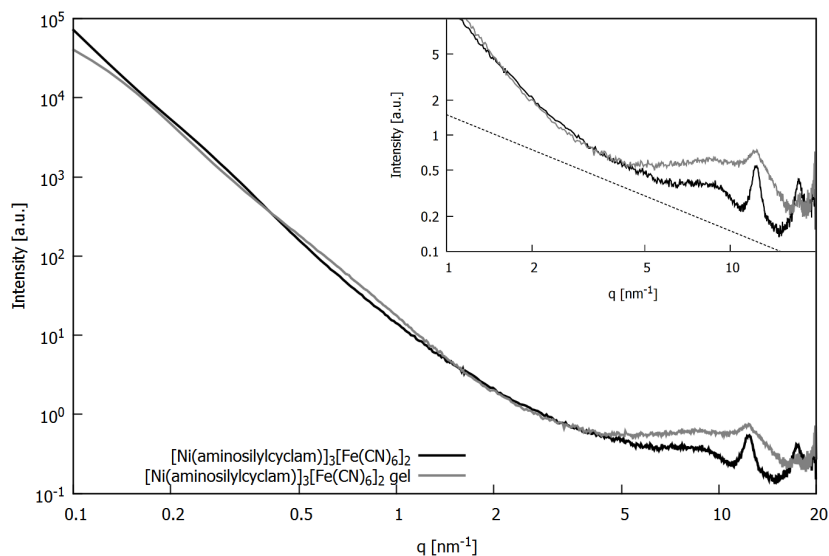


**Figure 10.12:** SWAXS measurements of  $[\text{Ni}(\text{silyl-6-aminocyclam})]_3[\text{Fe}(\text{CN})_6]_2$  and  $[\text{Ni}(\text{silyl-6-aminocyclam})]_3[\text{Fe}(\text{CN})_6]_2$  gel.

The SWAXS curve of  $[\text{Ni}(\text{silyl-6-aminocyclam})]_3[\text{Fe}(\text{CN})_6]_2$  gel (gray curve in Fig. 10.12) shows no distinctive reflections, although one at  $\sim 12 \text{ nm}^{-1}$  overlain by a broad signal is discernible. This means that the weak 3D crystalline order that was present in the cyanometallate is mostly destroyed after sol-gel processing. The fact that the broad peak arises in the same position as in the cyanometallate before sol-gel processing indicates, however, that some order is retained. Determining whether the



slope of  $q$  stays the same ( $q^{-1}$ ) between 5 and 15  $\text{nm}^{-1}$  is not possible as a big bump is present in this range. This means that the preservation of the cyanometallate structure may only be concluded from the FTIR spectrum shown in Fig. 10.9 due to the presence of bridging and non-bridging cyano groups.

## 10.5 SQUID

Field cooled (FC) and zero-field cooled (ZFC) measurements of  $[\text{Ni}(\text{silyl-6-aminocyclam})]_3[\text{Fe}(\text{CN})_6]_2$  gel were performed at different temperatures and external fields. The experimental results were corrected for diamagnetic contributions with the theoretical value calculated according to Pascal's method described in Subsection 12.4.5, p. 105.

Measurement of  $\chi_m$  at different temperatures and external fields (Fig. 10.13) yields curves that are a clear indication of paramagnetic behavior of the material.  $\chi_m$  is positive but small and no effects besides an increase with decreasing temperature occur as expected from Curie's law (Subsection 3.1.1, p. 22).

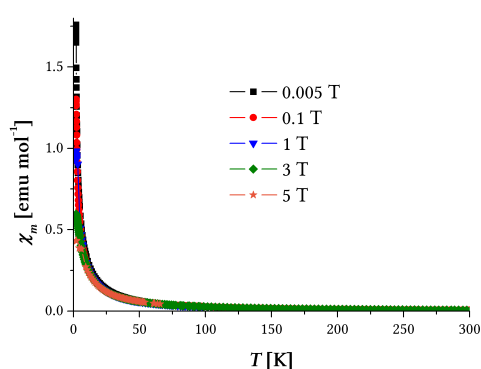


**Figure 10.13:**  $\chi_m$  vs.  $T$  of  $[\text{Ni}(\text{silyl-6-aminocyclam})]_3[\text{Fe}(\text{CN})_6]_2$  gel at various external fields.

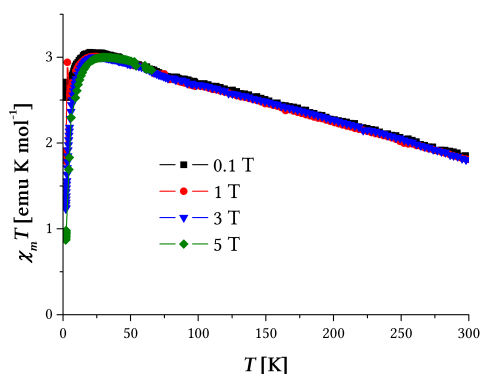


**Figure 10.14:**  $\chi_m T$  vs.  $T$  of  $[\text{Ni}(\text{silyl-6-aminocyclam})]_3[\text{Fe}(\text{CN})_6]_2$  gel at various external fields.

The Curie constant  $C$  can be calculated according to Curie's law ( $C = \chi_m \cdot T$ , Subsection 3.1.1, p. 22) from the  $\chi_m T$  vs.  $T$  plot in Fig. 10.14 by fitting a straight line with slope = 0. The average value obtained for the measurements at external fields of 0.1 T, 1 T and 3 T is 2.33. This gives a  $\mu_{eff}$  of 4.32  $\mu_B$  ( $\mu_{eff} = 2.82787\sqrt{C}$ ).

An alternative route to calculate  $C$  is from the slope of  $1/\chi_m$  vs.  $T$  (Fig. 10.15), which is equal to  $1/C$  ( $1/\chi_m = T/C$ ). An average for  $C$  of 2.14 is obtained by this method from the measurements at external fields of 0.1 T, 1 T and 3 T. The  $\mu_{eff}$  is therefore 4.14  $\mu_B$ .

The average  $\mu_{eff}$  is 4.23  $\mu_B$ . This is well below the spin-only value for three  $\text{Ni}^{\text{II}}$  ( $S = 1$ ,  $g = 2$ ) and two low-spin  $\text{Fe}^{\text{III}}$  ( $S = 1/2$ ,  $g = 2$ ) of 8.94  $\mu_B$ . Partial antiferromagnetic arrangement of neighboring chains/sheets of the cyanometallate structure may be the reason for the lower  $\mu_{eff}$ . Another explanation would be that not all of the metal centers couple because the structural arrangement is not favorable for exchange interactions.

The magnetization  $M$  versus external field  $\mu_0 H$  was measured at various temperatures (Fig. 10.16). The curves are characteristic of a paramagnet with a linear increase of  $M$  with

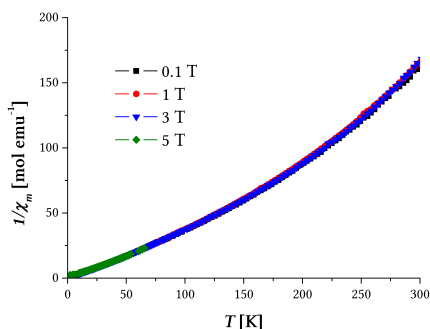


**Figure 10.15:**  $1/\chi_m$  vs.  $T$  of  $[\text{Ni}(\text{silyl-6-aminocyclam})]_3[\text{Fe}(\text{CN})_6]_2$  gel at various external fields.

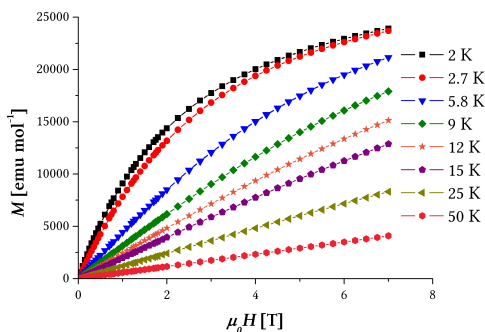


**Figure 10.16:**  $M$  vs.  $\mu_0 H$  of  $[\text{Ni}(\text{silyl-6-aminocyclam})]_3[\text{Fe}(\text{CN})_6]_2$  gel at various temperatures.

the external field, following Curie's law. Deviation from linear behavior occurs only at low temperatures and high fields. This is due to saturation effects which arise because all magnetic dipoles are already aligned with the external field and an increase cannot lead to further magnetization of the sample. At 2 K the saturation magnetization of  $[\text{Ni}(\text{silyl-6-aminocyclam})]_3[\text{Fe}(\text{CN})_6]_2$  gel is nearly reached at 7 T and lies at  $\sim 24,000$  emu mol<sup>-1</sup>.

## 10.6 Conclusions

The cyclic tetramine ligand 6-aminocyclam was synthesized by a two-step route from 2,3,2-tetramine with a yield of 86%. It was subsequently modified by reaction with 3-isocyanopropyltrimethoxysilane. This yielded mostly mono substitution at the primary amine, but also some products with substitutions at several amine functions. The mixture was used as obtained for the synthesis of the Ni<sup>II</sup>–Fe<sup>III</sup> cyanometallate  $[\text{Ni}(\text{silyl-6-aminocyclam})]_3[\text{Fe}(\text{CN})_6]_2$  embedded in SiO<sub>2</sub>.

The FTIR spectrum of  $[\text{Ni}(\text{silyl-6-aminocyclam})]_3[\text{Fe}(\text{CN})_6]_2$  gel shows bands for Fe<sup>III</sup>–C≡N–Ni<sup>II</sup> cyanide bridges and the condensation of the trialkoxysilyl groups during the sol-gel process. A Ni:Fe ratio of  $\sim 3:2.1$  is found by EDX which is close to 3:2, expected due to charge balance. Structural investigation by SWAXS shows presence of a crystalline phase and 1D elongated structures in a  $[\text{Ni}(\text{silyl-6-aminocyclam})]_3[\text{Fe}(\text{CN})_6]_2$  sample. After sol-gel processing the material is mostly amorphous, but some order is probably retained giving rise to a broad peak in the SWAXS curve. As the FTIR spectrum clearly shows characteristic bands for bridging cyano groups, at least part of the cyanometallate structure is retained in the gel.

SQUID measurements show that  $[\text{Ni}(\text{silyl-6-aminocyclam})]_3[\text{Fe}(\text{CN})_6]_2$  gel is a paramagnet. The susceptibility follows the Curie law. An effective magnetic moment  $\mu_{eff}$  of 4.23  $\mu_B$  is found which is lower than the spin-only value. This may be due to spin-orbit coupling of Ni<sup>II</sup> and Fe<sup>III</sup> in the cyanometallate network. The different behavior compared to ferromagnetic  $[\text{Ni}(\text{AEAPTS})_2]_3[\text{Fe}(\text{CN})_6]_2$  gel may be due to higher flexibility of the diamine ligands AEAPTS compared to the tetramine. This may enable re-adjustment of the AEAPTS containing cyanometallate network in the SiO<sub>2</sub> matrix to still allow for

ferromagnetic coupling of Fe<sup>III</sup> and Ni<sup>II</sup>. E.g. *cis* arrangement of the cyano bridges at Ni<sup>II</sup>, which is usually structurally not favored, may occur to ease stress in the structure.

Comparison with the material with silylcyclam as blocking ligand (Chapter 9, p. 67) indicates that the larger side chain or the additional amino group that may also coordinate to Ni<sup>II</sup> influence the structure. Good crystalline order was not found in [Ni(silyl-6-amino-cyclam)]<sub>3</sub>[Fe(CN)<sub>6</sub>]<sub>2</sub> as opposed to K[Ni(silylcyclam)][Fe(CN)<sub>6</sub>]. The metal ion ratio suggests similarity to the structures obtained with modified 2,3,2-tetramine (Chap. 7 and 8), but the  $\mu_{eff}$  is rather low and closer to the value found for the material incorporating silylcyclam. The  $\mu_{eff}$  may be lower due to the worse crystal order of the cyanometallate, indicated by the SWAXS measurements.



## Summary and Conclusion

In this work the influence of embedding  $\text{Ni}^{\text{II}}\text{-Fe}^{\text{III}}$  cyanometalltes in a sol-gel  $\text{SiO}_2$  matrix on the structure and magnetic properties was studied. Five structures with different blocking ligands at  $\text{Ni}^{\text{II}}$  were synthesized and characterized. The employed polyamine blocking ligands are shown in Fig. 11.1.

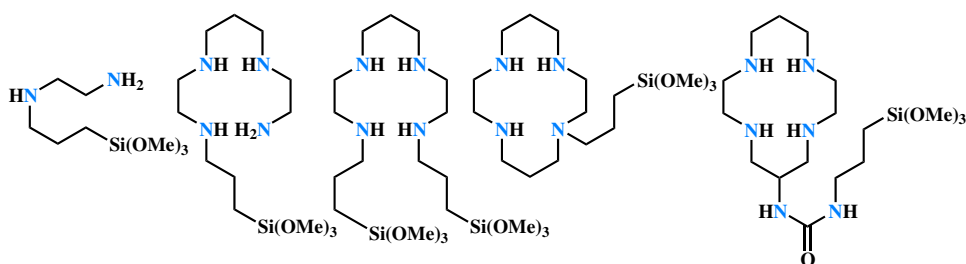


**Figure 11.1:** AEAPTS (“silyl-ethylenediamine”), silyl-2,3,2-tetramine, bissilyl-2,3,2-tetramine, silylcyclam and silyl-6-aminocyclam.

The materials were characterized regarding their structure by FTIR spectroscopy, SEM, EDX and SWAXS, and the magnetic properties determined by SQUID measurements. A summary of the results is given in Tab. 11.1.

**Table 11.1:** Summary of  $\text{Ni}^{\text{II}}\text{-Fe}^{\text{III}}$  cyanometallates in this work.

	structure	magn.	$\mu_{eff}$	$T_C$
$[\text{Ni}(\text{AEAPTS})_2]_3[\text{Fe}(\text{CN})_6]_2$ gel	1D	ferro	4.46; 8.60 <sup>a</sup>	10.6
$[\text{Ni}(\text{silyl-2,3,2-tetramine})_2]_3[\text{Fe}(\text{CN})_6]_2$ gel	1D	para	5.40	–
$[\text{Ni}(\text{bissilyl-2,3,2-tetramine})_2]_3[\text{Fe}(\text{CN})_6]_2$ gel	1D	para	6.81	–
$\text{K}[\text{Ni}(\text{silylcyclam})][\text{Fe}(\text{CN})_6]$ gel	1D	para	3.34	–
$[\text{Ni}(\text{silyl-6-aminocyclam})_2]_3[\text{Fe}(\text{CN})_6]_2$ gel	(1D)	para	4.23	–

<sup>a</sup> first value at room temperature, second value at maximum below  $T_C$

The FTIR spectra of the cyanometallates before and after embedding in  $\text{SiO}_2$  typically showed two bands in the region characteristic of cyano groups. The bands at higher

wavenumbers (2090–2115  $\text{cm}^{-1}$ ) were assigned to non-bridging cyano groups, and the bands with the maximum at lower wavenumbers (2035–2060  $\text{cm}^{-1}$ ) to cyano groups of  $\text{Ni}^{\text{II}}-\text{C}\equiv\text{N}-\text{Fe}^{\text{III}}$  bridges. This is primary evidence of the formation of a cyanometallate network. The presence of the blocking ligand in the cyanometallate is affirmed by the bands characteristic of amino groups and comparison to the spectra of the ligands.

SEM showed the homogeneity of the materials. No phase separation of cyanometallate and  $\text{SiO}_2$  was found for any of the materials at 5000 or 10000-fold magnification.

The metal ratios in the materials were determined by quantitative EDX analysis. For most cyanometallates in  $\text{SiO}_2$  a Ni:Fe ratio of 3:2 was found, as expected for charge balance. In such systems each  $[\text{Fe}(\text{CN})_6]^{3-}$  has three bridging and three non-bridging cyano groups, while every  $\text{Ni}^{\text{II}}$  is coordinated by two cyano groups and four amino groups of the blocking ligand(s). The material with silyl cyclam, however, had a Ni:Fe ratio of 1:1. Charge balance is kept in this case by  $\text{K}^+$  incorporated in the structure, which was found in a nearly equivalent atomic percentage. In this case each  $[\text{Fe}(\text{CN})_6]^{3-}$  has two bridging and four non-bridging cyano groups, while  $\text{Ni}^{\text{II}}$  is coordinated as described above. The  $\text{K}^+$  ions act as counterions, but are not covalently attached to the cyanometallate.

Structural changes occurring during sol-gel processing were studied by SWAXS measurements before and after embedding in  $\text{SiO}_2$ . The cyanometallates before embedding typically showed distinct Bragg reflections indicating high crystallinity. The reflections disappeared after sol-gel processing, but a slope of  $q^{-1}$  was typically found in the region 2–7  $\text{nm}^{-1}$  indicating the presence of elongated 1D objects. These were rationalized by isolated (double) chain-like structures of the cyanometallates built by cyanide bridges. This disruption is illustrated in the sketch shown in Fig. 11.2.

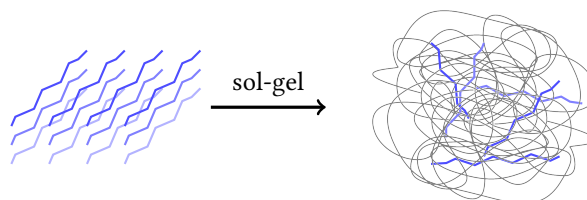


**Figure 11.2:** Cross-linking and embedding of isolated 1D cyanometallates by sol-gel  $\text{SiO}_2$ .

Fitting the reflections observed before sol-gel processing gave an orthorhombic lattice for the cyanometallates with AEAPTS, silyl-2,3,2-tetramine and bissilyl-2,3,2-tetramine. An arrangement of 1D double chains similar to  $[\text{Ni}(\text{en})_2]_3[\text{Fe}(\text{CN})_6]_2 \cdot n \text{H}_2\text{O}$  [156, 206] was assumed.  $\text{K}[\text{Ni}(\text{silyl cyclam})][\text{Fe}(\text{CN})_6]$  could be fitted with a monoclinic lattice with similar lattice constants as the structures discussed above. An alignment of double chains in this lattice was assumed. The cyanometallate with silyl-6-aminocyclam as blocking ligand, however, showed fewer and less pronounced reflections, preventing the determination of a unit cell. The characteristic band for bridging cyano groups in the FTIR spectrum, however, proved the formation of the cyanide network. Periodic alignment may be disturbed by the large side chain of the blocking ligand. The embedded cyanometallate was assumed to behave similarly to the ones described above with isolated (double) chains

immersed in SiO<sub>2</sub> due to the slope of  $q^{-1}$  of the SWAXS curve after sol-gel processing.

The magnetic properties of the materials were studied by SQUID measurements at various temperatures and external fields. Four of the five studied Ni<sup>II</sup>-Fe<sup>III</sup> cyanometallates embedded in SiO<sub>2</sub> were found to be paramagnetic at least down to 2 K, while the material with AEAPTS as ligand showed magnetic order below 22 K. This material also showed a narrow hysteresis at low temperatures and a positive  $T_C$ , indicating ferromagnetic order. The difference in magnetic behavior was suspected to arise from the higher flexibility of the AEAPTS diamine ligands that enables rearrangement of the structure to allow for ferromagnetic coupling of Ni<sup>II</sup> and Fe<sup>III</sup>.

In conclusion, the influence of the modifications and procedures employed in this work on the cyanometallate structure and its properties were significant. The introduction of alkyl side chains with trialkoxysilyl groups affected the cyanometallate structure and led to a preference of 1D arrangements that order in parallel in the crystal lattice. This 3D order was disrupted during sol-gel processing, but isolated (double) chains of the cyanometallate were preserved. Weaker magnetic coupling resulted from this disorder which led to a lowering of  $\mu_{eff}$  for AEAPTS, or loss of magnetic order altogether for the tetramine ligands.

A material containing a Cu<sup>II</sup>-Fe<sup>III</sup> cyanometallate embedded in SiO<sub>2</sub> was synthesized with AEAPTS as blocking ligand to study the influence of the metal ions on the structure and magnetic behavior. The synthesis and characterization was performed analogously to the Ni<sup>II</sup>-Fe<sup>III</sup> materials. The FTIR spectra of the cyanometallate before and after embedding showed one broad band with a maximum at 2043 cm<sup>-1</sup> and a small shoulder at 2113 cm<sup>-1</sup>, representing bridging and non-bridging cyano groups, respectively. SEM again showed no phase separation and by EDX a Cu:Ni ratio of 3:2 was found, which confirmed analogy of the [Cu(AEAPTS)<sub>2</sub>]<sub>3</sub>[Fe(CN)<sub>6</sub>]<sub>2</sub> gel to the corresponding Ni<sup>II</sup> compound. Structural analysis by SWAXS confirmed high crystallinity of the cyanometallate before sol-gel processing, but multiple crystal phases were present and fitting of the Bragg reflections was not possible. A slope of the curve of  $q^{-1}$  between 2 and 5 nm<sup>-1</sup> after embedding again indicated 1D elongated objects dispersed in the material, which were rationalized as isolated (double) chains of the cyanometallate network analogous to the Ni<sup>II</sup> materials discussed above. SQUID measurements at various temperatures and external fields showed paramagnetic behavior of the material. The different behavior compared to the analogous [Ni(AEAPTS)<sub>2</sub>]<sub>3</sub>[Fe(CN)<sub>6</sub>]<sub>2</sub>, which showed magnetic order below 22 K, was expected due to Cu<sup>II</sup> being a d<sup>9</sup> ion. Only one unpaired electron can couple with the unpaired electron of low-spin Fe<sup>III</sup> which results in weaker interaction and, ultimately, the absence of (ferro)magnetic order.





## **Part III**

# **Experimental**



# Materials and Methods

## 12.1 Materials

The chemicals employed in the syntheses were obtained from commercial suppliers (Sigma Aldrich, ABCR, Acros, Alfa Aesar, Fluka, merck) in standard reagent grade and used without further purification.

Experiments requiring inert atmosphere were performed by standard Schlenk techniques. Solvents were purified and dried for this purpose by conventional methods [271] and stored under argon over molecular sieve (3 or 4 Å). MeOH, THF and toluene were dried by means of a PureSolv commercial apparatus applying dynamic drying with molecular sieve.

## 12.2 Nuclear Magnetic Resonance (NMR)

$^1\text{H}$  and  $^{13}\text{C}$  NMR solution spectra were recorded on a Bruker AVANCE 250 spectrometer ( $^1\text{H}$  250.13 MHz,  $^{13}\text{C}$  62.86 MHz) equipped with a 5 mm inverse-broadband probe head and a z-gradient unit. Samples were typically dissolved in ~0.5 mL deuterated solvent. Interpretation of the obtained spectra was carried out using Bruker TopSpin 2.1 software.

## 12.3 Fourier Transform Infrared Spectroscopy (FTIR)

FTIR spectra were recorded on a Bruker Tensor 27 spectrometer operated through OPUS 4.0 software. Powder samples were measured under ambient conditions from 4000–600  $\text{cm}^{-1}$  on a diamond ATR unit. 32 scans of the background and subsequently 32 scans of the sample were typically performed at a resolution of 4  $\text{cm}^{-1}$ .

## 12.4 Superconducting Quantum Interference Device (SQUID)

The SQUID is the most sensitive magnetic sensor known and is therefore widely used in research and industry. Resolutions of up to some femto Tesla ( $10^{-15}$  T, fT) may be reached. The SQUID magnetometer exploits two phenomena: flux quantization in superconductors and the Josephson effect, which will be described in the following. [272–274]

### 12.4.1 Flux quantization in superconductors

Superconductivity is a thermodynamic state of a material that is characterized by the formation of “Cooper pairs”. These are pairs of conduction electrons with opposite momentum and spin which carry electric current without loss. At absolute zero all electrons are paired, while at higher temperature pair breaking due to thermal excitations occurs. This leads to the formation of “quasi-particles” of lone electrons. At a critical temperature  $T_c$ , finally, all Cooper pairs are broken and superconductivity is lost. [272–274]

In a closed superconducting loop the flux is quantized as all Cooper pairs have the same phase [275]. This changes when an external field is applied and a phase shift of  $2\pi n$  ( $n \dots$  number of flux quanta  $\phi_0$ ) arises. This phase shift of the quantized flux is exploited in SQUID magnetometers. [272–274]

### 12.4.2 Josephson effect

The Josephson effect [276, 277] describes tunnelling of Cooper pairs between two superconductors that are separated by a thin layer of insulator (SIS junction), a metal (SMS junction) or a narrow constriction in a superconducting loop. The voltage between the two superconducting electrodes is zero until a critical current  $I_c$  is reached by applying an external voltage. This critical current may be modulated by an external magnetic field [278] which is harnessed for SQUID measurements. [272–274]

### 12.4.3 SQUID Setups

There are two principal setups of SQUIDs. The radio frequency (rf) SQUID is based on the ac (alternating current) Josephson effect which uses only one Josephson junction as shown in Fig. 12.1a. The dc (direct current) SQUID, on the other hand, which is shown in Fig. 12.1b, is made up of two Josephson junctions arranged in parallel on a superconducting loop. [272–274]

The rf SQUID loop is coupled to a resonant tank circuit, and a current stronger than  $I_c$  is applied. The inductance and thus the resonant frequency of the tank circuit change by applying an external magnetic field. This frequency change is recorded as the output signal. The rf SQUID presents higher intrinsic noise levels, but the noise does not increase with temperature. Therefore, it is mainly used for magnetometers built of high- $T_c$  superconductors, but in general it is less common than the dc SQUID. [272–274]

In the dc SQUID the input current is split along the superconducting loop and passes the two Josephson junctions. An external magnetic field induces a screening current  $I_s$  in the superconducting loop that gives rise to a magnetic field that cancels the externally

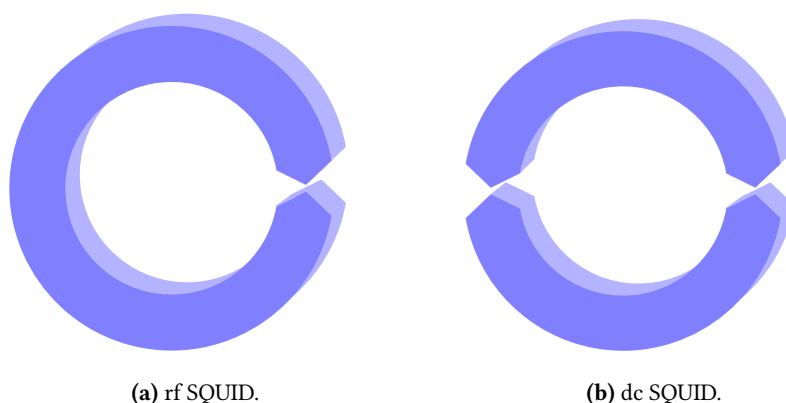


**Figure 12.1:** Typical setups of SQUID magnetometers: Superconducting loops with narrow constrictions as Josephson junctions.

applied. This behavior is due to flux quantization in superconductors which prohibits magnetic fluxes that are non-integer multiples of  $\phi_0$ . At external fields higher than  $\phi_0/2$ , therefore, the screening current changes direction to increase the internal flux to  $\phi_0$ . This leads to an oscillation of  $I_c$  depending on the external magnetic field. In resistive mode, where the applied current is stronger than  $I_c$ , the resulting voltage is thus also dependent on the applied field. [272–274]

#### 12.4.4 Measurement Instrument and Conditions

All magnetic measurements presented in this work were performed on a S700X SQUID magnetometer (Cryogenic Ltd.) in dc setup. Free-powder samples were put in a gelatine capsule and the magnetic moments corrected for the diamagnetic background of the capsule. In the temperature range 2–300 K various external fields were applied and zero field cooled (ZFC, i.e. cooling of the sample is performed in absence of an external field) and field cooled (FC) data collected. The measurements of magnetization  $M$  vs. external field  $\mu_0 \cdot H$  at different temperatures were carried out after cooling the samples in zero field.

#### 12.4.5 Pascal's Method

As explained in Sec. 3.1, p. 21, all materials are diamagnetic. In order to obtain correct values for the para-, ferro-, ferri- or antiferromagnetic molar susceptibilities  $\chi_m$ , the measured susceptibility  $\chi_{meas}$  has to be corrected for these diamagnetic contributions. This can be done by subtracting the diamagnetic susceptibility  $\chi_d$  of the sample from  $\chi_{meas}$ :

$$\chi_m = \chi_{meas} - \chi_d \quad (12.1)$$

Pascal showed in the early 1900s [279–282] that the diamagnetic susceptibility of a molecule may be determined by adding all diamagnetic susceptibilities of atoms ( $\chi_{d_i}$ ) and bonds ( $\lambda_i$ ) in the molecule:

$$\chi_d = \sum_i \chi_{d_i} + \sum_i \lambda_i \quad (12.2)$$

$\chi_d$  and  $\lambda_i$  are called Pascal's constants, and tables of measured values can be found in reference books [283, 284].

### 12.4.6 Effective Magnetic Moment

The effective magnetic moment is an important physical quantity for comparison of magnetic properties. It describes the magnitude of the paramagnetism of materials and is usually close to the spin-only value. Spin-orbit coupling, however, may cause deviation from this value.

The effective magnetic moments  $\mu_{eff}$  were calculated according to the equation

$$\mu_{eff} = \sqrt{\frac{3 k_B}{N_A \mu_B^2} \chi_m T} = 2.828 \sqrt{\chi_m T}, \quad (12.3)$$

where  $k_B$  is the Boltzmann constant,  $N_A$  Avogadro's constant and  $\mu_B$  the Bohr magneton. The latter physical quantity relates to the number of unpaired electrons present in the molecule.

## 12.5 Small- and Wide-Angle X-Ray Scattering (SWAXS)

SWAXS is a measurement method employing elastic X-ray scattering in the same manner as conventional X-ray diffraction. It combines measurements of small diffraction angles (SAXS), typically 0.1–10°, and wide diffraction angles (WAXS), typically 10–90°. SAXS gives information about small scale objects, thus allowing for the characterisation of inhomogeneous samples, such of low crystallinity, nanocomposites, proteins, polymers etc. WAXS, on the other hand, probes long range order, similar to conventional X-ray diffraction. In general, this means that SAXS provides information about a material's morphology and WAXS about its (crystal) structure. [285–287]

In Fig. 12.2 a typical setup of a SWAXS device is shown. X-rays are generated in a radiation source and subsequently monochromatized and focused on the sample. Transmitted, but scattered X-rays are collected on a detector a certain distance away, depending on the diffraction angles to be studied, for a fixed period of time. The primary beam is blocked by a beamstop to avoid damage to the detector due to very high intensities. The 2D scattering patterns are evaluated to get intensity vs. scattering vector  $q$  plots which can then be further interpreted to gain information on the morphology and structure of the studied material. With SWAXS it is not only possible to measure solids, but also solution and suspensions can be studied. [285–287]

### 12.5.1 Measurement Instrument and Conditions

Small- and wide-angle experiments were performed on a Bruker Nanostar, equipped with a 2D-position sensitive detector (Vantec 2000). Göbel mirrors and a pinhole system were used to monochromatize and collimate the Cu  $K_\alpha$  radiation. For SAXS and WAXS measurements the sample-to-detector distance was 108 cm and 13 cm, respectively. The scattering patterns were recorded typically during 600 s. The radially integrated data were

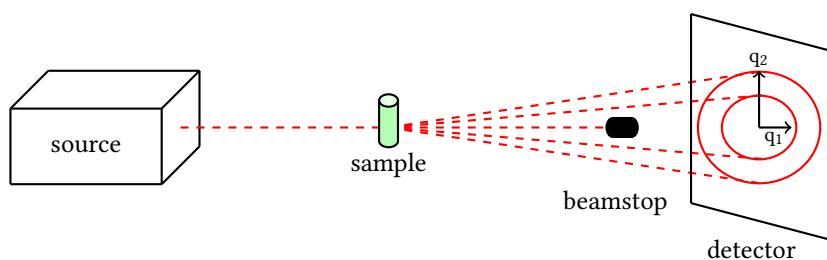


**Figure 12.2:** Setup of the SWAXS measurement.

corrected for background scattering. Small- and wide-angle integrated scattering data were merged to result in a plot of the scattering intensities in dependence on the scattering vector  $q = (4\pi/\lambda) \sin \theta$  in the range  $q = 0.1\text{--}20 \text{ nm}^{-1}$ , where  $2\theta$  is the scattering angle and  $\lambda = 1.542 \text{ \AA}$  the X-ray wavelength.

## 12.6 pH Measurement

Determination of the pH of reaction solutions was performed at  $25 \text{ }^\circ\text{C}$  using a Mettler Toledo pH meter with glass electrode.

## 12.7 Scanning Electron Microscopy (SEM) and Energy-Dispersive X-ray Spectroscopy (EDX)

SEM were recorded on a FEI Quanta 200 scanning electron microscope with a tungsten filament electron gun at acceleration voltages of 5 or 10 kV. EDX analysis was carried out with a EDAX Genesis energy dispersive spectrometer mounted on the SEM chamber.

Powder samples were immobilized on carbon tape and sputter-coated with gold to ensure electrical conduction.

## 12.8 Powder X-Ray Diffraction (pXRD)

pXRD measurements were carried out on a PANalytical XPert Pro MPD instrument with a  $\theta/\theta$  geometry in *Bragg-Brentano* arrangement and a XCelerator multi-channel detector.  $\text{Cu K}\alpha$  ( $\lambda = 1.542 \text{ \AA}$ ) radiation was used. Powder samples were mounted on silicon single-crystal wafers and measured under ambient conditions. Phase characterization was performed using TOPAS software employing Rietveld refinement.

## 12.9 UV-Vis Spectroscopy

UV-Vis absorption spectra were recorded on a PerkinElmer Lambda 35 UV-Vis spectrophotometer. Samples were dissolved in  $\text{H}_2\text{O}$  or EtOH and measured simultaneously with the background in a double beam setup.

Spectra were evaluated using PerkinElmer UV WinLab V6.0 to assess absorption maxima.





## Ligand Syntheses

### 13.1 Modified 2,3,2-Tetramine

#### **N,N'-(*propane-1,3-diyl*)bis(*ethane-1,2-diamine*) (2,3,2-tetramine) [258]**

1,3-Dibromopropane (141.2 g, 71.3 mL, 0.7 mol, 1 eq) was dissolved in 250 mL of dry ethanol. Ethylenediamine (190 g, 211 mL, 3.2 mol, 4.28 eq) was added dropwise during a period of 2h. The reaction mixture was heated to 70 °C and stirred for 1h. KOH (200 g, 3.6 mmol, 4.80 eq) was added and the reaction stirred another hour at 70 °C. KBr and excess KOH were filtered off after cooling and the solvent of the filtrate removed under reduced pressure. The resulting yellow-orange viscous liquid was distilled under reduced pressure ( $2.6 \cdot 10^{-3}$  mbar) at 102 °C to yield the desired 2,3,2-tetramine as a colourless viscous liquid (52.9 g, 0.33 mmol, 47%).

$^1\text{H}$  NMR [ppm] ( $\text{CDCl}_3$ , 250 MHz): 1.05 (s, 6 H, *NH*, *NH*<sub>2</sub>), 1.43–1.52 (q, 2 H, *CH*<sub>2</sub>(–*CH*<sub>2</sub>–*NH*)<sub>2</sub>), 2.40–2.62 (m, 12 H, *CH*<sub>2</sub>–*NH*, *CH*<sub>2</sub>–*NH*<sub>2</sub>);

$^{13}\text{C}$  NMR [ppm] (acetone-*d*<sub>6</sub>, 62.9 MHz): 30.67 (*CH*<sub>2</sub>(–*CH*<sub>2</sub>–*NH*)<sub>2</sub>), 43.06 (*CH*<sub>2</sub>–*NH*<sub>2</sub>), 48.12 (*CH*<sub>2</sub>(–*CH*<sub>2</sub>–*NH*)<sub>2</sub>), 51.70 (*NH*–*CH*<sub>2</sub>–*CH*<sub>2</sub>–*NH*<sub>2</sub>);

IR [ $\text{cm}^{-1}$ ]: 752 (s), 811 (s), 1120 (s), 1301 (w), 1352 (w), 1455 (m), 1599 (w), 2815 (s), 2922 (s), 3277 (m), 3354 (w).

#### **N<sup>1</sup>-(2-aminoethyl)-N<sup>3</sup>-(2-((3-(trimethoxysilyl)propyl)amino)ethyl)propane-1,3-diamine (silyl-2,3,2-tetramine) [259, 260]**

2,3,2-Tetramine (3.64 g, 22.73 mmol, 1 eq) was dissolved in 600 mL of dry THF and cooled in an ice bath under argon atmosphere. NaH (600 mg, 25.00 mmol, 1.1 eq) was added in small batches and the suspension stirred for one hour at room temperature. 3-Iodopropyl-trimethoxysilane (6.60 g, 22.73 mmol, 1 eq) was added dropwise and the reaction heated to reflux overnight. THF was removed under reduced pressure, the residue dissolved in 10 mL of dry  $\text{CH}_2\text{Cl}_2$  and filtered under argon atmosphere.  $\text{CH}_2\text{Cl}_2$  was removed under reduced pressure and the procedure repeated with 5 mL of dry toluene. Evaporation yielded silyl-2,3,2-tetramine as a slightly yellow viscous liquid (2.29 g, 7.1 mmol, 31%).

$^1\text{H}$  NMR [ppm] (MeOD, 250 MHz): 0.54–0.67 (m, 2 H, *CH*<sub>2</sub>–Si), 1.45–1.75 (m, 4 H,

$CH_2(CH_2-NH)_2$ ,  $CH_2-CH_2-Si$ ), 2.37–2.74 (m, 14 H,  $CH_2-NH_2$ ,  $CH_2-NH$ ), 3.52 (s, 9 H,  $CH_3O-Si$ );

$^{13}C$  NMR [ppm] ( $CDCl_3$ , 62.9 MHz): 6.70 ( $CH_2-Si$ ), 23.21 ( $CH_2-CH_2-Si$ ), 29.83 ( $CH_2-(CH_2-NH)_2$ ), 40.93 ( $CH_2-NH_2$ ), 49.08, 49.67, 50.20, 50.55 ( $CH_2-NH$ ), 50.12 ( $CH_3O-Si$ ), 51.84 ( $CH_2-CH_2-CH_2-Si$ );

IR [ $cm^{-1}$ ]: 776 (s), 813 (s), 1074 (s), 1189 (m), 1458 (m), 1593 (w), 2835 (m), 2934 (m), 3254 (w).

**$N^1,N^{1'}$ -(propane-1,3-diyl)bis( $N^2$ -(3-(trimethoxysilyl)propyl)ethane-1,2-diamine) (bissilyl-2,3,2-tetramine)**

1,3-Dibromopropane (2.14 g, 1.08 mL, 10.60 mmol, 1 eq) in 10 mL of dry methanol was added dropwise to [3-(2-aminoethylamino)propyl]trimethoxysilane (AEAPTS) (10 g, 9.72 mL, 44.48 mmol, 4.25 eq) under argon atmosphere. After the addition was completed, the mixture was heated to reflux for 1h. Triethylamine (3.86 g, 5.32 mL, 38.16 mmol, 3.6 eq) was added and the reaction kept at reflux overnight. During cooling a white precipitate ( $HNEt_3^+Br^-$ ) formed which was filtered off under argon atmosphere after the solvent had been removed under reduced pressure. A slightly yellow viscous liquid was obtained after drying (1.24 g, 2.56 mmol, 24%).

$^1H$  NMR [ppm] ( $CDCl_3$ , 250 MHz): 0.53–0.72 (m, 4 H,  $CH_2-Si$ ), 1.50–1.71 (m, 4 H,  $CH_2-CH_2-Si$ ), 1.71–1.95 (m, 2 H,  $CH_2(-CH_2-NH)_2$ ), 2.42–3.13 (m, 16 H,  $CH_2-NH$ ), 3.52 (s, 18 H,  $CH_3O-Si$ );

$^{13}C$  NMR [ppm] ( $CDCl_3$ , 62.9 MHz): 6.69 ( $CH_2-Si$ ), 20.26 ( $CH_2(-CH_2-NH)_2$ ), 22.67 ( $CH_2-CH_2-Si$ ), 40.98 ( $CH_2-(CH_2-NH)_2$ ), 50.45, 51.39 ( $CH_2-NH$ ), 50.62 ( $CH_3O-Si$ ), 52.04 ( $CH_2CH_2-CH_2-Si$ );

IR [ $cm^{-1}$ ]: 778 (s), 811 (s), 1075 (s), 1189 (m), 1308 (w), 1354 (w), 1411 (w), 1460 (m), 1595 (w), 2838 (m), 2939 (m), 3264 (w).

## 13.2 Modified Cyclam

### 13.2.1 Cyclam via Bisaminal (Butanedione)

**(3a<sup>1r,9ar</sup>)-3a<sup>1</sup>,9a-dimethyloctahydro-1*H*,4*H*,7*H*-1,3a,6a,9-tetraazaphenalene (2,3,2-tetramine butyl bisaminal) [262]**

2,3,2-Tetramine (2.0 g, 12.48 mmol, 1 eq) was dissolved in 25 mL of dry acetonitrile and the solution cooled to 0 °C. Butanedione (1.02 g, 1.1 mL, 12.48 mmol, 1 eq) was dissolved in 25 mL of dry acetonitrile and added dropwise to the solution of 2,3,2-tetramine. The reaction mixture was stirred for 2h at 0 °C. The solvent was removed under reduced pressure to yield 2,3,2-tetramine butyl bisaminal as a yellow solid (2.06 g, 9.79 mmol, 78%).

$^1H$  NMR [ppm] ( $CDCl_3$ , 250 MHz) 1.13 (s, 3 H,  $CH_3-C(-NH)_2$ ), 1.26 (s, 3 H,  $CH_3-C(-N)_2$ ), 2.04–2.19 (m, 2 H,  $CH_2(-CH_2-NH)_2$ ), 2.27–2.52 (m, 2 H,  $CH_2-N$ ), 2.58–3.36 (m, 8 H,  $N-CH_2-CH_2-NH$ );

$^{13}C$  NMR [ppm] ( $CDCl_3$ , 62.9 MHz) 10.86 ( $CH_3-C(-N)_2$ ), 18.41 ( $CH_3-C(-NH)_2$ ), 23.53 ( $CH_2(-CH_2-NH)_2$ ), 39.29, 42.06, 45.58, 46.76, 49.11, 51.21 ( $CH_2-NH$ ,  $CH_2-N$ ), 68.58

( $\text{CH}_3\text{-C(-NH)}_2$ ), 73.47 ( $\text{CH}_3\text{-C(-N)}_2$ );

IR [ $\text{cm}^{-1}$ ]: 797 (m), 912 (m), 1069 (m), 1144 (s), 1190 (s), 1233 (s), 1334 (s), 1368 (m), 1440 (m), 1476 (w), 1578 (s), 1631 (m), 2817 (m), 2845 (m), 2926 (m), 3130 (w), 3229 (w).

**3a<sup>1</sup>,5a<sup>1</sup>-dimethyldecahydro-1H,6H-3a,5a,8a,10a-tetraazapyrene (cyclam butyl bisaminal) [262]**

2,3,2-Tetramine butyl bisaminal (1.0 g, 4.75 mmol, 1 eq) was dissolved in 50 mL of dry acetonitrile and  $\text{K}_2\text{CO}_3$  (6.57 g, 47.6 mmol, 10 eq) added to the solution. 1,3-Dibromopropane (0.96 g, 0.5 mL, 4.75 mmol, 1 eq) was added and the reaction solution stirred at room temperature overnight. KBr was filtered off after complete reaction, and the solvent of the filtrate removed under reduced pressure. Column chromatography of the crude residue was performed on aluminium oxide with a solvent gradient ( $\text{CHCl}_3$  to  $\text{EtOH:H}_2\text{O}$  1:1). The product was obtained as a light yellow solid (0.58 g, 2.32 mmol, 49%).

$^1\text{H NMR}$  [ppm] ( $\text{CDCl}_3$ , 250 MHz): 1.13 (s, 6 H,  $\text{C-CH}_3$ ), 1.90–2.11 (m, 4 H,  $\text{CH}_2\text{(-CH}_2\text{-N)}_2$ ), 2.11–2.65, 2.97–3.15 (m, 16 H,  $\text{CH}_2\text{-N}$ );

$^{13}\text{C NMR}$  [ppm] ( $\text{CDCl}_3$ , 62.9 MHz): 11.13 ( $\text{C-CH}_3$ ), 17.96 ( $\text{CH}_2\text{(-CH}_2\text{-N)}_2$ ), 44.97, 46.72, 49.34, 50.34 ( $\text{CH}_2\text{-N}$ ), 71.67 ( $\text{N-C-N}$ );

IR [ $\text{cm}^{-1}$ ]: 612 (w), 630 (w), 655 (m), 754 (m), 797 (w), 819 (m), 830 (m), 850 (w), 878 (s), 914 (m), 938 (m), 979 (w), 1047 (s), 1099 (s), 1113 (m), 1131 (m), 1159 (s), 1183 (s), 1233 (m), 1257 (w), 1295 (w), 1311 (m), 1351 (s), 1364 (m), 1439 (m), 1480 (w), 1633 (w), 2496 (w), 2782 (w), 2819 (w), 2929 (m), 3377 (w).

**1,4,8,11-tetraazacyclotetradecane tetrahydrochloride (cyclam · 4 HCl) [262]**

Cyclam butyl bisaminal (0.58 g, 2.32 mmol, 1 eq) was dissolved in 20 mL of ethanol. HCl 10% (40 mL, ~116 mmol, 50 eq) was slowly added while stirring. The reaction mixture was heated to reflux during 48 h and the solvent evaporated under reduced pressure. The obtained residue was recrystallized from ethanol to yield cyclam · 4 HCl as a light yellow powder (0.62 g, 1.79 mmol, 77%).

$^1\text{H NMR}$  [ppm] ( $\text{CDCl}_3$ , 250 MHz): 1.93–2.11 (m, 4 H,  $\text{CH}_2\text{(-CH}_2\text{-NH)}_2$ ), 3.20–3.32 (t, 8 H,  $\text{CH}_2\text{(-CH}_2\text{-NH)}$ ), 3.44–3.51 (s, 8 H,  $\text{NH-CH}_2\text{-CH}_2\text{-NH}$ );

$^{13}\text{C NMR}$  [ppm] ( $\text{CDCl}_3$ , 62.9 MHz): 22.61 ( $\text{CH}_2\text{(-CH}_2\text{-NH)}_2$ ), 44.22, 44.83 ( $\text{CH}_2\text{-NH}$ );

IR [ $\text{cm}^{-1}$ ]: 679 (w), 745 (w), 919 (w), 984 (w), 1044 (w), 1273 (w), 1376 (w), 1462 (m), 1525 (m), 1597 (m), 2020 (w), 2168 (w), 2367 (m), 2414 (m), 2463 (m), 2508 (m), 2706 (s), 2945 (s), 3361 (m).

**1,4,8,11-tetraazacyclotetradecane (cyclam)**

Cyclam · 4 HCl was dissolved in  $\text{H}_2\text{O}$  and eluted over a column packed with the ion exchange resin Amberlyst A26 ( $\text{OH}^-$  form).  $\text{H}_2\text{O}$  was distilled off under reduced pressure and cyclam obtained as a dark orange precipitate. The residue was dissolved in ethanol and filtered over activated carbon to remove the color to quantitatively yield cyclam as a nearly colourless precipitate.

$^1\text{H NMR}$  [ppm] ( $\text{CDCl}_3$ , 250 MHz): 1.80–1.87 (m, 4 H,  $\text{CH}_2\text{(-CH}_2\text{-NH)}_2$ ), 2.94 (s, 8 H,  $\text{NH-CH}_2\text{-CH}_2\text{-NH}$ ), 2.99–3.06 (t, 8 H,  $\text{CH}_2\text{(-CH}_2\text{-NH)}_2$ );

$^{13}\text{C NMR}$  [ppm] ( $\text{CDCl}_3$ , 62.9 MHz): 28.50 ( $\text{CH}_2\text{(-CH}_2\text{-NH)}_2$ ), 45.27, 46.50 ( $\text{CH}_2\text{-NH}$ );

IR [ $\text{cm}^{-1}$ ]: 791 (w), 829 (m), 894 (w), 910 (w), 693 (w), 966 (w), 1068 (w), 1121 (m), 1206 (w),

1278 (m), 1461 (s), 1474 (s), 1578 (m), 1638 (m), 2731 (m), 2802 (m), 2866 (m), 2923 (w), 3185 (m), 3263 (s), 3423 (s).

### 13.2.2 Cyclam via Bisaminal (1,2-Cyclohexanedione)

#### (8ar,12ar)-octahydro-2H,6H-8a,1-(epiminoethano)pyrimido[1,2-d]quinoxaline (2,3,2-tetramine cyclohexyl bisaminal) [263]

2,3,2-Tetramine (800 mg, 0.83 mL, 5 mmol, 1 eq) was dissolved in 30 mL of ethanol and cooled in an ice bath. 1,2-Cyclohexane (560 mg, 5 mmol, 1 eq) in 30 mL of ethanol was added dropwise. The reaction mixture was stirred at 0 °C during 3h. Afterwards the solvent was removed under reduced pressure. 50 mL of diethyl ether were added to the resulting orange residue. The solution was filtered and the solvent of the filtrate removed under reduced pressure. The obtained white precipitate was recrystallized from hexane to yield 2,3,2-tetramine cyclohexyl bisaminal as white needles (0.88 g, 3.71 mmol, 74%).

<sup>1</sup>H NMR [ppm] (CDCl<sub>3</sub>, 250 MHz): 0.87–1.22 (dd, 2 H, CH<sub>2</sub>–CH<sub>2</sub>–C(–N)<sub>2</sub>), 1.38–2.94 (m, 18 H, CH<sub>2</sub>–CH<sub>2</sub>–C(–NH)<sub>2</sub>, CH<sub>2</sub>(–CH<sub>2</sub>–N)<sub>2</sub>, CH<sub>2</sub>–C(–NH)<sub>2</sub>, CH<sub>2</sub>–C(–N)<sub>2</sub>, N–CH<sub>2</sub>–CH<sub>2</sub>–NH, N–CH<sub>2</sub>–CH<sub>2</sub>–NH), 3.14–3.78 (m, 4 H, CH<sub>2</sub>(–CH<sub>2</sub>–N)<sub>2</sub>);

<sup>13</sup>C NMR [ppm] (CDCl<sub>3</sub>, 62.9 MHz): 17.45, 18.26, 21.25, 22.39 (CH<sub>2</sub>(–CH<sub>2</sub>–N)<sub>2</sub>, CH<sub>2</sub>–CH<sub>2</sub>–C(–N)<sub>2</sub>, CH<sub>2</sub>–CH<sub>2</sub>–C(–NH)<sub>2</sub>, CH<sub>2</sub>–C(–N)<sub>2</sub>), 33.01 (CH<sub>2</sub>–C(–NH)<sub>2</sub>), 39.07, 41.24 (CH<sub>2</sub>–NH), 45.72, 45.80, 48.00, 50.34 (CH<sub>2</sub>–N), 67.06 (C(–NH)<sub>2</sub>), 73.02 (C(–N)<sub>2</sub>);

IR [cm<sup>-1</sup>]: 760 (s), 820 (s), 962 (w), 1028 (m), 1075 (m), 1109 (m), 1189 (w), 1347(w), 1439 (w), 2805 (m), 2930 (m), 3243 (w).

#### (12ar,16ar)-decahydro-2H,9H-1,12-ethanodipyrimido[1,2-d:2',1'-j]quinoxaline (cyclam cyclohexyl bisaminal) [263]

2,3,2-Tetramine cyclohexyl bisaminal (0.535 g, 2.26 mmol, 1 eq) and Cs<sub>2</sub>CO<sub>3</sub> (2.95 g, 9.05 mmol, 4 eq) were suspended in 10 mL of dry acetonitrile. 1,3-Dibromopropane (0.503 g, 251 μL, 2.49 mmol, 1.1 eq) was added dropwise and the reaction mixture stirred at 40 °C for 3 days. The precipitates were filtered off after cooling and the solvent of the filtrate removed under reduced pressure. The residue was recrystallized from hexane to obtain cyclam cyclohexyl bisaminal as a light yellow powder (0.523 g, 1.90 mmol, 84%).

<sup>1</sup>H NMR [ppm] (CDCl<sub>3</sub>, 250 MHz): 1.00–1.17 (m, 2 H, CH<sub>2</sub>(–CH<sub>2</sub>–N)<sub>2</sub>), 1.31–1.57 (m, 4 H, CH<sub>2</sub>–C(–N)<sub>2</sub>), 1.97–2.21 (m, 4 H, CH<sub>2</sub>–CH<sub>2</sub>–C(–N)<sub>2</sub>), 2.21–2.60 (m, 10 H, CH<sub>2</sub>–(CH<sub>2</sub>N)<sub>2</sub>, CH<sub>2</sub>–N), 2.60–2.85 (m, 4 H, CH<sub>2</sub>–N), 3.12–3.36 (m, 2 H, CH<sub>2</sub>–N), 3.78–3.99 (t, 2 H, CH<sub>2</sub>–N);

<sup>13</sup>C NMR [ppm] (CDCl<sub>3</sub>, 62.9 MHz): 17.04, 17.63 (CH<sub>2</sub>(CH<sub>2</sub>–N)<sub>2</sub>, CH<sub>2</sub>–CH<sub>2</sub>–C(–N)<sub>2</sub>), 21.52 (CH<sub>2</sub>–C(–N)<sub>2</sub>), 44.98, 45.59, 48.18, 49.51 (CH<sub>2</sub>–N), 72.82 (C(–N)<sub>2</sub>);

IR [cm<sup>-1</sup>]: 652 (w), 742 (w), 772 (w), 860 (w), 932 (w), 971 (w), 999 (w), 1040 (w), 1080 (m), 1174 (m), 1199 (s), 1262 (s), 1297 (m), 1329 (w), 1368 (w), 1430 (m), 1515 (s), 1631 (m), 1662 (m), 2823 (w), 2951 (w), 3173 (w).

**1,4,8,11-tetraazacyclotetradecane (cyclam) [263]**

Cyclam cyclohexyl bisaminal (607 mg, 2.19 mmol, 1 eq) was dissolved in 44 mL of 1M HCl and heated to 60 °C overnight. The aqueous solution was extracted with CHCl<sub>3</sub> (~120 mL) and the water removed under reduced pressure. The resulting brown precipitate was suspended in 40 mL of acetonitrile and K<sub>2</sub>CO<sub>3</sub> (1.21 g, 8.78 mmol, 4 eq) was added. The suspension was stirred for 3 days at room temperature and subsequently filtered. Acetonitrile of the filtrate was removed under reduced pressure and the obtained light yellow residue recrystallized from acetonitrile. After washing with hexane cyclam was obtained as white powder (250 mg, 1.25 mmol, 57%).

<sup>1</sup>H NMR [ppm] (D<sub>2</sub>O, 250 MHz): 1.64–1.77 (m, 4 H, CH<sub>2</sub>(–CH<sub>2</sub>–NH)<sub>2</sub>), 2.79–2.85 (s, 8 H, CH<sub>2</sub>–NH), 2.85–2.95 (t, 8 H, CH<sub>2</sub>(–CH<sub>2</sub>–NH)<sub>2</sub>);

<sup>13</sup>C NMR [ppm] (D<sub>2</sub>O, 62.9 MHz): 28.29 (CH<sub>2</sub>(–CH<sub>2</sub>–NH)<sub>2</sub>), 48.71, 50.55 (CH<sub>2</sub>–NH);

IR [cm<sup>-1</sup>]: 699 (w), 791 (s), 874 (w), 893 (w), 909 (w), 967 (m), 1017 (s), 1067 (s), 1093 (s), 1206 (w), 1260 (s), 1334 (w), 1432 (w), 1460 (m), 1517 (w), 1599 (w), 2655 (w), 2731 (w), 2801 (m), 2866 (m), 2923 (m), 2962 (m), 3186 (m), 3264 (m).

**13.2.3 Cyclam via Tosyl Protecting Groups****Ethane-1,2-diyl bis(4-methylbenzenesulfonate) (bistosyl ethylene glycol) [288]**

Ethylene glycol (1.0 mL, 17.93 mmol, 1 eq) was dissolved in 10 mL of dry THF, and Et<sub>3</sub>N (5.04 mL, 35.9 mmol, 2 eq) was added. *p*-Toluenesulfonyl chloride (7.18 g, 37.7 mmol, 2.1 eq) in 5 mL of dry THF was added dropwise. A white precipitate was formed after stirring the reaction mixture overnight. Water was added and the aqueous phase extracted with CH<sub>2</sub>Cl<sub>2</sub>. The organic phase was dried over MgSO<sub>4</sub>, filtered and the solvent removed under reduced pressure. The resulting white powder was recrystallized from ethyl acetate to yield bistosyl ethylene glycol as a white crystalline substance (4.44 g, 11.99 mmol, 67%).

<sup>1</sup>H NMR [ppm] (CDCl<sub>3</sub>, 250 MHz): 2.45 (s, 6 H, CH<sub>3</sub>–Ph), 4.18 (s, 4 H, O–CH<sub>2</sub>–CH<sub>2</sub>–O), 7.29–7.38 (d, 4 H, CH<sub>3</sub>–C–CH–CH–C–S), 7.68–7.77 (d, 4 H, CH<sub>3</sub>–C–CH–CH–C–S);

<sup>13</sup>C NMR [ppm] (CDCl<sub>3</sub>, 62.9 MHz): 21.82 (CH<sub>3</sub>–Ph), 66.82 (O–CH<sub>2</sub>–CH<sub>2</sub>–O), 128.11 (CH<sub>3</sub>–C–CH–CH–C–S), 130.11 (CH<sub>3</sub>–C–CH–CH–C–S), 132.48 (CH<sub>3</sub>–C), 145.51 (CS);

IR [cm<sup>-1</sup>]: 662 (s), 704 (w), 768 (s), 799 (m), 816 (m), 913 (s), 962 (w), 978 (w), 1017 (m), 1035 (m), 1093 (m), 1122 (w), 1176 (s), 1191 (m), 1233 (w), 1296 (w), 1309 (w), 1359 (s), 1372 (m), 1401 (w), 1452 (w), 1494 (w), 1596 (w).

***N,N'*-(propane-1,3-diyl)bis(4-methyl-*N*-(2-((4-methylphenyl)sulfonamido)ethyl)benzenesulfonamide) (tetratosyl 2,3,2-tetramine) [264]**

2,3,2-Tetramine (1.0 g, 6.24 mmol, 1 eq) and NaOH (998 mg, 24.96 mmol, 4 eq) were dissolved in 10 mL of H<sub>2</sub>O. *p*-Toluenesulfonyl chloride (4.76 g, 24.96 mmol, 4 eq) was dissolved in 60 mL of diethyl ether and the solution added dropwise to the aqueous solution. The resulting two-phase mixture was stirred for 1h at room temperature and a white precipitate formed. Diethyl ether was removed under reduced pressure and the aqueous residue extracted with ethyl acetate. The organic phase was washed with 3M HCl, dried over MgSO<sub>4</sub>, filtered and the solvent removed under reduced pressure. After drying tetratosyl 2,3,2-tetramine was obtained as a reddish precipitate (4.73 g, 6.08 mmol, 94%).

$^1\text{H}$  NMR [ppm] ( $\text{CDCl}_3$ , 250 MHz): 1.65–1.83 (q, 2 H,  $\text{CH}_2(-\text{CH}_2-\text{NTs})_2$ ), 2.35–2.46 (s, 12 H,  $\text{CH}_3-\text{Ph}$ ), 3.01–3.23 (m, 12 H,  $\text{NHTs}-\text{CH}_2-\text{CH}_2-\text{NTs}$ ,  $\text{CH}_2(-\text{CH}_2-\text{NTs})_2$ ), 7.32–7.47 (d, 8 H,  $\text{CH}_3-\text{C}-\text{CH}_2$  from NHTs and NTs), 7.60–7.69 (d, 4 H,  $\text{CH}_3-\text{C}-\text{CH}_2-\text{CH}_2$  from NTs), 7.71–7.79 (d, 4 H,  $\text{CH}_3-\text{C}-\text{CH}_2-\text{CH}_2$  from NHTs);

$^{13}\text{C}$  NMR [ppm] ( $\text{CDCl}_3$ , 62.9 MHz): 21.64 ( $\text{CH}_3-\text{Ph}$ ), 28.62 ( $\text{CH}_2(-\text{CH}_2-\text{NTs})_2$ ), 43.45 ( $\text{CH}_2-\text{NHTs}$ ), 48.53 ( $\text{CH}_2(-\text{CH}_2-\text{NTs})_2$ ), 50.27 ( $\text{NTs}-\text{CH}_2-\text{CH}_2-\text{NHTs}$ ), 127.21, 127.45 ( $\text{S}-\text{C}-\text{CH}_2$ ), 129.86, 130.04 ( $\text{S}-\text{C}-\text{CH}_2-\text{CH}_2$ ), 134.88 ( $\text{N}-\text{S}-\text{C}(\text{Ph})$ ), 136.97 ( $\text{NH}-\text{S}-\text{C}(\text{Ph})$ ), 143.50, 143.96 ( $\text{CH}_3-\text{C}(\text{Ph})$ );

IR [ $\text{cm}^{-1}$ ]: 658 (s), 718 (m), 813 (m), 934 (w), 976 (w), 1089 (m), 1154 (s), 1251 (w), 1327 (m), 1424 (w), 1493 (w), 1598 (w), 1663 (w), 1737 (w), 2870 (w), 3283 (w).

***N,N'*-(ethane-1,2-diyl)bis(4-methyl-*N*-(3-((4-methylphenyl)sulfonamido)propyl)benzenesulfonamide) (tetratosyl 3,2,3-tetramine) [264]**

3,2,3-Tetramine (1.0 g, 5.74 mmol, 1 eq) and NaOH (918 mg, 22.95 mmol, 4.1 eq) were dissolved in 10 mL of  $\text{H}_2\text{O}$ . *p*-Toluenesulfonyl chloride (4.38 g, 22.95 mmol, 4.1 eq) was dissolved in 60 mL of diethyl ether and the solution added dropwise to the aqueous solution. The resulting two-phase mixture was stirred for 1h at room temperature and a white precipitate formed. Diethyl ether was removed under reduced pressure and the aqueous residue extracted with ethyl acetate. The organic phase was washed with 3M HCl, dried over  $\text{MgSO}_4$ , filtered and the solvent removed under reduced pressure. Tetratosyl 3,2,3-tetramine was obtained as a light yellow precipitate after drying (3.53 g, 4.46 mmol, 78%).

$^1\text{H}$  NMR [ppm] ( $\text{CDCl}_3$ , 250 MHz): 1.73–1.86 (q, 4 H,  $\text{CH}_2(-\text{CH}_2-\text{N})_2$ ), 2.40–2.43 (s, 6 H,  $\text{CH}_3-\text{Ph}-\text{S}-\text{NH}$ ), 2.43–2.45 (s, 6 H,  $\text{CH}_3-\text{Ph}-\text{S}-\text{N}$ ), 2.92–3.03 (m, 4 H,  $\text{CH}_2-\text{NHTs}$ ), 3.10–3.20 (t, 4 H,  $\text{CH}_2-\text{NTs}$ ), 3.20–3.25 (s, 4 H,  $\text{N}-\text{CH}_2-\text{CH}_2-\text{N}$ ), 7.27–7.36 (t, 8 H,  $\text{CH}_3-\text{C}-\text{CH}_2$ ), 7.63–7.76 (dd, 8 H,  $\text{CH}_3-\text{C}-\text{CH}_2-\text{CH}_2$ );

$^{13}\text{C}$  NMR [ppm] ( $\text{CDCl}_3$ , 62.9 MHz): 21.65 ( $\text{CH}_3-\text{Ph}$ ), 29.13 ( $\text{CH}_2(-\text{CH}_2-\text{N})_2$ ), 40.13 ( $\text{CH}_2-\text{NHTs}$ ), 47.31 ( $\text{CH}_2-\text{NTs}$ ), 49.03 ( $\text{N}-\text{CH}_2-\text{CH}_2-\text{N}$ ), 127.17 ( $\text{CH}_2-\text{C}-\text{S}-\text{NTs}$ ), 127.38 ( $\text{CH}_2-\text{C}-\text{S}-\text{NHTs}$ ), 129.90 ( $\text{CH}_2-\text{CH}_2-\text{C}-\text{S}-\text{NTs}$ ), 130.12 ( $\text{CH}_2-\text{CH}_2-\text{C}-\text{S}-\text{NHTs}$ ), 135.25 ( $\text{C}-\text{S}-\text{NTs}$ ), 136.88 ( $\text{C}-\text{S}-\text{NHTs}$ ), 143.57 ( $\text{CH}_3-\text{C}-\text{CH}_2-\text{CH}_2-\text{C}-\text{S}-\text{NTs}$ ), 144.05 ( $\text{CH}_3-\text{C}-\text{CH}_2-\text{CH}_2-\text{C}-\text{S}-\text{NHTs}$ );

IR [ $\text{cm}^{-1}$ ]: 646 (s), 699 (s), 715 (s), 813 (m), 867 (m), 964 (m), 1012 (m), 1045 (w), 1066 (w), 1090 (m), 1106 (w), 1156 (s), 1185 (w), 1216 (w), 1238 (w), 1293 (m), 1304 (m), 1330 (s), 1352 (w), 1373 (w), 1465 (w), 1493 (w), 1597 (w), 1738 (w), 2943 (w), 3296 (w).

**1,4,8,11-tetratosyl-1,4,8,11-tetraazacyclotetradecane (tetratosyl cyclam) via tetratosyl 2,3,2-tetramine [265]**

Tetratosyl 2,3,2-tetramine (11.66 g, 15 mmol, 1 eq) and  $\text{K}_2\text{CO}_3$  (20.7 g, 150 mmol, 10 eq) were suspended in 450 mL of dry acetonitrile and heated to reflux for 30 min. 1,3-Dibromopropane (3.6 g, 1.8 mL, 18 mmol, 1.2 eq) was dissolved in 300 mL of dry acetonitrile and added dropwise to the hot reaction solution over a period of 4h. The resulting mixture was further heated to reflux for 3 days. The cooled suspension was subsequently filtered and the solvent of the filtrate removed under reduced pressure. This yielded tetratosyl cyclam as a light yellow precipitate (8.85 g, 10.8 mmol, 72%).

$^1\text{H}$  NMR [ppm] (acetone- $d_6$ , 250 MHz): 1.83–1.99 (q, 4 H,  $\text{CH}_2\text{-CH}_2\text{-N}$ ), 2.35–2.50 (s, 12 H,  $\text{CH}_3\text{-Ph}$ ), 3.10–3.70 (m, 16 H,  $\text{CH}_2\text{-N}$ ), 7.38–7.50 (d, 8 H,  $\text{CH}_3\text{-C-CH}_2$ ), 7.68–7.80 (d, 8 H,  $\text{CH}_3\text{-C-CH}_2\text{-CH}_2$ );

$^{13}\text{C}$  NMR [ppm] ( $\text{CDCl}_3$ , 62.9 MHz): 21.63 ( $\text{CH}_3\text{-Ph}$ ), 28.62 ( $\text{CH}_2\text{-CH}_2\text{-N}$ ), 48.02 ( $\text{CH}_2\text{-CH}_2\text{-N}$ ), 50.25 ( $\text{N-CH}_2\text{-CH}_2\text{-N}$ ), 127.43 ( $\text{S-C-CH}_2$ ), 130.03 ( $\text{S-C-CH}_2\text{-CH}_2$ ), 135.27 ( $\text{N-S-C(Ph)}$ ), 143.60 ( $\text{CH}_3\text{-C(Ph)}$ );

IR [ $\text{cm}^{-1}$ ]: 656 (w), 690 (s), 752 (w), 778 (w), 816 (m), 879 (m), 918 (w), 948 (w), 1013 (s), 1041 (s), 1089 (w), 1128 (s), 1183 (s), 1193 (s), 1219 (m), 1255 (w), 1376 (s), 1404 (s), 1599 (w), 2253 (m), 2293 (w), 2944 (w).

#### **1,4,8,11-tetratosyl-1,4,8,11-tetraazacyclotetradecane (tetratosyl cyclam) via tetratosyl 3,2,3-tetramine [266]**

Tetratosyl 3,2,3-tetramine (0.79 g, 1 mmol, 1 eq) and  $\text{K}_2\text{CO}_3$  (1.38 g, 10 mmol, 10 eq) were suspended in 20 mL of dry acetonitrile and heated to reflux for 30 min. Bistosyl ethylene glycol (0.37 g, 1 mmol, 1 eq) was dissolved in 30 mL of dry acetonitrile and added dropwise to the hot reaction solution overnight. The resulting mixture was further heated to reflux for 3 days. The cooled suspension was subsequently filtered and the solvent of the filtrate removed under reduced pressure. This yielded tetratosyl cyclam as a light yellow precipitate (0.77 g, 0.94 mmol, 94%).

$^1\text{H}$  NMR [ppm] ( $\text{CDCl}_3$ , 250 MHz): 1.80–1.94 (q, 4 H,  $\text{CH}_2\text{-CH}_2\text{-N}$ ), 2.37–2.48 (s, 12 H,  $\text{CH}_3\text{-Ph}$ ), 3.08–3.19 (t, 8 H,  $\text{CH}_2\text{-CH}_2\text{-N}$ ), 3.19–3.26 (s, 8 H,  $\text{N-CH}_2\text{-CH}_2\text{-N}$ ), 7.30–7.38 (d, 8 H,  $\text{CH}_3\text{-C-CH}_2$ ), 7.66–7.73 (d, 8 H,  $\text{CH}_3\text{-C-CH}_2\text{-CH}_2$ );

$^{13}\text{C}$  NMR [ppm] ( $\text{CDCl}_3$ , 62.9 MHz): 21.58 ( $\text{CH}_3\text{-Ph}$ ), 28.72 ( $\text{CH}_2\text{-CH}_2\text{-N}$ ), 48.00 ( $\text{CH}_2\text{-CH}_2\text{-N}$ ), 49.89 ( $\text{N-CH}_2\text{-CH}_2\text{-N}$ ), 127.40 ( $\text{S-C-CH}_2$ ), 130.02 ( $\text{S-C-CH}_2\text{-CH}_2$ ), 135.23 ( $\text{N-S-C(Ph)}$ ), 143.58 ( $\text{CH}_3\text{-C(Ph)}$ );

IR [ $\text{cm}^{-1}$ ]: 655 (s), 693 (m), 717 (m), 778 (w), 815 (m), 879 (m), 918 (w), 950 (w), 1017 (s), 1043 (s), 1089 (w), 1121 (s), 1183 (s), 1193 (s), 1219 (m), 1255 (w), 1376 (s), 1404 (s), 1599 (w), 2252 (m), 2293 (w), 2941 (w).

#### **1,4,8,11-tetraazacyclotetradecane (cyclam) [264]**

Tetratosyl cyclam (4.0 g, 4.9 mmol, 1 eq) was dissolved in 17 mL of conc.  $\text{H}_2\text{SO}_4$  and the mixture heated to reflux for 3 days. 60 mL of ethanol and 50 mL of diethyl ether were added slowly after cooling. The formed light brown precipitate was filtered off, dissolved in 75 mL of water and 2M NaOH added to reach a pH of ~12. The basic solution was extracted with  $\text{CHCl}_3$ . The organic phase was dried over  $\text{MgSO}_4$ , filtered and the solvent removed under reduced pressure to yield cyclam as a white solid (177 mg, 0.88 mmol, 18%).

$^1\text{H}$  NMR [ppm] ( $\text{CDCl}_3$ , 250 MHz): 1.65–1.80 (q, 4 H,  $\text{CH}_2\text{-(-CH}_2\text{-NH)}_2$ ), 2.68–2.73 (s, 8 H,  $\text{N-CH}_2\text{-CH}_2\text{-N}$ ), 2.73–2.81 (t, 8 H,  $\text{CH}_2\text{-(-CH}_2\text{-NH)}_2$ );

$^{13}\text{C}$  NMR [ppm] ( $\text{CDCl}_3$ , 62.9 MHz): 28.29 ( $\text{CH}_2\text{-(-CH}_2\text{-NH)}_2$ ), 48.71, 50.55 ( $\text{CH}_2\text{-NH}$ );

IR [ $\text{cm}^{-1}$ ]: 699 (w), 791 (s), 874 (w), 893 (w), 909 (w), 967 (m), 1017 (s), 1067 (s), 1093 (s), 1206 (w), 1260 (s), 1334 (w), 1432 (w), 1460 (m), 1517 (w), 1599 (w), 2655 (w), 2731 (w), 2801 (m), 2866 (m), 2923 (m), 2962 (m), 3186 (m), 3264 (m).

### 13.2.4 Silylcyclam

#### 3-Iodopropyltrimethoxysilane [289]

NaI (3.77 g, 25.16 mmol, 1 eq) was dissolved in 50 mL of dry acetone under argon atmosphere. 3-Chloropropyltrimethoxysilane (5.0 g, 4.64 mL, 25.16 mmol, 1 eq) was added and the reaction mixture heated to reflux for 24h. The solvent was removed under reduced pressure and 100 mL of dry diethyl ether added to the residue. Precipitated NaCl was filtered off and the solvent of the filtrate removed under reduced pressure. The residue was distilled under vacuum to yield 3-iodopropyltrimethoxysilane as a colourless liquid (5.75 g, 19.82 mmol, 79%).

$^1\text{H}$  NMR [ppm] ( $\text{CDCl}_3$ , 250 MHz): 0.67–0.83 (m, 2 H,  $\text{CH}_2\text{-Si}$ ), 1.79–2.00 (m, 2 H,  $\text{CH}_2\text{-CH}_2\text{-Si}$ ), 3.15–3.26 (t, 2 H,  $\text{CH}_2\text{-I}$ ), 3.53–3.63 (s, 9 H,  $\text{CH}_3\text{O-Si}$ );

$^{13}\text{C}$  NMR [ppm] ( $\text{CDCl}_3$ , 62.9 MHz): 10.58 ( $\text{CH}_2\text{-I}$ ), 11.03 ( $\text{CH}_2\text{-Si}$ ), 27.37 ( $\text{CH}_2\text{-CH}_2\text{-Si}$ ), 50.70 ( $\text{CH}_3\text{O-Si}$ );

IR [ $\text{cm}^{-1}$ ]: 610 (w), 650 (w), 679 (w), 756 (m), 801 (s), 896 (w), 926 (w), 954 (w), 995 (w), 1075 (s), 1189 (m), 1207 (m), 1292 (w), 1341 (w), 1411 (w), 1436 (w), 1456 (w), 2839 (m), 2942 (m).

#### 1-(3-(trimethoxysilyl)propyl)-1,4,8,11-tetraazacyclotetradecane (silylcyclam) [259, 260]

Cyclam (2.50 g, 12.5 mmol, 1 eq) was suspended in 200 mL of dry acetonitrile under argon atmosphere. NaH (300 mg, 12.5 mmol, 1 eq) was added in small portions and resulted in the evolution of hydrogen. The resulting mixture was heated to reflux for 1h. 3-iodopropyltrimethoxysilane dissolved in 100 mL of dry acetonitrile was subsequently added dropwise and the reaction mixture heated to reflux overnight. The solvent was removed under reduced pressure and the residue washed three times with dry  $\text{CH}_2\text{Cl}_2$  (~60 mL) and filtered. To obtain the modified cyclam as a brownish oil (4.13 g, 11.45 mmol, 92%)  $\text{CH}_2\text{Cl}_2$  was removed under reduced pressure.

$^1\text{H}$  NMR [ppm] ( $\text{CDCl}_3$ , 250 MHz): 0.44–0.70 (m, 2 H,  $\text{CH}_2\text{-Si}$ ), 1.36–1.88 (m, 6 H,  $\text{CH}_2\text{-CH}_2\text{-Si}$ ,  $\text{CH}_2\text{-N}$ ), 2.26–3.17 (m, 18 H,  $\text{CH}_2\text{-N}$ ), 3.47–3.58 (s, 9 H,  $\text{CH}_3\text{O-Si}$ ), broad peaks indicating mixture of mono-, bis-, tris- and tetrakis silyl derivatives;

$^{13}\text{C}$  NMR [ppm] ( $\text{CDCl}_3$ , 62.9 MHz): 8.6 ( $\text{CH}_2\text{-Si}$ ), 18.9 ( $\text{CH}_2\text{-CH}_2\text{-Si}$ ), 26.9, 29.6 ( $\text{CH}_2\text{-N}$ ), 48.4, 48.7, 49.6, 50.0, 50.1, 51.6, 53.9, 55.2, 56.1 ( $\text{CH}_2\text{-N}$ ,  $\text{CH}_3\text{O-Si}$ ), 58.9 ( $\text{N-CH}_2\text{-CH}_2\text{-CH}_2\text{-Si}$ );

IR [ $\text{cm}^{-1}$ ]: 695 (w), 814 (s), 1072 (s), 1189 (m), 1300 (w), 1364 (w), 1461 (m), 1600 (m), 1638 (w), 2186 (w), 2810 (w), 2837 (w), 2939 (s), 3201 (w), 3305 (w).

### 13.2.5 Silyl-6-aminocyclam

#### 6-amino-1,4,8,11-tetraazacyclotetradecane-5,7-dione (6-aminodioxocyclam) [267]

Diethyl aminomalonate hydrochloride (5.3 g, 25 mmol, 1 eq) and 2,3,2-tetramine (4.0 g, 25 mmol, 1 eq) were dissolved in 500 mL of dry methanol and heated to reflux during 3 days under argon atmosphere. After cooling the solvent was removed under reduced



pressure and the residue recrystallized from ethanol/6M HCl (1:1). 6-aminodioxocyclam · 5 HCl was collected by filtration, dissolved in H<sub>2</sub>O and converted to the free amine form by elution over a column packed with the ion exchange resin Amberlyst A26 (OH<sup>-</sup> form). Evaporation of H<sub>2</sub>O under reduced pressure yielded 6-aminodioxocyclam as a yellow solid (5.58 g, 22.93 mmol, 92%).

<sup>1</sup>H NMR [ppm] (D<sub>2</sub>O, 250 MHz): 1.69–1.88 (q, 2 H, CH<sub>2</sub>–(CH<sub>2</sub>–NH)<sub>2</sub>), 2.83–3.06 (m, 8 H, CH<sub>2</sub>–(CH<sub>2</sub>–NH)<sub>2</sub>, CH<sub>2</sub>–(CH<sub>2</sub>–NH–CH<sub>2</sub>)<sub>2</sub>), 3.21–3.75 (m, 4 H, C(O)–NH–CH<sub>2</sub>), 4.16 (s, 0.6 H due to resonance structure with conjugated double bonds as discussed in Sec. 10.1, p. 86, NH<sub>2</sub>–CH–C(O));

<sup>13</sup>C NMR [ppm] (D<sub>2</sub>O, 62.9 MHz): 25.20 (CH<sub>2</sub>–(CH<sub>2</sub>–NH)<sub>2</sub>), 38.12 (C(O)–NH–CH<sub>2</sub>), 47.85, 49.76 (CH<sub>2</sub>–(CH<sub>2</sub>–NH)<sub>2</sub>, C(O)–NH–CH<sub>2</sub>–CH<sub>2</sub>), 57.76 (CH–NH<sub>2</sub>), 171.63 (C=O);

IR [cm<sup>-1</sup>]: 727 (w), 903 (w), 961 (w), 1054 (w), 1124 (m), 1197 (w), 1290 (m), 1341 (w), 1365 (w), 1456 (s), 1561 (s), 1638 (s), 1664 (s), 2830 (m), 2932 (m), 3066 (m), 3258 (s).

#### **1,4,8,11-tetraazacyclotetradecan-6-amine (6-aminocyclam) [269, 270]**

6-Aminodioxocyclam (0.72 g, 3 mmol, 1 eq) and NaBH<sub>4</sub> (1.13 g, 30 mmol, 10 eq) were suspended in 25 mL of dry THF under argon atmosphere and cooled to 0 °C. Iodine (3.05 g, 12 mmol, 4 eq) was dissolved in 20 mL of dry THF and added dropwise over a period of 2.5h. After the addition of iodine was completed, the reaction mixture was heated to reflux overnight. Subsequently the reaction mixture was cooled and carefully quenched at 0 °C with 15 mL of H<sub>2</sub>O and 15 mL of concentrated HCl to destroy excess NaBH<sub>4</sub>. It was again heated to reflux for 2h. Afterwards THF was removed under reduced pressure. Precipitates were filtered off, the aqueous phase was extracted with diethyl ether and H<sub>2</sub>O removed under reduced pressure. The resulting yellow precipitate (6-aminocyclam · 5 HCl) was dissolved in H<sub>2</sub>O and converted to the free amine form by elution over a column packed with the ion exchange resin Amberlyst A26 (OH<sup>-</sup> form). Evaporation of H<sub>2</sub>O under reduced pressure yielded a white solid that was dissolved in ethanol and precipitated by addition of 47% HBr. The precipitate was filtered off, dissolved in H<sub>2</sub>O and, once again, converted to the free amine form by elution over a column packed with the ion exchange resin Amberlyst A26 (OH<sup>-</sup> form). 6-Aminocyclam was obtained as a light yellow precipitate (0.62 g, 2.8 mmol, 96%) after evaporation of H<sub>2</sub>O under reduced pressure.

<sup>1</sup>H NMR [ppm] (D<sub>2</sub>O, 250 MHz): 1.56–1.76 (m, 2 H, CH<sub>2</sub>–(CH<sub>2</sub>–NH)<sub>2</sub>), 2.39–2.89 (m, 16 H, CH<sub>2</sub>–NH), 2.93–3.06 (m, 1 H, CH–NH<sub>2</sub>);

<sup>13</sup>C NMR [ppm] (D<sub>2</sub>O, 62.9 MHz): 26.07 (CH<sub>2</sub>–(CH<sub>2</sub>–NH)<sub>2</sub>), 46.55, 46.89, 47.82, 48.35 (CH<sub>2</sub>–NH), 54.52 (CH–NH<sub>2</sub>);

IR [cm<sup>-1</sup>]: 707 (w), 780 (m), 810 (w), 849 (m), 1053 (s), 1117 (s), 1206 (w), 1402 (s), 1449 (s), 1600 (w), 2183 (m), 2365 (m), 2437 (m), 2842 (s), 2947 (s), 3254 (m), 3393 (w).

#### **1-(1,4,8,11-tetraazacyclotetradecane)-3-(3-(triethoxysilyl)propyl)urea (silyl-6-aminocyclam) [259, 260]**

6-Aminocyclam (0.5 g, 2.32 mmol, 1 eq) was suspended in 200 mL of dry MeCN and 60 mL of dry pyridine. 3-Isocyanopropyltrimethoxysilane (0.57 g, 0.57 mL, 2.32 mmol, 1 eq) in 10 mL of dry MeCN was added dropwise. The reaction mixture was heated to reflux over

night. The mixture was filtered and the solvents of the filtrate removed under reduced pressure after cooling. Silyl-6-aminocyclam was obtained after drying as light brown very viscous liquid (1.04 g, 2.25 mmol, 97%).

$^1\text{H}$  NMR [ppm] ( $\text{CDCl}_3$ , 250 MHz): 0.54–0.69 (t, 2 H,  $\text{CH}_2\text{-Si}$ ), 1.14–1.25 (t, 9 H,  $\text{Si-O-CH}_2\text{CH}_3$ ), 1.48–1.69 (m, 2 H,  $\text{Si-CH}_2\text{-CH}_2$ ), 1.69–2.03 (m, 2 H,  $\text{CH}_2\text{-(CH}_2\text{-NH)}_2$ ), 2.34–3.58 (m, 19 H,  $\text{CH}_2\text{-NH}$ ,  $\text{CH-NH}$ ), 3.71–3.90 (q, 6 H,  $\text{Si-O-CH}_2\text{-CH}_3$ ).

$^{13}\text{C}$  NMR [ppm] ( $\text{CDCl}_3$ , 62.9 MHz): 13.47 ( $\text{Si-O-CH}_2\text{-CH}_3$ ), 18.46 ( $\text{Si-O-CH}_2\text{-CH}_3$ ), 22.28 ( $\text{CH}_2\text{-(CH}_2\text{-NH)}_2$ ), 24.85 ( $\text{Si-CH}_2\text{-CH}_2$ ), 42.38 ( $\text{NH-CH}_2\text{-CH}_2\text{-NH}$ ), 44.64 ( $\text{CH}_2\text{-(CH}_2\text{-NH)}_2$ ), 45.68 ( $\text{Si-CH}_2\text{-CH}_2\text{-CH}_2$ ), 52.22 ( $\text{NH-C(O)-CH-CH}_2$ ), 57.91 ( $\text{NH-C(O)-CH}$ ), 58.48 ( $\text{Si-O-CH}_2\text{-CH}_3$ ), 157.62 ( $\text{C=O}$ ).

IR [ $\text{cm}^{-1}$ ]: 681 (w), 765 (m), 953 (m), 1073 (s), 1101 (s), 1165 (m), 1190 (w), 1264 (s), 1293 (s), 1365 (w), 1389 (w), 1407 (w), 1441 (w), 1536 (m), 1624 (m), 2885 (m), 2926 (m), 2972 (m), 3294 (w).

# Complex Syntheses

## 14.1 Ni<sup>II</sup> Complexes

### General Procedure [255]

To a heated solution (50 °C) of anhydrous NiCl<sub>2</sub> (1 eq) in 15 mL/mmol of dry ethanol a solution of the polyamine ligand (3 eq diamine, 1 eq tetramine) in 8 mL/mmol of dry ethanol was added slowly. The reaction mixture was stirred 1h at 50 °C and afterwards its volume reduced to produce a violet or brown precipitate. The pure product was obtained with ~70% yield after filtering off, washing with dry diethyl ether and drying under vacuum.

### [Ni(AEAPTS)<sub>3</sub>]Cl<sub>2</sub>

The compound was obtained as a violet powder.

IR [cm<sup>-1</sup>]: 682 (m), 786 (s), 812 (s), 893 (w), 974 (m), 1071 (s), 1191 (m), 1277 (w), 1314 (w), 1335 (w), 1411 (w), 1460 (m), 1598 (m), 2839 (m), 2882 (w), 2938 (m), 3149 (m).

### [Ni(AEAPTS)<sub>2</sub>]Cl<sub>2</sub>

The compound was obtained as a violet powder.

IR [cm<sup>-1</sup>]: 670 (m), 683 (m), 787 (s), 811 (s), 896 (w), 953 (s), 974 (m), 1074 (s), 1166 (m), 1191 (m), 1333 (w), 1390 (w), 1459 (w), 2839 (m), 2882 (m), 2927 (m), 2970 (m), 3143 (m), 3221 (w).

### [Ni(silyl-2,3,2-tetramine)]Cl<sub>2</sub>

The compound was obtained as a bright violet powder.

IR [cm<sup>-1</sup>]: 691 (w), 800 (s), 880 (m), 1054 (s), 1190 (m), 1262 (w), 1463 (m), 2931 (m), 3152 (m).

### [Ni(bissilyl-2,3,2-tetramine)]Cl<sub>2</sub>

The compound was obtained as a brown powder.

IR [cm<sup>-1</sup>]: 646 (w), 679 (w), 785 (s), 813 (s), 896 (w), 971 (m), 1072 (s), 1190 (s), 1277 (w), 1316 (w), 1460 (m), 1591 (w), 2840 (m), 2942 (m), 3244 (m).

**[Ni(silylcyclam)]Cl<sub>2</sub>**

The compound was obtained as a brown powder.

IR [cm<sup>-1</sup>]: 688 (w), 811 (s), 1069 (s), 1190 (m), 1261 (w), 1457 (m), 1591 (m), 2840 (m), 2944 (m).

**[Ni(silyl-6-aminocyclam)]Cl<sub>2</sub>**

The compound was obtained as a brown powder.

IR [cm<sup>-1</sup>]: 680 (w), 781 (m), 949 (m), 1072 (s), 1166 (m), 1262 (s), 1509 (s), 1613 (s), 2880 (m), 2926 (m), 2970 (m), 3217 (m), 3315 (w).

## 14.2 Cu<sup>II</sup> Complexes

**General Procedure [255]**

To a heated solution (50 °C) of anhydrous CuCl<sub>2</sub> (1 eq) in 15 mL/mmol of dry ethanol a solution of the polyamine ligand (3 eq diamine, 1 eq tetramine) in 8 mL/mmol of dry ethanol was added slowly. The reaction mixture was stirred 1h at 50 °C and afterwards its volume reduced to produce a violet, blue or green precipitate. The pure product was obtained with ~70% yield after filtering off, washing with dry diethyl ether and drying under vacuum.

**[Cu(AEAPTS)<sub>3</sub>]Cl<sub>2</sub>**

The compound was obtained as a violet powder.

IR [cm<sup>-1</sup>]: 644 (w), 677 (m), 705 (m), 759 (m), 784 (s), 809 (s), 849 (m), 957 (s), 1012 (s), 1032 (s), 1079 (s), 1189 (m), 1277 (w), 1305 (w), 1432 (m), 1457 (m), 1590 (m), 2839 (m), 2937 (m), 3126 (m), 3233 (m).

**[Cu(silyl-2,3,2-tetramine)<sub>3</sub>]Cl<sub>2</sub>**

The compound was obtained as a green powder.

IR [cm<sup>-1</sup>]: 688 (m), 800 (s), 887 (m), 1035 (s), 1053 (s), 1190 (m), 1261 (m), 1285 (w), 1317 (w), 1377 (w), 1461 (m), 1584 (w), 1767 (w), 2839 (m), 2872 (m), 2930 (m), 3125 (w), 3204 (w).

**[Cu(bissilyl-2,3,2-tetramine)<sub>3</sub>]Cl<sub>2</sub>**

The compound was obtained as a blue powder.

IR [cm<sup>-1</sup>]: 647 (w), 679 (w), 779 (s), 813 (s), 901 (m), 978 (w), 1005 (w), 1070 (s), 1190 (m), 1316 (w), 1460 (m), 1585 (w), 2839 (m), 2942 (m), 2974 (w), 3132 (w), 3202 (w).

# Cyanometallate Network Syntheses

## 15.1 Ni<sup>II</sup>/Fe<sup>III</sup> Cyanometallates

### General Procedure

To a heated (50 °C) solution of [Ni(polyamine)<sub>n</sub>]Cl<sub>2</sub> (n = 1, 3) (3 eq) in 40 mL/mmol of dry methanol a heated solution of K<sub>3</sub>[Fe(CN)<sub>6</sub>] (2 eq) in 65 mL/mmol of dry methanol was slowly added. A precipitate formed immediately and was filtered off, washed with dry ethanol and dried under vacuum to obtain the Ni<sup>II</sup>/Fe<sup>III</sup> cyanometallate (n = 1, 2) in quantitative yield.

### [Ni(AEAPTS)<sub>2</sub>]<sub>3</sub>[Fe(CN)<sub>6</sub>]<sub>2</sub>

The compound was obtained as a brown powder.

IR [cm<sup>-1</sup>]: 690 (m), 821 (s), 900 (w), 975 (m), 1067 (s), 1192 (m), 1279 (w), 1318 (w), 1457 (m), 1592 (m), 2035 (m), 2106 (m), 2842 (w), 2943 (m), 3245 (m).

### [Ni(silyl-2,3,2-tetramine)]<sub>3</sub>[Fe(CN)<sub>6</sub>]<sub>2</sub>

The compound was obtained as a brown powder.

IR [cm<sup>-1</sup>]: 879 (w), 956 (m), 1062 (s), 1192 (w), 1262 (m), 1435 (w), 1590 (w), 1664 (w), 1786 (w), 2043 (m), 2117 (m), 2878 (m), 2925 (m), 3146 (m).

### [Ni(bissilyl-2,3,2-tetramine)]<sub>3</sub>[Fe(CN)<sub>6</sub>]<sub>2</sub>

The compound was obtained as a brown powder.

IR [cm<sup>-1</sup>]: 688 (w), 802 (m), 971 (m), 1072 (s), 1415 (m), 1610 (w), 2057 (s), 2094 (s), 2840 (m), 2942 (m), 3244 (m).

### K[Ni(silylclam)][Fe(CN)<sub>6</sub>]

The compound was obtained as a brown powder.

IR [cm<sup>-1</sup>]: 687 (w), 753 (w), 797 (w), 913 (m), 1093 (s), 1196 (s), 1418 (m), 1465 (m), 1622 (m), 2095 (s), 2876 (w), 2942 (w), 3240 (m), 3367 (m).

**[Ni(silyl-6-aminocyclam)]<sub>3</sub>[Fe(CN)<sub>6</sub>]<sub>2</sub>**

The compound was obtained as a brown powder.

IR [cm<sup>-1</sup>]: 679 (w), 771 (m), 953 (m), 1074 (s), 1164 (w), 1193 (w), 1261 (w), 1387 (w), 1447 (w), 1543 (m), 1622 (m), 2059 (m), 2091 (s), 2880 (m), 2929 (m), 2972 (m), 3266 (m), 3340 (m).

**15.2 Cu<sup>II</sup>/Fe<sup>III</sup> Cyanometallates****General Procedure**

To a heated (50 °C) solution of [Cu(polyamine)<sub>n</sub>]Cl<sub>2</sub> (n = 1, 3) (3 eq) in 40 mL/mmol of dry methanol a heated solution of K<sub>3</sub>[Fe(CN)<sub>6</sub>] (2 eq) in 65 mL/mmol of dry methanol was slowly added. A precipitate formed immediately and was filtered off, washed with dry ethanol and dried under vacuum to obtain [Cu(polyamine)<sub>n</sub>]<sub>3</sub>[Fe(CN)<sub>6</sub>]<sub>2</sub> (n = 1, 2) in quantitative yield.

**[Cu(AEAPTS)<sub>2</sub>]<sub>3</sub>[Fe(CN)<sub>6</sub>]<sub>2</sub>**

The compound was obtained as a green powder.

IR [cm<sup>-1</sup>]: 633 (m), 694 (w), 798 (m), 941 (m), 1030 (s), 1150 (s), 1207 (s), 1461 (w), 1592 (w), 2040 (m), 2873 (w), 2933 (w), 3268 (w).

**[Cu(silyl-2,3,2-tetramine)]<sub>3</sub>[Fe(CN)<sub>6</sub>]<sub>2</sub>**

The compound was obtained as a brown powder.

IR [cm<sup>-1</sup>]: 821 (w), 890 (w), 1062 (s), 1193 (w), 1262 (w), 1456 (m), 1605 (w), 2047 (s), 2102 (m), 2115 (m), 2839 (w), 2878 (m), 2937 (m), 2962 (w), 3127 (w), 3210 (w).

**[Cu(bissilyl-2,3,2-tetramine)]<sub>3</sub>[Fe(CN)<sub>6</sub>]<sub>2</sub>**

The compound was obtained as a brown powder.

IR [cm<sup>-1</sup>]: 692 (w), 782 (m), 819 (m), 896 (w), 1075 (s), 1193 (m), 1457 (m), 1609 (w), 2084 (s), 2840 (w), 2941 (w).

# Sol-Gel Processing

## 16.1 Ni<sup>II</sup>/Fe<sup>III</sup> Gels

### General Procedure

The Ni<sup>II</sup>/Fe<sup>III</sup> cyanometallate (1 eq) and tetraethoxysilane (TEOS) (2 eq) were dispersed in 330  $\mu\text{L}/(\text{mg cyanometallate})$  of 0.2 mol/L  $\text{NH}_3$  and stirred for 2 days at 70 °C. The reaction mixture was cooled to room temperature and allowed to dry on a glass plate. The network embedded in silica was obtained as a fine powder in quantitative yield after scraping off and washing with water.

### [Ni(AEAPTS)<sub>2</sub>]<sub>3</sub>[Fe(CN)<sub>6</sub>]<sub>2</sub> gel

The compound was obtained as a brown powder.

IR [ $\text{cm}^{-1}$ ]: 691 (m), 789 (m), 938 (s), 1044 (s), 1447 (w), 1650 (m), 2044 (s), 2109 (w), 2941 (w), 3281 (w).

EDX: C(K) 57.55%, N(K) 14.01%, O(K) 13.83%, Si(K) 10.52%, Fe(K) 1.55%, Ni(K) 2.54%.

Ferromagnetic;  $T_C = 10.6$  K;  $C = 3.95$  emu K mol<sup>-1</sup>;  $\mu_{eff} = 4.46$   $\mu_B$  at room temperature, 8.60  $\mu_B$  at maximum.

### [Ni(silyl-2,3,2-tetramine)]<sub>3</sub>[Fe(CN)<sub>6</sub>]<sub>2</sub> gel

The compound was obtained as a brown powder.

IR [ $\text{cm}^{-1}$ ]: 690 (w), 797 (m), 929 (m), 1071 (s), 1415 (s), 1641 (m), 2057 (s), 2094 (s), 2879 (w), 2934 (m), 3235 (m).

EDX: C(K) 60.74%, N(K) 13.66%, O(K) 12.18%, Si(K) 8.32%, Fe(K) 2.01%, Ni(K) 2.58%.

Paramagnetic;  $C = 3.64$  emu K mol<sup>-1</sup>;  $\mu_{eff} = 5.40$   $\mu_B$ .

### [Ni(bissilyl-2,3,2-tetramine)]<sub>3</sub>[Fe(CN)<sub>6</sub>]<sub>2</sub> gel

The compound was obtained as a brown powder.

IR [ $\text{cm}^{-1}$ ]: 668 (w), 692 (w), 784 (m), 883 (m), 946 (s), 1056 (s), 1098 (s), 1464 (m), 1647 (m), 1958 (w), 2045 (s), 2088 (w), 2871 (m), 2931 (m), 2956 (m), 3270 (m).

EDX: C(K) 56.86%, N(K) 12.29%, O(K) 10.79%, Si(K) 9.5%, Fe(K) 3.81%, Ni(K) 5.42%.

Paramagnetic;  $C = 5.80$  emu K mol<sup>-1</sup>;  $\mu_{eff} = 6.81$   $\mu_B$ .

**K[Ni(silylcyclam)][Fe(CN)<sub>6</sub>] gel**

The compound was obtained as a brown powder.

IR [cm<sup>-1</sup>]: 869 (w), 795 (w), 916 (m), 1095 (s), 1301 (w), 1418 (m), 1466 (m), 1626 (m), 2096 (s), 2879 (w), 2950 (w), 3277 (m), 3378 (m).

EDX: C(K) 38.41%, N(K) 34.67%, O(K) 18.37%, Si(K) 3.60%, Cl(K) 0.25%, K(K) 1.12%, I(L) 0.20%, Fe(K) 1.62%, Ni(K) 1.76%.

Paramagnetic;  $C = 1.39 \text{ emu K mol}^{-1}$ ;  $\mu_{eff} = 3.34 \mu_B$ .

**[Ni(silyl-6-aminocyclam)]<sub>3</sub>[Fe(CN)<sub>6</sub>]<sub>2</sub> gel**

The compound was obtained as a brown powder.

IR [cm<sup>-1</sup>]: 689 (w), 767 (w), 945 (w), 1056 (s), 1083 (s), 1265 (w), 1371 (w), 1415 (m), 1549 (s), 1607 (s), 2046 (m), 2093 (m), 2884 (w), 2945 (w), 3270 (s), 3347 (s).

EDX: C(K) 38.77%, N(K) 31.99%, O(K) 19.77%, Si(K) 5.31%, K(K) 0.61%, Fe(K) 1.47%, Ni(K) 2.08%.

Paramagnetic;  $C = 2.24 \text{ emu K mol}^{-1}$ ;  $\mu_{eff} = 4.23 \mu_B$ .

**16.2 Cu<sup>II</sup>/Fe<sup>III</sup> Gels****General Procedure**

[Cu(polyamine)<sub>n</sub>]<sub>3</sub>[Fe(CN)<sub>6</sub>]<sub>2</sub> (n = 1, 2) (1 eq) and tetraethoxysilane (TEOS) (2 eq) were dispersed in 330 mL/(mg cyanometallate) of 0.2 mol/L NH<sub>3</sub> and stirred for 2 days at 70 °C. The reaction mixture was cooled to room temperature and allowed to dry on a glass plate. The network embedded in silica was obtained as a fine powder in quantitative yield after scraping off and washing with water.

**[Cu(AEAPTS)<sub>2</sub>]<sub>3</sub>[Fe(CN)<sub>6</sub>]<sub>2</sub> gel**

The compound was obtained as a purple powder.

IR [cm<sup>-1</sup>]: 688 (m), 787 (m), 937 (s), 1043 (s), 1452 (w), 1601 (m), 1650 (m), 2043 (m), 2878 (m), 1942 (m), 3280 (m).

EDX: C(K) 55.23%, N(K) 11.31%, O(K) 13.62%, Si(K) 12.72%, Cl(K) 0.17%, Fe(K) 2.61%, Cu(K) 4.35%.

Paramagnetic;  $C = 1.56 \text{ emu K mol}^{-1}$ ;  $\mu_{eff} = 3.52 \mu_B$ .

**[Cu(silyl-2,3,2-tetramine)]<sub>3</sub>[Fe(CN)<sub>6</sub>]<sub>2</sub> gel**

The compound was obtained as a violet powder.

IR [cm<sup>-1</sup>]: 686 (w), 798 (w), 949 (m), 1058 (s), 1416 (w), 1466 (w), 1648 (w), 2089 (s), 2945 (w), 3245 (w).

EDX: C(K) 37.81%, N(K) 30.71%, O(K) 17.90%, Si(K) 7.50%, K(K) 0.54%, I(L) 0.19%, Fe(K) 2.22%, Cu(K) 3.12%.

**[Cu(bissilyl-2,3,2-tetramine)]<sub>3</sub>[Fe(CN)<sub>6</sub>]<sub>2</sub> gel**

The compound was obtained as a violet powder.

IR [cm<sup>-1</sup>]: 683 (w), 199 (w), 1077 (s), 1412 (m), 1637 (w), 2084 (s), 3250 (w).

EDX: C(K) 16.92%, N(K) 14.55%, O(K) 14.58%, Al(K) 0.39%, Si(K) 18.95%, K(K) 7.66%, Fe(K) 14.73%, Cu(K) 12.22%.



## **Part IV**

# **Appendix**



# Glossary

**ref.** references

## Chemicals

**AEAPTS** N-(2-aminoethyl)-3-aminopropyltrimethoxysilane, “silyl-ethylenediamine”

**d<sub>6</sub>-acetone** deuterated acetone

**6-aminocyclam** 1,4,8,11-tetraazacyclotetradecane-6-amine

**ampy** 2-aminomethylpyridine

**2,2'-bipy** 2,2'-bipyridine

**bissilyl-2,3,2-tetramine** N<sup>1</sup>,N<sup>1'</sup>-(propane-1,3-diyl)bis(N<sup>2</sup>-(3-(trimethoxysilyl)propyl)-ethane-1,2-diamine)

**BPDS** biphenyl-4,4'-disulfonate

**bpm** bis(1-pyrazolyl)methane

**BzO** benzoate

**C<sub>3</sub>H<sub>5</sub>N<sub>5</sub>-azacyclam** 2,4-diamino-1,3,5-triazin-6-yl-3-(1,3,5,8,12-pentaazacyclotetradecane)

**chxn** 1,2-diaminocyclohexane

**rac-CTH** *rac*-5,7,7,12,14,14-hexamethyl-1,4,8,11-tetraazacyclotetradecane

**cyclam** 1,4,8,11-tetraazacyclotetradecane

**dipn** diethylenetriamine

**1,1-dmen** 1,1-dimethylethylenediamine

**en** ethylenediamine

**Et** ethyl (CH<sub>3</sub>CH<sub>2</sub>-)

**Et<sub>2</sub>azacyclam** 3,10-diethyl-1,3,5,8,10,12-hexaazacyclotetradecane

**Et<sub>3</sub>N** triethylamine

**EtOH** ethanol

**ITO** indium tin oxide

**Me** methyl (CH<sub>3</sub>-)

**Me<sub>2</sub>azacyclam** 3,10-dimethyl-1,3,5,8,10,12-hexaazacyclotetradecane

**MeCN** acetonitrile

**MeOD, d<sub>4</sub>-MeOD** deuterated methanol

**MeOH** methanol

**N-men** N-methylethylenediamine

**(OH)<sub>2</sub>azacyclam** 3,10-dihydroxyethyl-1,3,5,8,10,12-hexaazacyclotetradecane

**pn** 1,2-diaminopropane

**PhBSO<sub>3</sub><sup>-</sup>** p-phenylbenzenesulfonate

**silyl-6-aminocyclam** 1-(1,4,8,11-tetraazacyclotetradecane)-3-(3-(triethoxysilyl)propyl)-  
urea

**silylcyclam** 1-(3-(trimethoxysilyl)propyl)-1,4,8,11-tetraazacyclotetradecane

**silyl-2,3,2-tetramine** N<sup>1</sup>-(2-aminoethyl)-N<sup>3</sup>-(2-((3-(trimethoxysilyl)propyl)amino)-  
ethyl)propane-1,3-diamine

**TEOS** tetraethoxysilane

**2,3,2-tetramine** N,N'-bis(2-aminoethyl)-1,3-propanediamine

**3,2,3-tetramine** N,N'-bis(3-aminopropyl)-1,2-ethanediamine

**Tf** trifluoromethanesulfonate

**THF** tetrahydrofurane

**tn** trimethylenediamine

**TolSO<sub>3</sub>** p-toluenesulfonate

**tosyl** p-toluenesulfonyl

**Tp** trispyrazolylborate

**tren** tris(2-aminoethyl)amine

## Physical quantities and constants

$B = \mu_0 H$ , external magnetic field (in Tesla T)

$C$  Curie constant

$\chi_m$  molar magnetic susceptibility

$T_C$  Curie temperature

$T_N$  Néel temperature

$\theta$  Weiss constant

**emu** electromagnetic unit, equivalent 1 cm<sup>3</sup>

$g$  gyromagnetic ratio

$H$  external magnetic field (in Ampere per meter)

$h_c$  coercive field

$J$  coupling constant

$k_B$  Boltzmann constant

$M$  magnetization

$m_r$  remanent magnetization

$m_s$  saturation magnetization

**MHz** Megahertz

$\mu$  magnetic permeability

$\mu_0$  vacuum permeability

$\mu_B$  Bohr magneton,  $9.27400968(20) \cdot 10^{-24} \text{ J T}^{-1}$

$\mu_{eff}$  effective magnetic moment

$N_A$  Avogadro constant

$\mathbf{q}$  scattering vector

$S$  spin

$T$  temperature

**Characterization Methods**

**EDX** energy-dispersive X-ray spectroscopy

**FTIR** Fourier transformed infrared spectroscopy

**NMR** nuclear magnetic resonance

**pXRD** powder X-ray diffraction

**SEM** scanning electron microscope

**SWAXS** small- and wide-angle X-ray scattering

**SQUID** semiconducting quantum interference device

**ac** alternating current

**dc** direct current

**FC** field cooled

**ZFC** zero-field cooled

**NMR**

$\delta$  chemical shift

**ppm** parts per million

**s** singlet

**d** doublet

**t** triplet

**q** quartet

**m** multiplet

**FTIR**

**s** strong

**m** middle

**w** weak

# Bibliography

- (1) Ebelmen *Liebigs Ann. Chem.* **1846**, *57*, 319–355.
- (2) Geffcken, W.; Berger, E. Verfahren zur Änderung des Reflexionsvermögens optischer Gläser., German pat., 736411, May 1939.
- (3) Hurd, C. B. *Chem. Rev.* **1938**, *22*, 403–422.
- (4) Kistler, S. S. *The Journal of Physical Chemistry* **1931**, *36*, 52–64.
- (5) Dislich, H. *Angew. Chem. Int. Ed.* **1971**, *10*, 363–370.
- (6) Levene, L.; Thomas, I. Process of converting metalorganic compounds and high purity products obtained therefrom. pat., 3640093 A, Feb. 1972.
- (7) Chantrell, P. G.; Popper, P. a. In *Special Ceramics 1964*, ed. by Popper, P., Academic Press: New York, 1965, pp 87–103.
- (8) Brinker, C. J.; Scherer, G. W., *Sol-gel science: the physics and chemistry of sol-gel processing*; Academic Press, Inc.: 1990.
- (9) Schubert, U.; Hüsing, N., *Synthesis of Inorganic Materials, Third Edition*, 3rd ed.; Wiley-VCH Verlag & Co. KGaA: 2012, pp 165–191.
- (10) Buckley, A. M.; Greenblatt, M. *Journal of Chemical Education* **1994**, *71*, 599–602.
- (11) Silva, R. F.; Vasconcelos, W. L. *Mat. Res.* **1999**, *2*, 197–200.
- (12) Twej, W. A. A. *Iraqi J. Sci.* **2009**, *50*, 43–49.
- (13) Castanedo-Pérez, R.; Jiménez-Sandoval, O.; Jiménez-Sandoval, S.; Márquez-Marín, J.; Mendoza-Galván, A.; Torres-Delgado, G.; Maldonado-Alvarez, A. *J. Vac. Sci. Technol. A* **1999**, *17*, 1811–1816.
- (14) Morrison, R. T.; Boyd, R. N., *Organic Chemistry*, 6, illustrated; Prentice Hall: 1992.
- (15) Kyaw, A. K. K.; Sun, X. W.; Jiang, C. Y.; Lo, G. Q.; Zhao, D. W.; Kwong, D. L. *Appl. Phys. Lett.* **2008**, *93* 221107, 221107.
- (16) Flory, P. J., *Principles of polymer chemistry*, 1. publ. 1953, 8. print.; Cornell Univ. Press: Ithaca, New York, 1971.
- (17) Granqvist, C. G. *Sol. Energy Mat. Sol. Cells* **2007**, *91*, 1529–1598.
- (18) Fahland, M; Karlsson, P; Charton, C *Thin Solid Films* **2001**, *392*, 334 –337.
- (19) Kim, H.; Gilmore, C. M.; Piqué, A.; Horwitz, J. S.; Mattoussi, H.; Murata, H.; Kafafi, Z. H.; Chrisey, D. B. *J. Appl. Phys.* **1999**, *86*, 6451–6461.

- (20) Kim, H.; Horwitz, J. S.; Kushto, G.; Piqué, A.; Kafafi, Z. H.; Gilmore, C. M.; Chrisey, D. B. *J. Appl. Phys.* **2000**, *88*, 6021–6025.
- (21) Tak, Y.-H.; Kim, K.-B.; Park, H.-G.; Lee, K.-H.; Lee, J.-R. *Thin Solid Films* **2002**, *411*, 12–16.
- (22) Hamberg, I.; Svensson, J. S. E. M.; Eriksson, T. S.; Granqvist, C.-G.; Arrenius, P.; Norin, F. *Appl. Opt.* **1987**, *26*, 2131–2136.
- (23) Guglielmi, M. *English J. Sol-Gel Sci. Technol.* **1997**, *8*, 443–449.
- (24) Tanaka, N.; Kobayashi, H.; Ishizuka, N.; Minakuchi, H.; Nakanishi, K.; Hosoya, K.; Ikegami, T. *J. Chrom. A* **2002**, *965*, 35–49.
- (25) Mallik, R.; Hage, D. S. *J. Sep. Sci.* **2006**, *29*, 1686–1704.
- (26) Russell-Floyd, R. S.; Harris, B.; Cooke, R. G.; Laurie, J.; Hammett, F. W.; Jones, R. W.; Wang, T. *J. Am. Ceram. Soc.* **1993**, *76*, 2635–2643.
- (27) Wu, Y.; Zhang, L.; Li, G.; Liang, C.; Huang, X.; Zhang, Y.; Song, G.; Jia, J.; Zhixiang, C. *Mat. Res. Bull.* **2001**, *36*, 253–263.
- (28) Trimmel, G.; Lembacher, C.; Kickelbick, G.; Schubert, U. *New J. Chem.* **2002**, *26*, 759–765.
- (29) Malenovska, M.; Martinez, S.; Neouze, M.-A.; Schubert, U. *Eur. J. Inorg. Chem.* **2007**, *2007*, 2609–2611.
- (30) Pauthe, M.; Bernstein, E.; Dumas, J.; Saviot, L.; Pradel, A.; Ribes, M. *J. Mater. Chem.* **1999**, *9*, 187–191.
- (31) Yang, P.; Song, C. F.; Lǎ¼, M. K.; Yin, X.; Zhou, G. J.; Xu, D.; Yuan, D. R. *Chem. Phys. Lett.* **2001**, *345*, 429–434.
- (32) Jia, W.; Wang, Y.; Fernandez, F.; Wang, X.; Huang, S.; Yen, W. *Mat. Sci. Engin.: C* **2001**, *16*, 55–58.
- (33) Yang, P.; Lü, M. K.; Song, C. F.; Zhou, G. J.; Xu, D.; Yuan, D. R. *Inorg. Chem. Comm.* **2002**, *5*, 187–191.
- (34) Lifshitz, E.; Yassen, M.; Bykov, L.; Dag, I.; Chaim, R. *NATO ASI Series E: Appl. Sci.* **1994**, *260*, 503–507.
- (35) Othmani, A.; Plenet, J.; Berstein, E.; Bovier, C.; Dumas, J.; Riblet, P.; Gilliot, P.; Lǎ©vy, R.; Grun, J. *J. Cryst. Growth* **1994**, *144*, 141–149.
- (36) Licciulli, A.; De, G.; Mazzoldi, P.; Catalano, M.; Mirengghi, L.; Tapfer, L. *Adv. Cryst. Growth* **1996**, *203*, 59–64.
- (37) Renteria, V.; Campero, A.; Garcia M, J. *English J. Sol-Gel Sci. Technol.* **1998**, *13*, 663–666.
- (38) Fick, J.; Schell, J.; Martucci, A.; Guglielmi, M. *Proc. SPIE* **1999**, *3620*, 198–205.
- (39) Moggi, P.; Predieri, G.; Silvestri, F. D.; Ferretti, A. *Appl. Cat. A: General* **1999**, *182*, 257–265.



- (40) Lange, C.; De Caro, D.; Gamez, A.; Storck, S.; Bradley, J. S.; Maier, W. F. *Langmuir* **1999**, *15*, 5333–5338.
- (41) Bönnemann, H.; Endruschat, U.; Tesche, B.; Rufinska, A.; Lehmann, C.; Wagner, F.; Filoti, G.; Pârvulescu, V.; Pârvulescu, V. *Eur. J. Inorg. Chem.* **2000**, *2000*, 819–822.
- (42) Pârvulescu, A.; Gagea, B.; Alifanti, M.; Pârvulescu, V.; Pârvulescu, V.; Nae, S.; Răzuș, A.; Poncelet, G.; Grange, P. *J. Catal.* **2001**, *202*, 319–323.
- (43) Tanaka, S.; Mizukami, F.; Niwa, S.; Toba, M.; Maeda, K.; Shimada, H.; Kunimori, K. *Appl. Cat. A: General* **2002**, *229*, 165–174.
- (44) Pârvulescu, V. I.; Pârvulescu, V.; Endruschat, U.; Filoti, G.; Wagner, F. E.; Kübel, C.; Richards, R. *Chem. Eur. J.* **2006**, *12*, 2343–2357.
- (45) Yang, H.; Wang, X.; Shi, H.; Xie, S.; Wang, F.; Gu, X.; Yao, X. *Appl. Phys. Lett.* **2002**, *81*, 5144–5146.
- (46) Yang, H.; Wang, X.; Shi, H.; Wang, F.; Gu, X.; Yao, X. *J. Cryst. Growth* **2002**, *236*, 371–375.
- (47) Yang, P.; Lü, M.; Song, C. F.; Zhou, G.; Xu, D.; Yuan, D. R. *J. Phys. Chem. Sol.* **2002**, *63*, 2047–2051.
- (48) Selvan, S. T.; Bullen, C.; Ashokkumar, M.; Mulvaney, P. *Adv. Mat.* **2001**, *13*, 985–988.
- (49) Jiang, H.; Yao, X.; Che, J.; Wang, M.; Kong, F. *Ceram. Int.* **2004**, *30*, 1685–1689.
- (50) Reda, S. *Acta Mat.* **2008**, *56*, 259–264.
- (51) Hübert, T.; Shimamura, A.; Klyszcz, A. *English J. Sol-Gel Sci. Technol.* **2004**, *32*, 131–135.
- (52) Xie, J.; Guo, W.; Wang, J. *English J. Wuhan Univ. Techn.-Mater. Sci. Ed.* **2011**, *26*, 216–221.
- (53) Ponce-Castaneda, S.; Martínez, J.; Ruiz, F.; Palomares-Sánchez, S.; Matutes-Aquino, J. *J. Magn. Magn. Mater.* **2002**, *250*, 160–163.
- (54) Popovici, M.; Gich, M.; Nižanský, D.; Roig, A.; Savii, C.; Casas, L.; Molins, E.; Zaveta, K.; Enache, C.; Sort, J.; de Brion, S.; Chouteau, G.; Nogués, J. *Chem. Mater.* **2004**, *16*, 5542–5548.
- (55) Ennas, G.; Falqui, A.; Marras, S.; Sangregorio, C.; Marongiu, G. *Chem. Mater.* **2004**, *16*, 5659–5663.
- (56) García-Cerda, L.; Montemayor, S. M. *J. Magn. Magn. Mater.* **2005**, *294*, e43–e46.
- (57) Gich, M.; Roig, A.; Frontera, C.; Molins, E.; Sort, J.; Popovici, M.; Chouteau, G.; Martín y Marero, D.; Nogués, J. *Journal of Applied Physics* **2005**, *98*, 044307–1–044307–5.
- (58) Răileanu, M.; Crișan, M.; Crișan, D.; Brăileanu, A.; Drăgan, N.; Zaharescu, M.; Stan, C.; Predoi, D.; Kuncser, V.; Marinescu, V. E.; Hodorogea, S. M. *J. Non-Cryst. Sol.* **2008**, *354*, 624–631.

- (59) Mitra, S.; Mandal, K.; Choi, E. S. *IEEE Trans. Magn.* **2008**, *44*, 2974–2977.
- (60) Teng, Z.; Li, J.; Yan, F.; Zhao, R.; Yang, W. *J. Mater. Chem.* **2009**, *19*, 1811–1815.
- (61) Vejpravova, J. P.; Brazda, P.; Mantlikova, A.; Niznansky, D.; Rohovec, J. *J. Phys.: Conf. Ser.* **2011**, *266*, 012123.
- (62) Burianova, S.; Vejpravova, J. P.; Holec, P.; Niznansky, D.; Plocek, J. *IOP Conference Series: Materials Science and Engineering* **2011**, *18*, 022015.
- (63) Zhen, B.; Jiao, Q.; Zhang, Y.; Wu, Q.; Li, H. *Applied Catalysis A: General* **2012**, *445–446*, 239–245.
- (64) Barvinschi, P.; Stefanescu, O.; Dippong, T.; Sorescu, S.; Stefanescu, M. *English J. Therm. Anal. Calorim.* **2013**, *112*, 447–453.
- (65) Valverde-Aguilar, G.; Pérez-Mazariego, J. L.; Marquina, V.; Gómez, R.; Aguilar-Franco, M.; Garcia-Macedo, J. *English J. Mater. Sci.* **2015**, *50*, 704–716.
- (66) García, R.; del Solar, M. R.; González-Leal, J.; Blanco, E.; Domínguez, M. *Mat. Chem. Phys.* **2015**, *154*, 1–9.
- (67) Avnir, D.; Levy, D.; Reisfeld, R. *J. Phys. Chem.* **1984**, *88*, 5956–5959.
- (68) Levy, D. *J. Non-Cryst. Sol.* **1992**, *147–148*, 508–517.
- (69) Levy, D.; del Monte, F.; López-Amo, M.; Otón, J. M.; Datta, P.; Matías, I. *J. Appl. Phys.* **1995**, *77*, 2804–2805.
- (70) Gilliland, J. W.; Yokoyama, K.; Yip, W. T. *Chem. Mater.* **2005**, *17*, 6702–6712.
- (71) Subbiah, S.; Mokaya, R. *Chem. Commun.* **2003**, 860–861.
- (72) Opallo, M.; Kukulka, J. *Electrochem. Commun.* **2000**, *2*, 394–398.
- (73) Opallo, M.; Kukulka-Walkiewicz, J. *Electrochim. Acta* **2001**, *46*, 4235–4242.
- (74) Maggini, M.; Scorrano, G.; Prato, M.; Brusatin, G.; Innocenzi, P.; Guglielmi, M.; Renier, A.; Signorini, R.; Meneghetti, M.; Bozio, R. *Adv. Mat.* **1995**, *7*, 404–406.
- (75) Subbiah, S.; Mokaya, R. *Chem. Commun.* **2003**, 92–93.
- (76) Zayat, M.; Pardo, R.; Levy, D. *J. Mater. Chem.* **2003**, *13*, 2899–2903.
- (77) Zheng, C.; Chen, W.; Ye, X.; Cai, S.; Xiao, X.; Wang, M. *Mater. Lett.* **2011**, *65*, 150–152.
- (78) Morpurgo, M.; Teoli, D.; Palazzo, B.; Bergamin, E.; Realdon, N.; Guglielmi, M. *Il Farmaco* **2005**, *60*, 675–683.
- (79) Langer, R. *Acc. Chem. Res.* **1993**, *26*, 537–542.
- (80) Raileanu, M.; Todan, L.; Crisan, M.; Braileanu, A.; Rusu, A.; Bradu, C.; Carpov, A.; Zaharescu, M. *J. Environ. Prot.* **2010**, *1*, 302–313.
- (81) Mahltig, B.; Fiedler, D.; Fischer, A.; Simon, P. *English J. Sol-Gel Sci. Technol.* **2010**, *55*, 269277.
- (82) Böttcher, H.; Kallies, K.-H.; Haufe, H.; Seidel, J. *Adv. Mat.* **1999**, *11*, 138–141.

- (83) Savini, I.; Santucci, R.; Venere, A.; Rosato, N.; Strukul, G.; Pinna, F.; Avigliano, L. *English Appl. Biochem. Biotechnol.* **1999**, *82*, 227–241.
- (84) Di, J.; Shen, C.; Peng, S.; Tu, Y.; Li, S. *Analyt. Chim. Acta* **2005**, *553*, 196–200.
- (85) Massari, A. M.; Finkelstein, I. J.; Fayer, M. D. *J. Am. Chem. Soc.* **2006**, *128*, 3990–3997.
- (86) Badjić, J. D.; Kostić, N. M. *J. Phys. Chem. B* **2001**, *105*, 7482–7489.
- (87) Velarde-Ortiz, R.; Larsen, G. *Chem. Mater.* **2002**, *14*, 858–866.
- (88) Lin, H.; Tang, J.; Wang, C. *Mater. Lett.* **2007**, *61*, 1637–1640.
- (89) Prasad, B. B.; Jauhari, D.; Verma, A. *Talanta* **2014**, *120*, 398–407.
- (90) Holleman, A. F.; Wiberg, E.; Wiberg, N., *Lehrbuch der Anorganische Chemie*; Walter de Gruyter Verlag: Berlin, 2007.
- (91) Riedel, E., *Anorganische Chemie*, 6. Aufl.; Walter de Gruyter Verlag: Berlin, 2004.
- (92) Sharpe, A., *The Chemistry of Cyano Complexes of the Transition Metals*; Maitlis, P. M., Stone, F. G. A., West, R., Eds.; Academic Press, Inc. (London) LTD.: 1976.
- (93) Navaza, A.; Chevrier, G.; Alzari, P. M.; Aymonino, P. J. *Acta Cryst. C* **1989**, *45*, 839–841.
- (94) Nanba, Y.; Asakura, D.; Okubo, M.; Zhou, H.; Amemiya, K.; Okada, K.; Glans, P.-A.; Jenkins, C. A.; Arenholz, E.; Guo, J. *Phys. Chem. Chem. Phys.* **2014**, *16*, 7031–7036.
- (95) Osiry, H.; Cano, A.; Lemus-Santana, A.; Rodríguez, A.; Carbonio, R.; Reguera, E. *J. Sol. State Chem.* **2015**, *230*, 374–380.
- (96) Rodríguez-Hernández, J.; Reguera, L.; Lemus-Santana, A.; Reguera, E. *Inorg. Chim. Acta* **2015**, *428*, 51–56.
- (97) Bowman, D. N.; Jakubikova, E. *Inorg. Chem.* **2012**, *51*, 6011–6019.
- (98) Bhattarai, N.; Stanbury, D. M. *Inorg. Chem.* **2012**, *51*, 13303–13311.
- (99) Bunn, A. G.; Carroll, P. J.; Wayland, B. B. *Inorg. Chem.* **1992**, *31*, 1297–1299.
- (100) Son, J.-S.; Lim, S.-C.; Lee, H.; Hong, S.-T. *Acta Cryst. E* **2015**, *71*, m135–m136.
- (101) Bowmaker, G. A.; Kennedy, B. J.; Reid, J. C. *Inorg. Chem.* **1998**, *37*, 3968–3974.
- (102) Gadet, V.; Bujoli-Doeuff, M.; Force, L.; Verdaguer, M.; Malkhi, K. E.; Deroy, A.; Besse, J. P.; Chappert, C.; Veillet, P.; Renard, J. P.; Beauvillain, P. In: Gatteschi, D., Kahn, O., Miller, J. S., Palacio, F., Eds.; *E: Applied Sciences*, Vol. 198; Springer Netherlands: New York, 1991; Chapter Towards High  $T_C$  Ferro and Ferrimagnetic Bi and Tridimensional Materials from Molecular Precursors, pp 281–295.
- (103) Hozumi, T.; Hashimoto, K.; Ohkoshi, S.-i. *J. Am. Chem. Soc.* **2005**, *127*, 3864–3869.
- (104) Zhong, Z. J.; Seino, H.; Mizobe, Y.; Hidai, M.; Verdaguer, M.; Ohkoshi, S.-i.; Hashimoto, K. *Inorg. Chem.* **2000**, *39*, 5095–5101.
- (105) Chelebaeva, E.; Larionova, J.; Guari, Y.; Sá Ferreira, R. A.; Carlos, L. D.; Almeida Paz, F. A.; Trifonov, A.; Guérin, C. *Inorg. Chem.* **2008**, *47*, 775–777.

- (106) Herrera, J. M.; Bleuzen, A.; Dromzée, Y.; Julve, M.; Lloret, F.; Verdaguer, M. *Inorg. Chem.* **2003**, *42*, 7052–7059.
- (107) Pearson, R. G. *Journal of the American Chemical Society* **1963**, *85*, 3533–3539.
- (108) Shriver, D. F. In *Structure And Bonding*; Structure and Bonding, Vol. 1; Springer Berlin Heidelberg: 1966, pp 32–58.
- (109) Verdaguer, M.; Girolami, G. In, Miller, J. S., Drillon, M., Eds.; Wiley VCH: 2004; Chapter 9 Magnetic Prussian Blue Analogs, pp 283–346.
- (110) Anonymous *Misc. Berol. Increm. Scient. (Berlin)* **1710**, *1*, 377–378.
- (111) Woodward, J. *Phil. Trans.* **1724**, *33*, 15–17.
- (112) Brown, J. *English Phil. Trans.* **1724**, *33*, 17–24.
- (113) Davidson, D.; Welo, L. A. *The Journal of Physical Chemistry* **1928**, *32*, 1191–1196.
- (114) Ito, A.; Suenaga, M.; Ono, K. *J. Chem. Phys.* **1968**, *48*, 3597–3599.
- (115) Robin, M. B. *Inorg. Chem.* **1962**, *1*, 337–342.
- (116) Robin, M. B.; Day, P. In *Advances in Inorganic Chemistry and Radiochemistry*, Emeléus, H., Sharpe, A., Eds.; Advances in Inorganic Chemistry and Radiochemistry, Vol. 10; Academic Press: 1968, pp 247–422.
- (117) Fluck, E.; Kerler, W.; Neuwirth, W. *Angew. Chem. Int. Ed.* **1963**, *2*, 277–287.
- (118) Epstein, L. M. *J. Chem. Phys.* **1962**, *36*, 2731–2737.
- (119) Duncan, J. F.; Wigley, P. W. R. *J. Chem. Soc.* **1963**, 1120–1125.
- (120) Buser, H. J.; Schwarzenbach, D.; Petter, W.; Ludi, A. *Inorg. Chem.* **1977**, *16*, 2704–2710.
- (121) Buser, H. J.; Ludi, A.; Petter, W.; Schwarzenbach, D. *J. Chem. Soc., Chem. Commun.* **1972**, 1299–1299.
- (122) Keggin, J. F.; Miles, F. D. *Nature* **1936**, *137*, 577–578.
- (123) Bozorth, R. M.; Williams, H. J.; Walsh, D. E. *Phys. Rev.* **1956**, *103*, 572–578.
- (124) Wilde, R. E.; Ghosh, S. N.; Marshall, B. J. *Inorg. Chem.* **1970**, *9*, 2512–2516.
- (125) Herren, F.; Fischer, P.; Ludi, A.; Haelg, W. *Inorganic Chemistry* **1980**, *19*, 956–959.
- (126) Entley, W. R.; Treadway, C. R.; Girolami, G. S. *Mol. Cryst. Liq. Cryst.* **1995**, *273*, 153–166.
- (127) Ludi, A.; Guedel, H. U.; Rugg, M. *Inorg. Chem.* **1970**, *9*, 2224–2227.
- (128) Ludi, A.; Güdel, H. U. English In *Structure and Bonding*; Structure and Bonding, Vol. 14; Springer Berlin Heidelberg: 1973, pp 1–21.
- (129) Shatruck, M.; Avendano, C.; Dunbar, K. R. In *Progress in Inorganic Chemistry*, Karlin, K. D., Ed.; John Wiley & Sons, Inc.: 2009; Chapter Cyanide-Bridged Complexes of Transition Metals: A Molecular Magnetism Perspective, pp 155–334.
- (130) Herrera, J. M.; Marvaud, V.; Verdaguer, M.; Marrot, J.; Kalisz, M.; Mathoniere, C. *Angew. Chem. Int. Ed.* **2004**, *43*, 5468–5471.

- (131) Mathoniere, C.; Podgajny, R.; Guionneau, P.; Labrugere, C.; Sieklucka, B. *Chem. Mater.* **2005**, *17*, 442–449.
- (132) Kou, H.-Z.; Zhou, B.; Si, S.-F.; Wang, R.-J. *Eur. J. Inorg. Chem.* **2004**, *2004*, 401–408.
- (133) Sieklucka, B.; Szklarzewicz, J.; Kemp, T. J.; Errington, W. *Inorg. Chem.* **2000**, *39*, 5156–5158.
- (134) Rombaut, G.; Verelst, M.; Golhen, S.; Ouahab, L.; Mathoniere, C.; Kahn, O. *Inorg. Chem.* **2001**, *40*, 1151–1159.
- (135) Bonadio, F.; Gross, M.; Stoeckli-Evans, H.; Decurtins, S. *Inorg. Chem.* **2002**, *41*, 5891–5896.
- (136) Pradhan, R.; Desplanches, C.; Guionneau, P.; Sutter, J.-P. *Inorg. Chem.* **2003**, *42*, 6607–6609.
- (137) Chang, F.; Sun, H.-L.; Kou, H.-Z.; Gao, S. *Inorg. Chem. Comm.* **2002**, *5*, 660–663.
- (138) Boskovic, C.; Bircher, R.; Tregenna-Piggott, P. L. W.; Güdel, H. U.; Paulsen, C.; Wernsdorfer, W.; Barra, A.-L.; Khatsko, E.; Neels, A.; Stoeckli-Evans, H. *J. Am. Chem. Soc.* **2003**, *125*, 14046–14058.
- (139) Schelter, E. J.; Prosvirin, A. V.; Dunbar, K. R. *J. Am. Chem. Soc.* **2004**, *126*, 15004–15005.
- (140) Song, Y.; Zhang, P.; Ren, X.-M.; Shen, X.-F.; Li, Y.-Z.; You, X.-Z. *J. Am. Chem. Soc.* **2005**, *127*, 3708–3709.
- (141) Li, D.; Parkin, S.; Wang, G.; Yee, G. T.; Clérac, R.; Wernsdorfer, W.; Holmes, S. M. *J. Am. Chem. Soc.* **2006**, *128*, 4214–4215.
- (142) Pilkington, M.; Decurtins, S. *CHIMIA Int. J. Chem.* **2000**, *54*, 593–601.
- (143) Berlinguette, C. P.; Vaughn, D.; Cañada Vilalta, C.; Galán-Mascarós, J. R.; Dunbar, K. R. *Angew. Chem. Int. Ed.* **2003**, *42*, 1523–1526.
- (144) Beltran, L. M. C.; Long, J. R. *Acc. Chem. Res.* **2005**, *38*, 325–334.
- (145) Mallah, T.; Auberger, C.; Verdaguer, M.; Veillet, P. *Chem. Commun.* **1995**, 61–62.
- (146) Rebilly, J.-N.; Mallah, T. English In *Single-Molecule Magnets and Related Phenomena*, Winpenny, R., Ed.; Structure and Bonding, Vol. 122; Springer Berlin Heidelberg: 2006, pp 103–131.
- (147) Sato, O. *Acc. Chem. Res.* **2003**, *36*, 692–700.
- (148) Miyasaka, H.; Matsumoto, N. *Chem. Lett.* **1997**, *5*, 427–428.
- (149) Lescouëzec, R.; Toma, L. M.; Vaissermann, J.; Verdaguer, M.; Delgado, F.; Ruiz-Pérez, C.; Lloret, F.; Julve, M. *Coord. Chem. Rev.* **2005**, *249*, 2691–2729.
- (150) Li, G.; Yan, P.; Sato, O.; Einaga, Y. *J. Sol. St. Chem.* **2005**, *178*, 36–40.
- (151) Re, N.; Gallo, E.; Floriani, C.; Miyasaka, H.; Matsumoto, N. *Inorg. Chem.* **1996**, *35*, 5964–5965.
- (152) Li, G.; Akitsu, T.; Sato, O.; Einaga, Y. *J. Am. Chem. Soc.* **2003**, *125*, 12396–12397.

- (153) You, Y. S.; Kim, D.; Do, Y.; Oh, S. J.; Hong, C. S. *Inorg. Chem.* **2004**, *43*, 6899–6901.
- (154) Kou, H.-Z.; Gao, S.; Ma, B.-Q.; Liao, D.-Z. *Chem. Commun.* **2000**, 713–714.
- (155) Shyu, H.-L.; Wei, H.-H.; Wang, Y. *Inorg. Chim. Acta* **1999**, *290*, 8–13.
- (156) Ohba, M.; Maruono, N.; Ōkawa, H.; Enoki, T.; Latour, J.-M. *J. Am. Chem. Soc.* **1994**, *116*, 11566–11567.
- (157) Toma, L.; Toma, L.; Delgado, F.; Ruiz-Pérez, C.; Sletten, J.; Cano, J.; Clemente-Juan, J.; Lloret, F.; Julve, M. *Coord. Chem. Rev.* **2006**, *250*, 2176–2193.
- (158) Yokoyama, T.; Okamoto, K.; Ohta, T.; Ohkoshi, S.-i.; Hashimoto, K. *Phys. Rev. B* **2002**, *65*, 064438.
- (159) Larionova, J.; Gross, M.; Pilkington, M.; Andres, H.; Stoeckli-Evans, H.; Güdel, H.; Decurtins, S. *Angew. Chem.* **2000**, *112*, 1667–1672.
- (160) Breuning, E.; Ruben, M.; Lehn, J.-M.; Renz, F.; Garcia, Y.; Ksenofontov, V.; Gütllich, P.; Wegelius, E.; Rissanen, K. *Angew. Chem. Int. Ed.* **2000**, *39*, 2504–2507.
- (161) Ruben, M.; Breuning, E.; Gisselbrecht, J.-P.; Lehn, J.-M. *Angew. Chem. Int. Ed.* **2000**, *39*, 4139–4142.
- (162) Marvilliers, A.; Riviere, E.; Audiere, J.-P.; Mallah, T.; Parsons, S. *Chem. Commun.* **1999**, 2217–2218.
- (163) Kim, Y.; Park, S.-M.; Nam, W.; Kim, S.-J. *Chem. Commun.* **2001**, 1470–1471.
- (164) Ruben, M.; Lehn, J.-M.; Vaughan, G. *Chem. Commun.* **2003**, 1338–1339.
- (165) Ohkoshi, S.-i.; Arimoto, Y.; Hozumi, T.; Seino, H.; Mizobe, Y.; Hashimoto, K. *Chem. Commun.* **2003**, 2772–2773.
- (166) Korzeniak, T.; Stadnicka, K.; Pelka, R.; Bałanda, M.; Tomala, K.; Kowalski, K.; Sieklucka, B. *Chem. Commun.* **2005**, 2939–2941.
- (167) Ruben, M.; Breuning, E.; Barboiu, M.; Gisselbrecht, J.-P.; Lehn, J.-M. *Chem. Eur. J.* **2003**, *9*, 291–299.
- (168) Ruben, M.; Breuning, E.; Lehn, J.-M.; Ksenofontov, V.; Renz, F.; Gütllich, P.; Vaughan, G. B. M. *Chem. Eur. J.* **2003**, *9*, 4422–4429.
- (169) Arimoto, Y.; Ohkoshi, S.-i.; Zhong, Z. J.; Seino, H.; Mizobe, Y.; Hashimoto, K. *Chem. Lett.* **2002**, *31*, 832–833.
- (170) Li, D.-f.; Zheng, L.-m.; Wang, X.-y.; Huang, J.; Gao, S.; Tang, W.-x. *Chem. Mater.* **2003**, *15*, 2094–2098.
- (171) Larionova, J.; Clérac, R.; Donnadiou, B.; Willemin, S.; Guérin, C. *Cryst. Growth Des.* **2003**, *3*, 267–272.
- (172) Szklarzewicz, J.; Podgajny, R.; Lewinski, K.; Sieklucka, B. *CrystEngComm* **2002**, *4*, 199–201.
- (173) Kania, R.; Lewinski, K.; Sieklucka, B. *Dalton Trans.* **2003**, 1033–1040.

- (174) Podgajny, R.; Korzeniak, T.; Stadnicka, K.; Dromzee, Y.; Alcock, N. W.; Errington, W.; Kruczala, K.; Balanda, M.; Kemp, T. J.; Verdaguer, M.; Sieklucka, B. *Dalton Trans.* **2003**, 3458–3468.
- (175) Podgajny, R.; Balanda, M.; Sikora, M.; Borowiec, M.; Spalek, L.; Kapusta, C.; Sieklucka, B. *Dalton Trans.* **2006**, 2801–2809.
- (176) Nowicka, B.; Bałanda, M.; Gawel, B.; Ćwiak, G.; Budziak, A.; Łasocha, W.; Sieklucka, B. *Dalton Trans.* **2011**, 40, 3067–3073.
- (177) Miyasaka, H.; Matsumoto, N.; Re, N.; Gallo, E.; Floriani, C. *Inorg. Chem.* **1997**, 36, 670–676.
- (178) Miyasaka, H.; Ieda, H.; Re, N.; Crescenzi, R.; Floriani, C. *Inorg. Chem.* **1998**, 37, 255–263.
- (179) Colacio, E.; Ghazi, M.; Stoeckli-Evans, H.; Lloret, F.; Moreno, J. M.; Pérez, C. *Inorg. Chem.* **2001**, 40, 4876–4883.
- (180) Przychodzeń, P.; Lewiński, K.; Bałanda, M.; Pelka, R.; Rams, M.; Wasiutyński, T.; Guyard-Duhayon, C.; Sieklucka, B. *Inorg. Chem.* **2004**, 43, 2967–2974.
- (181) Korzeniak, T.; Stadnicka, K.; Rams, M.; Sieklucka, B. *Inorg. Chem.* **2004**, 43, 4811–4813.
- (182) Lim, J. H.; Kang, J. S.; Kim, H. C.; Koh, E. K.; Hong, C. S. *Inorg. Chem.* **2006**, 45, 7821–7827.
- (183) Chelebaeva, E.; Larionova, J.; Guari, Y.; Ferreira, R. A. S.; Carlos, L. D.; Paz, F. A. A.; Trifonov, A.; Guérin, C. *Inorg. Chem.* **2009**, 48, 5983–5995.
- (184) Kou, H.-Z.; Ni, Z.-H.; Zhou, B.; Wang, R.-J. *Inorg. Chem. Comm.* **2004**, 7, 1150–1153.
- (185) Miyasaka, H.; Matsumoto, N.; Okawa, H.; Re, N.; Gallo, E.; Floriani, C. *J. Am. Chem. Soc.* **1996**, 118, 981–994.
- (186) Arimoto, Y.; Ohkoshi, S.-i.; Zhong, Z. J.; Seino, H.; Mizobe, Y.; Hashimoto, K. *J. Am. Chem. Soc.* **2003**, 125, 9240–9241.
- (187) Yuan, A.-H.; Shen, X.-P.; Wu, Q.-J.; Huang, Z.-X.; Xu, Z. *J. Coord. Chem.* **2002**, 55, 411–420.
- (188) Hozumi, T.; Ohkoshi, S.-i.; Arimoto, Y.; Seino, H.; Mizobe, Y.; Hashimoto, K. *J. Phys. Chem. B* **2003**, 107, 11571–11574.
- (189) Lim, J. H.; Yoo, H. S.; Yoon, J. H.; Koh, E. K.; Kim, H. C.; Hong, C. S. *Polyhedron* **2008**, 27, 299–303.
- (190) Ali, S. I.; Majid, K. *Thermochim. Acta* **1998**, 317, 141–149.
- (191) Shen, Z.; Zuo, J.-L.; Shi, F.-N.; Xu, Y.; Song, Y.; You, X.-Z. *Trans. Met. Chem.* **2001**, 26, 345–350.
- (192) Colacio, E.; Dominguez-Vera, J.; Ghazi, M.; Moreno, J.; Kivekäs, R.; Lloret, F.; Stoeckli-Evans, H. *Chem. Commun.* **1999**, 987–988.
- (193) Li, C.; Wong, W.-T. *Tetrahedron Lett.* **2002**, 43, 3217–3220.

- (194) Ohba, M.; Usuki, N.; Fukita, N.; Ōkawa, H. *Angew. Chem. Int. Ed.* **1999**, *38*, 1795–1798.
- (195) Chen, F.-T.; Li, D.-F.; Gao, S.; Wang, X.-Y.; Li, Y.-Z.; Zheng, L.-M.; Tang, W.-X. *Dalton Trans.* **2003**, 3283–3287.
- (196) Mallah, T.; Thiébaud, M.; Verdaguer, M.; Veillet, P. *Science* **1993**, *262*, 1554–1557.
- (197) Entley, W. R.; Girolami, G. S. *Science* **1995**, *268*, 397–400.
- (198) Güdel, H.; Stucki, H.; Ludi, A. *Inorg. Chim. Acta* **1973**, *7*, 121–124.
- (199) Sieklucka, B.; Podgajny, R.; Korzeniak, T.; Nowicka, B.; Pinkowicz, D.; Kozieł, M. *Eur. J. Inorg. Chem.* **2011**, *3*, 305–326.
- (200) Przychodzeń, P.; Korzeniak, T.; Podgajny, R.; Sieklucka, B. *Coord. Chem. Rev.* **2006**, *250*, 2234–2260.
- (201) Sieklucka, B.; Podgajny, R.; Przychodzeń, P.; Korzeniak, T. *Coord. Chem. Rev.* **2005**, *249*, 2203–2221.
- (202) Černák, J.; Orendáč, M.; Potočňák, I.; Chomič, J.; Orendáčová, A.; Skoršepa, J.; Feher, A. *Coord. Chem. Rev.* **2002**, *224*, 51–66.
- (203) Ohba, M.; Ōkawa, H. *Coord. Chem. Rev.* **2000**, *198*, 313–328.
- (204) Atanasov, M.; Comba, P.; Hausberg, S.; Martin, B. *Coord. Chem. Rev.* **2009**, *253*, 2306–2314.
- (205) Verdaguer, M.; Bleuzen, A.; Marvaud, V.; Vaissermann, J.; Seuleiman, M.; Desplanches, C.; Sculler, A.; Train, C.; Garde, R.; Gelly, G.; Lomenech, C.; Rosenman, I.; Veillet, P.; Cartier, C.; Villain, F. *Coord. Chem. Rev.* **1999**, *190–192*, 1023–1047.
- (206) Herchel, R.; Tuček, J.; Trávníček, Z.; Petridis, D.; Zbořil, R. *Inorg. Chem.* **2011**, *50*, 9153–9163.
- (207) Podgajny, R.; Chmel, N. P.; Balanda, M.; Tracz, P.; Gawel, B.; Zajac, D.; Sikora, M.; Kapusta, C.; Lasocha, W.; Wasiutynski, T.; Sieklucka, B. *J. Mater. Chem.* **2007**, *17*, 3308–3314.
- (208) Tanase, S.; Ferbinteanu, M.; Andruh, M.; Mathoniere, C.; Strenger, I.; Rombaut, G. *Polyhedron* **2000**, *19*, 1967–1973.
- (209) Van Langenberg, K.; Batten, S. R.; Berry, K. J.; Hockless, D. C. R.; Moubaraki, B.; Murray, K. S. *Inorg. Chem.* **1997**, *36*, 5006–5015.
- (210) Van Langenberg, K.; Hockless, D. C. R.; Moubaraki, B.; Murray, K. S. *Synth. Met.* **2001**, *122*, 573–580.
- (211) Ōkawa, H.; Ohba, M. In *Molecule-Based Magnetic Materials*, ed. by Turnbull, M.; *et al.*; Chapter 22, Am. Chem. Soc.: Washington, DC, 1996, pp 319–328.
- (212) Ohba, M.; Fukita, N.; Ōkawa, H. *Dalton Trans.* **1997**, 1733–1738.
- (213) Ōkawa, H.; Ohba, M. *Bull. Chem. Soc. Jpn.* **2002**, *75*, 1191–1203.
- (214) Colacio, E.; Domínguez-Vera, J. M.; Lloret, F.; Rodríguez, A.; Stoeckli-Evans, H. *Inorg. Chem.* **2003**, *42*, 6962–6964.



- (215) Ohba, M.; Usuki, N.; Fukita, N.; Ōkawa, H. *Inorg. Chem.* **1998**, *37*, 3349–3354.
- (216) Muga, I.; Vitoria, P.; Gutiérrez-Zorrilla, J. M.; Luque, A.; Román, P. *Acta Cryst.* **2002**, *E58*, m524–m526.
- (217) Nowicka, B.; Hagiwara, M.; Wakatsuki, Y.; Kisch, H. *Bull. Chem. Soc. Jpn.* **1999**, *72*, 441–445.
- (218) Colacio, E.; Dominguez-Vera, J.-M.; Ghazi, M.; Kivekäs, R.; Lloret, F.; Moreno, J.-M.; Stoeckli-evans, H. *Mol. Cryst. Liq. Cryst.* **1999**, *335*, 283–292.
- (219) Bellouard, F.; Clemente-León, M.; Coronado, E.; Galán-Mascarós, J. R.; Gómez-García, C. J.; Romero, F.; Dunbar, K. R. *Eur. J. Inorg. Chem.* **2002**, *2002*, 1603–1606.
- (220) Coronado, E.; Gómez-García, C. J.; Nuez, A.; Romero, F. M.; Waerenborgh, J. C. *Chem. Mater.* **2006**, *18*, 2670–2681.
- (221) Fukita, N.; Ohba, M.; Ōkawa, H. *Mol. Cryst. Liq. Cryst.* **2000**, *342*, 217–224.
- (222) Coronado, E.; Gómez-García, C. J.; Nuez, A.; Romero, F. M.; Rusanov, E.; Stoeckli-Evans, H. *Inorg. Chem.* **2002**, *41*, 4615–4617.
- (223) Coronado, E.; Giménez-Saiz, C.; Martínez-Agudo, J.; Nuez, A.; Romero, F.; Stoeckli-Evans, H. *Polyhedron* **2003**, *22*, 2435–2440.
- (224) Nayak, M.; Kundu, P.; Lemoine, P.; Koner, R.; Wei, H.-H.; Mohanta, S. *Polyhedron* **2006**, *25*, 2007–2014.
- (225) Ohba, M.; Ōkawa, H.; Ohto, A. *Chem. Commun.* **1995**, 1545–1546.
- (226) Ohba, M.; Ōkawa, H. *Mol. Cryst. Liq. Cryst.* **1996**, *286*, 101–108.
- (227) Ohba, M.; Ōkawa, H.; Fukita, N.; Hashimoto, Y. *J. Am. Chem. Soc.* **1997**, *119*, 1011–1019.
- (228) Ohba, M.; Iwamoto, T.; Ōkawa, H. *Chem. Lett.* **2002**, *10*, 1046–1047.
- (229) Usuki, N.; Ohba, M.; Okawa, H. *Bull. Chem. Soc. Jpn.* **2002**, *75*, 1693–1698.
- (230) Usuki, N.; Ohba, M.; Okawa, H. *English Mol. Cryst. Liq. Cryst.* **2002**, *376*, 59–64.
- (231) Kou, H.-Z.; Bu, W.-M.; Liao, D.-Z.; Jiang, Z.-H.; Yan, S.-P.; Fan, Y.-G.; Wang, G.-L. *Dalton Trans.* **1998**, 4161–4164.
- (232) Koo, J.-e.; Kim, D.-h.; Kim, Y.-S.; Do, Y. *Inorg. Chem.* **2003**, *42*, 2983–2987.
- (233) Kou, H.-Z.; Gao, S.; Bu, W.-M.; Liao, D.-Z.; Ma, B.-Q.; Jiang, Z.-H.; Yan, S.-P.; Fan, Y.-G.; Wang, G.-L. *Dalton Trans.* **1999**, 2477–2480.
- (234) Kou, H.-Z.; Gao, S.; Ma, B.-Q.; Liao, D.-Z. *Chem. Commun.* **2000**, 1309–1310.
- (235) Kou, H.-Z.; Bu, W.-M.; Gao, S.; Liao, D.-Z.; Jiang, Z.-H.; Yan, S.-P.; Fan, Y.-G.; Wang, G.-L. *Dalton Trans.* **2000**, 2996–3000.
- (236) Fukita, N.; Ohba, M.; Ōkawa, H.; Matsuda, K.; Iwamura, H. *Inorg. Chem.* **1998**, *37*, 842–848.
- (237) Zhang, S.-W.; Fu, D.-G.; Sun, W.-Y.; Hu, Z.; Yu, K.-B.; Tang, W.-X. *Inorg. Chem.* **2000**, *39*, 1142–1146.

- (238) Ohba, M.; Yamada, M.; Usuki, N.; Ōkawa, H. *Mol. Cryst. Liq. Cryst.* **2002**, *379*, 241–246.
- (239) Yanai, N.; Kaneko, W.; Yoneda, K.; Ohba, M.; Kitagawa, S. *J. Am. Chem. Soc.* **2007**, *129*, 3496–3497.
- (240) Ohba, M.; Yoneda, K.; Kitagawa, S. *CrystEngComm* **2010**, *12*, 159–165.
- (241) Saha, M. K.; Moón, M. C.; Palacio, F.; Bernal, I. *Inorg. Chem.* **2005**, *44*, 1354–1361.
- (242) El Fallah, M. S.; Rentschler, E.; Caneschi, A.; Sessoli, R.; Gatteschi, D. *Angew. Chem. Int. Ed.* **1996**, *35*, 1947–1949.
- (243) Atanasov, M.; Comba, P.; Förster, S.; Linti, G.; Malcherek, T.; Miletich, R.; Prikhod'ko, A. I.; Wadepohl, H. *Inorg. Chem.* **2006**, *45*, 7722–7735.
- (244) Jiles, D., *Introduction to magnetism and magnetic materials*, 1. ed.; Chapman and Hall: London [u.a.], 1991.
- (245) Coey, J. M. D., *Magnetism and magnetic materials*, 1. publ.; Cambridge Univ. Press: Cambridge [u.a.], 2010.
- (246) Stroppe, H., *Physik*; Fachbuchverlag Leipzig: 2005.
- (247) Néel, L. *Ann. Phys. (Paris)* **1948**, *3*, 137–198.
- (248) Holden, A. N.; Matthias, B. T.; Anderson, P. W.; Lewis, H. W. *Phys. Rev.* **1956**, *102*, 1463–1463.
- (249) Griebler, W.-D.; Babel, D. *Z. Naturforsch.* **1982**, *37b*, 832–837.
- (250) Henkel, H.; Babel, D. *Z. Naturforsch.* **1984**, *39b*, 880–886.
- (251) Babel, D. *Comments Inorg. Chem.* **1986**, *5*, 285–320.
- (252) Klenze, R.; Kanellakopoulos, B.; Trageser, G.; Eysel, H. H. *The Journal of Chemical Physics* **1980**, *72*, 5819–5828.
- (253) Gadet, V.; Mallah, T.; Castro, I.; Verdaguer, M.; Veillet, P. *J. Am. Chem. Soc.* **1992**, *114*, 9213–9214.
- (254) Griffith, J. S.; Orgel, L. E. *Q. Rev. Chem. Soc.* **1957**, *11*, 381–393.
- (255) Bosnich, B.; Tobe, M. L.; Webb, G. A. *Inorg. Chem.* **1965**, *4*, 1109–1112.
- (256) Bertini, I.; Luchinat, C.; Mani, F.; Scozzafava, A. *Inorg. Chem.* **1980**, *19*, 1333–1336.
- (257) Bennett, A. M.; Foulds, G. A.; Thornton, D. A.; Watkins, G. M. *Spectrochim. Acta A* **1990**, *46*, 13–22.
- (258) Van Alphen, J. *Rec. Trav. Chim. Pays-Bas* **1936**, *55*, 835–840.
- (259) Hack, T.; Raps, D.; Supplit, R.; Schubert, U. Korrosionsschutzschicht für Aluminium- und Magnesiumlegierungen., German pat., 2010/081757 A1 (Willy-Messerschmitt-Straße, 85521 Ottobrunn (DE)), July 2010.
- (260) Basnar, B.; Litschauer, M.; Abermann, S.; Bertagnolli, E.; Strasser, G.; Neouze, M.-A. *Chem. Commun.* **2011**, 361–363.
- (261) Bartlett, B. M.; Harris, T. D.; DeGroot, M. W.; Long, J. R. *Z. Anorg. Allg. Chem.* **2007**, *633*, 2380–2385.

- (262) Hervé, G.; Bernard, H.; Le Bris, N.; Yaouanc, J.-J.; Handel, H.; Toupet, L. *Tetrahedron Lett.* **1998**, *39*, 6861–6864.
- (263) Prokhorov, A.; Bris, N. L.; Bernard, H.; Claudon, G.; Handel, H. *Synth. Commun.* **2006**, *36*, 3271–3282.
- (264) Meunier, I.; Mishra, A. K.; Hanquet, B.; Guillard, R.; Cocolios, P. *Can. J. Chem.* **1995**, *73*, 685–695.
- (265) Chavez, F.; Sherry, A. D. *J. Org. Chem.* **1989**, *54*, 2990–2992.
- (266) Rubio, M.; Astorga, C.; Alfonso, I.; Rebolledo, F.; Gotor, V. *Synth. Commun.* **2002**, *32*, 2441–2452.
- (267) Kimura, E.; Haruta, M.; Koike, T.; Shionoya, M.; Takenouchi, K.; Iitaka, Y. *Inorg. Chem.* **1993**, *32*, 2779–2784.
- (268) Boschetti, F.; Denat, F.; Espinosa, E.; Lagrange, J.-M.; Guillard, R. *Chem. Commun.* **2004**, 588–589.
- (269) Prasad, A. S. B.; Kanth, J. V. B.; Periasamy, M. *Tetrahedron* **1992**, *48*, 4623–4628.
- (270) Takenouchi, K.; Watanabe, K.; Kato, Y.; Koike, T.; Kimura, E. *J. Org. Chem.* **1993**, *58*, 1955–1958.
- (271) Armarego, W. L.; Chai, C. L. L., *Purification of Laboratory Chemicals*, Fifth Edition; Armarego, W. L., Chai, C. L. L., Eds.; Butterworth-Heinemann: Burlington, 2003, pp 389–499.
- (272) Boll, R. et al., *Sensors: a comprehensive survey*. Boll, R., Göpel, W., Zemel, J. N., Eds.; VCH-Verl.-Ges.: Weinheim [u.a.], 1989; Vol. 5. Magnetic sensors.
- (273) Braginski, A. I.; Clarke, J.; Cantor, R.; Chesca, B.; Drung, D.; Foley, C. P.; Keene, M. N., *The SQUID handbook*; Clarke, J., I., B. A., Eds.; Wiley-VCH: Weinheim, 2004; Vol. 1. Fundamentals and technology of SQUIDs and SQUID systems.
- (274) Braginski, A. I.; Drung, D.; Cantor, R.; Foley, C. P.; Chesca, B.; Keene, M. N.; Clarke, J.; Kleiner, R., *The SQUID handbook*; Clarke, J., I., B. A., Eds.; Wiley-VCH: Weinheim, 2006; Vol. 2. Applications of SQUIDs and SQUID systems.
- (275) London Fritz Wolfgang, .-. , *Superfluids: Macroscopic Theory of Superconductivity*; Structure of matter series; Wiley; Chapman & Hall, Limited: New York; London, 1950.
- (276) Josephson, B. *Phys. Lett.* **1962**, *1*, 251–253.
- (277) Anderson, P. W.; Rowell, J. M. *Phys. Rev. Lett.* **1963**, *10*, 230–232.
- (278) Rowell, J. M. *Phys. Rev. Lett.* **1963**, *11*, 200–202.
- (279) Pascal, M. P. *Ann. Chim. Phys.* **1910**, *19*, 5–70.
- (280) Pascal, M. P. *Ann. Chim. Phys.* **1912**, *25*, 289–377.
- (281) Pascal, M. P. *Ann. Chim. Phys.* **1913**, *29*, 218–243.
- (282) Bain, G. A.; Berry, J. F. *J. Chem. Educ.* **2008**, *85*, 532–536.

- (283) König, E.; König, G., *Landolt-Börnstein*; Hellwege, K.-H., Hellwege, A. M., Eds.; Springer-Verlag Berlin Heidelberg: 1984; Vol. 12a, pp 4–5, 12–14.
- (284) Lueken, H., *Magnetochemie*; Vieweg+Teubner Verlag, Wiesbaden: 1999, pp 426–427.
- (285) Ohara, S.; Adschiri, T.; Ida, T.; Yashima, M.; Mikayama, T.; Abe, H.; Setsuhara, Y.; Nogi, K.; Miyahara, M.; Kaneko, K.; Ohtomo, A. In *Nanoparticle Technology Handbook*, Yokoyama, M., Hosokawa, K., Nogi, M., Naito, T. U., Eds.; Elsevier: Amsterdam, 2008, pp 267–315.
- (286) Guinier, A.; Fournet, G., *Small-Angle Scattering of X-rays*; Mayer, M. G., Ed.; Wiley; Chapman & Hall, Limited: New York; London, 1955.
- (287) Glatter, O.; Holmes, K. C.; Kirste, R.; Kosterz, G.; Kratky, O.; Laggner, P.; Leopold, H.; Müller, K.; Oberthür, R. C.; Pilz, I.; Porod, G.; Stuhmann, H.; Vonk, C. G.; Zipper, P., *Small Angle X-ray Scattering*; Glatter, O., Kratky, O., Eds.; Academic Press: 1982.
- (288) Hendricks, J. A.; Gullá, S. V.; Budil, D. E.; Hanson, R. N. *Bioorg. Med. Chem. Lett.* **2012**, *22*, 1743–1746.
- (289) Booth, B. L.; Ofunne, G. C.; Stacey, C.; Tait, P. J. T. *J. Organomet. Chem.* **1986**, *315*, 143–156.

**CV**



## Elisabeth Felbermair

---

PLACE AND DATE OF BIRTH: Braunau/Inn, Austria | 29 December 1986  
ADDRESS: Quellenstraße 109/16, 1100 Vienna, Austria  
PHONE: +43 650 9830032  
EMAIL: [e.felbermair@inrane.de](mailto:e.felbermair@inrane.de)

### WORK EXPERIENCE

---

- |                           |  |
|---------------------------|--|
| Oct 2012– <i>Current</i>  | Project Assistant at Institute of Materials Chemistry, TU Wien, Austria<br>Topic “Covalent Embedding of Cyanometallate Networks in Silica by Sol-Gel Processing”.<br>Supervision of master students in lab.  |
| Jul–Aug 2009              | Summer Intern at AMAG Austria Metall AG, Department Surface Technology, Austria<br>Study of the influence of degreasing procedures on the surface of aluminium sheets.   |
| Feb & Aug 2008            | Scientific assistant in the laboratory of Prof. Dr. Walter Weissensteiner University of Vienna, Institute of Organic Chemistry, Austria<br>Synthesis of ferrocenyl-aryl based <i>trans</i> -chelating diphosphine ligands for enantio-selective hydrogenation. |
| Jul/Aug 2003, 2006 & 2007 | Summer Intern at ALU-Stiftung GmbH Ranshofen, Austria<br>Secretarial work and billing.   |
| Jul/Aug 2004 & 2005       | Summer Intern at Dr. Hans Rant & Dr. Kurt Freyler Rechtsanwälte OEG, Austria<br>Secretarial work.  |

## EDUCATION

---

Oct 2012– <i>Current</i>	Doctoral School “Solids4Fun” (Building Solids for Function), TU Wien, Austria Student speaker: representation of students in faculty meetings, assistance for Summer School organisation.
Oct 2011– <i>Current</i>	Doctoral Study in Chemistry, TU Wien, Austria Thesis: “Cross-Linked Cyanometallate Networks of Ni(II) and Fe(II) in Silica” Advisor: Prof. Ulrich Schubert
Sep 2009–Jun 2010	Erasmus Stay at University of Salamanca, Spain
Oct 2005–Nov 2011	Diploma Study in Chemistry, University of Vienna, Austria Thesis: “Total Synthesis of (-)-Peanonisuffrone mono- and di-acetate” Advisors: Prof. F. Bermejo-González, Prof. W. Reischl Completed with distinction (grade point average: 1.0)
Sep 1997–Jun 2005	High School “Bundesgymnasium und Bundesrealgymnasium Braunau am Inn”, Austria Graduation with distinction (grade point average: 1.2)

## LANGUAGES

---

German:	Mothertongue
English:	Fluent
Spanish:	Fluent
French:	Intermediate Knowledge
Russian:	Basic Knowledge

## COMPUTER SOFTWARE

---

Excellent Knowledge:	L <sup>A</sup> T <sub>E</sub> X, gnuplot, Libre Office, MS Office
Intermediate Knowledge:	Origin
Basic Knowledge:	Adobe Photoshop & Indesign

## MEMBERSHIPS

---

2006– <i>Current</i>	Austrian Chemical Society (GÖCH - Gesellschaft Österreichischer Chemiker)
2014– <i>Current</i>	Member of Faculty Council, Faculty of Chemistry, TU Wien
2012–2014	List of Candidates for Faculty Council, Faculty of Chemistry, TU Wien
2012– <i>Current</i>	Choir of the TU Wien (TU Chor) Including concert coordination and other organisational tasks.

## PUBLICATIONS

---

### Articles

- ◇ E. Felbermair, A. Sidorenko, S. Paschen, J. Akbarzadeh, H. Peterlik, U. Schubert: “Covalent Embedding of Ni<sup>2+</sup>/Fe<sup>3+</sup> Cyanometallate Structures in Silica by Sol-Gel Processing”; *Chemistry – A European Journal*, **20** (2014), *30*, 9212–9215.

### Oral Presentations

- ◇ E. Felbermair, J. Akbarzadeh, A. Sidorenko, H. Peterlik, S. Paschen, U. Schubert: “Covalent Embedding of Ni<sup>2+</sup>-Fe<sup>3+</sup> Cyanometallates with Intriguing Magnetic Properties in Silica by Sol-Gel Processing”; 16. Austrian Chemistry Days 2013, University of Innsbruck, Innsbruck, Austria; 21.–24.09.2015.
- ◇ E. Felbermair, A. Sidorenko, J. Akbarzadeh, H. Peterlik, S. Paschen, U. Schubert: “Ni<sup>2+</sup>-Fe<sup>3+</sup> Cyanometallates Exhibiting Intriguing Magnetic Properties Covalently Embedded in Silica by Sol-Gel Processing”; Fourth International Conference on Multifunctional, Hybrid and Nanomaterials, Sitges, Spain; 09.–13.03.2015.
- ◇ E. Felbermair, J. Akbarzadeh, A. Sidorenko, U. Schubert: “Covalent Embedding of 2D Ni<sup>2+</sup>-Fe<sup>3+</sup> Cyanide Networks in Silica by Sol-Gel Processing”; 17th International Symposium on Silicone Chemistry, Berlin, Germany; 03.–08.08.2014.
- ◇ E. Felbermair, U. Schubert: “Kovalent in SiO<sub>2</sub> eingebettete 2D M<sup>2+</sup>-Eisen(III)-cyanid-Netzwerke durch Sol-Gel-Prozess”; 8. Workshop Anorganische Chemie in Österreich, Salzburg, Austria; 14.–15.04.2014.
- ◇ E. Felbermair, J. Akbarzadeh, H. Peterlik, A. Sidorenko, U. Schubert: “Covalent Embedding of 2D Metal Cyanide Networks by Sol-Gel Processing”; 15. Austrian Chemistry Days 2013, TU-Graz, Graz, Austria; 23.–26.09.2013.
- ◇ E. Felbermair, U. Schubert: “Cross-linking of 2D Metal Cyanide Networks by Sol-Gel Processing”; Third International Conference on Multifunctional, Hybrid and Nanomaterials, Sorrento, Italy; 03.–07.03.2013.



- ◇ E. Felbermair; U. Schubert: “Verknüpfung von 2D Metalcyanid-Netzwerken durch Sol-Gel-Prozess”; 7. Workshop Anorganische Chemie in Österreich, Innsbruck, Austria; 02.–03.04.2012.

### Poster Presentations

- ◇ E. Felbermair, J. Akbarzadeh, A. Sidorenko, U. Schubert: “Covalent Tethering and Cross-Linking of Ni<sup>2+</sup>-Fe<sup>3+</sup> Cyanometallates by Sol-Gel Processing”; 5<sup>th</sup> EuCheMS Chemistry Congress, Istanbul, Turkey; 31.08.2014–05.09.2014.
- ◇ E. Felbermair, J. Akbarzadeh, A. Sidorenko, U. Schubert: “Covalent Embedding Of M<sup>2+</sup>-Iron(III) Cyanide Networks In Silica By Sol Gel Processing”; 14th International Conference on Molecule-Based Magnets, Saint Petersburg, Russia; 05.07.2014–10.07.2014.
- ◇ E. Felbermair, U. Schubert: “Cross-Linking of 2-Dimensional Metal Cyanide Networks by Sol-Gel Processing”; 4<sup>th</sup> EuCheMS Chemistry Congress, Prague, Czech Republic; 26.08.2012–30.08.2012.
- ◇ D. Clemente-Tejeda; R. Galán-Fernández; E. Felbermair; F. Bermejo; “Total Synthesis of polyoxygenated Terpenoids isolated from *Paeonia albiflora* Pallas”; Twelfth Tetrahedron Symposium, Sitges, Spain; 21.–24.6.2011.